REPUBLIC OF TURKEY
YILDIZ TECHNICAL UNIVERSITY
GRADUATE SCHOOL OF NATURAL AND APPLIED SCIENCE

ZINC OXIDE BASED TRANSPARENT CONDUCTIVE OXIDE THIN FILMS DEPOSITED BY R.F. MAGNETRON SPUTTERING FOR PHOTOVOLTAIC APPLICATIONS

NİLÜFER DUYGULU

Ph.D. THESIS
DEPARTMENT OF METLAURGY AND MATERIALS ENGINEERING METALLURGY PROGRAM

ADVISOR
PROF. DR. AHMET EKERİM

ISTANBUL, 2013

REPUBLIC OF TURKEY
YILDIZ TECHNICAL UNIVERSITY
GRADUATE SCHOOL OF NATURAL AND APPLIED SCIENCES

ZINC OXIDE BASED TRANSPARENT CONDUCTIVE OXIDE THIN FILMS DEPOSITED BY R.F. MAGNETRON SPUTTERING FOR PHOTOVOLTAIC APPLICATIONS

A thesis submitted by Nilüfer DUYGULU in partial fulfillment of the requirements for the degree of **Doctor of Philosophy** is approved by the committee on 19.11.2013 in Department of Metallurgy and Materials Engineering, Metallurgy Program.

Thesis Advisor
Prof. Dr. Ahmet EKERİM
Yıldız Technical University

Co- Advisor
Assoc. Prof. Dr. Alp Osman KODOLBAŞ
TUBITAK

Approved By the Examining Committee

Prof. Dr. Ahmet EKERİM
Yıldız Technical University _____

Prof. Dr. Onuralp YÜCEL
Istanbul Technical University _____

Assoc. Prof. Dr. Muhlis Nezihi SARIDEDE
Yıldız Technical University _____

Prof. Dr. Bünyamin AKSAKAL
Yıldız Technical University _____

Prof. Dr. Filiz ÇINAR ŞAHİN
Istanbul Technical University _____

This research has been supported by Yildiz Technical University Scientific Research Projects Coordination Department. Project number: 2012-07-02-DOP03.

ACKNOWLEDGEMENTS

I would like to thank to my supervisor, Prof. Dr. Ahmet EKERİM for his guidance and encouragement throughout this work.

I would like to express my deepest gratitude to my co-supervisor Assoc. Prof. Dr. Alp Osman KODOLBAS. He believed in me and support at any time since we met. His open mind behavior with professional approach for any kind of problem helped me to improve my perspective. During work, we spent lots of enjoyable time with our group. This thesis would not have been possible without him.

I would like to thank the wonderful staff members Özlem Pehlivan, Okan Yılmaz, Deneb Menda, Rıfat Kangı and Adem Yenisoy. Their huge support in both work and moral made this thesis possible. Also, their helpful suggestions made the experimental part easier and they provide a very pleasant working atmosphere.

I would like to acknowledge every member of Photonics and Electronics Sensors Laboratory for their hospitality.

A special word of thanks goes to my best friends Aylin Bekem and Burak Birol for all the time spent both in and out of work.

I would like to thank Cem Berk and Rahmi Özdilli for giving me a helping hand any time.

I also wish to thank to my family especially my mother, my father, my sister and my nephew. Also I want to thank each and every single of my friends for their patience and worthy supports during my entire study.

Specially, I want to thank my love, my great husband Özgür Duygulu.

November, 2013

Nilüfer DUYGULU

TABLE OF CONTENTS

Page

LIST OF SYMBOLS vi
LIST OF ABBREVIATIONS vii
LIST OF FIGRURES viii
LIST OF TABLES xiii
ABSTRACT xvi
ÖZET xviii
CHAPTER 1 1
INTRODUCTION 1
1.1 Literature Review 1
1.2 Objective of the Thesis 2
1.3 Hypothesis 3
CHAPTER 2 5
LITERATURE SURVEY 5
2.1 Transparent Conductive Oxide (TCO) 5
2.2 Application Areas of Transparent Conductive Oxides 5
2.3 Transparent Conductive Oxides Materials 6
2.3.1 Zinc Oxide (ZnO) 7
2.3.2 Thermodynamic Properties of ZnO 8
2.3.3 Zinc Oxide Requirements as TCO Material 11
2.3.4 Doping elements for ZnO thin films 11
2.3.5 Zinc Oxide Deposition Techniques 13
2.4 Thin Film Growth Processes 13
2.4.1 Deposited layers 14
2.4.2 Thermodynamic descriptions of thin film deposition 15
2.4.3 Thin Film Deposition Process 18
2.4.4 Basic Sputtering Mechanisms 20
2.4.5 Plasmas in Deposition Processes 21
2.5 Sputtering Systems 21
2.5.1 Direct Current Magnetron Sputtering 23
2.5.2 Radio-Frequency Magnetron Sputtering 23
2.5.3 r.f. Magnetron Sputtering Parameters 25
2.5.3.1 r.f. Power 25
2.5.3.2 Target-to-substrate distance (D_{TS}) 25
2.5.3.3 Process gas pressure 26

2.5.3.4 Process gas pressure composition 26
2.5.3.5 Deposition rate/ Sputtering temperature 27
2.5.3.6 Structure Zone Models 28
2.6 Solar cell applications 32
2.6.1 Heterojunction with intrinsic thin layer (HIT) solar cell 35
CHAPTER3 37
EXPERIMENTAL STUDIES 37
3.1 TCO Sputtering 37
3.2 Target Materials 40
3.3 Substrate Cleaning Studies 40
3.3.1 Glass Cleaning 40
3.3.2 Wafer Cleaning 41
3.4 TCO Characterization Techniques 41
3.4.1 Four point probe 42
3.4.2 Ultraviolet–visible (UV–VIS) spectrophotometer 43
3.4.3 Scanning electron microscopy (SEM) 43
3.4.4 X-ray diffraction (XRD) 43
3.4.5 Transmission electron microscopy (TEM) 44
3.4.6 Atomic force microscopy AFM 45
3.5 a-Si/c-Si:H Solar Cell Fabrication 45
3.6 Solar Cell Characterizations 47
CHAPTER4 49
RESULTS and DISCUSSIONS 49
4.1 Investigation the Effect of Sputtering Parameters on Zinc Oxide ZnO Thin Films 49
4.1.1 Effect of r.f. power on ZnO thin films 50
4.1.1.1 Electrical properties of ZnO thin films sputtered at different r.f. powers 50
4.1.1.2 Structural properties of ZnO thin films sputtered at different r.f. powers 53
4.1.1.3 Morphological properties of ZnO thin films sputtered at different r.f. powers 56
4.1.1.4 Optical investigation of ZnO thin films sputtered at different r.f. powers 61
4.1.1.5 Summary of the r.f. power variation influence on ZnO thin film properties 64
4.1.2 Effect of target-to-substrate distance (D_{TS}) on ZnO thin films 66
4.1.2.1 Electrical properties of ZnO thin films sputtered at different D_{TS} 66
4.1.2.2 Structural properties of ZnO thin films sputtered at different D_{TS} 69
4.1.2.3 Morphological properties of ZnO thin films sputtered at different D_{TS} 71
4.1.2.4 Optical investigation of ZnO thin films sputtered at different D_{TS} 75
4.1.2.5 Summary of the D_{TS} variation influence on ZnO thin film properties 79
4.1.3 Effect of argon gas pressure on ZnO thin films 80
4.1.3.1 Electrical properties of ZnO thin films sputtered at different Ar pressures 81

4.1.3.2 Structural properties of ZnO thin films sputtered at different Ar pressures 83
4.1.3.3 Morphological properties of ZnO thin films sputtered at different Ar pressures 85
4.1.3.4 Optical investigation of ZnO thin films sputtered at different Ar pressures 88
4.1.3.5 Summary of the Ar pressure variation influence on ZnO thin film properties 91
4.1.4 Effect of deposition time on ZnO thin films 92
4.1.4.1 Electrical properties of ZnO thin films sputtered at different deposition times 93
4.1.4.2 Morphological properties of ZnO thin films sputtered at different deposition times 94
4.1.4.3 Optical investigation of ZnO thin films sputtered at different deposition times 96
4.1.4.4 Summary of the deposition time variation influence on ZnO thin film properties 98
4.1.5 TEM-HRTEM investigations of ZnO thin films 100
4.2 Investigation the Effect of Sputtering Parameters on Aluminum Doped Zinc Oxide ZnO:Al Thin Films 104
4.2.1 Effect of r.f. power on ZnO:Al thin films 104
4.2.1.1 Electrical properties of ZnO:Al thin films sputtered at different r.f. powers 105
4.2.1.2 Structural properties of ZnO:Al thin films sputtered at different r.f. powers 107
4.2.1.3 Morphological investigation of ZnO:Al thin films sputtered at different r.f. power 110
4.2.1.4 Optical investigation of ZnO:Al thin films sputtered at different r.f. power 112
4.2.1.5 Summary of the r.f. power variation influence on ZnO:Al thin film properties 116
4.2.2 Effect of target-to-substrate distance (D_{TS}) on ZnO:Al thin films .. 117
4.2.2.1 Electrical properties of ZnO:Al thin films sputtered at different D_{TS} 118
4.2.2.2 Structural properties of ZnO:Al thin films sputtered at different D_{TS} 120
4.2.2.3 Morphological properties of ZnO:Al thin films sputtered at different D_{TS} 122
4.2.2.4 Optical properties of ZnO:Al thin films sputtered at different D_{TS} 124
4.2.2.5 Summary of the ZnO:Al thin films sputtered at different D_{TS} ... 126
4.2.3 Effect of argon gas pressure on ZnO:Al thin films 129
4.2.3.1 Electrical properties of ZnO:Al thin films sputtered at different Ar pressures 129
4.2.3.2 Structural properties of ZnO:Al thin films sputtered at different Ar pressures 131
4.2.3.3 Morphological investigation of ZnO:Al thin films sputtered at different Ar pressures 133
4.2.3.4 Optical investigation of ZnO:Al thin films sputtered at different Ar pressures 136

4.2.3.5 Summary of the Ar pressure variation influence on ZnO:Al thin film properties 138
4.2.4 TEM-HRTEM investigations of ZnO:Al thin films 140
4.3 Structural Zone Behavior of ZnO:Al Thin Films 144
4.4 Application of ZnO:Al Thin Film to a-Si/c-Si:H Solar Cells 145
CHAPTER 5 148
CONCLUSIONS and FUTURE STUDIES 148
REFERENCES 155

LIST OF SYMBOLS

Å	Equal to 10^{-10} m
nm	Equal to 10^{-9} m
ζ	Supersaturation ratio
P	Condensate pressure
P_{VP}	Vapor pressure
J	Flux
$\Gamma_{c\text{-}v}$	Positive free energy of a new surface between the condensate and the vapor phase
$\Gamma_{s\text{-}c}$	Surface free energy between the substrate and the condensate
$\Gamma_{(s\text{-}v)}$	Surface free energy between the substrate and the vapor phase
r	Radius
V	System volume
S	Entropy
Ω	Volume of an adatom
ΔG^*	Gibbs energy
k_B	Boltzmann constant
ρ	Resistivity(Ω.cm)
η	Efficiency
V_{OC}	Open circuit voltages
Jsc	Short circuit current density
Rq	Root mean square roughness (nm)
Ra	Average roughness (nm)
sccm	Standard cubic centimeter per minutes at STP

LIST OF ABBREVIATIONS

D_{TS}	Distance From Target-To-Substrate
FWHM	Full Width At Half Maximum (Degree)
Wafer	A Thin Slice Of Semiconductor (Such As Silicon) Used As a Base For an Electronic Component, or Substrate
Substrate	The Material Made of ; a Si Wafer or Glass Slide
RMS	Root Mean Square
FOM	Figure Of Merrit
PVD	Physical Vapor Deposition
CVD	Chemical Vapor Deposition
ZnO	Zinc Oxide
ZnO:Al	Aluminum Doped Zinc Oxide
ITO	Indium Tin Oxide
SEM	Scanning Electron Microscope
HRSEM	High-Resolution Scanning Electron Microscopy
FESEM	Field Emission Scanning Electron Microscopy
TEM	Transmission Electron Microscopy
HRTEM	High-Resolution Transmission Electron Microscopy
FFT	Fast Fourier Transform
EDS	Energy-Dispersive X-Ray Spectroscopy
SAED	Selected Area Diffraction
AFM	Atomic Force Microscopy
XRD	X-Ray Diffraction
RCA	Radio Corporation Of America
PECVD	Plasma Enhanced Chemical Vapor Deposition
HIT	The Heterojunction solar cell with Intrinsic Thin layer

LIST OF FIGRURES

Page

Figure 2.1 The crystal structures of ZnO: (a) View along the c-axis on the oxygen terminated (00-1) plane, and (b): perspective view perpendicular to the c-axis (Large balls; oxygen and small balls; zinc) [52] 8
Figure 2.3 The relation between the defect formation and the Fermi energies with occupied and unoccupied formations [66] 10
Figure 2.4 Three modes of thin film growth processes; (a) Volmer–Weber, (b) Frank–Van der Merwe (c) Stranski–Krastanoff [78, 79] 15
Figure 2.5 Schematic representations of processes leading to three-dimensional nucleation and film growth [79] 15
Figure 2.6 Schematic diagram showing free energy vs. the radius r of spherical nuclei [93] 17
Figure 2.7 Schematic representation of the sputtering process [80] 19
Figure 2.8 Interactions of ions with surfaces [86] 20
Figure 2.9 Magnetron sputtering sources (a) cylindrical (b) planar [80] 22
Figure 2.10 Schematic views of dc magnetron sputtering system [87] 23
Figure 2.11 Schematic view of r.f. magnetron sputtering system [85] 24
Figure 2.12 A schematic drawing showing the effect of temperature on the growth structure [105] 29
Figure 2.13 Structure zone model for sputtered films of metals [38] 30
Figure 2.14 SZM for thick films showing the effects of both bombardment and thermal-induced mobility [107] 31
Figure 2.15 Schematic views of structure models; (a) Grovenor and (b) Barna-Adamik [107,109] 32
Figure 2.16 a-Si:H/c-Si solar cell structure in Sanyo [114] 35
Figure 3.1 Pictures of r.f. magnetron sputtering system 38
Figure 3.2 The schematic representation of r.f. magnetron sputtering system 39
Figure 3.3 Schematic representation of glass substrate cleaning procedure 40
Figure 3.4 Schematic flow of thin film characterization process 41
Figure 3.5 Schematic view of a conducting sheet used for electrical resistance measurements 42
Figure 3.6 (a) Schematic view of four point probing and (b) picture of the four point probe 43
Figure 3.7 The c-Si/a-Si:H solar cell production steps 46
Figure 3.8 c-Si/a-Si:H cell structure with TCO and contact layers 47
Figure 3.9 Picture of the I-V measurement system 47
Figure 3.10 Typical J-V curve and characterization parameters [119] 48
Figure 4.1 Variation of resistivity and deposition rate with r.f. power of ZnO thin films 51

Figure 4.2 Cross sectional FESEM image of the ZnO thin films deposited at different r.f. power values: (a) 145 W, (b) 150 W (c) 155 W, (d) 160 W, (e) 165 W, (f) 170 W and (g) 175 W 53
Figure 4.3 X-ray diffraction pattern of ZnO thin films deposited at different r.f. powers 54
Figure 4.4 FESEM surface morphology images of the ZnO thin films deposited at different r.f. powers (a) 145 W, (b) 150 W, (c) 155 W and (d) 160 W ... 57
Figure 4.5 AFM images and RMS of ZnO thin films deposited at different r.f. powers: (a) 145W, (b) 150 W, (c) 155 W, (d) 160 W, (e) 165 W, (f) 170 W and (g) 175 W 60
Figure 4.6 Total transmittance spectra of ZnO thin films prepared at various r.f. powers 61
Figure 4.7 $(\alpha h\nu)^2$ versus $h\nu$ graphs of ZnO thin films deposited at different r.f. power 62
Figure 4.8 $(\alpha h\nu)^2$ versus $h\nu$ of ZnO graphs thin films deposited at different r.f. powers: (a) 145 W, (b) 150 W, (c) 155 W, (d) 160 W, (d) 165 W, (f) 170 W and (g) 175 W 63
Figure 4.9 Effect of r.f. powers on average transmittance, resistivity and the figure of merit of ZnO thin films 65
Figure 4.10 Resistivity and deposition rate of the ZnO thin films as D_{TS} varied between 35 mm to 65 mm 67
Figure 4.11 Cross-sectional HRSEM images of the ZnO thin films deposited at different D_{TS}; (a) 35 mm, (b) 45 mm, (c) 55 mm and (d) 65 mm 68
Figure 4.12 X-ray diffraction pattern of ZnO thin films deposited at different D_{TS} . 70
Figure 4.13 HRSEM surface morphology images of the ZnO thin films deposited at different DTS: (a) 35 mm, (b) 40 mm, (c) 45 mm and (d) 50 mm 72
Figure 4.14 AFM images of ZnO thin films deposited at a D_{TS} of: (a) 35 mm, (b) 40 mm, (c) 45 mm, (d) 50 mm, (e) 55 mm, (f) 60 mm, and (g) 65 mm 74
Figure 4.15 Total transmittance spectra of ZnO thin films prepared at different D_{TS} values 76
Figure 4.16 $(\alpha h\nu)^2$ versus $h\nu$ graph of ZnO thin films deposited at different D_{TS} values 77
Figure 4.17 $(\alpha h\nu)^2$ versus $h\nu$ of ZnO graphs thin films deposited at different D_{TS}: (a) 35 mm, (b) 40 mm, (c) 45 mm, (d) 50 mm, (d) 55 mm, (f) 60 mm, and (g) 65 mm 78
Figure 4.18 Effect of D_{TS} on average transmittance, resistivity and the figure of merit of ZnO thin films 80
Figure 4.19 Cross sectional view SEM images of ZnO thin films deposited at various argon gas pressures: (a) 0.15 Pa, (b) 0.20 Pa, (c) 0.30 Pa, (d) 0.40 Pa, (e) 0.50 Pa and (f) 0.60 Pa 82
Figure 4.20 Resistivity and deposition rate variations at different argon gas pressures of ZnO thin films 83
Figure 4.21 X-ray diffraction pattern of ZnO thin films deposited at different argon pressures 84
Figure 4.22 FESEM surface morphology images of the ZnO thin films deposited at different gas pressures (a) 0.15 Pa, (b) 0.20 Pa, (c) 0.30 Pa, (d) 0.40 Pa, (e) 0.50 Pa and (f) 0.60 Pa 86
Figure 4.23 AFM images and RMS of ZnO thin films deposited at different gas pressures: (a) 0.15 Pa, (b) 0.20 Pa, (c) 0.30 Pa, (d) 0.40 Pa, (e) 0.50 Pa and (f) 0.60 Pa 87

Figure 4.24 Total transmittance spectra of ZnO thin films prepared at different gas pressures 88
Figure 4.25 $(\alpha h\nu)^2$ versus $h\nu$ of ZnO thin films deposited at different gas pressure.. 89
Figure 4.26 $(\alpha h\nu)^2$ versus $h\nu$ graphs of ZnO thin films deposited at different gas pressures; (a) 0.15 Pa, (b) 0.20 Pa, (c) 0.30 Pa, (d) 0.40 Pa, (d) 0.50 Pa and (f) 0.60 Pa 90
Figure 4.27 Effect of argon pressure on average transmittance, resistivity and the figure of merit of ZnO thin films 92
Figure 4.28 Cross sectional SEM image of the ZnO thin films deposited at different deposition time values: (a) 30 min, (b) 20 min, (c) 15 min and (d) 10 min 93
Figure 4.29 Resistivity and deposition rate variations at different deposition times of ZnO thin films 94
Figure 4.30 SEM surface morphology images of the ZnO thin films deposited at different deposition time values: (a) 30 min, (b) 20 min, (c) 15 min and (d) 10 min 94
Figure 4.31 AFM analyses for deposition time variations for ZnO thin films: (a) 30 min, (b) 20 min (c) 15 min and (d) 10 min 95
Figure 4.32 Total transmittance spectra of ZnO thin films prepared at different deposition time values 96
Figure 4.33 $(\alpha h\nu)^2$ versus $h\nu$ graph of ZnO thin films deposited at different deposition time values 97
Figure 4.34 $(\alpha h\nu)^2$ versus $h\nu$ of ZnO graphs thin films deposited at different deposition time values: (a) 30 min, (b) 20 min, (c) 15 min and (d) 10 min 98
Figure 4.35 Effect of deposition time on average transmittance, resistivity and the figure of merit of ZnO thin films 99
Figure 4.36 Low magnification TEM images of ZnO thin film deposited at 165 W 100
Figure 4.37 Cross-sectional bright field (BF) and dark field (DF) HRTEM images of ZnO thin film with a D_{TS} of 45 mm 101
Figure 4.38 SAED of the ZnO thin film shown in Figure 4.37 101
Figure 4.39 HRTEM images of ZnO thin film deposited at 165 W 102
Figure 4.40 HRTEM images of nano-island structured grains. ((b) is enlarged and filtered view of the square in (a) showing d distances of 2.6 A (002)) and (c) FFT diffractogram of (b) which shows (002) spots with an angle variation of ±15°) 103
Figure 4.41 Plan view TEM, HRTEM images and also corresponding diffraction pattern for ZnO thin film sputtered on glass substrate at 165 W r.f. Power, 45 mm D_{TS} 103
Figure 4.42 Plan view TEM, HRTEM images and also corresponding diffraction pattern for ZnO thin film sputtered on glass substrate 104
Figure 4.43 Resistivity and deposition rate variations at different r.f. power 106
Figure 4.44 Cross sectional FESEM image of the ZnO:Al thin films deposited at different r.f. power values: (a)100 W, (b) 150 W (c) 160 W, (d) 165 W, (e) 170 W, (f) 175 W and (g) 200 W 107
Figure 4.45 X-ray diffraction pattern of ZnO:Al thin films deposited at different r.f. powers 108
Figure 4.46 AFM images and RMS of ZnO:Al thin films deposited at different r.f. powers; (a) 100 W, (b) 150 W, (c) 160 W, (d) 165 W, (e) 170 W, (f) 175 W and (g) 200 W 110

Figure 4.47 Crystallite size and RMS variations of ZnO:Al thin films at different r.f. powers 112
Figure 4.48 Total transmittance spectra of ZnO:Al thin films prepared at various r.f. power..... 113
Figure 4.49 $(\alpha h\nu)^2$ versus hν graphs of ZnO:Al thin films prepared at various r.f power..... 114
Figure 4.50 Extrapolated $(\alpha h\nu)^2$ versus hν graphs of ZnO:Al thin films prepared at various r.f. powers..... 115
Figure 4.51 Effect of r.f. power on deposition rate, resistivity and the figure of merit of ZnO:Al thin films..... 117
Figure 4.52 Resistivity and deposition rate of the ZnO:Al thin films as D_{TS} varied between 40 mm to 70 mm..... 119
Figure 4.53 Cross-sectional HRSEM images of the ZnO:Al thin films deposited at different D_{TS}: (a) 40 mm, (b) 45 mm, (c) 50 mm, (d) 60 mm and (e) 70 mm..... 120
Figure 4.54 X-ray diffraction pattern of ZnO:Al thin films deposited at different D_{TS} 121
Figure 4.55 AFM images and RMS of ZnO:Al thin films deposited at different D_{TS}: (a) 40 mm, (b) 45 mm, (c) 50 mm, (d) 60 mm and (e) 70 mm 123
Figure 4.56 Total transmittance spectra of ZnO:Al thin films prepared at different D_{TS} values..... 124
Figure 4.57 $(\alpha h\nu)^2$ versus hν graphs of ZnO:Al thin films prepared at various D_{TS} values..... 125
Figure 4.58 Extrapolated $(\alpha h\nu)^2$ versus h*ν* graphs of ZnO:Al thin films prepared at various D_{TS} 126
Figure 4.59 Effect of argon pressure on deposition rate, resistivity and the figure of merit of ZnO:Al thin films 128
Figure 4.60 Cross sectional SEM image of the ZnO:Al thin films deposited at different process pressures: (a) 0.20 Pa, (b) 0.30 Pa, (c) 0.40 Pa, (d) 0.50 Pa and (e) 0.60 Pa..... 129
Figure 4.61 Resistivity and deposition rate variations at different argon gas pressures of ZnO:Al thin films..... 130
Figure 4.62 X-ray diffraction patterns of ZnO:Al thin films deposited at different argon gas pressures 131
Figure 4.63 AFM images and RMS of ZnO:Al thin films deposited at different argon pressures: (a) 0.2 Pa, (b) 0.3 Pa, (c) 0.4 Pa, (d) 0.5 Pa, and (e) 0.6 Pa . 134
Figure 4.64 Crystallite size and RMS variations of ZnO:Al thin films at different argon pressures..... 135
Figure 4.65 Total transmittance spectra of ZnO:Al thin films prepared at various argon pressures..... 136
Figure 4.66 $(\alpha h\nu)^2$ versus hν graphs of ZnO:Al thin films prepared at various argon pressures..... 137
Figure 4.67 Extrapolated $(\alpha h\nu)^2$ versus h*ν* graphs of ZnO:Al thin films prepared at various argon pressures 138
Figure 4.68 Effect of argon pressure on deposition rate, resistivity and the figure of merit of ZnO:Al thin films 140
Figure 4.69 (a) Bright field (BF) (b) dark field (DF) TEM pictures and (c) selected area electron diffraction (SAED) pattern of ZnO:Al thin film sputtered on (100) Si substrate for 165 W r.f. power and 0.3 Pa..... 141

Figure 4.70 TEM-EDS spectrum and elemental composition of plan view ZnO:Al TEM sample (Si element is from the substrate and Cu element is from the TEM holder)..... 141
Figure 4.71 (a) Bright field TEM image and corresponding TEM-EDS map of: (b) O. (c) Zn and (d) Al elements for plan view ZnO:Al TEM sample..... 142
Figure 4.72 (a) Plan-view HRTEM picture, (b) enlarged and filtered view showing indexed atomic lattice and (c) Fast Fourier Transformation (FFT) diffractogram on [021] zone axis of ZnO 143
Figure 4.73 (a) Cross-sectional TEM and (b) HRTEM picture, and (c) SAED pattern of (a) for ZnO:Al thin films deposited at 165 W r.f. power and 0.3 Pa on glass substrate..... 144
Figure 4.74 The modified Thornton model for ZnO:Al thin films..... 145
Figure 4.75 HRTEM picture of ZnO:Al, a-Si:H/c-Si structure. 146
Figure 4.76 I-V curve of the solar cell after the optimization studies under AM 1.5G solar simulator light..... 147

LIST OF TABLES

		Page
Table 2.1	TCO semiconductors for thin-film transparent electrodes [50]	6
Table 2.2	Physical properties of ZnO [53]	8
Table 2.3	Classification of Coating Processes [80]	19
Table 2.4	Transparent conductive oxides employed in photovoltaic devices [47]	33
Table 4.1	Thickness, resistivity and deposition rate variations at different r.f. powers of ZnO thin films	51
Table 4.2	Position of (200), intensity of (002), (002) peak intensity per unit thickness, position of (100), relative intensity of (100), position of (101), relative intensity of (101) peak for ZnO thin films at different r.f. powers	55
Table 4.3	FWHM and crystallite sizes of ZnO thin films at different r.f. powers	55
Table 4.4	r.f. power and corresponding RMS, Ra, Rq and average height variations of ZnO thin films	59
Table 4.5	r.f. power, average transmittance and energy band gap variations	62
Table 4.6	Resistivity, average transmittance and figure of merit values at different r.f. powers of ZnO thin films	64
Table 4.7	Deposition parameters of the ZnO thin films	66
Table 4.8	Resistivity, thickness and deposition rate variations at different target-to-substrate distance values of ZnO thin films	67
Table 4.9	The position and intensity of (002) peak, (002) peak intensity per unit thickness, position and relative intensity of (100) peak, position and relative intensity of (101) peak of ZnO thin films at different D_{TS}	70
Table 4.10	Full width at half maximum and crystallite size variations at different D_{TS} of ZnO thin films	71
Table 4.11	RMS, Ra, Rq and average height values of ZnO thin films at different D_{TS} values	75
Table 4.12	D_{TS}, average transmittance and energy band gap variations of ZnO thin films	77
Table 4.13	D_{TS}, average transmittance and energy band gap variations of ZnO thin films	79
Table 4.14	The working pressure variations with argon pressure and amount of ZnO thin films	81
Table 4.15	Thickness, resistivity and deposition rate variations of ZnO thin films at different argon gas pressures	82
Table 4.16	The position and intensity of (002) peak, (002) peak intensity per unit thickness, position and relative intensity of (100) peak, position and relative intensity of (101) peak of ZnO thin films at different argon gas pressures	85

Table 4.17 Full width at half maximum and crystallite size variations at different argon pressures of ZnO thin films 85
Table 4.18 Argon gas pressure and corresponding RMS, Ra, Rq and average height variations of ZnO thin films 88
Table 4.19 Argon gas pressure, average transmittance and energy band gap variations of ZnO thin films 91
Table 4.20 Resistivity, deposition rate, average transmittance and figure of merit values at argon pressure of ZnO thin films 91
Table 4.21 Resistivity, thickness and deposition rate variations at different deposition times of ZnO thin films 93
Table 4.22 Roughness variations for ZnO thin films at different deposition times .. 95
Table 4.23 Deposition time, average transmittance and energy band gap variations. 97
Table 4.24 Resistivity, deposition rate, average transmittance and figure of merit values at different deposition times 98
Table 4.25 Thickness, resistivity and deposition rate variations at different r.f. powers 105
Table 4.26 Position of (200), intensity of (002), (002) peak intensity per unit thickness, position of (100), relative intensity of (100), position of (101), relative intensity of (101) peak for ZnO:Al thin films at different r.f. powers. 109
Table 4.27 FWHM and crystalline sizes of ZnO:Al thin films at r.f. powers 109
Table 4.28 r.f. power and corresponding RMS, Ra, Rq and average height variations of ZnO:Al thin films 111
Table 4.29 r.f power, average transmittance and energy band gap variations. 114
Table 4.30 Resistivity, deposition rate, average transmittance and figure of merit values at r.f. power variations of ZnO:Al thin films 116
Table 4.31 Thickness, resistivity and deposition rate variations of ZnO:Al thin films at different D_{TS} 118
Table 4.32 The position and intensity of (002) peak, (002) peak intensity per unit thickness, position and relative intensity of (100) peak, position and relative intensity of (101) peak of ZnO:Al thin films at different D_{TS} .. 121
Table 4.33 Full width at half maximum and crystallite size variations at different D_{TS} 122
Table 4.34 D_{TS} values and corresponding RMS, Ra, Rq and average height variations 123
Table 4.35 D_{TS}, average transmittance and energy band gap variations 125
Table 4.36 D_{TS}, average transmittance and energy band gap variations of ZnO:Al thin films 127
Table 4.37 Thickness, resistivity and deposition rate variations at different argon gas pressures of ZnO:Al thin films 130
Table 4.38 The position and intensity of (002) peak, (002) peak intensity per unit thickness, position and relative intensity of (100) peak, position and relative intensity of (101) peak of ZnO:Al thin films at different argon pressures 132
Table 4.39 FWHM and crystalline sizes of ZnO:Al thin films at different argon pressures 133
Table 4.40 Argon gas pressure and corresponding RMS, Ra, Rq and average height variations of ZnO:Al thin films 135
Table 4.41 Argon gas pressure, average transmittance and energy band gap variations of ZnO:Al thin films 137

Table 4.42 Argon pressure, average transmittance and energy band gap variations of ZnO:Al thin films 139

ABSTRACT

ZINC OXIDE BASED TRANSPARENT CONDUCTIVE OXIDE THIN FILMS DEPOSITED BY R.F. MAGNETRON SPUTTERING FOR PHOTOVOLTAIC APPLICATIONS

Nilüfer DUYGULU

Department of Metallurgical and Materials Engineering

Ph.D. Thesis

Advisor: Prof. Dr. Ahmet EKERİM

Co- Advisor: Assoc. Prof. Dr. Alp Osman KODOLBAŞ

Transparent conductive oxides (TCO) are photovoltaic materials with high optical transmittance and low resistivity have a common area of use in energy efficient, low-emission windows applications, touch screens and control panels, etc. Due to their electrical conductivity and transparency properties they are used for solar cells and flat panel displays as front-surface electrode.

Nowadays, the usage of zinc oxide (ZnO) and aluminum doped zinc oxide (ZnO:Al) as a new generation TCO materials are increasing rapidly. They have enhanced properties as high optical transmission, lower electrical resistivity, cheaper raw material cost and absence of toxicity. Also, they are appropriate for various deposition techniques, and magnetron sputtering is one of them.

According to many investigations, deposition parameters of sputtering such as deposition rate, r.f. power, and target – to - substrate distance (D_{TS}), heating, process pressure etc. have a critical importance on the quality of thin film properties. To identify the influence of these parameters both ZnO and standard 2% Al doped ZnO thin films were deposited on glass by using r.f. magnetron sputtering without intentional heating. All the depositions were carried non-reactively. The r.f. power was varied in the range of 145 W to 175 W while, D_{TS} was changed from 35 mm to 65 mm. The process gas; argon pressure was changed from 0.15 to 0.60 Pa. The investigations were carried on in small variation ranges.

Moreover, characterization of the growth thin films carried on using various techniques. These are; X-ray diffraction (XRD), atomic force microscopy (AFM), scanning electron

microscopy (SEM), high resolution transmission electron microscopy (HRTEM), four point probe and ultraviolet - visible (UV - VIS) spectrophotometer.

According to the obtained results, for un-doped ZnO thin films with higher qualities as lowest resistivity ($1.16\times10^{-3}\Omega$.cm) and highest transparency (80%) were achieved at 165 W r.f. power, 45 mm D_{TS} and 0.30 Pa. However, for ZnO:Al thin films better results were obtained at around 165 W, 45 mm D_{TS} and 0.30 Pa process gas pressure. All the thin films were oriented with the crystallographic c-(002) axis perpendicular to the substrate surface. Also, ZnO:Al thin films had lower resistivity ($1.1\times10^{-3}\Omega$.cm) and higher transmittance values (86%) than ZnO thin films. The electrical band gap was changed from 3.45 eV to 3.87 eV for ZnO:Al thin films. Surface roughness (RMS) values were obtained as 5.44 nm for ZnO and as 2.36 nm for ZnO:Al.

The achieved results were examined in structural zone model and the morphology behaved as Zone 2 with denser and columnar grain structure. In addition to the studies, deposition parameters of ZnO:Al thin film was applied as TCO layer in a-Si:H/c-Si heterojunction solar cell and the efficiency was measured as 9.2% at the active area of 72 cm^2 under AM1.5G conditions.

Keywords: Transparent conductive oxide (TCO), Zinc oxide (ZnO), Aluminum doped Zinc oxide (ZnO:Al), r.f. magnetron sputtering, low temperature deposition**.**

ÖZET

ÇİNKO OKSİT ALAŞIMLI SAYDAM İLETKEN OKSİT İNCE FİLMLERİN FOTOVOLTAİK UYGULAMALAR İÇİN R.F. MANYETİK SIÇRATMA TEKNİĞİYLE BİRİKTİRİLMESİ

Nilüfer DUYGULU

Metalurji ve Malzeme Mühendisliği Anabilim Dalı

Doktora Tezi

Tez Danışmanı: Prof. Dr. Ahmet EKERİM

Eş Danışman: Doç. Dr. Alp Osman KODOLBAŞ

Saydam iletken oksit tabakalar (SİO) yüksek optik geçirgenlikli ve düşük öz dirence, sahip fotovoltayik malzemelerdir. Enerji tasarruflu, düşük emisyonlu pencere uygulamaları, dokunmatik ekran ve kontrol panelleri kullanım alanlarından bazılarıdır Malzeme özelliklerine bağlı olarak, yaygın bir kullanım alanına sahiptirler. Ayrıca, elektriksel iletkenlikleri ve saydamlık özellikleri sayesinde güneş pilleri ve düz panel ekranlarda ön yüzey elektrotu olarak da kullanılmaktadırlar.

Günümüzde, yüksek optik geçirim, düşük elektriksel direnç, ucuz hammadde maliyeti, toksik olmama gibi özellikleri sayesinde çinko oksit (ZnO) ve alüminyum katkılı çinko oksitlerin (ZnO:Al) yeni nesil SİO malzemesi olarak kullanımı günden güne artmaktadır. Ayrıca, bu tabakalar birçok biriktirme tekniğine kolaylıkla adapte edilebilmektedir ve manyetik alanda sıçratma bu tekniklerden biridir.

Yapılan birçok araştırmaya göre, biriktirme hızı, uygulanan r.f. gücü, hedef-altlık mesafesi, ısıtma, proses basıncı, vb. sıçratma parametrelerinin elde edilen ince film özelliklerine etkisi kritik önem taşımaktadır. Bu parametre etkilerini anlamak için, ZnO ve 2% Al katkılı ZnO ince filmler cam altlık üzerine r.f. manyetik alanda sıçratma yöntemi kullanılarak ısıtma işlemi uygulanmaksızın büyütülmüştür. Uygulanan r.f. gücü 145 W-175 W arasında değişirken, hedef-altlık mesafesi 35 mm - 65 mm aralığında belirlenmiştir. Proses gazı olarak argon kullanılmış ve basınç 0.15 Pa - 0.60 Pa aralığında değişmiştir. İncelemeler küçük değişim aralıklarında gerçekleştirilmiştir.

Büyütülen ince filmlerin karakterizasyonunda çok çeşitli teknikler kullanılmıştır. Bunlar; X-ışınları difraksiyonu (XRD), atomik kuvvet mikroskopisi (AFM), taramalı elektron mikroskopisi (SEM), yüksek çözünürlüklü geçirimli elektron mikroskopisi (HRTEM), dört uçlu ölçüm probu ve optik geçirim (UV–VIS) şeklindedir.

Elde edilen sonuçlara göre katkısız ZnO ince filmler için en düşük öz direnç ($1.16\times 10^{-3}\Omega$.cm) ve en yüksek optik geçirim (80%) gibi özellikler; 165 W r.f. gücünde, 45 mm hedef - altlık mesafesinde ve 0.30 Pa değerlerinde elde edilirmiştir. Ancak, ZnO:Al ince filmler için en iyi sonuçlar 165 W r.f. gücünde, 45 mm hedef - altlık mesafesinde ve 0.30 Pa proses gaz basıncında elde edilmiştir. Elde edilen bütün ince filmler, c-(002) kristolografik ekseninde altlık yüzeyine dik olarak yönlenmiştir. Ayrıca ZnO:Al ince filmler ZnO ince filmlere kıyasla daha düşük öz direnç ($1.1\times 10^{-3}\ \Omega$.cm) ve daha yüksek optik geçirim (86%) değerine sahiptir. Elektriksel bant geçirim aralıkları ise, 3.45 eV - 3.87 eV aralığında değişmiştir. Yüzey pürüzlülük değerleri (RMS) ZnO için 5.44 nm ZnO:Al için 2.36 nm olarak ölçülmüştür.

Elde edilen sonuçlar yapısal bölge modeline göre incelendiğinde, yoğun ve kolonsal tanecik yapısı morfolojinin Bölge 2'de yer aldığı görülmüştür. Bu çalışmalara ilaveten ZnO:Al ince film büyütme parametreleri a-Si:H/c-Si Heteroeklem güneş pilline uygulanmış, ve verim 72 cm2lik aktif alan altında AM1.5G koşullarında 9.2% olarak ölçülmüştür.

Anahtar Kelimeler: Saydam iletken oksit (SİO), Çinko oksit (ZnO), Alüminyum katkılı çinko oksit (ZnO:Al), r.f. manyetik alanda sıçratma, düşük sıcaklık biriktirme.

CHAPTER 1

INTRODUCTION

1.1 Literature Review

Nowadays, the interest on finding and developing alternative energy sources are increasing rapidly. Solar energy is one of the most popular energy sources with its enhanced properties such as causing lower emissions, being clean and renewable. According to the European Commission, Photovoltaic (PV) status report, solar cell production in the world, ranged between 30 GW to 37 GW in 2011, market predictions for the 2013 PV additional installation is 31 GW to 39.7 GW and it is expected to reach around 200 GW in 2015 [1]. These assumptions will force not only solar cell production, but also production of other components of photovoltaics. For instance, Transparent Conducting Oxides (TCOs) are known as one of the important constituents of photovoltaics.

TCOs are specialized with their high optical transmittance and low resistivity characteristics. Therefore, they reached a wide range of application areas such as light emitting diodes [2], film transistors [3], heat mirrors [4], gas sensors [5] and solar cells [6,7].Commonly, indium tin oxide (ITO) is chosen as a TCO material due to its high transmittance in the visible region and low resistivity characteristics [8]. However, the toxic and high-cost properties of ITO forced to search for alternative TCO materials [9, 10].

Zinc oxide (ZnO) is an excellent applicant to take the place of ITO owing to its enhanced properties. ZnO is an II–VI semiconductor with a wide and direct band gap, has excellent chemical and thermal stability, and specific electrical and optoelectronic properties [11, 12]. The only unfavorable property of pure ZnO film is its unstable electrical property at high temperature ranges [13]. However, this can be exceeded by

adding doping elements to ZnO thin films. Also, ZnO and doped ZnO are named as "new generation" TCO materials. According to various investigations, group-III elements showed high performances as doping agent. Especially, aluminum (Al) as group-III element is known as one of the most preferable dopants for ZnO, due to its smaller ionic size (0.57 Å and 0.72 Å, for $Al3^{+}$ and Zn^{2+}, respectively) [14- 16].

ZnO-based TCOs can be grown using various deposition techniques, such as pulsed laser deposition [17], vacuum coating [18], reactive evaporation [19], spray pyrolysis [20], sol–gel process [21], spin coating [22] and magnetron sputtering [23-28]. Among these techniques, sputtering can be performed at low temperatures and yields films with better adhesion with the substrate and higher density deposits; these advantages make sputtering a popular technique for industrial applications [28].

In sputtering, the deposition parameters such as substrate temperature, argon/oxygen partial pressure, sputtering power and target-to-substrate distance [29] greatly influence the film properties. Therefore, researches on ZnO based thin films are typically focused on improving three parameters: electrical conductivity, optical transmittance and crystalline texture [30]. Other subjects of investigations include photoconductivity [31], photoluminescence [32], annealing [33] and doping [34-36].

Also, in the literature, most studies use the Thornton model to understand the morphology of the thin films by considering the effect of temperature and total gas pressure during deposition [37, 38]. ZnO thin films with lower resistivity and higher transparency have been achieved through reactive sputtering by controlling substrate temperature or post annealing of the deposited films [39-41].

1.2 Objective of the Thesis

The basic aim of this study is achieving high transparency and low resistivity characteristic of a TCO layer cheaply. Therefore, zinc oxide and aluminum doped zinc oxide with their lower production costs were chosen as new generation TCO materials.

r.f. magnetron sputtering technique was selected since it has high deposition density and it can be easily applied to industrial applications. Also, it provides working at low temperature ranges, which is one of the most preferred property for PV applications. According to various investigations, the sputtering conditions play a critical role to determine the TCO properties. Consequently, in the present study, the influences of

process power, target-to-substrate distance and process pressure parameters were investigated.

All the depositions were carried on at room temperature conditions, without intentional heating. Argon was used as process gas. The experiments were done to understand the influence of deposition parameters on thin film properties.

In order to clarify the effect of r.f. power, the studies were examined in the range of 100 W to 200 W, while the target-to-substrate distance was maintained from 35 mm to 65 mm. The influence of process gas pressure was investigated for low pressures from 0.15 Pa to 0.6 Pa.

The characterizations of the films were done in a wide area. Some of these techniques were: four point probe, ultraviolet–visible (UV–VIS) spectrophotometer, scanning electron microscopy (SEM) and atomic force microscopy (AFM). Also, for structural investigations, X-ray diffraction (XRD), transmission electron microscopy (TEM) and high resolution transmission electron microscopy (HRTEM) techniques were performed. The structure zone model behavior of the ZnO:Al thin films were examined by selecting the T_S/T_M variation constant. The achieved results were compared with the results in the literature.

Moreover, ZnO:Al films with optimized properties were used as top electrode in a-Si:H/c-Si heterojunction solar cell.

1.3 Hypothesis

In order to enlarge the PV application areas of new generation TCO materials, ZnO and ZnO:Al, were deposited by r.f. magnetron sputtering technique. The influence of three important sputtering parameters: r.f. power, target-to-substrate distance and argon pressure and on ZnO and ZnO:Al thin films were investigated in small variation ranges.

Instead of heating support, all the depositions were done at room temperature conditions. Moreover, the sputter was carried on un-reactively; argon was used as the process gas. The growth behavior of thin films was analyzed by using various characterization techniques and with the help of structural zone models. The observed results revealed that, small deposition parameter variations had great influence on electrical, structural and optical properties of thin films. Also morphological

investigation results showed that ZnO and ZnO:Al thin films with different roughness due to small variations, can be applied to several PV applications.

CHAPTER 2

LITERATURE SURVEY

2.1 Transparent Conductive Oxide (TCO)

Transparent Conducting Oxides are a class of materials that exhibit high visible wavelength transparency and electrical conductivity simultaneously [42, 43, and 44]. They have good electrical conductivity like metals, but they reflect or absorb the solar radiation. Moreover, these oxides are generally, transparent to light but also are optimal electrical insulators [44].

These materials are widely used in display, photovoltaic, low-e window, and flexible electronic applications [45].Their applications range from silicon heterojunctions to polymer solar cells [42, 46, 47, and 48].

TCOs as transparent electrodes are polycrystalline or have amorphous structure, and exhibit an electrical resistivity in an order of 10^{-3} Ω.cm or less and the average transmittance are above 80 % in the visible range. Also, their band-gap energy is above approximately 3 eV and they are degenerated n-type or p-type semiconductors [49].

2.2 Application Areas of Transparent Conductive Oxides

Generally, the use of TCOs in industry is dominated by just a few materials. The most common markets for TCOs are: architectural windows, flat panel display (FPD) and photovoltaic industry applications. These applications will be explained in the following:

- Architectural applications;

TCOs are commonly used as building windows to improve the energy efficiency, because the free electrons reflect the infrared radiation for wavelengths longer than the

plasma wavelength. Generally, fluorine-doped tin oxide (SnO_2:F) is chosen as a TCO material for this application.

- Flat panel display (FPD) applications;

The application area of TCOs is wide with various styles and material alternatives for FPDs as a front electrode. Etchability is very critical for forming patterns in the transparent conductive electrode. Especially, indium-tin-oxide (ITO) is selected for the applications because of its easy etchability. Furthermore, in some future displays, ZnO can take the place of ITO because of its low cost and ease of etching compared to ITO.

- Photovoltaic applications;

TCOs are generally used as a current-collecting electrode and placed as the front surfaces of solar cells. ITO or ZnO is chosen for this purpose because both compounds can be deposited successfully at low temperatures (typically 200 °C).

TCO materials can also be used as electrochromic mirrors and windows, defrosting windows, oven windows, static dissipation, and touch-panel controls, electromagnetic shielding and invisible security circuits [42, 45, and 47].

2.3 Transparent Conductive Oxides Materials

Generally, the investigations on developing the TCO thin film materials focused on using n-type semiconductors consisting of metal oxides. Zn, Sn, In, Ga, and Cd Oxides are the most common TCO materials for thin-film transparent electrodes as listed in Table 2.1[45, 50].

Table 2.1 TCO semiconductors for thin-film transparent electrodes [50]

Material	Dopant or compound
SnO_2	Sb, F, As, Nb, Ta
In_2O_3	Sn, Ge, Mo, F, Ti, Zr, Hf, Nb, Ta, W,Te
ZnO	Al, Ga, B, In, Y,Sc, F, V, Si, Ge, Ti, Zr, Hf
CdO	In, Sn
ZnO–SnO_2	Zn_2SnO_4, $ZnSnO_3$
ZnO–$In2O_3$	$Zn_2In_2O_5$, $Zn_3In_2O_6$
In_2O_3–SnO_2	$In_4Sn_3O_{12}$
CdO–SnO_2	Cd_2SnO_4, $CdSnO_3$
CdO–In_2O_3	$CdIn_2O_4$
$GaInO_3$, (Ga, In)$2O_3$	Sn, Ge
$CdSb_2O_6$	Y
ZnO–In_2O_3–SnO_2	$Zn_2In_2O_5$−$In_4Sn_3O_{12}$
CdO–In_2O_3–SnO_2	$CdIn_2O_4$−Cd_2SnO_4
ZnO–CdO–In_2O_3–SnO_2	

There are some important criteria to select the best TCO material. These are listed below:

- high transparency in the range of the solar spectrum,
- low resistivity ($\leq 10^{-3}$ Ω.cm),
- high carrier mobility,
- well suited refractive index for coupling of light into the silicon absorber material,
- grown or patterned TCO films with surface texture for optimum light scattering,
- high chemical stability of the bulk material and of the contact to silicon,
- non-toxic and sustainable materials,
- low cost [51].

ITO is the most popular TCO material due to its better properties. However, the scarcity of indium makes the ITO an expensive one.

Nowadays, ZnO, ZnO:Al, ZnO:Ga and ZnO:In seem to be the most promising aspirant and alternative to ITO thin films due to their low cost, non-toxicity, requirement of relatively low deposition temperature and good stability. Also, they have low electric resistance and high transparency in the visible wavelength range.

2.3.1 Zinc Oxide (ZnO)

Currently, ZnO is one of the most widely used TCOs due to its optoelectronic and photovoltaic conversion properties, with its large band gap (~3.3 eV) [8], abundance in nature and absence of toxicity [9].

Zinc oxide is a ceramic material naturally occurring as the rare mineral zincite and it crystallizes in the hexagonal wurtzite structure P63mc [17].It has been investigated already in 1912 and has been widely studied since 1935 [52].

The interest in ZnO is increasing day by day by developing new growth technologies for the fabrication of ZnO-based electronic and optoelectronic devices. At ambient pressure and temperature, ZnO crystallizes in the wurtzite (B4 type) structure, as shown in Figure 2.1.

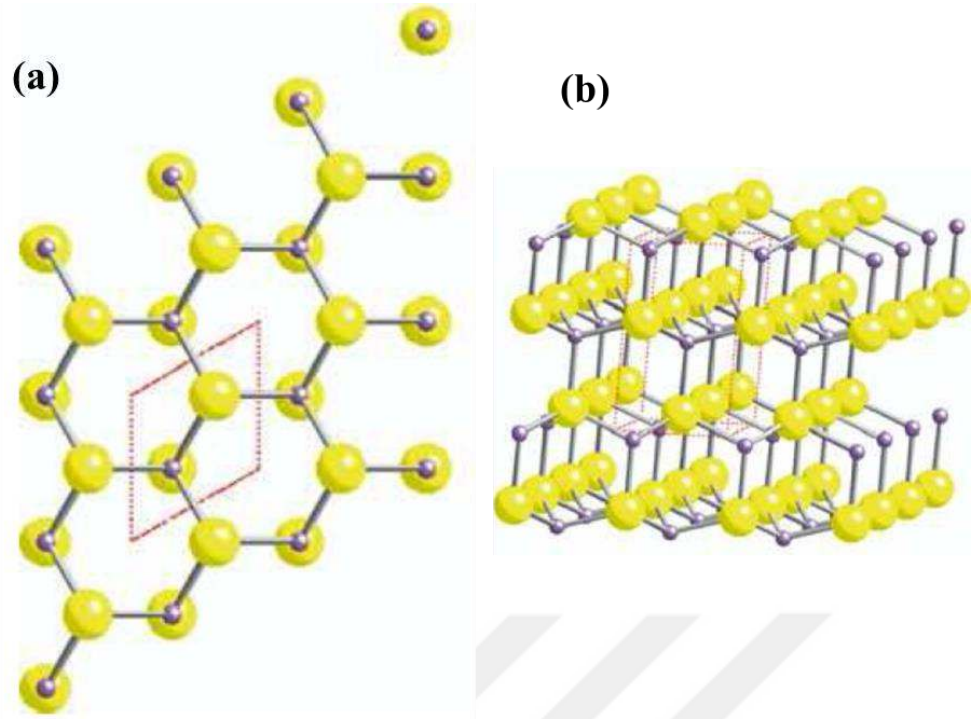

Figure 2.1 The crystal structures of ZnO: (a) View along the c-axis on the oxygen terminated (00-1) plane, and (b): perspective view perpendicular to the c-axis (Large balls; oxygen and small balls; zinc) [52]

Zinc oxide is a direct semiconductor with a band gap energy greater than 3.3 eV, leading to a transparency for wavelength >360 nm [53]. Also, some of the structural and physical properties of the ZnO are present in Table 2.2.

Table 2.2 Physical properties of ZnO [53]

Crystal structure	Hexagonal wurtzite
Space group	$P6_3m$
Lattice parameters of the hexagonal unit cell	a = 3:24 Å and c = 5:19 Å
T melting °C	1975±25 °C
Hardness	4 Mohs
Density	5.665×10^3 kg/m^3
Thermal expansion coefficient (1/°C)	$\alpha_{11}=4.0\times10^{-6}$, $\alpha_{33}=2.1\times10^{-6}$
Energy band gap, type	3.2–3.3 eV , n-type

2.3.2 Thermodynamic Properties of ZnO

A movement or removal of lattice atoms from the ideal structure is called as intrinsic point defects. These point defects influence both electrical and optical properties of the semiconductors, especially, of ZnO. The potential intrinsic defects can be listed as; vacancies, interstitials, and antisites. For ZnO, V_{Zn} and V_O stand for vacancies, Z_{ni} and O_i for interstitials and Zn_O and O_{Zn} are shown as antisites [48, 53].

Furthermore, Schottky (cation and anion vacancy) and Frenkel (cation vacancy and cation interstitial) as neutral pairs can also be added to the defects list. Their short definitions are given below:

- Interstitials: The impurity atom A occupies a position in between the usual lattice sites. Interstitials are denoted by Ai (i.e. Zn_i, O_i)
- Vacancies: A missing atom A in the lattice results in a vacancy and deprives the crystal of one electron per broken bond. Vacancies are denoted by VA (i.e. V_{Zn}, V_O)
- Substitutionals: One of the constituent lattice atoms A is replaced by an impurity atom C. If the impurity atom provides fewer electrons than the atom it replaces, it will form an acceptor, otherwise a donor. Substitutionals are denoted by CA (i.e. N_O, Ga_{Zn})
- Antisites: A host atom A of one type occupies the lattice site of another host atom B. Antisites are denoted by AB (i.e. Zn_O, O_{Zn})
- Frenkel defect pair: The host atom A is displaced from a lattice site to a nearby interstitial site forming a complex. The defect pair is denoted by VA − IA (i.e. $V_{Zn} - I_{Zn}$, $V_{Li} - I_{Li}$) [54].

The antisite defects are more important for more covalently bonded compounds like the III–V semiconductors.

The formation of one mole of a defect requires an energy ΔH_d and equations below defines the number of defects in thermodynamic equilibrium.

$$\Delta G_d = \Delta H_d - TS \tag{2.3}$$

(where ΔG_d is the free energy of a crystal by defect formation, ΔH_d is the formation of one mole of a defect energy, S is the entropy of the system)

$$N_d = N exp(-{}^{\Delta H_d}/_{k_B T}) \tag{2.4}$$

(where N_d is the distribution of the created defects on the available sites, k_B is the Boltzmann constant, and T is the temperature.)

In intrinsic defects, the formation energy on the chemical potential and the Fermi level position in the gap is critical. The chemical potential relates to the concentration of a species, which is for gases especially its partial pressure. When the partial pressure of

oxygen increased, it leads ΔH_d reduction for defect reactions that add oxygen or remove Zn (O_i, V_{Zn}) and vice versa.

However, for charged defects, the enthalpy of the defect formation mostly depends on the Fermi energy. The Fermi energy is the chemical potential of the electrons and the holes. In Figure 2.3, the relation between the defect formation and the Fermi energies with occupied and unoccupied formations is shown. When Fermi energy is higher than the donor energy ($E_F > E_D$), the occupied donor becomes electrically neutral and the ΔH_d does not depend on E_F. However, when the Fermi energy is lower than the donor energy, unoccupied donor is positively charged and the electron(s) released from the donor is transferred to the electron reservoir (E_F) leading to an energy gain δ. Due to this movement, the defect formation enthalpy decreases with decreasing Fermi energy.

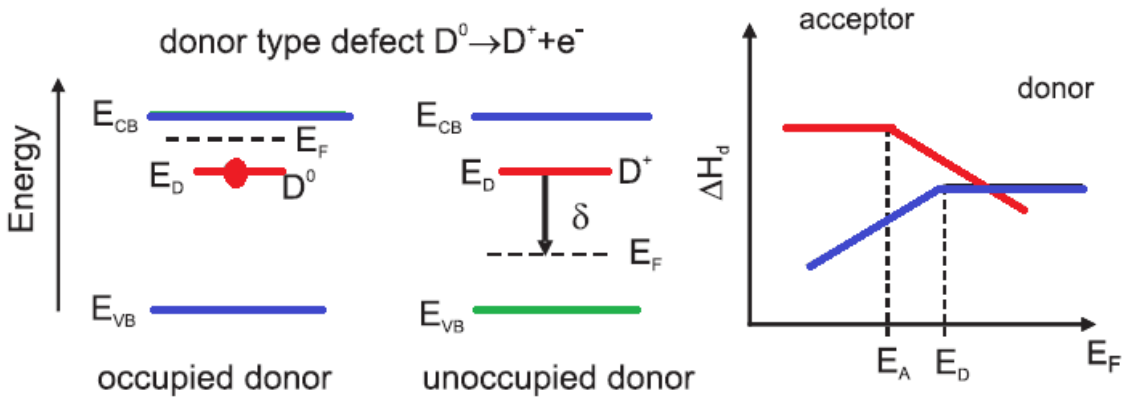

Figure 2.3 The relation between the defect formation and the Fermi energies with occupied and unoccupied formations [66]

The Fermi level position with respect to the defect energy E_D is known as a donor type defect and it can be neutral or positively charged depending on its occupation. When the Fermi level is above the defect level donors called occupied (neutral), and also, when it is below than the defect level is unoccupied (charged) donor. The Fermi energy is the energy in which the donor electron transferred to its reservoir. The gained energy is formulized as;

$$\delta = q(E_D - E_F) \tag{2.5}$$

(where q is the charge of the donor)

The formation enthalpy of the donors can be reduced, by lowering the Fermi level toward the valence band maximum.

During the defect formation enthalpy reduction by the movement of the Fermi energy, the defect concentration may increase. Generally, donor (acceptor) doping leads to an

increase of the Fermi energy, due to the lowering of the formation enthalpy of intrinsic acceptors (donors).This movement limits the Fermi level and this is called as self-compensation. This hypothesis plays a critical role for semiconductors to limit the doping [48, 53].

2.3.3 Zinc Oxide Requirements as TCO Material

There are some requirements that can be fulfilled by ZnO to be used as the transparent conductive electrode in thin film solar cells. These applications are:

- High transparency in the visible and near infrared spectral region,
- Possibility to prepare highly-doped films with free electron density $n > 10^{20}$ cm^{-3} and low resistivity ($< 10^{-3}\Omega cm$),
- Good contacts to the active semiconductors (absorber layers),
- Possibility to prepare the TCO layers on large areas ($>1m^2$) by deposition methods like magnetron sputtering or metal-organic chemical vapor deposition (MOCVD),
- Possibility to prepare ZnO films with suitable properties at low substrate temperature (< 200°C for Cu (In, Ga) $(S, Se)_2$ solar cells),
- Possibility for preparation of tailored surfaces with suitable light scattering properties for light trapping, which is particularly important for Si thin film solar cells,
- Low material costs, nontoxicity, and abundance in earth crust [53].

2.3.4 Doping elements for ZnO thin films

In order to enhance both the electrical and optical properties of ZnO thin films, tendency of doping elements were increased. According to many investigations, group III elements such as aluminum (Al), gallium (Ga) and Indium (In) were selected as dopants of ZnO [55]. These doping elements not only increase the carrier concentration, but also affect the structural properties as well [16].

Due to the doping agent, a lattice strain may occur and it influences the carrier mobility. However, such a strain can be reduced by using a dopant with ionic size comparable to or smaller than that of the host. When the ionic size is considered, Al^{+3} with ionic size

of 0.54 Å or Ga^{+3} with of 0.62 Å can be chosen as a dopant element for Zn^{+2} with ionic size of 0.72 Å.

There are various studies that concentrate on understanding the influence of doping element effect, on characteristics of ZnO thin films. Most of these revealed that, to achieve enhanced film properties such as electrical, optical and structural, doping elements play a critical role. Mostly, aluminum is selected as a doping element with its high temperature stability due to the doping effect is not caused by an oxygen deficit also ZnO:Al thin films exhibit a good resistance [56-59].

Also, in order to achieve better conductivity with higher transparency, Park et. al [60] deposited Mg–doped ZnO:Al on glass substrates by using ion beam sputtering technique. They observed that when the amount of Mg concentration was increased, both the transmittance and optical band gap values were increased. Moreover, to reduce the electrical resistivity of ZnO thin films, Al_2O_3, and F was used as doping elements. r.f. magnetron sputtering was used as the deposition system and all the processes were done at room temperature conditions. According to their results, the doping concentration of the AlF_3 was effective not only on electrical properties but also on structural orientation. 2 wt% AlF_3 showed a highly oriented crystalline structure in the (0 0 2) direction with lowest resistivity [61, 62,147].

Nowadays, gallium is one of the popular doping elements to achieve improved electrical and structural properties. According to the investigations on gallium doped ZnO thin films deposited by various techniques, Ga helped to reduce resistivity value due to its low ionic size [63, 64, and 65].

Also, other doping elements were selected as doping element for ZnO thin films. For instance, Chu et al [66] deposited lithium (Li_2CO_3) doped ZnO on silicon substrate by using r.f. magnetron sputtering, reactively. They achieved c-axis (002) orientation structure with high resistivities that can be applicable for piezoelectric applications. Indium is another chemically stable doping element which helps to obtain higher optical transmission with higher conductivity [67, 68, and 69]. Cao et al. [70] investigated the influence of Mn doping on ZnO thin film properties deposited by d.c. sputtering technique and they obtained resistivity values around 10^{-4} Ω.cm, while optical transmittance above 80% at the wavelength of 550 nm. They also observed that the band gap shifted from 3.40 eV to 3.48 eV.

2.3.5 Zinc Oxide Deposition Techniques

Deposition of ZnO thin films can be achieved by using various techniques such as pulsed laser deposition [71], chemical vapor deposition [72], atomic layer deposition [73], sol–gel process [74] and magnetron sputtering [24,25, and 26]. From these deposition techniques, magnetron sputtering has many advantages such as; high deposition rate, good surface adhesion and low substrate temperature [27, 28, 29, 75, and 76].

2.4 Thin Film Growth Processes

A thin film is a material less than one micron thickness deposited on a substrate. Thin films form by nucleation and growth. Thin film growth process steps are:

1. Production of the appropriate atomic/molecular/ionic species,

2. Transportation of the species to the substrate,

3. Condensation on the substrate.

Formation of a thin film takes place by means of nucleation and growth process. Firstly, the unit species are adsorbed on the surface of the substrate physically by losing their velocity normal to the substrate. Secondly, the adsorbed species interact among themselves to form big clusters or as called the nuclei. These nuclei are thermodynamically unstable and tend to be resolved depending on the deposition parameters. However, if a sufficient deposition parameter is obtained, the cluster collides with other adsorbed species and the size of the clusters increases. After reaching a certain critical size, nucleation barrier have been overcome and the cluster becomes thermodynamically stable. This step is also known as the nucleation stage in which, the formation of stable, chemisorbed, critical-sized nuclei occurred. When the saturated nucleation density is reached, the number of the critical nuclei grow is also increased.

Both the nucleation density and the average nucleus size are affected from various parameters such as: impinging species energy, impingement rate, and adsorption and desorption activation energies, thermal diffusion, the temperature, topography, and chemical nature of the substrate.

With the help of the surface diffusion of the adsorbed species, a nucleus can grow both parallel and perpendicular to the substrate. In general, the lateral growth rate is much higher than the perpendicular growth. The name of the grown nuclei is islands.

When the small islands start coalescing with each other in an attempt, they reduce the surface area and this stage is called as the coalescence stage. In this stage, the islands become bigger and that increases the surface mobility of the adsorbed species. During island growing, they may leave channel and holes on the substrate surface which causes discontinuous island occurrence. A completely continuous film is formed by filling of the channels and holes [77].

2.4.1 Deposited layers

A deposited layer can be formed in various ways as; crystal, amorphous, or liquid, islands or layers, monolayer or multilayer, aligned with the substrate or not, small islands that are mobile or stationary [78].

The initial nucleation and growth stages may be described as of (a) island type (called Volmer - Weber type), (b) layer type (called Frank-van der Merwe type), and (c) mixed type (called Stranski-Krastanov type) depending on the thermodynamic properties of both the deposit and the substrate surface (Figure2.4)[77].

Volmer–Weber

It is island growth, as illustrated in Figure 2.5. The islands are often three-dimensional rather than monolayers. The deposit nucleates as independent islands that may or may not be aligned with the substrate. Atoms can migrate across the surface to the islands. The islands grow, and then can merge or coalesce when they impinge on each other. This is also known as 3-D island growth.

Frank–Van der Merwe

Frank–Van der Merwe growth is layer by layer growth and also called as 2-D growth. The atoms can migrate across the surface to the edge of the step. This is the growth mode that provides good epitaxy.

Stranski–Krastanoff

It is island growth, but the islands form on top of a few monolayers of the same deposited material [78, 79].

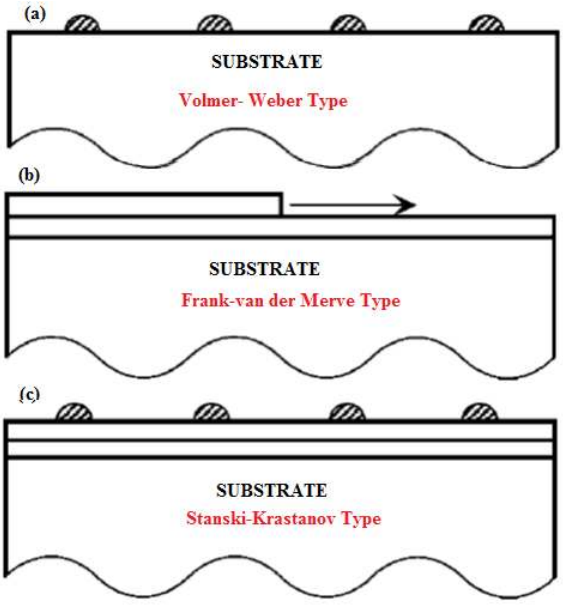

Figure 2.4 Three modes of thin film growth processes; (a) Volmer–Weber, (b) Frank–Van der Merwe (c) Stranski–Krastanoff [78, 79]

2.4.2 Thermodynamic descriptions of thin film deposition

In order to obtain a good deposited surface, thermodynamic properties of the deposition have to be considered. In Figure 2.5, the basic deposition mechanism is schematically shown.

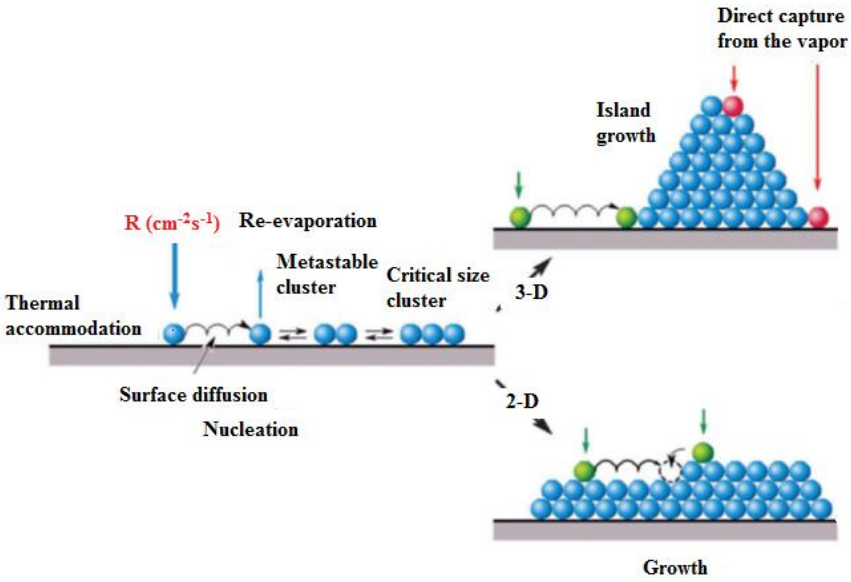

Figure 2.5 Schematic representations of processes leading to three-dimensional nucleation and film growth [79]

According to Figure 2.5, the minimum criterion to achieve a net deposition is obtaining equilibrium between the condensate pressure P in the gas phase and its vapor pressure

P_{VP} over the solid. Therefore, the equation given below has to be provided due to the higher vapor pressures of small clusters than the corresponding bulk material.

$$\zeta = {}^{P}/_{P_{VP}} > 1 \tag{2.6}$$

(where ζ is the supersaturation ratio, P; condensate pressure, P_{VP} vapor pressure)

Generally, in analyzing film growth mechanism, usage of ζ = J/Jvp is more convenient. (where the particle flux J is related to P via the kinetic definition of pressure as given in Equation 2.7:

$$J\ (cm^{-2}\ s^{-1}\ ) = 3.513\ \times 10^{22}\ {}^{P}/_{(mT)^{1/2}} \tag{2.7}$$

(in which m is the molecular weight in amu, T is the gas temperature in K, and P is in Pa)

In order to growth mechanism to occur, clusters must be greater than minimum critical size [93].

In order to understand the 3-D growth mechanism, both kinetic and thermodynamic equations have to be considered. When a cluster with a mean dimension (r) is formed on a solid surface with a surface area of a_1r^2 and a contact area a_2r^2 with the substrate, and a volume a_3r^3 where the a_i terms are constants of geometry is estimated, the total free energy of the cluster with respect to dissociation into the vapor phase ;

$$\Delta G = a_1 r^2 \Gamma_{c-v} + a_2 r^2 \Gamma_{s-c} - a_2 r^2 \Gamma_{s-v} + a_3 r^3 \Delta G_v \tag{2.8}$$

Γ_{c-v}: the positive free energy associated with the formation of a new surface between the condensate and the vapor phase

Γ_{s-c}: the surface free energy between the substrate and the condensate

$a_2 r^2 \Gamma_{s-v)}$: accounts for the disappearance of free substrate area

If the equation is simplified, the Equation 2.8 becomes,

$$\Delta G = {}^{4}/_{3}\,(\pi r^3)\Delta G_v + 4\pi r^2 \Gamma_{c-v} \tag{2.9}$$

Schematic diagram of free energy versus the radius r of spherical nuclei is shown in Figure 2.6.

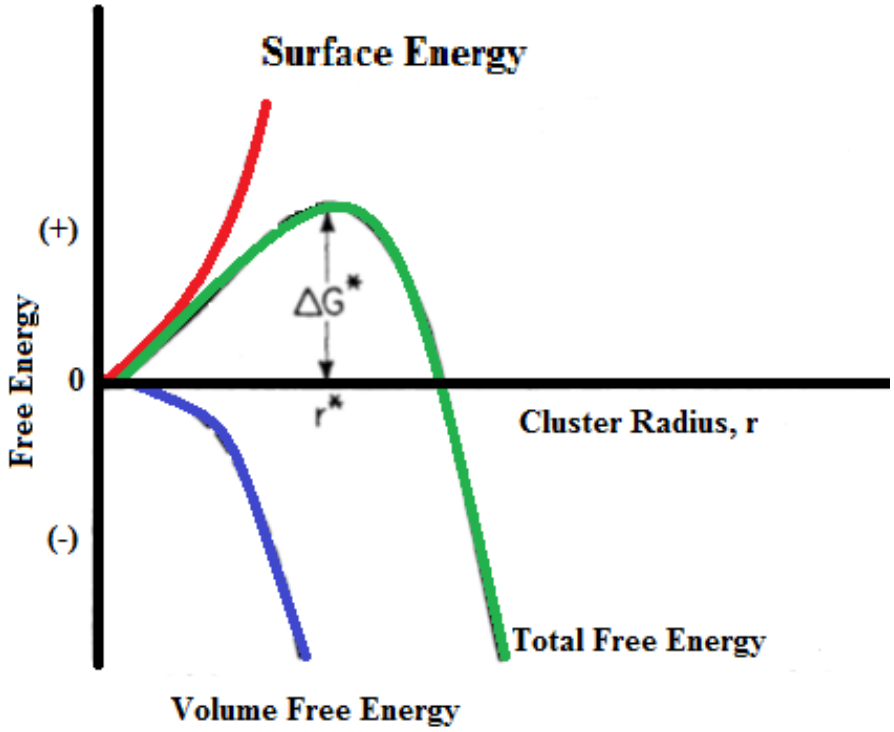

Figure 2.6 Schematic diagram showing free energy vs. the radius r of spherical nuclei [93]

ΔG*: is the activation free energy barrier to nucleation

r* : the critical size

An expression for the critical cluster size r* can be obtained by maximizing ΔG in Equation. 2.5, i.e., by setting δ (ΔG) /δr = 0, and solving to yield

$$r^* = -\frac{2\Gamma}{\Delta G_v} \tag{2.10}$$

(where Γ is used to represent Γ_{c-v})

The free energy barrier is then obtained by substituting Equation 2.9 into Equation 2.10 to give

$$\Delta G^* = \frac{16\pi\Gamma^3}{3(\Delta G_v)^2} \tag{2.11}$$

The term ΔGv in Equation 2.10 and 2.11 can be evaluated using a general expression of the combined first and second laws of thermodynamics

$$d(\Delta G) = VdP - SdT \tag{2.12}$$

(where V and S are the system volume and entropy, respectively.) Substituting the ideal gas law PV = kT at constant temperature,

$$d(\Delta G) = kT\frac{dP}{P} \tag{2.13}$$

Since ΔGv is just ΔG/Ω where Ω is the volume of an adatom, then

$$\Delta G_v = \frac{kT}{\Omega} In \frac{P}{P_e} = \frac{kT}{\Omega} In(S) \tag{2.14}$$

Substituting Equation 2.13 into 2.14 gives

$$r^* = -\frac{2\Omega\Gamma}{kTIn(S)} \tag{2.15}$$

Equation 2.15 shows that r* decreases as the super saturation S increases. S can be increased either by increasing P, i.e. increasing the incident flux of condensing species, or by decreasing Pe which depends exponentially on the growth temperature Ts. That is, r* decreases as Ts decreases [78 - 85].

2.4.3 Thin Film Deposition Process

There are several classifications of coating processes. One of the common classifications is given in Table 2.3. According to the table, deposition techniques are divided into two major categories as physical and chemical processes. Especially, the thin film TCO materials are formed by atomistic deposition techniques. In atomistic processes, the film formation occurs by condensing of the atoms onto a substrate and migrating to nucleation and growth sites.

Table 2.3 Classification of Coating Processes [80]

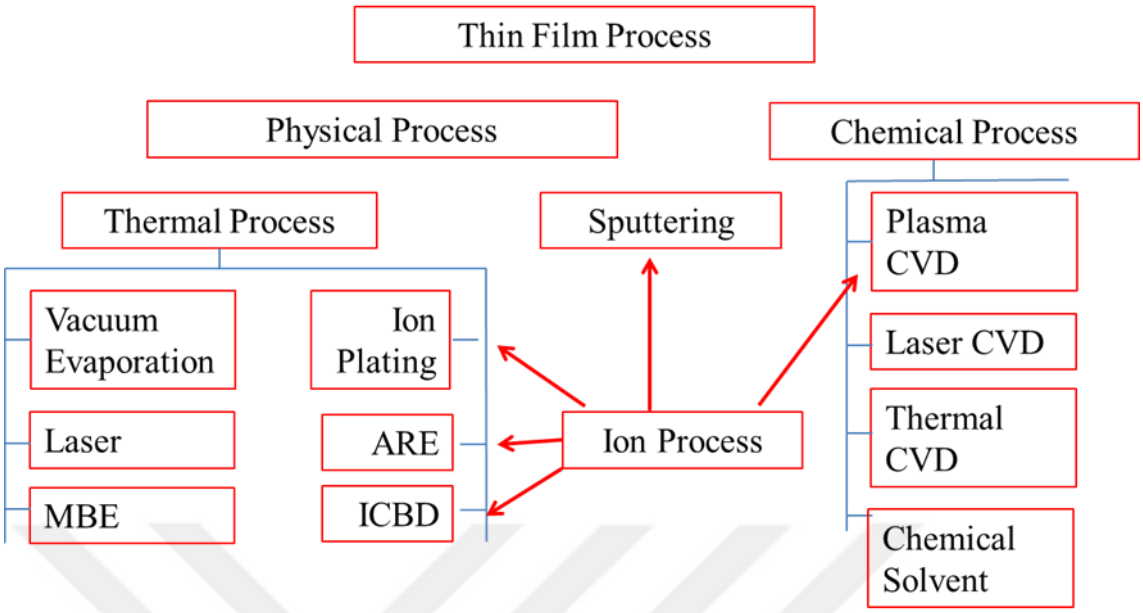

The objective of physical vapor deposition (PVD) processes is; to transfer the atoms from a source to a substrate, where the film formation and growth proceed atomistically. Commonly, PVD is classified into two categories as; thermal evaporation process and sputtering. In evaporation process, the atoms are removed from the source thermally by means of vaporizing the solid material to sufficiently high temperature.

Sputtering is also a kind of a PVD process with the meaning of in terms: bombardment of a substrate with energetic particles. In sputtering, there may be interaction between these particles and the surface which is shown schematically in Figure 2.7. Bombardment of the target material by high energy Ar ions that are extracted from plasma causes ejection of atoms. These atoms may redeposit on the substrate.

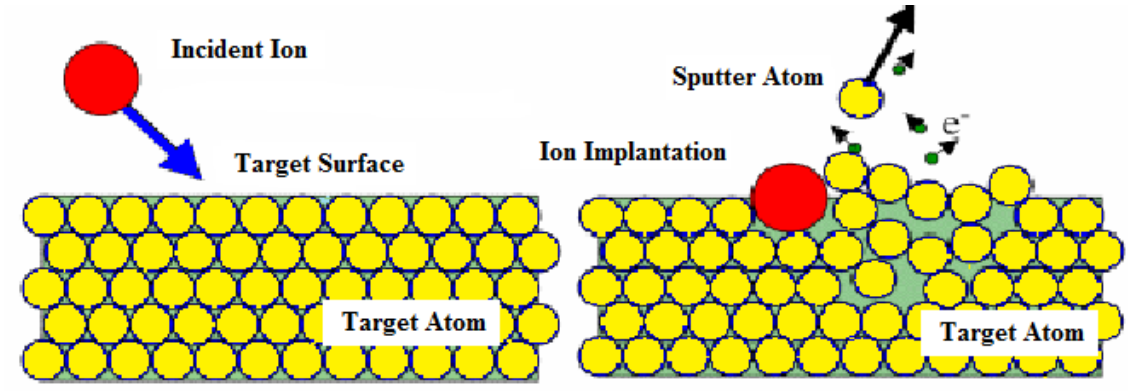

Figure 2.7 Schematic representation of the sputtering process [80]

2.4.4 Basic Sputtering Mechanisms

Basically, the sputtering process depends on the bombarding the surface with gas ions accelerated under high voltages [86]. In the sputter deposition, the bombarding particle transfers their kinetic energies to the target atoms and this causes an ejection of those atoms through the target surface. Bombardment of the target material by high energy gas ions that are extracted from plasma causes ejection of atoms. The mechanism of these movements is shown in Figure 2.8.

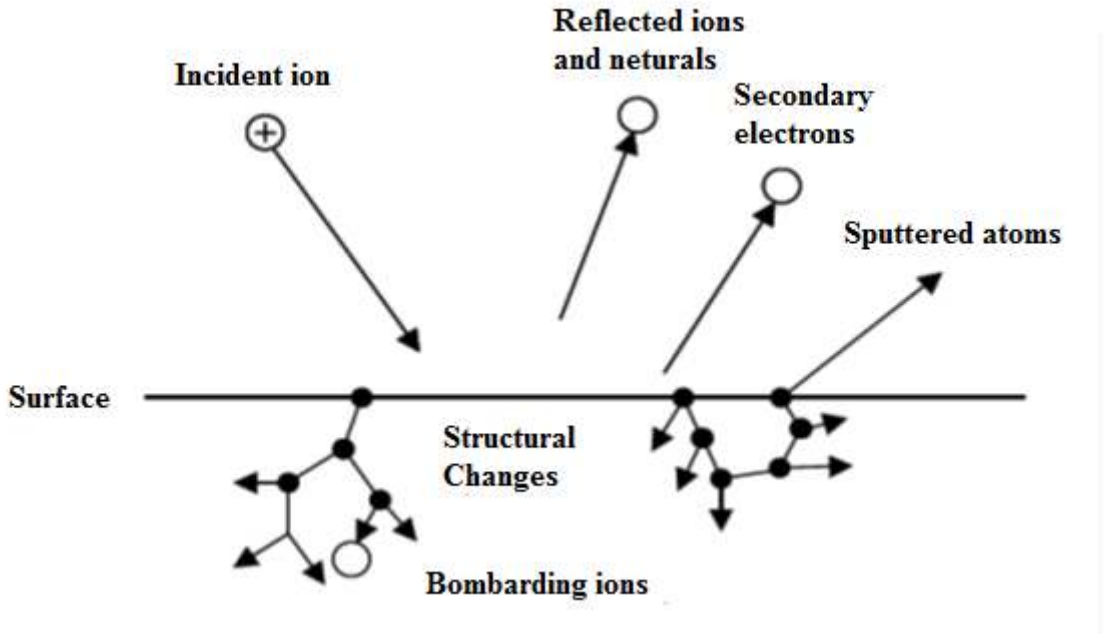

Figure 2.8 Interactions of ions with surfaces [86]

When the ion interactions are detail investigated, it is speculated that the incident atom may stop its movement and pass through the target or eject the target atom. The ejection of one of the target atom supports the idea of sputtering. However, the incident ion may be reflected and probably being neutralized in the process. Also, secondary electron may achieve from the target to eject an electron. The ion may become buried in the target and this is called as ion implantation. Moreover, this ion impact may also be responsible for some structural rearrangements in the target material. When a solid surface is bombarded with energetic particles due to the highly energetic species, the atoms will start to eject and this stage is called as sputtering.

A measure of the removal rate of surface atoms is called as the sputter yield S and it is defined as the mean number of atoms removed from the surface of a solid per incident ion and is given in Equation 2.16.

$$S = \frac{\text{atoms removed}}{incident\ ions} \tag{2.16}$$

Also, the sputtering yield can be influenced by some factors such as; the energy of incident particles, target materials, incident angles of particles and crystal structure of the target surface [85].

2.4.5 Plasmas in Deposition Processes

A low pressure gas which is partially ionized and includes positive and negative particles called as glow discharge plasma and generally used in deposition processes. Also, is can be seen as a medium in which electrical energy is transmitted, via an electric field, to a gas. Examples of application areas can be listed as; sputter deposition, activated reactive evaporation, ion plating, plasma-assisted chemical vapor deposition, plasma-assisted etching and plasma polymerization.

The probabilities of the gas-phase collisions are often expressed in terms of cross sections. The mean free path or average distance is the traversed by particles between collisions are known as the related parameter (Equation 2.17). Generally, the mean free path λ and collision cross section σ are defined by a simple relationship, thus the mean free path for electrons passing through a gas of particle density N is

$$\lambda = {}^{1}/_{(N\sigma)} \tag{2.17}$$

The total collision cross section can be written as Equation 2.18

$$\sigma_t = \sigma_{el} + \sigma_{ex} + \sigma_{\ ion} + \sigma_a + \sigma_{oth} \tag{2.18}$$

(where the subscripts el, ex, ion, a, and oth characterize the particular types of collisions, namely, elastic or momentum exchange, excitation, ionization, attachment, and other processes, respectively [79].)

2.5 Sputtering Systems

There are several glow discharge configurations due to their general geometry and the electric field the orientations [79]. In order to generate ions for sputter, two classes of systems are used as: plasmas and ion beams. In the plasma source system, the ions are

generated in the plasma while, in the ion beam case, the plasma is physically separated from the target, and an ion beam is extracted from the ion source to bombard the surface. Generally, plasma sources are categorized as diode, r.f. and magnetron plasmas.

Diode plasmas; are the simplest plasma devices with a diode, anode and a cathode inside a vacuum system. When adequate voltage is applied through the electrodes at an appropriate gas pressure, the gas will breakdown into a plasma discharge. In operation of conventional diode plasmas, cathode surface must insulate. The cathode itself is an insulator, or the process gas such as oxygen might make the surface of the cathode insulating.

The operation principles of r.f. diode plasmas are similar to diodes. The most distinctive difference is: in the r.f. diode the power supply is operated at high frequency around 13.56 MHz. Also, in the r.f. diode systems, the cathode and the anode are electrically reversed and this allows insulators or metals to be sputtered in reactive environments [87].

Also, magnetrons are used as cold cathode discharge devices in which magnetic fields are used in cathode surfaces to form traps. When a magnetic field may be supplied on the cathode, the plasma density increases with increasing both the current density and sputtering rate. The types of magnetron sputtering processes are; planar magnetron, cylindrical magnetron, dual magnetron, high-power pulsed magnetron, unbalanced magnetron, closed field magnetron, ion beam sputtering, diode, triode and reactive sputtering [80]. In Figure 2.9 (a) cylindrical and (b) planar magnetron sputtering sources are shown.

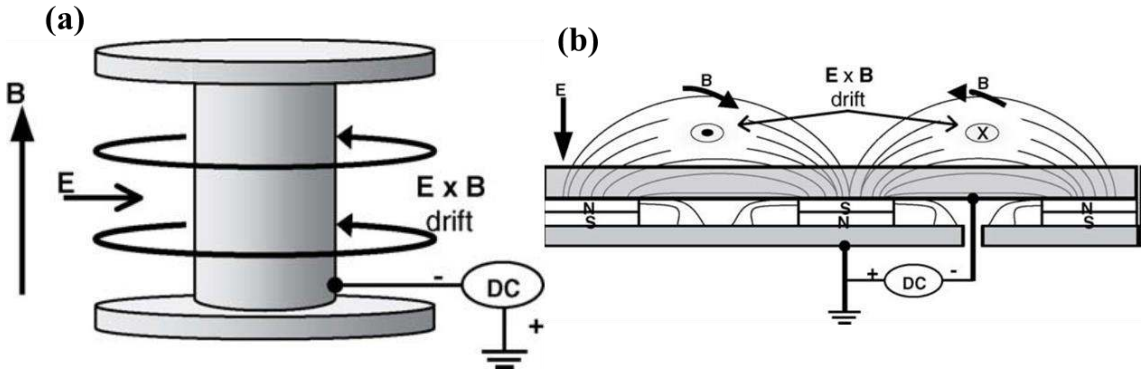

Figure 2.9 Magnetron sputtering sources (a) cylindrical (b) planar [80]

Magnetrons can be powered by a variety of methods as; radio frequency (r.f.), direct current (d.c.), pulsed d.c. and, recently, high-power impulse magnetron sputtering (HIPIMS).

2.5.1 Direct Current Magnetron Sputtering

The cheapest system to operate the magnetron is using a d.c. power supply. In this system, the target material is put on the cathode, and the substrate is on the anode [85]. The chamber is filled with the sputter gas. Mostly, non-conductive oxides from a metal target in pure O_2 or mixed Ar/O_2 discharges are sputtered with this system (Figure 2.10).

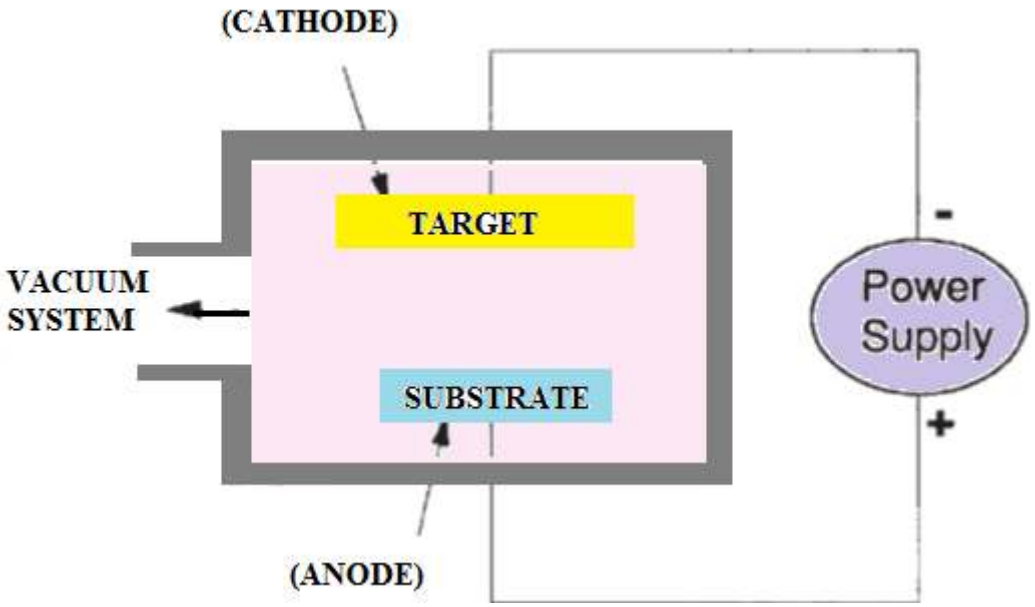

Figure 2.10 Schematic views of dc magnetron sputtering system [87]

2.5.2 Radio-Frequency Magnetron Sputtering

When the r.f power is applied, the electric field is changed rapidly and the entire electron distribution shifts up through the 'in-phase' collisions. The term 'in-phase' collisions refers that; in the discharge there is a fraction of the electron population when it is accelerated by an electric field instantly and that makes a collision before the field direction switches. Therefore, a velocity component in the direction of the switched field may occur. This distribution of electrons mechanism forces an increase in the energy. Moreover, the concentration of electrons which have energies above the gas ionization potential increases, while the overall discharge impedance decreases. The

positive/negative potential appearance occurred on the surface when r.f. potential is applied with a large voltage and coupled to an electrode capacitive. During part of each half cycle, this r.f. potential accelerated the ions through the surface and cause sputtering, while, on alternate half cycles, prevent the surface from any charge buildup.

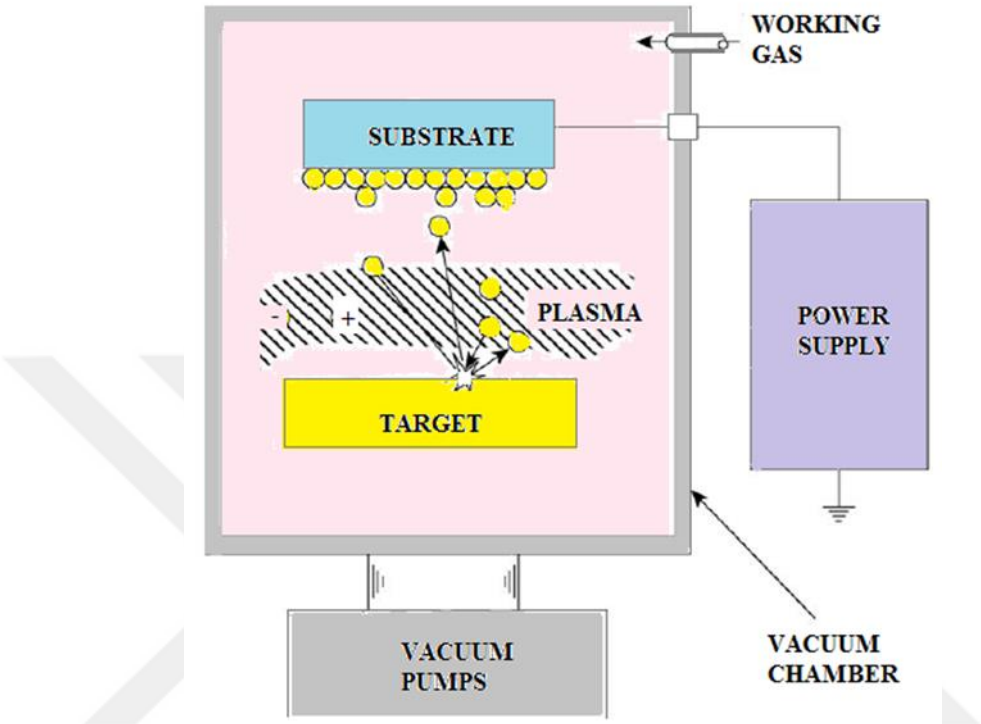

Figure 2.11 Schematic view of r.f. magnetron sputtering system [85]

r.f. magnetron sputtering can be performed at low temperature and yields films with better adhesion with the substrate and higher density deposits; these advantages make sputtering a popular technique for industrial applications [9, 29]. In sputtering, shown in Figure 2.11, physical and morphological properties of the thin films are strongly correlated with parameters such as substrate temperature, argon/oxygen partial pressure, sputtering power and target-to-substrate distance [88]. These parameters combine both the deposition rate and energy of sputtered particles, which control the stoichiometric composition, structural, electrical and optical properties of the film [89, 90]. To achieve a high quality thin film using sputtering, factors such as the angle-of-incidence of the adatom, the ratio of the deposition temperature to the melting temperature, the energy released on condensation, the deposition rate, surface roughness, mass transport and grain growth during deposition need to be carefully considered. The deposition parameters greatly influence the film properties, including resistivity and transmittance, along with product cost [90].

2.5.3 r.f. Magnetron Sputtering Parameters

Recently, the studies on ZnO thin film depositions are focused on understanding the effect of sputtering parameters such as: heating, gas pressure, gas composition, target-to-substrate distance, power etc. to achieve high quality thin films [22, 24, 26, 27, 28, 29, 88, and 90]. In the following sections these parameters will be explained:

2.5.3.1 r.f. Power

Mostly, the researches figured out the influence of r.f. power variation on the structural and optical properties of ZnO thin films by using different substrates such as silicon [91-95], quartz [96] and glass [29,97]. Kim and friends [95] deposited ZnO thin films on Si substrate at different r.f. power values, in order to investigate the influence of r.f. power of properties of the thin films. Their results revealed that, when the r.f. power increased from 150 to 300 W the surface became rougher and the intensity of (002) peak decreased.

Moreover, Yang and Liu [98] studied finding the optimum deposition parameter for ZnO:Al thin film deposition with r.f. magnetron sputtering technique. According to the results, at 300 W r.f. power value, the resistivity was measured as 4.62 $x10^{-4}$ Ω.cm, while the optical transmittance reached 93.7% in the visible range.

During sputtering, the r.f. power affects the growing process by changing the bombardment of species from both the sputtering target and the plasma. These variations play a critical role on both the crystal structure and morphological properties of the thin films [99, 143,144].

2.5.3.2 Target-to-substrate distance (D_{TS})

The distance from target-to-substrate (D_{TS}) is another important parameter to determine the mean free path of the sputtered species [100]. The increase of D_{TS} supported development of the mean free path of the sputtered species due to the collision decrease. According to Zhu and Wang [100], when the mean free path of the sputtered species is higher than the D_{TS}, the growth rate of thin films increases.

Gao [40] and Sundaram [23] examined the effect of D_{TS} on the deposition rate and resistivity of ZnO thin films deposited by r.f. sputtering with heated substrates. They found that the deposition rate and the resistivity of the films are inversely related. The

reason of this diversity can be explained as intentional heating effects the deposition differently. According to Sundam and Khan [23], the mobility of the atoms adsorbed at the surface is affected by temperature variations. A cool surface reduces the adatom mobility and tends to result in the formation of crystallites with porous and rough surfaces. On the other hand, higher substrate temperatures may cause re-evaporation and this may decrease the deposition rate of the film, which also increases the quality of the films.

2.5.3.3 Process gas pressure

The process gas pressure can also be named as working pressure; which is another critical parameter for r.f. magnetron sputtering technique. There are numerous studies about the amount of gas and the pressure and they examined that the variation of the pressure affects not only structural properties but also morphological and optical properties as well [13, 26, and 101]. Moreover, the achieved results showed variations related to the other deposition parameters.

For instance, Yue and Wu [13] reported that, when, the amount and energy of the sputtered particles are small under low sputtering power. Also, at high sputtering power values, the deposition rate of the films increased with improving the crystallite size [13]. However, Bai [102] focused on understanding the influence of process gas pressure on ZnO:Al thin films. They varied the argon pressure from 2.5 to 40 mTorr and the obtained results showed that the pressure variation demonstrated a noticeable effect on the microstructure of thin films. When the pressure increased, the growth rate of the ZnO:Al film decreased, due to the deficiency of no sufficient energy. Also, the collision probabilities of the depositing materials may be increased under higher working pressure. Therefore the deposition gas pressure has to be optimized related to the other deposition parameters.

2.5.3.4 Process gas pressure composition

A good structural quality can be gained at high pressure, which can be achieved by increasing the process gas amount with the formation of large grain size [40,146]. Also, Liao and friends [103] worked on understanding the influence of O_2/Ar flux ratio variation on ZnO films sputtered on glass substrates. Their observations revealed that,

this ratio is very important for controlling the surface roughness and crystallinity of the films.

Moreover, the effect of H_2/ (H_2+Ar) flow ratio on the quality of ZnO:Al thin films were studied by Zhu et al. [100].The achieved results revealed that; with increasing sputtering pressure, the crystallinity of the films decreases; the carrier concentration and mobility of the films show unusual change due to H_2 amount changes of microstructure and lattice defect.

2.5.3.5 Deposition rate/ Sputtering temperature

The deposition rate and the substrate temperature influence the crystal structure of sputtered films. Especially, the substrate temperature is very complicated and has different effects for different materials since it controls the surface mobility of the absorbed atoms and that effects the structural development of the film [145]. According to Sundaram et al. [23], a cool surface has low adatom mobility and tends to form the crystallite structure with high roughness. Also that may cause, achieving a rough surface with a porous structure. At high substrate temperature, adatom mobility tends increases and poorly combined structures re-evaporate. Moreover, due to the temperature, the deposition rate of the film either decreases or stays.

Chaabouni and friends [9] focused on understanding the substrate temperature influence on ZnO films deposited by using r.f. magnetron sputtering. They varied the substrate temperature from R.T. to 400 °C and they obtained at 400 °C, the intensity of the (0 0 2) peak increased by decreasing the FWHM value. They also examined that at higher substrate temperature values, both the crystallite size and the optical transmittance reached the maximum.

Furthermore, Jeong and friends investigated the preparation conditions of both ZnO and Al-doped thin films for an application of solar cell by using r.f. magnetron sputtering system [97]. They changed the substrate temperature from R.T. to 400 °C, and they obtained lower resistivity and higher transmittance values at R.T. conditions [97].

Also, Zhang group [46] studied the influence of deposition temperature on the crystallinity of Al-doped ZnO thin films at glass substrates prepared by r.f. magnetron sputtering method. They revealed that, the effect of substrate temperature is very critical for the quality of the films especially, on the structural, electrical and optical properties.

2.5.3.6 Structure Zone Models

The thin film growth process can be classified as initial and actual growth. In initial growth stage; nucleation, island growth and coalescence of islands occurrence follow each other. During these processes, the chemical and physical properties of the substrate and interaction between substrate and particles arriving to the substrate are critical parameters that have to be controlled [104].

Firstly, on the substrate, surface nucleation starts to force the island growth occurrence as called primary nucleation. Then, the substrate surface area continue developing like coalescence known as; secondary nucleation. The nucleation growing continues until it is limited by a surface covering layer (SCL) of an impurity phase. This is also known as repeated nucleation stage. As a summary, during the film growth mechanism; the nucleation starts to condense on the substrate surface simultaneously, while the secondary and the repeated nucleation initiates the starting of the growth locally in later stages of film formation [104].

The deposition material forms to condensed phase known as crystal growth can be considered as polycrystalline thin films in two main cases. One of them is the growth of discrete crystals dispersed on the substrate and the other is the growth of crystals as parts of a polycrystalline structure. When the crystals grow from random oriented nuclei, the coalescence of the crystals will touch to each other and this will cause grain coarsening. Due to this coarsening, discrete single crystals develop and the orientation is changed by minimization of the substrate–crystal interface energy. However, in polycrystalline structure the crystals have various grain sizes and orientations due to surface conditions and these structure conditions determine its behavior in the polycrystalline film structure [104].

The polycrystalline thin films can be obtained by using various techniques at a large scale of parameters. The important ones can be listed as; the energy of the particles arriving at the substrate film surface, energy absorption at the time of collision and the chemical and physical interaction between adatoms and the substrate-film surface as well as the temperature. These parameters determine size, morphology and orientation behavior of the crystallites. Moreover, the structural homogeneity of the film related with the thickness can be gained. Therefore, the structure zone models (SZM), which present an important guideline for systematizing both the experimental results and the

dependence of structures on the deposition temperature considering the homologous temperature, were formed. The historical order of these SZM's can be started with Movchan and Demchishin in 1969. They studied the effects of T_S /T_M (T_S; T is the substrate s temperature and T_M; is the melting point of the film) of material on evaporated layers of metals or oxides. In Figure 2.12 the schematic drawing of Movchan and Demchishin structure zone model is present [105].

According to this model, during the deposition process, the atoms transfer the energy into the substrate by increasing the temperature. This increase allows the arriving vapor atoms to travel further and faster in search of the lowest energy nucleation site. Thus, increasing the substrate temperature will lead to fewer nucleation sites and to larger crystals in the final thin film (Figure 2.12).

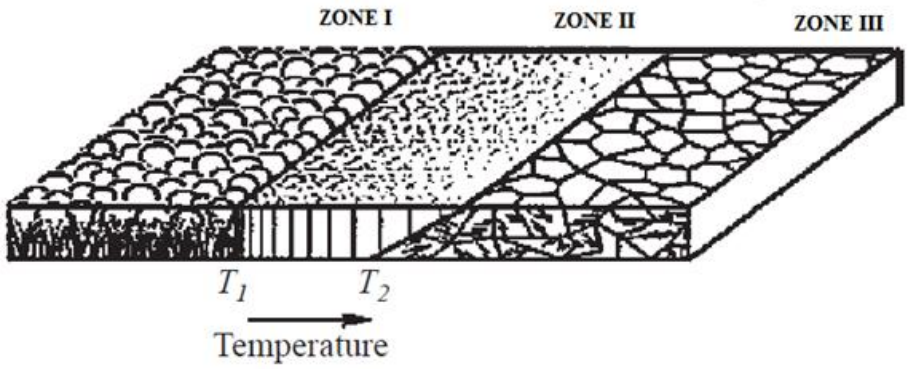

Figure 2.12 A schematic drawing showing the effect of temperature on the growth structure [105]

In Movchan and Demchishin model, evaporated layers of metals or oxides such as; Ti, Ni, W, ZrO_2, and $A1_2O_3$ were studied and their model contains three zones. However, Thornton extended this model by adding a fourth zone; the argon sputter gas pressure in early 1974's [38]. In Figure 2.13, schematic representation of the influence of substrate temperature and argon working pressure on the structure of metal coatings deposited by sputtering using cylindrical magnetron sources is shown.

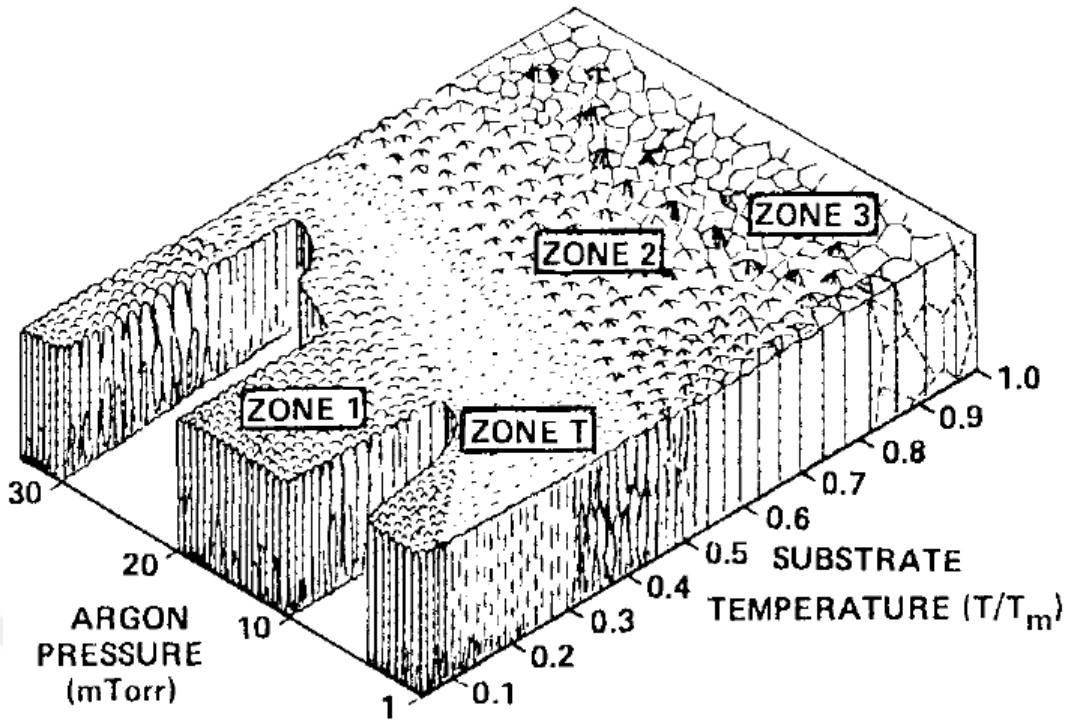

Figure 2.13 Structure zone model for sputtered films of metals [38]

T is the substrate temperature and Tm is the melting point of the coating material in absolute degrees. The Thornton structure zones exhibit the variation of substrate temperature and process pressure. The details are given below:

- **Zone 1;** the adatom diffusion is not sufficient to exceed the shadow effect. Therefore, in this structure, tapered crystals, with domed tops, which are separated by voided boundaries and tend to point in the direction of the arriving coating flux. The crystals are generally much larger than the crystallographic grain size. In fact, Zone 1 structures can occur in amorphous as well as crystalline deposits.
- **Zone 2**; adatom mobility is high enough to pass the shadow effect. The crystal growth is controlled by surface diffusion. Therefore, denser layers with small columnar grains from top to bottom are observed.
- **Zone 3;** the bulk diffusion has a dominant effect on the final structure. The grains may be columnar or equiaxed. Due to the bulk diffusion, smaller grains coalesce to form larger recrystallized grains.
- **Zone T**; (the fourth –transition zone) consists of a dense array of poorly defined fibre- like grains in which resolving of the grains are difficult [82,104,105].

In zone structure model, when the argon pressure is increased, the energy of the particles arriving from the substrate–film surface decreases, due to the collision of the argon atoms. This also revealed that, at high pressures, adsorbed argon limits adatom mobility. Therefore, the transition temperatures between zones 1, T and 2 increases with argon pressure, while it is independent of argon pressure between zone 2 and 3.

In 1984, Messier [106] tried to enlarge the Thornton's structure zone model (SZM) by drawing the zone I-T boundary as a linear boundary by adding the mobility behavior (Figure 2.14). Therefore, increasing ion bombardment compacts normally the porous zone 1 structure.

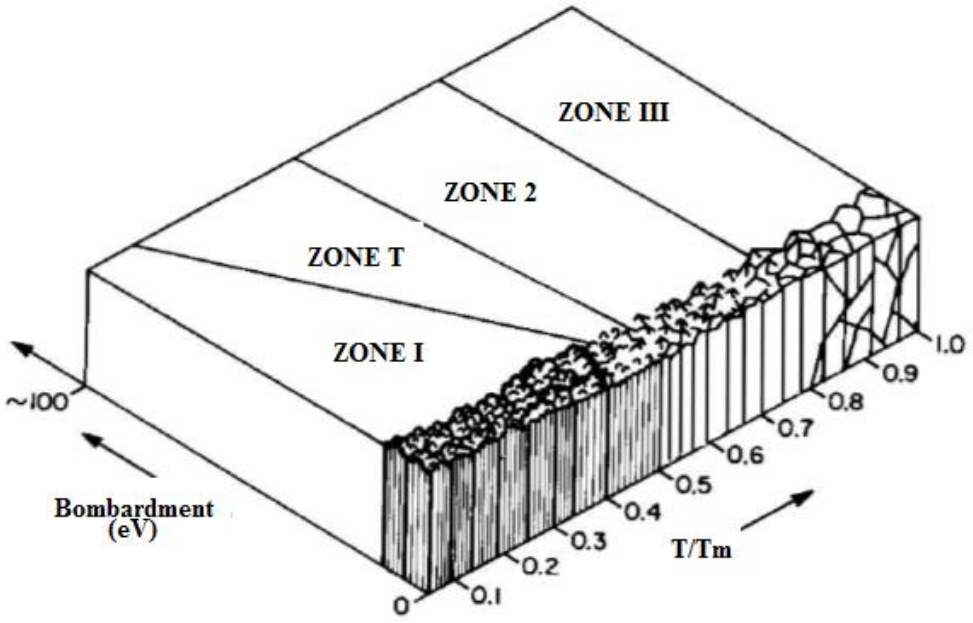

Figure 2.14 SZM for thick films showing the effects of both bombardment and thermal-induced mobility [107]

Moreover, in 1998 Grovenor and then Barna-Adamik tried to contribute SZM by concentrating on T_S/T_m variations. In Figure 2.16 both Grovenor [134] and Barna-Adamik's [135,109] structure models are shown.

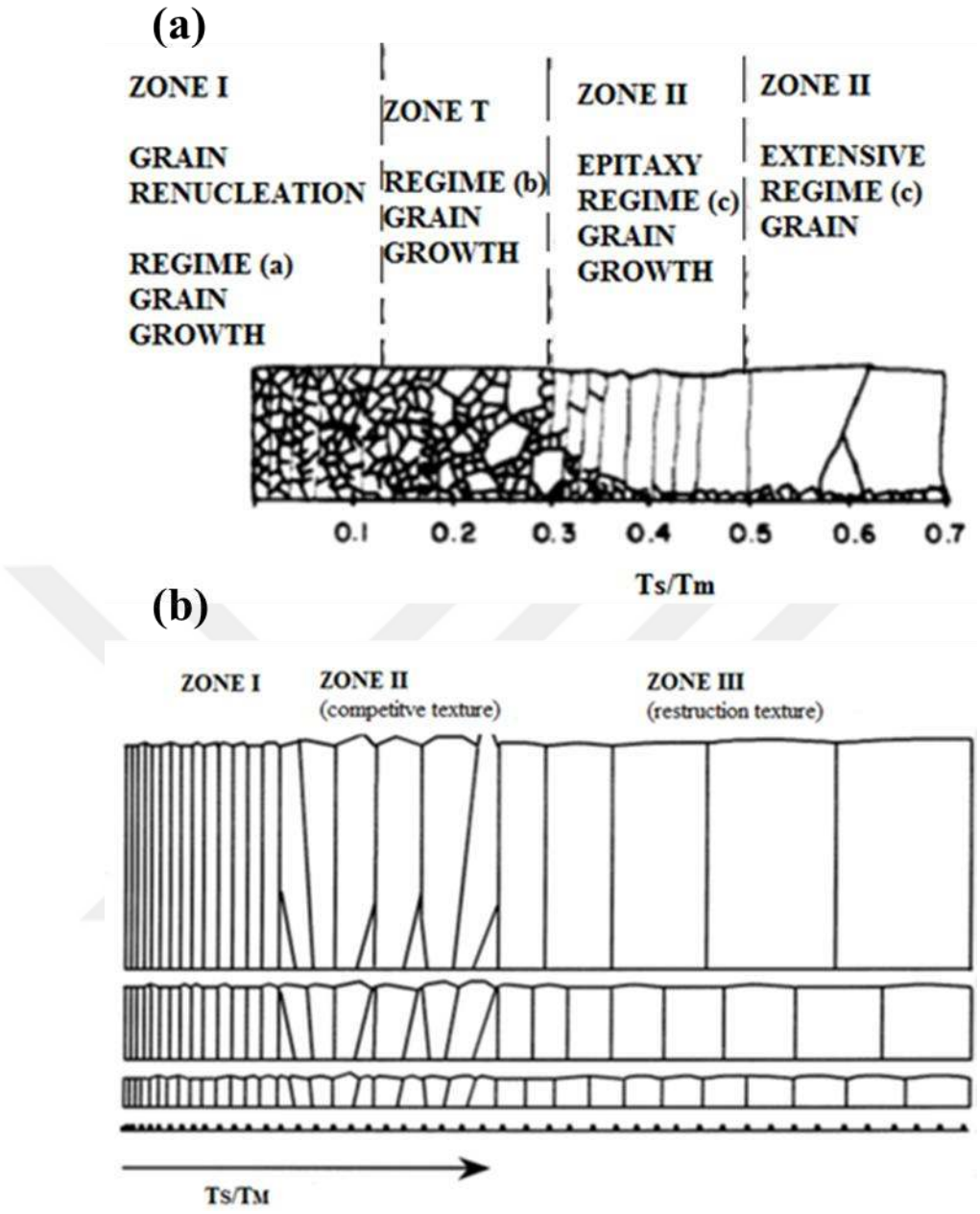

Figure 2.15 Schematic views of structure models; (a) Grovenor and (b) Barna-Adamik [107,109]

2.6 Solar cell applications

TCO in solar cell applications provides an average path length for light in the absorber longer than for a non-scattering film [48, 49, and 110]. They can be used as a ‘‘substrate cell’’ with facing the sun or a ‘‘superstrate cell’’ in which the solar radiation passes through the substrate before reaching the TCO layer [111]. They can be easily applied to various solar cells and some of the applications with their needs are present in Table 2.4.

Table 2.4 Transparent conductive oxides employed in photovoltaic devices [47]

Cell Type	TCO in Current Use	TCO Needs
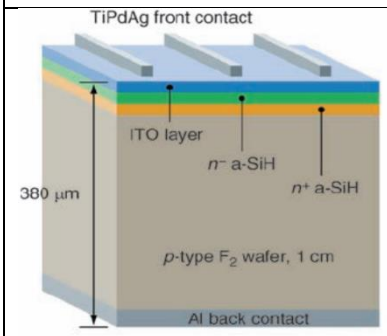 *Heterojunction with intrinsic thin layer (HIT) cell*	Indium tin oxide (ITO)	smooth, good interfacial properties, very good conductivity, low temperature deposition, light trapping
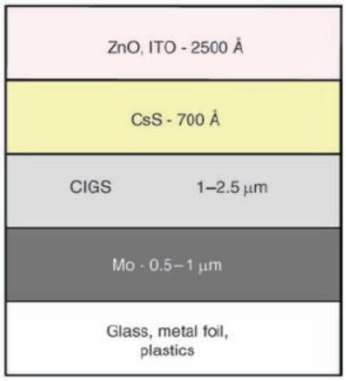 *Copper indium gallium selenide (CIGS)*	Intrinsic-ZnO/ ZnO: Al	Interfacial stability to CdS, low temperature deposition, resistance to diffusion and shorting, need to make /improve the junction
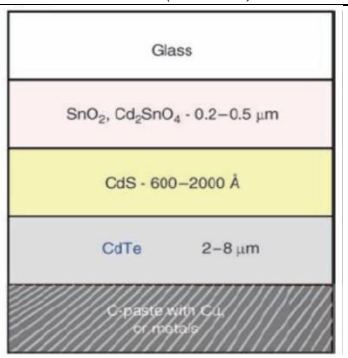 *CdTe*	$(SnO)_2$ Zn_2SnO_4/Cd_2SnO_4	stable interface to CdS/CdTe at temperature diffusion barrier

Table 2.4 (Continued) Transparent conductive oxides employed in photovoltaic devices

Cell Type	TCO in Current Use	TCO Needs
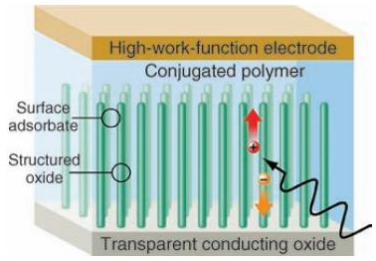 *Nano-hybrid polymer cell*	ZnO, SnO_2, TiO_2	nanostructure length with right length scale, work-function matching, interface with organic, correct doping level for carrier transport
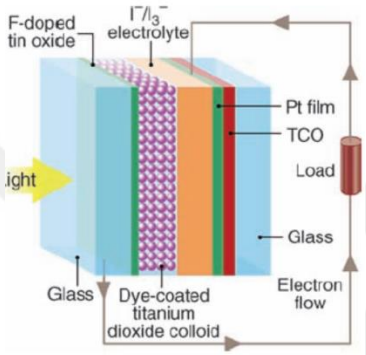 *Gratzel cell*	TiO_2	nanostructure with high electron mobility
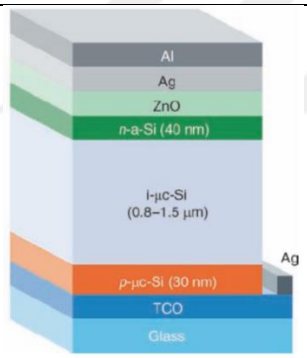 *Amorphous Si*	SnO_2, ITO and ZnO; many cell employ two TCOs	temperature stability, chemical stability, appropriate texture for both TCO layers

Generally, the performance of silicon based solar cells; due to the silicon's enhanced properties are higher than the others. It is non-toxic, very abundant, and can be easily applicable to microelectronic applications. The Si can be formed as: crystalline, polycrystalline or amorphous and hydrogenated. In crystalline form, it is cut from a single crystal ingot, while in polycrystalline structure; it is made from a multi-crystalline ingot. An amorphous and hydrogenated form can be achieved as films by using glow discharge deposition methods [112,113].

2.6.1 Heterojunction with intrinsic thin layer (HIT) solar cell

The heterojunction solar cell with intrinsic thin layer (HIT) is a new development structure achieved by the combination of crystalline and amorphous technologies in hetero-structures. The absorption of the sun mechanism occurs in a wafer of single or polycrystalline silicon

In 1990's the HIT solar cell is developed by the Sanyo Company [114]. The phosphorus doped n-type single-crystalline silicon wafer coated continuously with doped and intrinsic a-Si:H in sequence together. Also, TCO, front and back contacts are the other components of the device. In the HIT structure, the doped amorphous Si layers are deposited directly on the wafer by using advanced deposition systems. The structure of the HIT used by Sanyo Company is shown in Figure 2.16. In this structure, ITO was used as a TCO material and the role of the top ITO can be listed as: to achieve high lateral conductivity and to function as an anti-reflection coating.

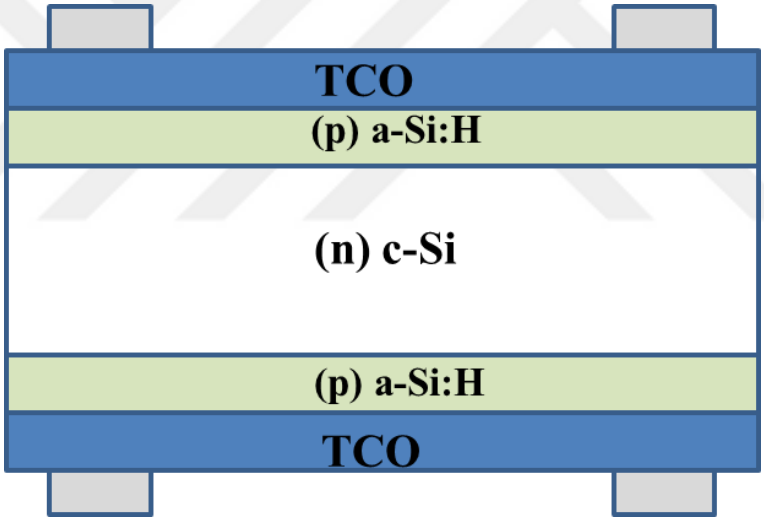

Figure 2.16 a-Si:H/c-Si solar cell structure in Sanyo [114]

The conversion efficiency of the HIT solar cell reach a level of 23.7% for a 100 cm^2 crystalline silicon substrate, while the Voc is 745 mV, short circuit current (J_{SC}) is 39.4 mA/cm^2 and fill factor is 80.9% [4]. However, the investigations to improve the efficiency values still continue. According to Sanyo, to attain a higher Voc, having high quality intrinsic a-Si:H layers and a-Si:H/c-Si interfaces are very important. In order to achieve this aim they applied some enhancements such as; cleaning the c-Si surface before a-Si:H deposition; deposition of high quality intrinsic a-Si:H layer and lower plasma applications during a-Si:H, TCO, and conductive electrode deposition [113, 114, and 115].

During development studies that involved for HIT solar cell, improvement of TCO properties plays a critical role such as, wide energy band gap, low electrical resistivity and good compatibility to other components.

CHAPTER3

EXPERIMENTAL STUDIES

ZnO and ZnO:Al thin films were deposited by using r.f. sputtering system to be able to use for PV applications. Electrical, optical, structural and morphological properties of the films deposited on silicon wafer and glass substrates were investigated using several techniques. In this chapter, experimental details about the deposition and application of TCO's are presented.

The experimental investigations were carried on separated groups such as; transparent conductive oxide deposition, substrate cleaning and characterization of the thin films. All the thin films were deposited by using radio frequency (r.f.) magnetron sputtering system.

Different TCO materials were used such as: un-doped zinc oxide and aluminum doped zinc oxide. During deposition, glass and silicon wafer were used as substrate materials. Before placement the substrates into the sputtering chamber, different cleaning procedures were applied.

The depositions of the thin films were maintained determining the optimum sputtering parameters. After sputtering, various characterization techniques were used to understand the influence of sputtering parameters on thin film properties. In order to achieve these aims; process gas pressure, r.f. power, target-to-substrate distance were changed.

3.1 TCO Sputtering

The depositions of the films were done by using 13.56 MHz radio frequency (r.f.) magnetron sputtering system. The schematic representation of the r.f sputtering system is given Figure 3.1.

Figure 3.1 Pictures of r.f. magnetron sputtering system

The sputtering system has stainless steel vacuum chamber evacuated by a pumping unit to ~10^{-5} Pa with the help of diffusion, mechanical and scroll pumps. Also, the schematic view of the r.f. sputtering system is shown in Figure 3.2.

Firstly, the substrate was placed into the holder and positioned. Then, the vacuum chamber was closed and the control unit of the system was opened. Before opening the mechanical pump, gas exhaust valve was closed. The diffusion cutoff and water valves were opened to prepare the diffusion pump. The mechanical pump was opened to vacuum the system until the diffusion system became ready. When the diffusion pump was opened, the system was vacuumed to ~10^{-5} Pa.

After reaching high vacuum levels, the process gas; argon was sent to the system. The balance between the system and the process gas pressure was maintained with the help of the scroll pump. The chamber was filled with the gas with an amount set by using mass flow controller.

The target shutter was also opened to fulfill with the process gas. When the equilibrium between the process gas pressure and the system was reached, r.f. power source was opened. Before sputtering, pre-sputtering was applied for 5 minutes and then sputtering was started by rotating the substrate over the target. After sputtering, the system was closed in an order as; r.f. power, gas flow, scroll pump and the system was left to become cold.

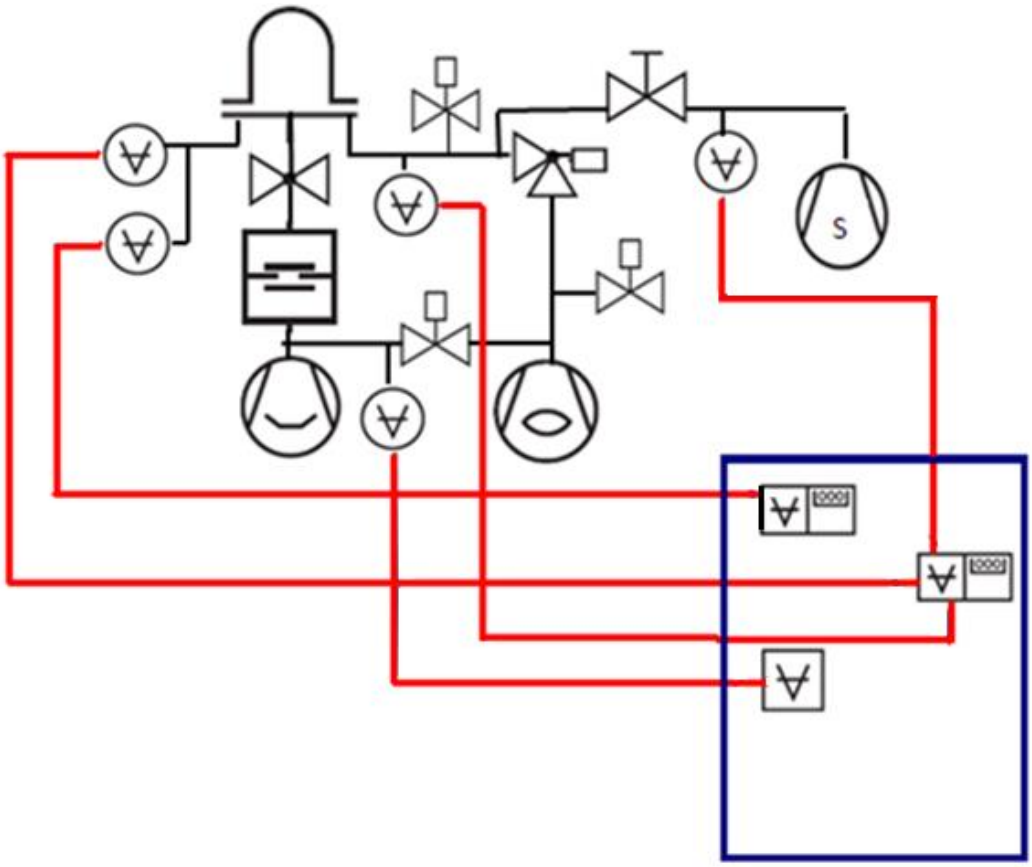

	Diffusion pump		solenoid
S	Scroll pump		Manual operation
	Rotary piston vacuum pump		Right angle valve
	Vacuum bell jar		Vacuum measurement, gauge head
	Baffle, general		Vacuum gauge control unit with digital indicator
	Isolating valve		Vacuum gauge, gauge control unit

Figure 3.2 The schematic representation of r.f. magnetron sputtering system

3.2 Target Materials

Experimental investigations were done by using three different TCO materials. These were; 10.16 cm (4" diameter) ZnO target (99.999 % purity, Kurt J. Lesker), and ZnO:Al; ZnO target mixed with 2 wt. % Al_2O_3 10.16 cm (4" diameter) (99.99% purity, 100 mm diameter, Kurt J. Lesker).

Generally, glass was used as the substrate material of TCO deposition. However, for TEM investigations and also for solar cell formation, Si wafers were also used. The properties of the glass was; 100 mm diameter, Corning 1737F glass, while for wafer; <100> oriented, p-type single crystal silicon.

3.3 Substrate Cleaning Studies

Before sputtering, cleaning of the substrates has great importance on the determination of the thin films properties. Therefore, the cleaning procedures were detailed in the following sections.

3.3.1 Glass Cleaning

The glass substrates were cleaned successively with isopropyl alcohol (IPA), acetone and deionized (D.I.) water in the ultrasonic cleaner for 5 minutes and were dried with nitrogen gas. Schematic representation of glass substrate cleaning procedure is shown in Figure 3.3 [108].

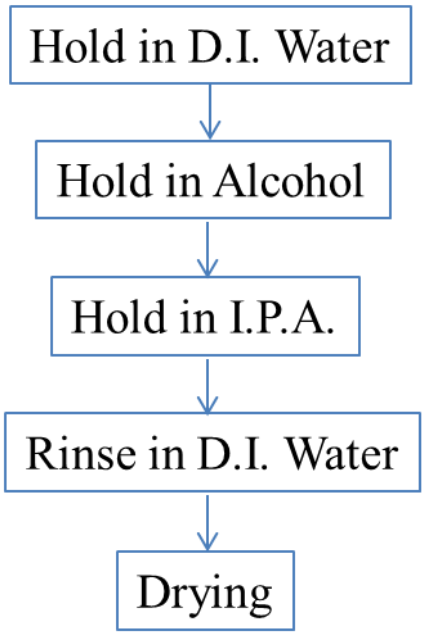

Figure 3.3 Schematic representation of glass substrate cleaning procedure

3.3.2 Wafer Cleaning

Wafer substrates were used a substrate for a-Si:H/c-Si heterojunction solar cell structure and TEM and HRTEM studies. The cleaning procedure of the wafer is critical for cell structure to arrange the surface for deposition. Therefore, wet chemical etching and dry cleaning were applied. In wet chemical etching procedure; hydrofluoric acid solutions were used as the etching agents [116].

3.4 TCO Characterization Techniques

Determination of the thin film properties such as thickness, electrical, optical, structural and morphological were done by using various characterization techniques (Figure 3.4).

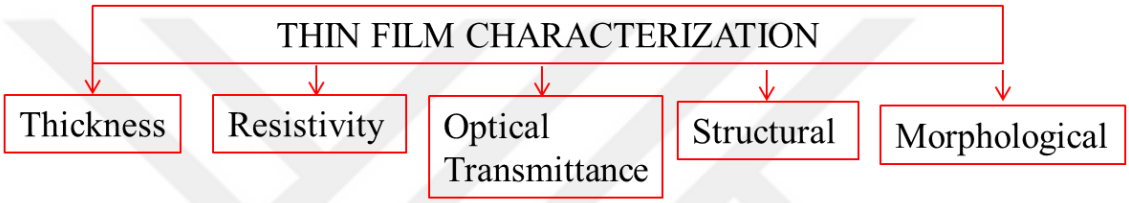

Figure 3.4 Schematic flow of thin film characterization process

The film thickness measurements were performed with scanning electron microscope (SEM) from cross-sectional view after fracturing the samples. The resistivity values of the films were obtained by four point probe technique and the ultraviolet–visible (UV–VIS) spectrophotometer was used for optical property determinations.

The phase and texture of the thin films were analyzed with X-ray diffraction (XRD) using the thin film mode. Also, transmission electron microscopy (TEM) and high resolution transmission electron microscopy (HRTEM) were used to investigate the microstructure, crystal structure and orientation of the thin films. Elemental analyses were performed with energy dispersive spectrometer (EDS) system attached to the TEM.

The general surface morphology and cross-sectional structure of the thin films were examined with high resolution scanning electron microscopy (HRSEM). Moreover, the surface morphology of the film was examined by atomic force microscopy (AFM).

The figure of merit (FOM) defined as the ratio of optical properties to electrical resistivity was measured using the following equation [109,117] was achieved the optimum deposition parameter;

$$FOM=\frac{T}{R_{sh}} \quad (3.1)$$

(where T is the average transmittance proportion to substrate in the visible spectrum and R_{sh} is the resistivity of the thin films.

3.4.1 Four point probe

The electrical resistivity defined as the availability of "free electrons" in the material. For the semiconductor materials it is often determined by using a four-point probe technique. In Figure 3.5, the surfaces of a material are shown for free electron movements. According to Figure 3.5, the current passes through the ends of the sheet from surface 1 to surface 2.

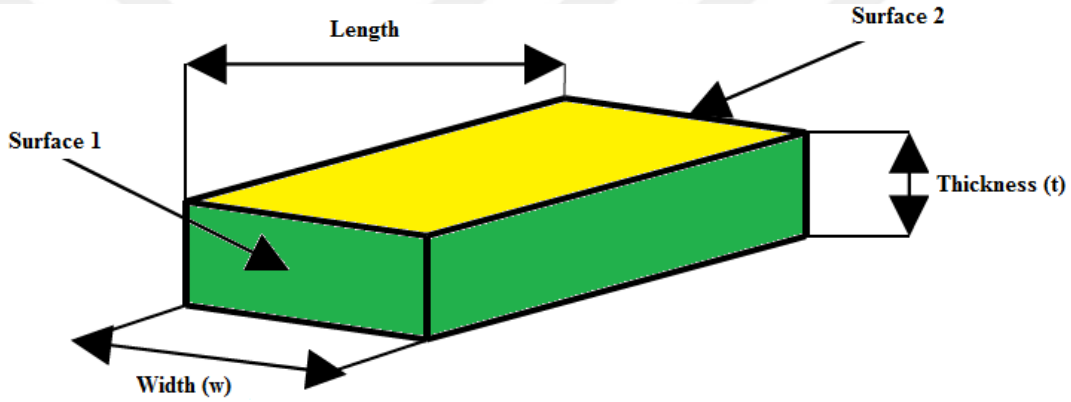

Figure 3.5 Schematic view of a conducting sheet used for electrical resistance measurements

The sheet has a length and a cross sectional area (A). The current generates a voltage difference between surfaces 1 and 2. The average resistance, «R», between surfaces 1 and 2 may be calculated from Ohm's Law as;

$$R = V/I \quad (3.2)$$

(where V is the voltage difference between surface 1 and surface 2 and I is the current.

R is also given by

$$R = \text{resistivity} \times \text{length} / A \quad (3.3)$$

(where resistivity is an electrical property of the material in ohm.cm (Ω.cm) and the length of the sheet is measured in cm.)

«A» is the cross sectional area surfaces 1 and 2 and is equal to t (thickness) x w (width) in cm x cm. Then;

$$R = \text{resistivity} \times \text{length}/ (t \times w) \quad (3.4)$$

In four point probe technique, the current is sent in two probes and the voltage is measured by two other probes as shown in Figure 3.6 (a). Therefore, the measured voltage is circulated into the sample with no current. So, there is no potential difference into the wires and contact; and spreading resistance are not high. Also, the picture of the four point system used in experimental studies is shown in Figure 3.6 (b).

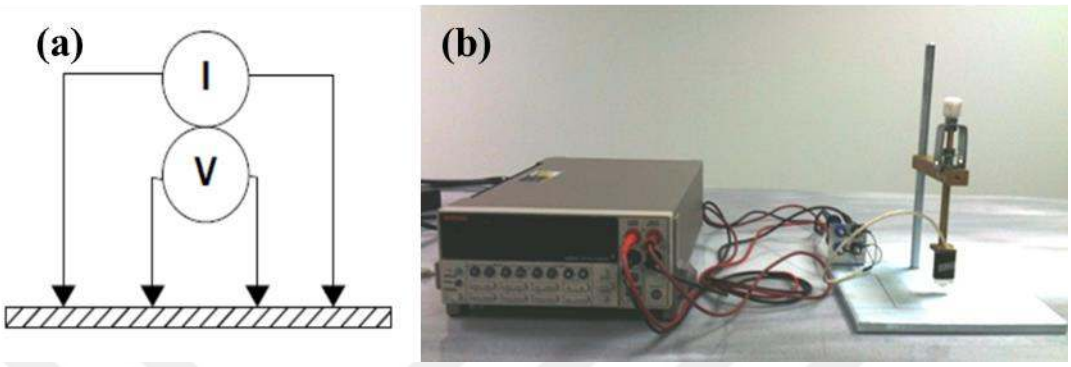

Figure 3.6 (a) Schematic view of four point probing and (b) picture of the four point probe

3.4.2 Ultraviolet–visible (UV–VIS) spectrophotometer

The ultraviolet–visible (UV–VIS) spectrophotometer (Varian Cary5000, 300-800 nm wavelengths) was used for optical property determinations. The optical band gaps of the thin films were determined with $(\alpha h\nu)^2$ versus $h\nu$ graph by extrapolating the linear portion the plots and the values were measured by using the Equation 3.5 given below:

$$T = \exp(-\alpha t) \qquad (3.5)$$

(where T is the optical transmittance, α is the optical absorption and t is the thickness of the film)

3.4.3 Scanning electron microscopy (SEM)

The film thickness measurements were performed with scanning electron microscope (the JEOL JSM 6335-F and the JEOL JSM 6510-LV) from cross-sectional view after fracturing the samples. SEM analyses were done at 20 kV.

3.4.4 X-ray diffraction (XRD)

The structural property was measured by X-ray diffraction (XRD) using a PanalyticalX'Pert Pro MPD diffractometer at 40 kV and 40 mA in thin film mode (Cu target: $\lambda = 0.1541$ nm). The crystallite sizes of the films were determined with the help of Sherrer formula [118]:

$$D=\frac{0.9\,\lambda}{B\cos\theta} \tag{3.6}$$

(where λ, θ and *B* are the X-ray wavelength. Bragg diffraction angle and full width half maximum (FWHM) of the ZnO:Al (002) diffraction peak, respectively.)The thin film patterns were determined with JCPDS- JCPDS-International Center for Diffraction Data (ICSD) Pdf number: 89-0510 space group no: 186ZnO x-ray card: Hexagonal system, P63mc (186) space group.

3.4.5 Transmission electron microscopy (TEM)

Transmission electron microscopy (TEM) was used to investigate the microstructure, crystal structure and orientation of the thin films. TEM specimens were cut by the Gatan 601 TPC ultrasonic disc cutter. Plan-view samples were cut as 3 mm discs. For cross-sectional studies, specimens were first cut and cured with the Gatan G1 epoxy-resin mixture on a hot plate inside a copper tube with a 2.3 mm inner diameter. Afterwards, samples were sliced by the StruersMinitom low speed diamond saw at a thickness of ~200 μm as 3 mm diameter discs. All TEM specimens were first ground to 80 μm by Gatan disc grinder. However, plan-view samples were ground from the substrate side only. Then, the center regions of the specimens were thinned down to ~10 μm with a Gatan 656 Dimple Grinder. A Gatan 691 precision ion polishing system (PIPS) was used to prepare the thin foils. Specimens were ion-polished first at 4 kV (plan-view samples were ion-milled from the substrate side), and then after transparent area are achieved at final step down to 1 kV.

TEM samples were investigated by the JEOL 2100 HRTEM with a LaB6 filament operated at 200 kV. Images were taken by the Gatan Model 694 Slow Scan CCD Camera with the Gatan Digital Micrograph software. A JEOL 31630 side entry double tilt goniometer was used. Dark field (DF), bright field (BF) and selected area electron diffraction (SAED) techniques were used to investigate the microstructure. For diffraction pattern analysis and crystallography purposes Single Crystal and Crystal Maker soft wares were used. Moreover, elemental analyses were performed with an Oxford Instruments INCA X-Sight 6498 Energy Dispersive Spectrometer (EDS) system.

3.4.6 Atomic force microscopy AFM

Atomic force microscopy (AFM) was used for more detailed surface structure studies and to compare between samples surface roughness parameters. AFM samples were investigated using the Q-Scope 400 by Ambios Technology Corporation at a scan rate of 1 Hz. The intermittent contact wavemode was used with an NSC16 silicon cantilever. The ScanAtomic V5.0.0 SPM control software was used for imaging.

The average height is determined by selecting the lowest point in the image as the height of zero and as a reference arrangement. The calculations were done automatically by software according to Equation 3.7.

$$\bar{Z} = \frac{1}{N}\sum_{n=1}^{n=N} Z_n \tag{3.7}$$

The standard deviation Rq (Root Mean Square) of the Z values in the image was measured by software as;

$$R_{q=}\sqrt{\frac{1}{N}\sum_{n=1}^{n=N}(Z_n - \bar{Z})^2} \tag{3.8}$$

The mean or average roughness (Ra) values were obtained as in Equation 3.9.

$$R_a = \frac{1}{N}\sum_{n=1}^{n=N}|Z_n - \bar{Z}| \tag{3}$$

The obtained Ra values were selected at surface roughness values.

3.5 a-Si/c-Si:H Solar Cell Fabrication

Figure 3.7 presents the a -Si/ c -Si:H solar cell production steps. p type, CZ, <100> c-Si wafer was used as substrate materials. In the substrate cleaning step, the wet chemical Radio Corporation of America (RCA) cleaning procedure was applied [59]. The deposition of both the intrinsic (i) and n doped a-Si:H layers were done deposited at 12 mW/cm^2 r.f. power density; 225 °C temperature; 0.6 Torr pressure conditions. During intrinsic layer deposition 40 sccm SiH_4 was flowed to the chamber, while for the n-

doped layer 20 sccm PH_3 has been added in the mixture. All the depositions were done by using plasma enhanced chemical vapor deposition (PECVD) system.

The TCO layer was deposited by using r.f. magnetron sputtering system on the top of the n doped a-Si:H layer. Back and grid shape front contacts were supplied by thermal evaporation of aluminum [116].

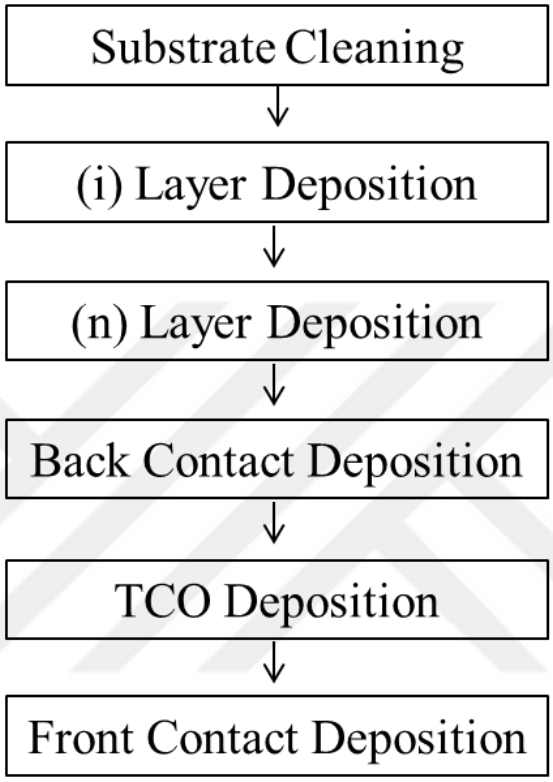

Figure 3.7 The c-Si/a-Si:H solar cell production steps

Moreover, for structural investments, TEM and HRTEM anayleses were done to achieve the c-Si/a-Si:H structure with TCO and contact layers as presented in Figure 3.8.

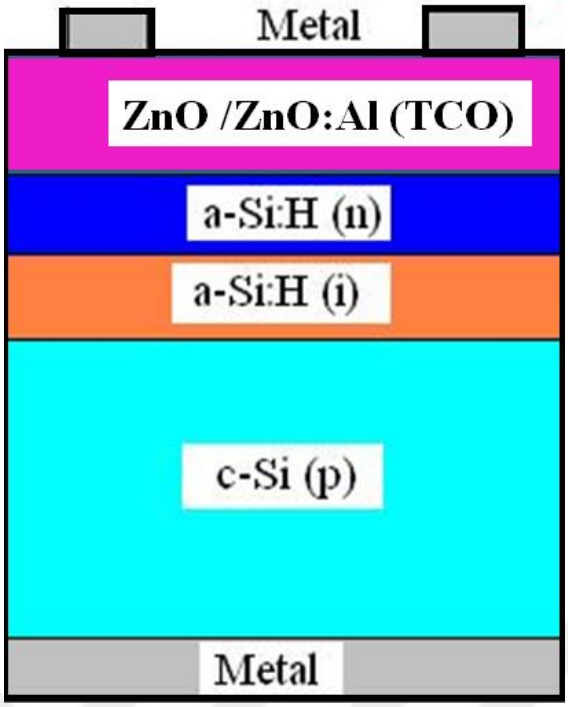

Figure 3.8 c-Si/a-Si:H cell structure with TCO and contact layers

3.6 Solar Cell Characterizations

The c-Si/a-Si:H solar cell performance was measured by using the current-voltage measurement system as shown in Figure 3.9. According to the figure, the solar cell is illuminated by the solar simulator and the current between the probes is recorded for each applied voltage. During the measurement, the solar cell is cooled with water circulation of the vacuum chuck. Wafer was put onto the chuck 10 minutes before the measurement in order to get the temperature stability. For preventing the heating of the wafers, shutter of the solar simulator lamp is opened just before the I-V measurements.

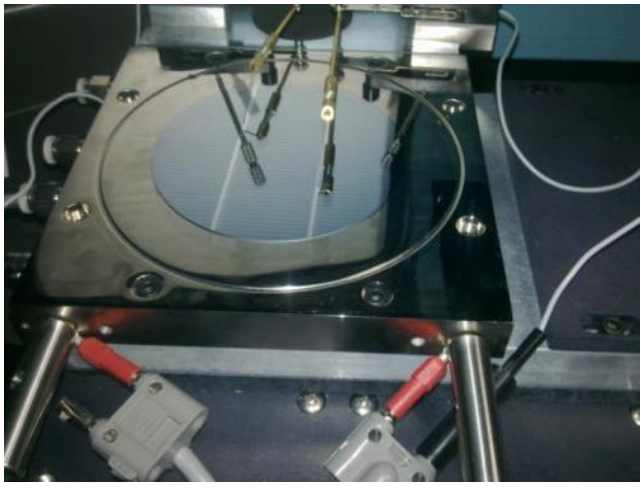

Figure 3.9 Picture of the I-V measurement system

Generally, current-voltage measurement system is used for solar cell performance characterizations. This system depends on the relation between the open circuit voltage and the short circuit current density. Also, in Figure 2.2, density-voltage curve is present [116].

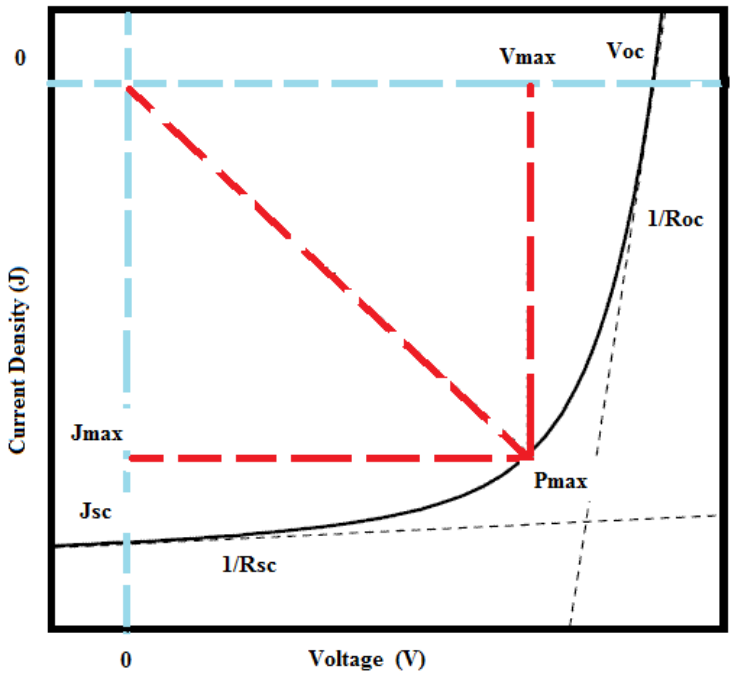

Figure 3.10Typical J-V curve and characterization parameters [119]

According to Figure 3.10, the open circuit voltage (V_{OC}) is the voltage that the solar cell carries without connected to load and it gives some details about both the material and the surface passivation quality. The short circuit current density (Jsc) is the current that is extracted from the device [120].

The fill factor (FF) is defined as the ratio of the maximum power density Pmax to the product of V_{oc}x J_{sc}as given in Equation 3.10.

$$FF = \frac{P_{max}}{V_{OC} * J_{SC}} \tag{3.10}$$

The efficiency of the solar cell η is defined as the ratio of P_{max} to the incident power density P_{light} (Equation 3.11)

$$\eta = \frac{P_{max}}{P_{light}} = \frac{FF * V_{OC} * J_{SC}}{P_{light}} \tag{3.11}$$

CHAPTER4

RESULTS and DISCUSSIONS

In this part of the thesis ZnO and ZnO:Al materials were used as sputtering target materials and they were deposited on glass or Si wafer substrates. The optimum deposition conditions were determined by using various characterization techniques. Some of these were: four point probe, UV–VIS spectrophotometer, SEM, AFM. Also, XRD, TEM and HRTEM techniques were performed for structural investigations. Furthermore, the influences of sputtering parameters such as; r.f. power, target-to-substrate distance and process gas pressure on thin films were investigated and discussed related with the structure zone models in detail. The observed results were compared with the literature and the optimum deposition parameters were determined. Moreover, ZnO:Al films with optimized properties were used as top electrode in a-Si:H/c-Si heterojunction solar cell.

4.1 Investigation the Effect of Sputtering Parameters on Zinc Oxide ZnO Thin Films

Sputtering parameters such as; substrate heating, reactive process gases, power, distance target-to-substrate distance have great importance to achieve a ZnO thin film with enhanced properties [88].To determine the optimum deposition parameters for this purpose, deposition power, target-to-substrate distance, process gas pressure and deposition time of zinc oxide thin films were changed and the investigations were done in this order. All the depositions were done at room temperature conditions, without intentional heating. Moreover, the sputtering was carried out non-reactively, and argon was used as process gas.

Electrical, structural, morphological and optical investigations were done with the help of various characterization techniques. Moreover, TEM and HRTEM investigations

were done for the optimum sputtering parameters to identify the structural growth mechanisms of the ZnO thin films.

4.1.1 Effect of r.f. power on ZnO thin films

To clarify the effect of r.f. power on structural, morphological, electrical and optical properties of ZnO thin films deposited on glass substrates without intentional heating. The r.f. power was changed in the range of 145 W to 175 W with small variations with steps of 5 W. The characterizations of the films were done in a wide area with XRD, HRTEM, SEM, AFM; and the atomic scale investigations were compared with the results in the literature.

All the process was carried on non-reactively, and the vacuum chamber was evacuated to the low vacuum (~10^{-5} Pa) range using a diffusion pump. Before the deposition, the target was pre-sputtered for 5 minutes to remove any contaminants from the target surface and to reach equilibrium conditions. The r.f. power was varied between 145 W to 175 W while, the working pressure, gas flow rate and deposition time were kept at 0.15 Pa, 5 sccm and 30 minutes, respectively. Also, target-to-substrate distance maintained as 45 mm.

4.1.1.1 Electrical properties of ZnO thin films sputtered at different r.f. powers

In Figure 4.1 resistivity and the deposition rate of ZnO thin films with r.f. power variation is shown. The deposition rates determined from the cross sectional SEM images were shown in Figure 4.2. Also, both the thickness and deposition rate values were present in Table 4.1. The resistivity values were measured as approximately 10^{-3} Ω.cm with the change of r.f. power. The minimum resistivity was measured as 0.9×10^{-4} Ω.cm at 165 W.

Table 4.1Thickness, resistivity and deposition rate variations at different r.f. powers of ZnO thin films

r.f. Power (W)	Thickness (nm)	Resistivity $\times 10^{-3}$ (Ω.cm)	Deposition Rate (Å/min)
145	440	3.99	146
150	430	2.34	143
155	420	1.90	140
160	310	1.83	103
165	230	0.94	76
170	420	4.19	140
175	460	4.38	153

The deposition rates were calculated by dividing the thickness value to deposition time. The achieved data were; 14.6 nm/sec,14.3 nm/sec, 14.0 nm/sec, 10.3 nm/sec, 10.0 nm/sec, 12.0 nm/sec and 14.0 nm/sec for 145 W,150 W, 155 W, 160 W, 165 W, 170 W and 175 W r.f. powers, respectively. It is obviously seen that the deposition rate showed a trend of increase–decrease–increase with the increase in sputtering power (Figure 4.1). Also, this provides, small r.f. power changes were efficient on both the thickness and the deposition rate. The investigations examined that at a fixed process pressure, deposition rate increased with increasing sputtering power, because of the improvement in the amount of the sputtering species [104,121].

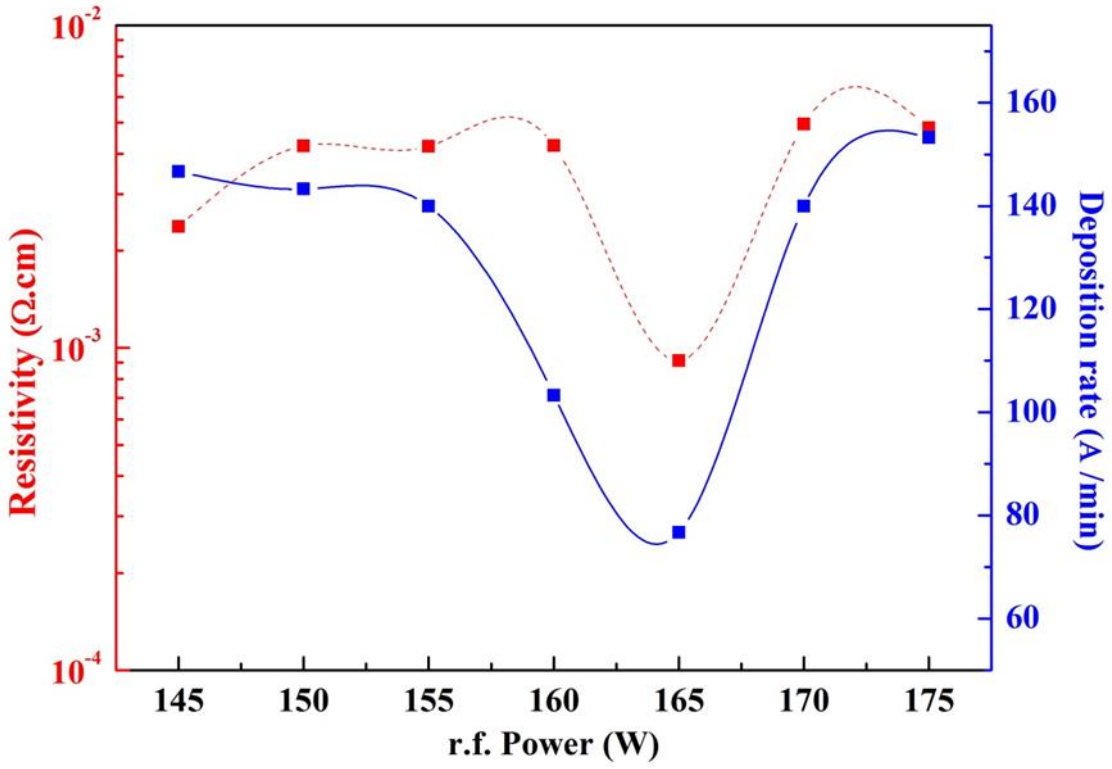

Figure 4.1 Variation of resistivity and deposition rate with r.f. power of ZnO thin films

During deposition, with the help of r.f. power many particles sputtered from the ZnO target under Ar ions bombardment [96].When the r.f power increased, both the amount and mean free path of the sputtered species were developed, due to the decrease of collision. Also, Zhu and Wang [100] observed when the mean free path of the sputtered species is higher than the target-to-substrate distance, the deposition rate of thin films increases.

Moreover, unintentional heating of the substrate may influence the obtained results [40].

Although, the substrate was not intentionally heated, sputter power may have caused a heat up on the substrate which affects the surface mobility of adatoms. Also, during deposition lower working pressure conditions may have increased the r.f. power effect.

The reasons for these resistivity variations can be explained as; at room temperature conditions, the ions sputtered from the ZnO target can not achieve an optimum bonding between substrate atoms and film atoms due to the inadequate heating energy. This leads some forming and growing difficulties of sputtered ion nucleation. Moreover, the bad adherence to the substrate causes high resistivity due to a strong contribution of the grain boundaries in charge scattering [122].

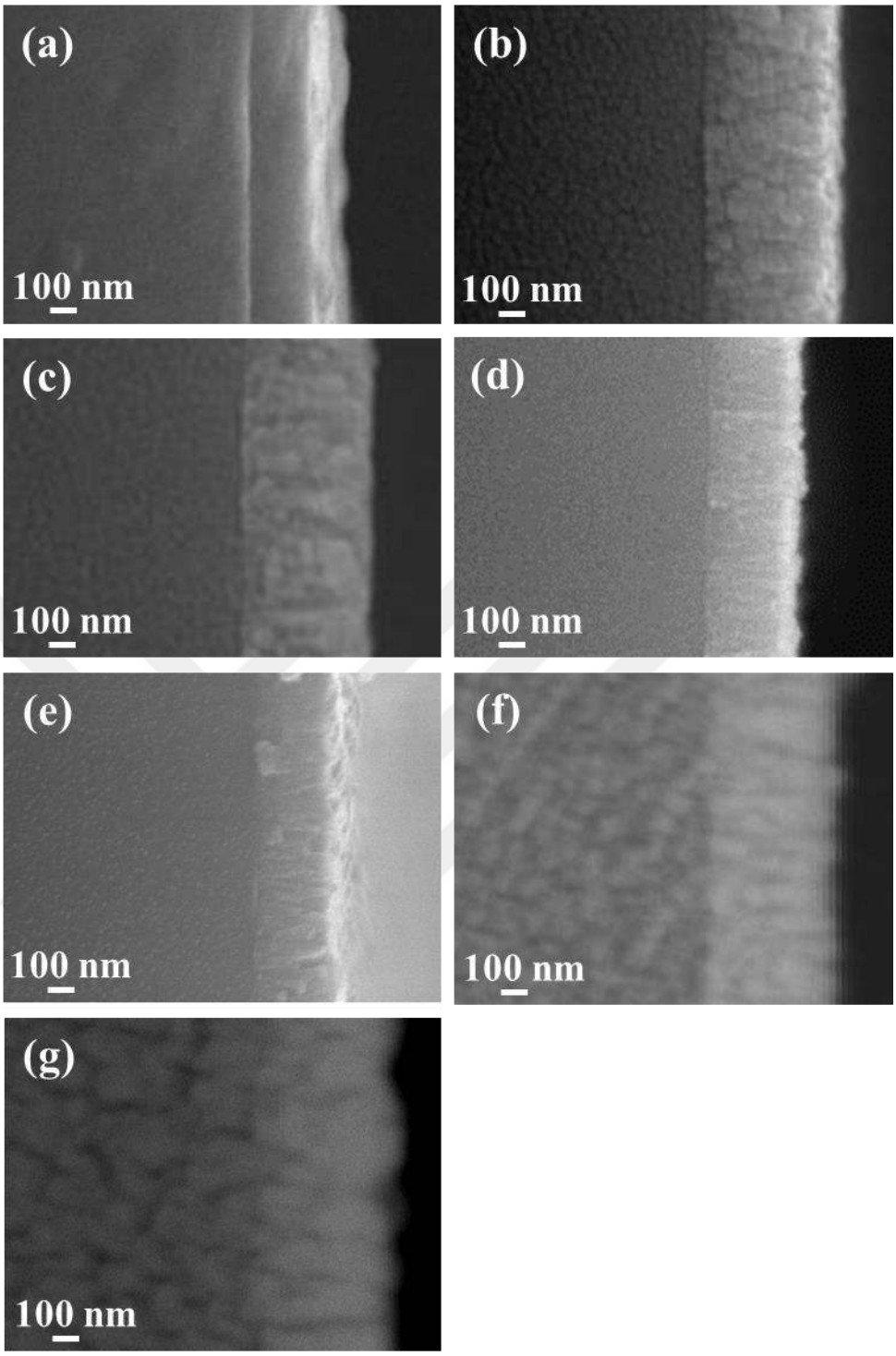

Figure 4.2 Cross sectional FESEM image of the ZnO thin films deposited at different r.f. power values: (a) 145 W, (b) 150 W (c) 155 W, (d) 160 W, (e) 165 W, (f) 170 W and (g) 175 W

4.1.1.2 Structural properties of ZnO thin films sputtered at different r.f. powers

Consequently, to understand the effect of r.f. power on structural properties, XRD investigations were done in the range of 150 W to 175 W with small changes in the r.f. power. In Figure 4.3, 2θ and intensity variations of ZnO thin films sputtered at different

r.f. powers are present. According to Figure 4.3, main peak was observed at around 34.40° ((002) peak) and this revealed that the films were growth perpendicular to the substrate surface. In Figure 4.3 and Table 4.2 position of (002) diffraction peaks showed variations which may be caused by the bombardment effect of sputtered species as also observed by different authors [29, 88, 96, and 123].

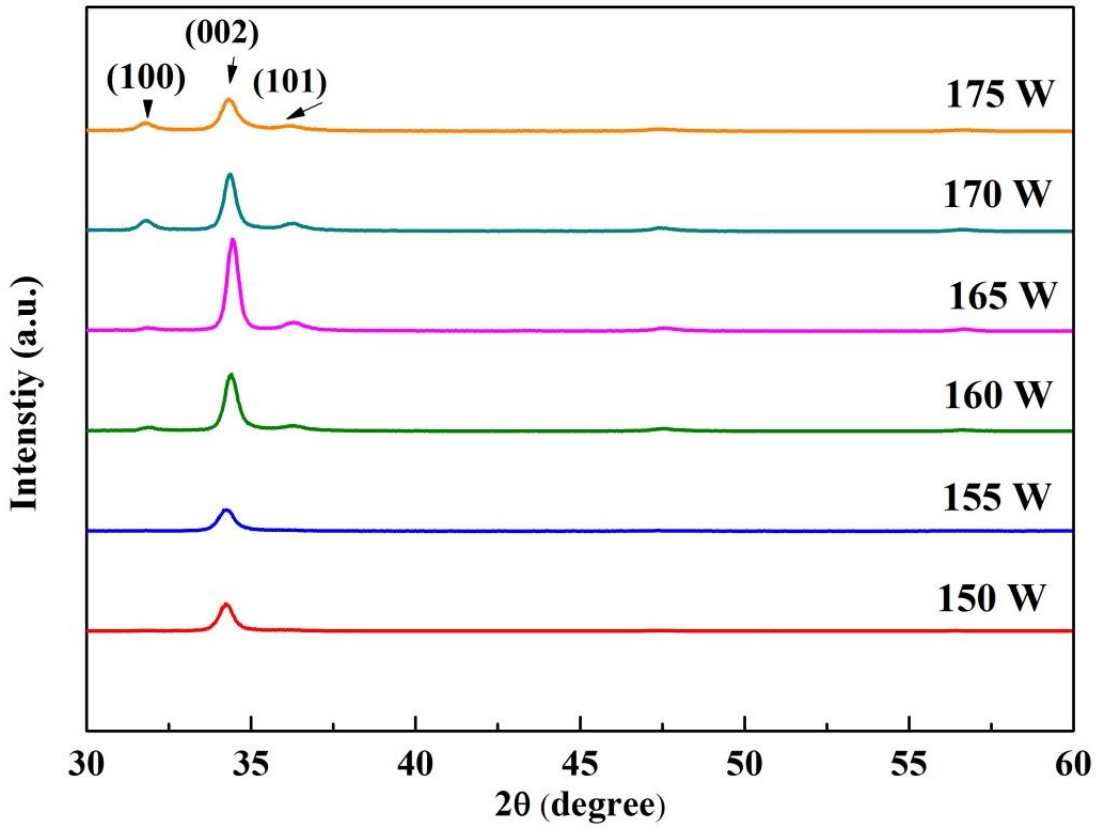

Figure 4.3 X-ray diffraction pattern of ZnO thin films deposited at different r.f. powers

Also, in Figure 4.3 (101) and (100) peaks, which cause degradation of preferred orientation, were seen for different r.f. powers; especially at higher powers such as 170 W and 175 W. According to Lin and Huang [124], when the film thicknesses were thicker than 500 nm, appearance of (101), (100) and (103) orientations were common. The thickness values of the ZnO thin films were measured by using SEM (Figure 4.2), and they were changed around 300 nm to 400 nm as shown in Table 4.1.

Park et al. [125] suggested that, film thickness and spot size of X-ray caused XRD peak intensity variation in ZnO thin films. In order to identify the thickness influence on crystal structure, the intensity achieved from (002) peak value was divided to measured thickness, and the results were presented in Table 4.2.

Table 4.2 Position of (200), intensity of (002), (002) peak intensity per unit thickness, position of (100), relative intensity of (100), position of (101), relative intensity of (101) peak for ZnO thin films at different r.f. powers

r.f. Power (W)	Position of (200) (Degree)	Intensity (002) (a.u.)	(002) Peak intensity per unit thickness (cps/nm)	Position of (100) (Degree)	(100) Rel. Int. (%)	Position of (101) (Degree)	(101) Rel. Int. (%)
150	34.25	2190.72	5.09	31.80	0.75	36.30	2.68
155	34.28	1719.53	4.09	31.80	0.58	36.34	3.27
160	34.36	4597.79	14.83	31.86	5.29	36.21	6.73
165	34.41	7392.22	24.64	31.86	2.38	36.29	8.79
170	34.37	4574.87	12.71	31.78	15.9	36.32	11.44
175	34.31	2652.76	6.32	31.77	22.91	36.14	12.63

The films with 400 nm thickness had the smallest (002) peak intensity per thickness ratio as around 4 - 5 cps/nm. On the other hand, the thinner samples with lower deposition rates had higher (002) peak intensity per unit thickness as 24.64 cps/nm. The reason of this can be explained as; instead of the film thickness, crystal orientation has greater importance on the structural developments. When the full width at half maximum (FWHM) were compared, the smallest value was obtained as 0.3576° for 165 W r.f. power (Table 4.3).

Table 4.3 FWHM and crystallite sizes of ZnO thin films at different r.f. powers

r.f. Power (W)	FWHM (degrees)	Crystallite Size (nm)
150	0.5072	16.21
155	0.5409	15.21
160	0.4288	19.19
165	0.3576	23.01
170	0.3582	22.97
175	0.5975	13.77

Furthermore, the crystallite sizes of the ZnO thin films were measured by using the Sherrer formula and they were calculated as approximately 15 nm to 23 nm. Mostly, the crystallinity of ZnO thin films increases with sputtering power as observed in the range from 150 W to 170 W with the help of the kinetic energy of sputtering species. The sputtering species play a critical role to determine the adatom mobility for crystallite growth. When the r.f. power increases, both the species energy and the mobility increase. This improvement of adatom mobility for crystallite growth exhibits the behavior of the crystallinity [71].

The reason of small crystallite size at 175 W can be explained as surface diffusion energy may be limited by the adatom mobility. According to Lee and his friends [122], the higher r.f. power value induces faster reaction rate and more damages on the surface and poor crystalline quality. They emphasize the sputtering power must be sufficiently low to have an efficient nucleation and growth. Moreover, Kim and his friends [93] reported that; the lower deposition rates were helpful for low temperature depositions to achieve c-axis crystal growth orientation with the support of XRD results. Also, in Figure 4.2 (e), it is clearly seen that the grain growth mechanism provides the columnar grain growth occurrence at 165 W r.f. power.

4.1.1.3 Morphological properties of ZnO thin films sputtered at different r.f. powers

The surface morphology with different r.f. powers were investigated by using both HRSEM and AFM. Figure 4.4 presents the plan view HRSEM images of the ZnO thin films. The compactness of the grains improved with the increase of the r.f. power. Before the r.f. power reached a value of 160 W, the grains were circular in shape, and above that power, triangular grain structure occurrence happened. The reasons of these film surface characteristics could be the bombardment of high energetic sputtering species which developed with the mobility of the surface [100].

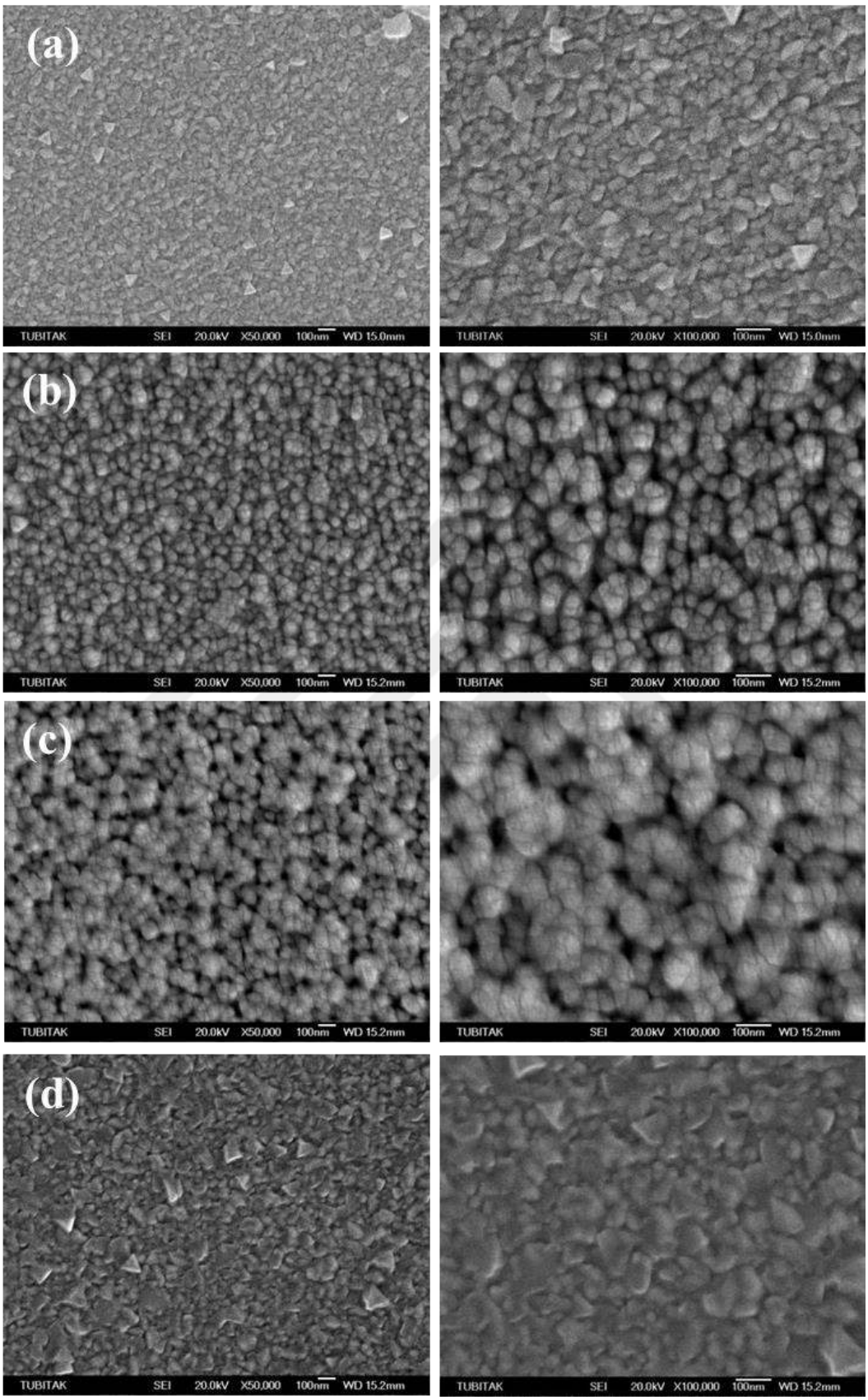

Figure 4.4 FESEM surface morphology images of the ZnO thin films deposited at different r.f. powers (a) 145 W, (b) 150 W, (c) 155 W and (d) 160 W

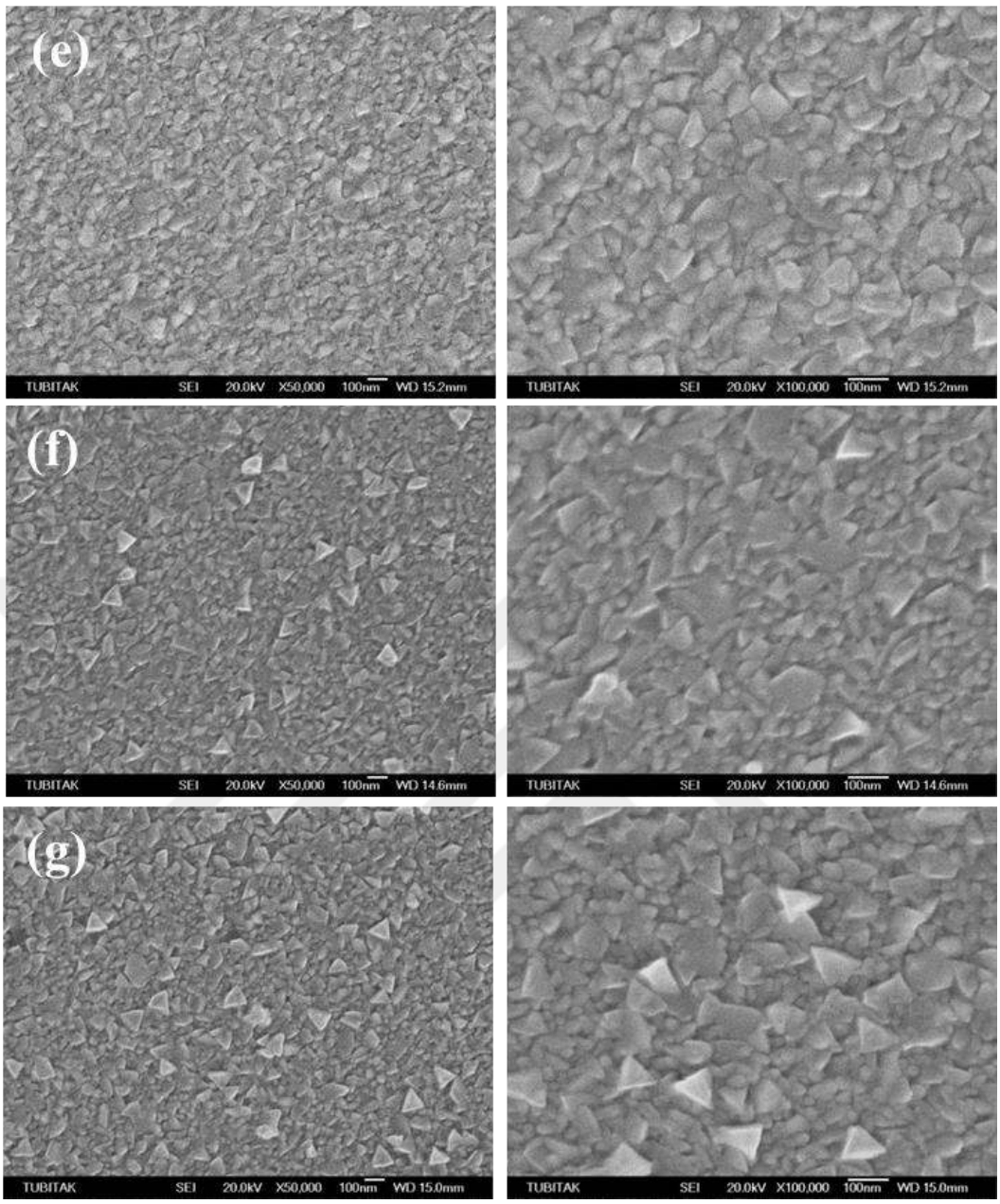

Figure 4.4 FESEM surface morphology images of the ZnO thin films deposited at different r.f. powers (e) 165 W, (f) 170 W and (g) 175 W

The AFM images of ZnO thin films obtained from the 5 × 5 μm^2 regions are shown in Figure 4.5. RMS changed as 10.9 nm, 5.50 nm, 7.89 nm, 9.30 nm, 5.80 nm, 7.36 nm and 13.80 from 145 W to 175 W r.f. powers, respectively (Table 4.4).

Table 4.4 r.f. power and corresponding RMS, Ra, Rq and average height variations of ZnO thin films

r.f. Power (W)	RMS (Sq) (nm)	Ra (nm)	Rq (nm)	Average Height (nm)
145	13.98	10.9	13.40	37.48
150	7.48	5.50	6.49	17.72
155	10.26	7.89	9.98	36.87
160	12.5	9.30	12.00	33.66
165	5.90	5.80	5.90	24.60
170	10.14	7.36	9.36	22.58
175	16.81	13.80	17.30	42.51

The obtained results showed that even the small r.f. power variations had great influence on roughness of the ZnO thin films. Furthermore, Yoo and Lee [126] advised that the small surface roughness were effective in light-trapping in thin film silicon solar cells. Similarly, Tari et al. [127] suggested that TCO films with texture were needed for certain photovoltaic (PV) applications where roughness is mostly high. Therefore, it is stated that even the value is needed as small or high, the roughness is critical and should be controlled by changing parameters such as r.f. power.

The smallest RMS and largest grain size calculated from XRD for ZnO thin films deposited was achieved at 165 W r.f. power. It could be suggested that the increase in grain size may have affected the roughness of the surface. However, Kim et al. [123] investigated the influence of r.f. power on ZnO thin films deposited on Si (001) substrates at room temperature and they recommended the larger grain size induced smallest roughness surface and their observation at around 150 W showed that RMS reached the minimum while the grain size was largest. Moreover, high energy sputtered ion bombardments could cause a surface damage that effects the RMS of deposited thin films, but they could be repaired with lower ion energy. According to this idea, the reason of rough and poor crystalline film occurrence could be explained as rate of surface damage was larger than the rate of repair [128].

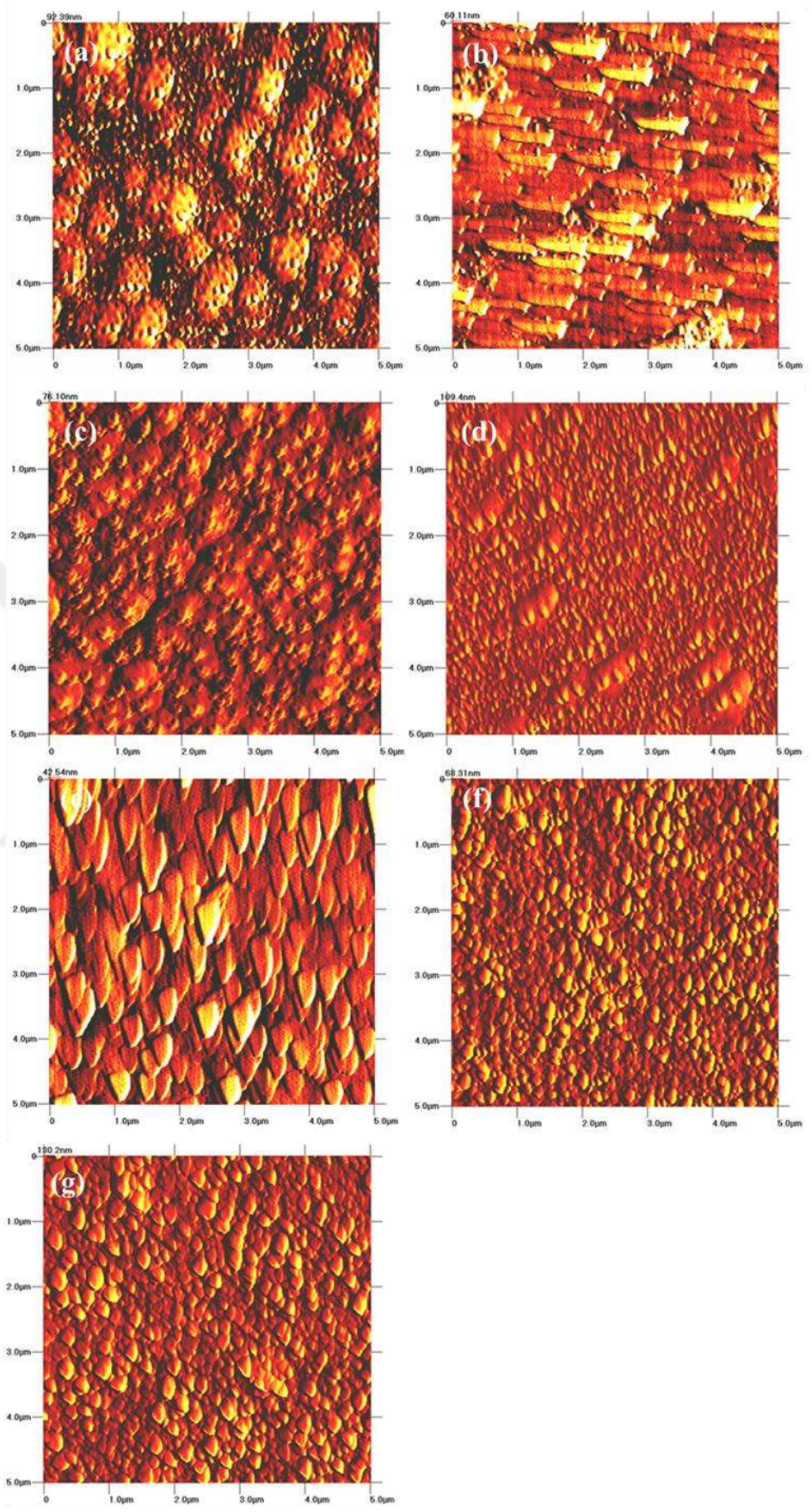

Figure 4.5 AFM images and RMS of ZnO thin films deposited at different r.f. powers: (a) 145W, (b) 150 W, (c) 155 W, (d) 160 W, (e) 165 W, (f) 170 W and (g) 175 W

4.1.1.4 Optical investigation of ZnO thin films sputtered at different r.f. powers

Figure 4.6 exhibits the optical transmittance spectra dependence of the wavelength of the ZnO thin films deposited on glass substrates at different r.f. powers. The results revealed the transmittance in the visible range achieve above 80 %. Similarly, Chaabouni and Abbab [9] were concentrated on the effect of sputtering temperature and observed that the optical transmittance was about 80 % at room temperature for ZnO thin films.

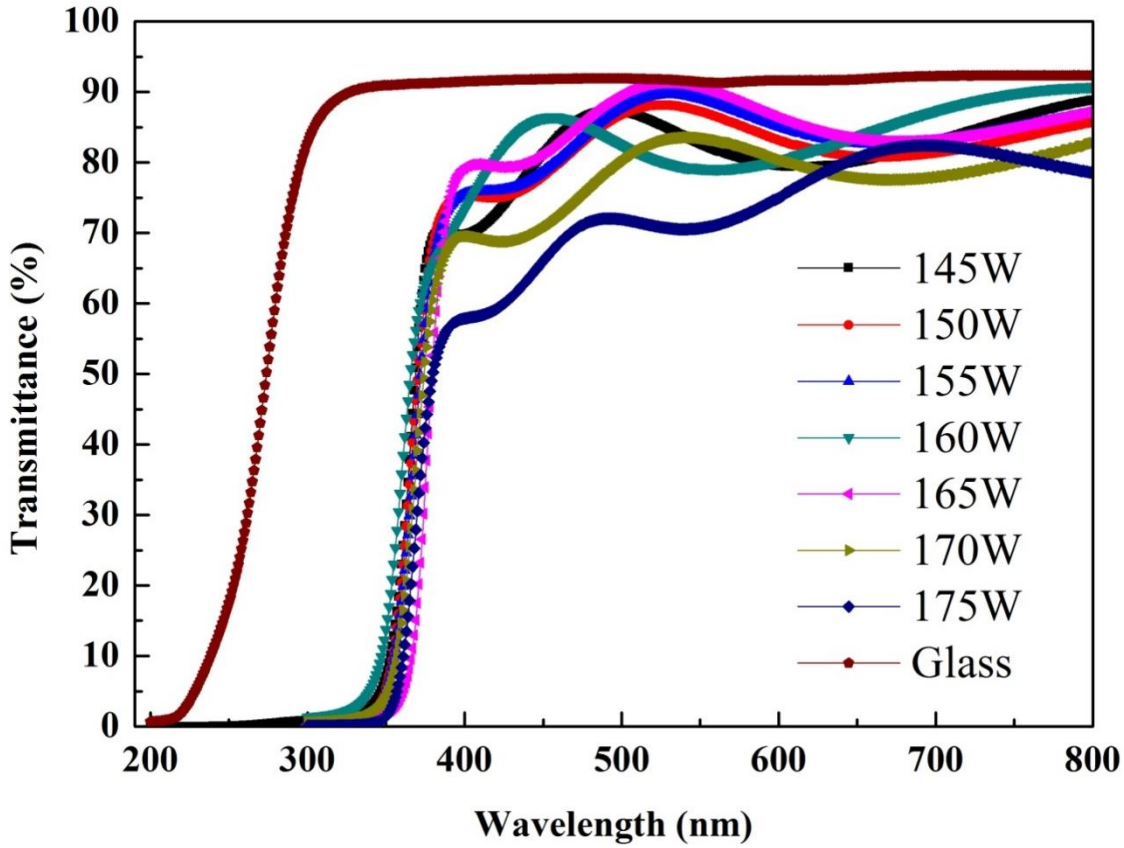

Figure 4.6 Total transmittance spectra of ZnO thin films prepared at various r.f. powers

The band gaps of the ZnO thin films were determined with $(\alpha h\nu)^2$ versus $h\nu$ graph (Figure 4.6) by extrapolating the linear portion the plots (Table 4.5 and Figure 4.7).

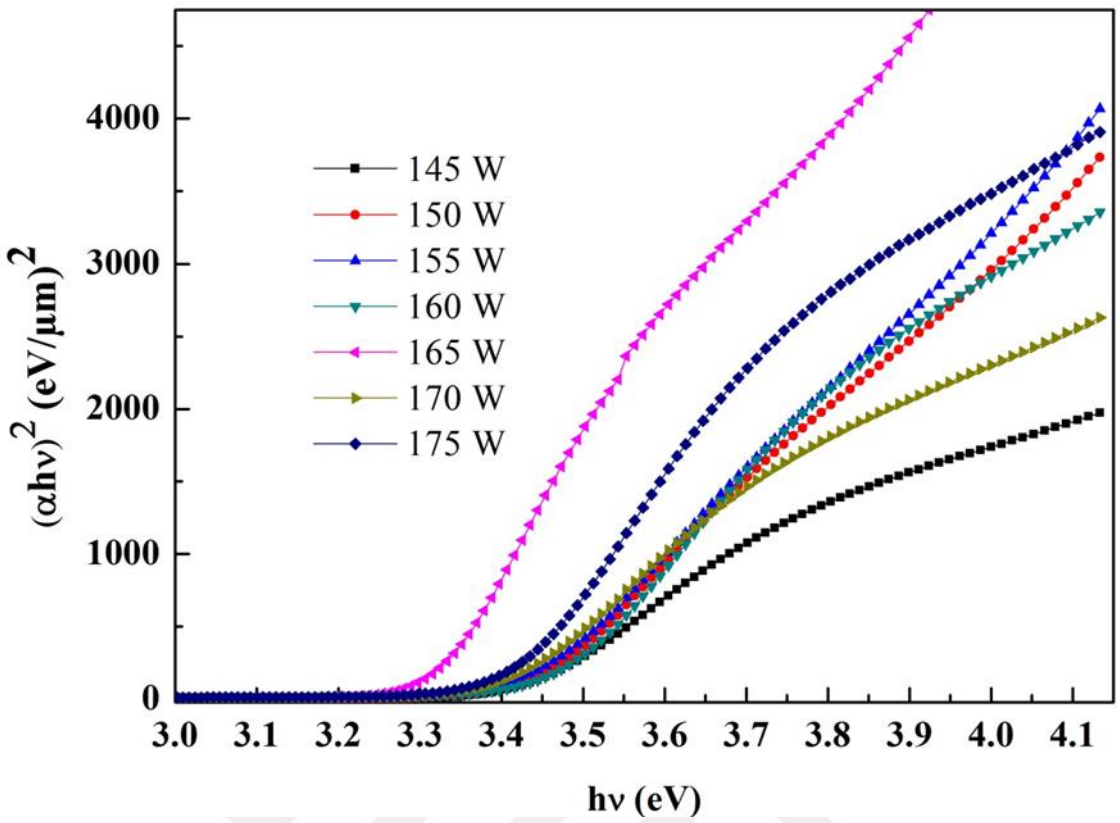

Figure 4.7 $(\alpha h\nu)^2$ versus hν graphs of ZnO thin films deposited at different r.f. power

According to the observed data, the band gap of the ZnO thin films were around 3.40 eV. The value of 3.45 eV was measured only at 165 W r.f. power condition.

Table 4.5 r.f. power, average transmittance and energy band gap variations

r.f. power (W)	Average Transmittance (%)	Egap (eυ)
145	82.39	3.42
150	82.60	3.45
155	84.02	3.44
160	84.08	3.45
165	85.30	3.35
170	78.25	3.41
175	74.45	3.40

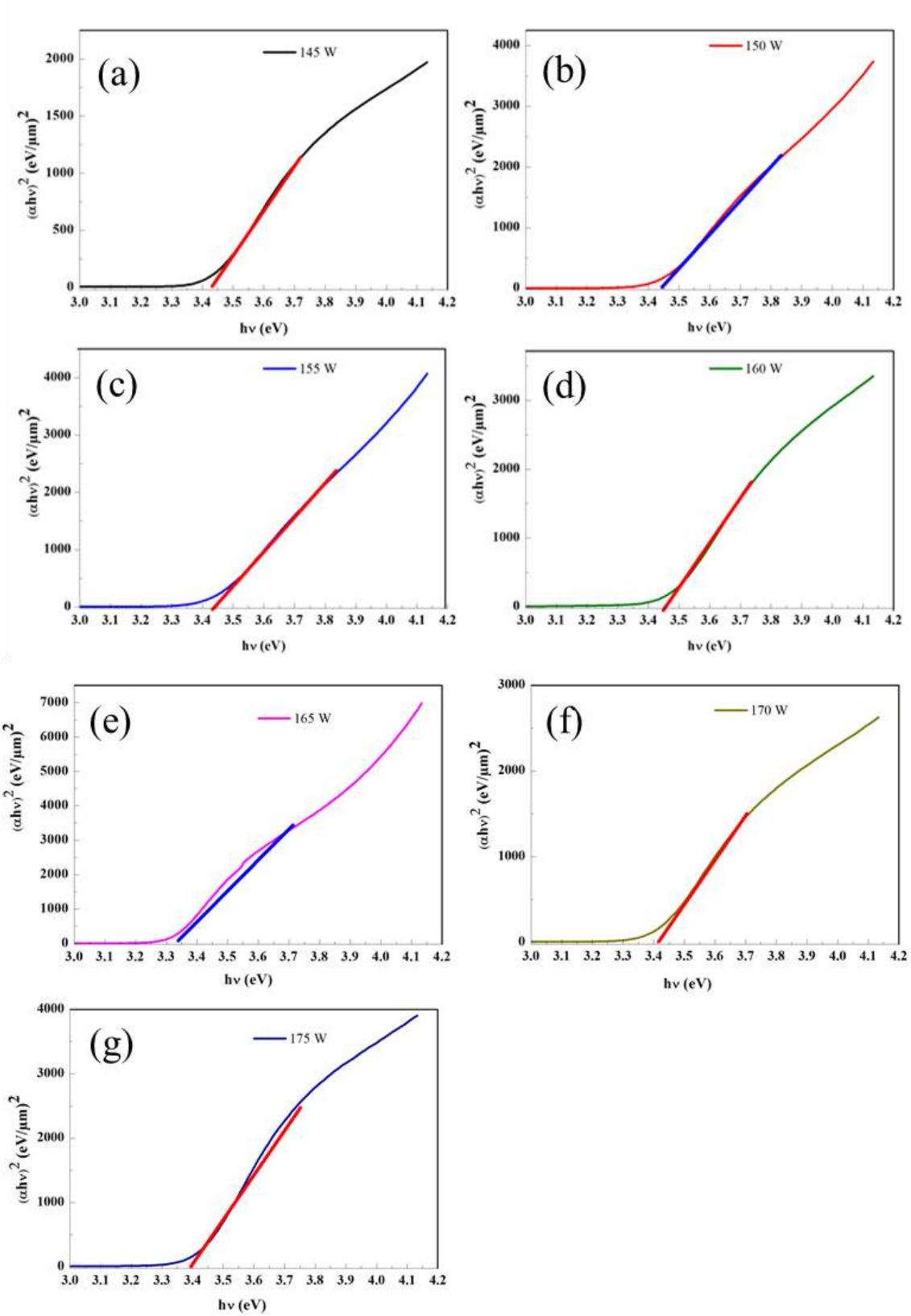

Figure 4.8 $(\alpha h\nu)^2$ versus hν of ZnO graphs thin films deposited at different r.f. powers: (a) 145 W, (b) 150 W, (c) 155 W, (d) 160 W, (d) 165 W, (f) 170 W and (g) 175 W

4.1.1.5 Summary of the r.f. power variation influence on ZnO thin film properties

The results revealed that, to make a right comparison between coating properties, figure of merit that depend on deposition parameters have to be handled. Therefore, FOM defined as the ratio of optical properties to electrical resistivity was measured for ZnO thin films deposited at different r.f. powers.

Table 4.6 Resistivity, average transmittance and figure of merit values at different r.f. powers of ZnO thin films

r.f. power (W)	**Average Transmittance (%)**	**Resistivity $\times 10^{-3}$ (Ω.cm)**	**FOM $\times 10^{4}(\Omega.cm)^{-1}$**
150	88.09	2.34	37.64
155	89.66	1.90	47.19
160	86.53	1.83	47.28
165	91.33	0.94	97.16
170	83.62	4.19	19.95
175	82.18	4.38	18.76

The obtained results given both in Table 4.6 and Figure 4.9, showed that at 165 W r.f. power, FOM reached the maximum as 971600 $(\Omega.cm)^{-1}$. This high FOM result for the ZnO thin film deposited at room temperature implies that 165 W r.f. power could be suitable for photovoltaic applications [129].

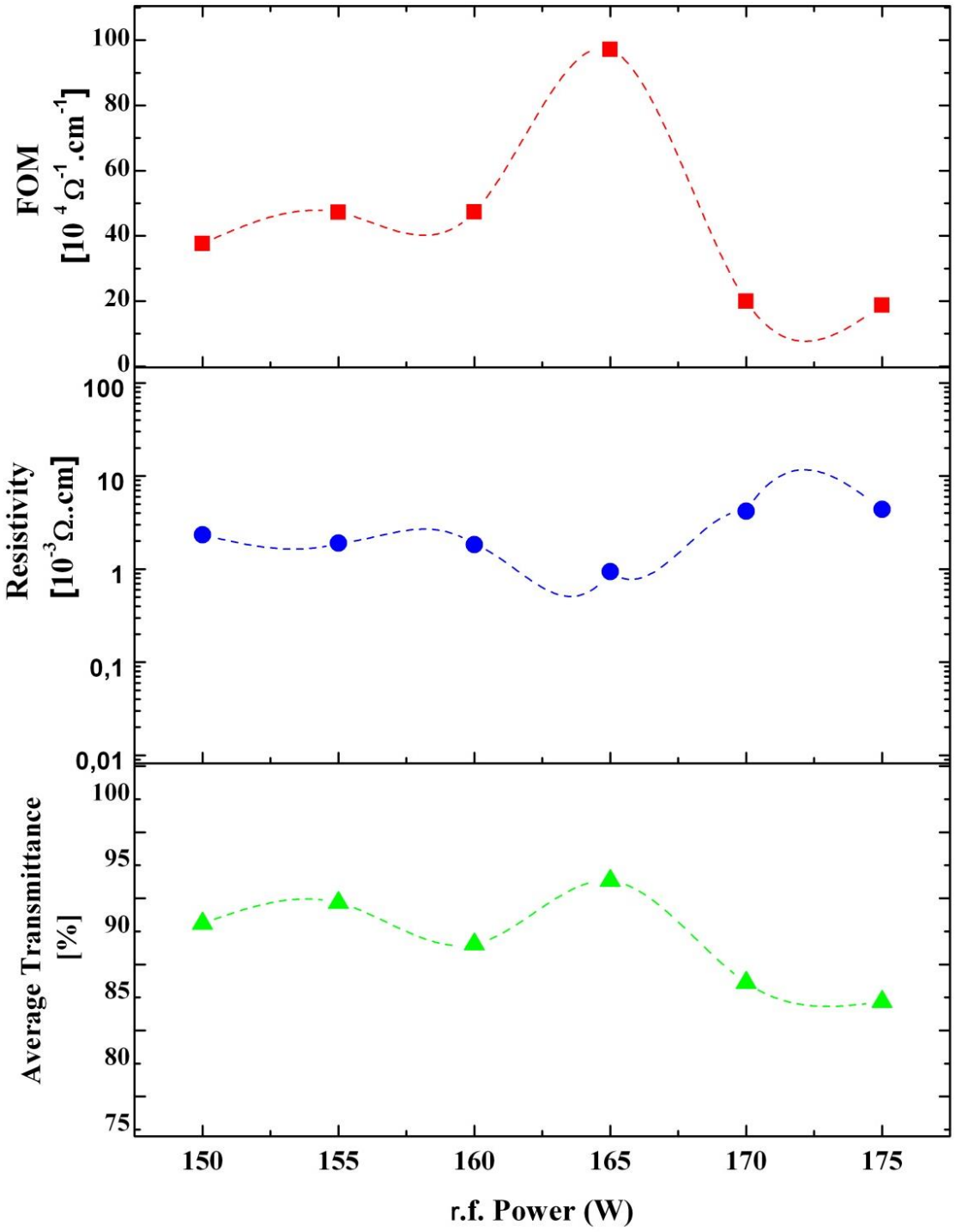

Figure 4.9 Effect of r.f. powers on average transmittance, resistivity and the figure of merit of ZnO thin films

4.1.2 Effect of target-to-substrate distance (D_{TS}) on ZnO thin films

In the present study, we also focused on understanding the effect of target-to-substrate distance on structural, morphological and optical properties of ZnO thin films. Moreover, characterization techniques including HRTEM and AFM were used to investigate the growth and key properties of ZnO thin films.

The D_{TS} was varied from 35 mm to 65 mm in 5 mm steps at 165 W r.f. power, while the working pressure, gas flow rate and deposition time were maintained at 0.15 Pa, 5 sccm and 30 minutes, respectively. The deposition conditions are summarized in Table 4.7.

Table 4.7 Deposition parameters of the ZnO thin films

Working Pressure (Pa)	0.153
Gas (Ar) flow (sccm)	5.0
r.f. power (W)	165
D_{TS} (mm)	35-65
Deposition time (min)	30
Substrate temperature (T_s)	Room Temperature

4.1.2.1 Electrical properties of ZnO thin films sputtered at different D_{TS}

Low electrical resistivity and high optical transmittance are the most important parameters required for TCO applications [26]. D_{TS} effect was investigated at 165 W without intentional heating. In Figure 4.10, the variations of both the resistivity and deposition rate are plotted when D_{TS} was changed in the range from 35 mm to 65 mm.

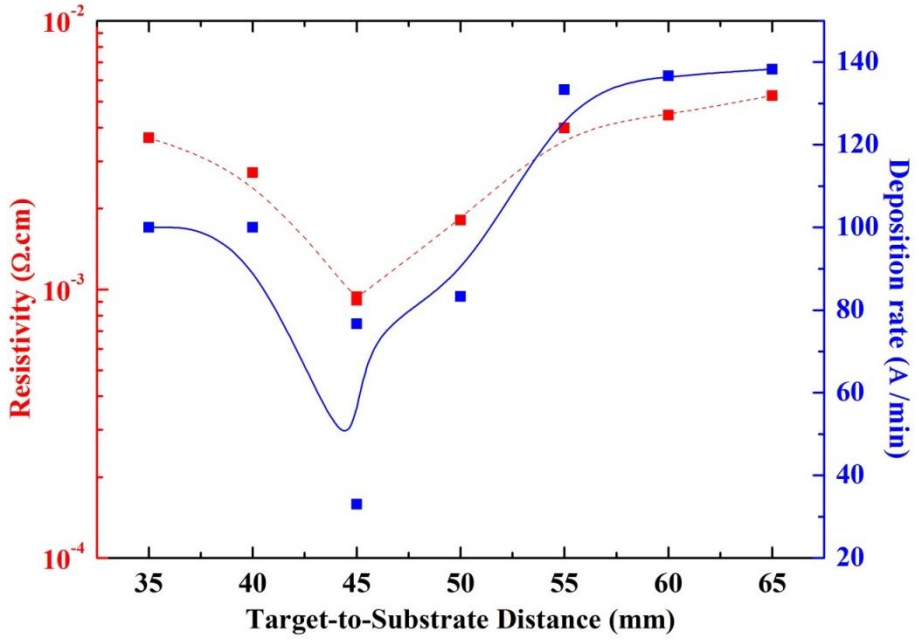

Figure 4.10 Resistivity and deposition rate of the ZnO thin films as D_{TS} varied between 35 mm to 65 mm

It is observed that both resistivity and deposition rate show a trend of increase–decrease–increase with increasing D_{TS}. This provides that, small D_{TS} variations were efficient on deposition rate and electrical properties of ZnO thin films. The particles sputtered from the ZnO target move on the substrate under Ar ions bombardment, with the help of r.f. power [96]. Also, target-to-substrate distance, resistivity, thickness and deposition rate variations were shown in Table 4.8. At 45 mm D_{TS} value the deposition was repeated at 45 mm D_{TS}, to check the correctness of the results once more. The thickness values were obtained from the cross sectional SEM investigations and they were shown in Figure 4.11.

Table 4.8 Resistivity, thickness and deposition rate variations at different target-to-substrate distance values of ZnO thin films

Target-to-Substrate Distance (mm)	**Thickness (nm)**	**Resistivity $\times 10^{-3}$ (Ω.cm)**	**Deposition Rate (Å/min)**
35	300	3.67	100
40	300	2.72	100
45	100	0.91	33
45	230	0.94	76
50	250	1.81	83
55	400	3.99	133
60	410	4.46	136
65	415	5.27	138

The behavior of the resistivity values obtained from D_{TS} variations (Figure 4.10) showed similarities to deposition rate. As D_{TS} was increased towards 45 mm, the resistivity values of ZnO films decreased from 3×10^{-3} Ω.cm to 9×10^{-4} Ω.cm. Below 45 mm, the value of the resistivity reached a maximum of 6×10^{-3} Ω.cm. Also, the minimum values shown in Figure 4.10 were verified multiple times. The achieved results revealed that the small D_{TS} variation could cause differences on electrical resistivity values. Since the formation and growing of the film are effected from D_{TS}, it also has great influence on ZnO thin film properties.

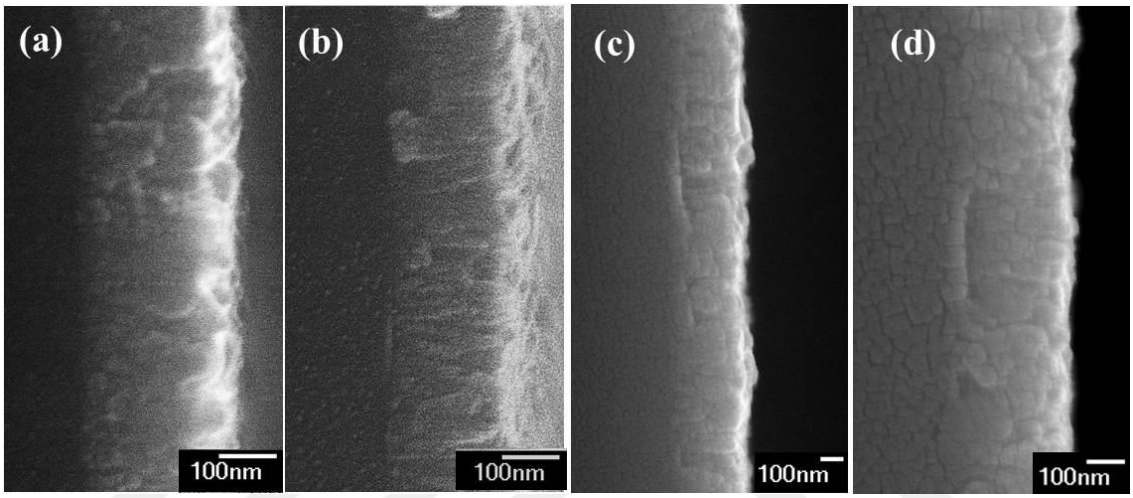

Figure 4.11 Cross-sectional HRSEM images of the ZnO thin films deposited at different D_{TS}; (a) 35 mm, (b) 45 mm, (c) 55 mm and (d) 65 mm

Gao [40] and Sundaram [23] examined the effect of D_{TS} on the deposition rate and resistivity of ZnO thin films deposited by r.f. sputtering with heated substrates. They found that the deposition rate and resistivity of the films are inversely related. The reason of this diversity can be explained as intentional heating effects the deposition differently. According to Sundam and Khan [23], the mobility of the atoms adsorbed at the surface is affected by temperature variations. A cool surface reduces the adatom mobility and tends to result in the formation of crystallites with porous and rough surfaces. On the other hand, higher substrate temperatures may cause re-evaporation and decrease the deposition rate of the film, which increases the quality of the films.

Furthermore, Bouderbala et al. [130] investigated the effects of substrate position on the structural, electrical and optical characteristics of ZnO films by r.f. sputtering. They found the lowest resistivity to be 10^{-3} Ω.cm for 300 nm thick samples at 80 mm D_{TS}, 25 mTorr working pressure and 200 W r.f. power.

Also, Sim et al. [129] focused on doping ZnO thin films with different elements by r.f. sputtering and found the resistivity to be 0.78 Ω.cm for un-doped, 600 nm thick ZnO film deposited at 175 W and 350 °C. Bouderbala [36] studied on the effect of ZnO film thickness by sputtering films at 200 W, 25 mTorr, 50 mm D_{TS} and at room temperature. According to their results, the resistivity behaved differently between the thickness ranges of less than 300 nm and more than 300 nm. The results showed that resistivity decreased from 1 to 10^{-3} Ω.cm below 300 nm. However, when the thickness was more than 300 nm, resistivity became independent of thickness and remained constant at approximately 10^{-3} Ω.cm.

Our results revealed that, without intentional heating, ZnO thin films with a resistivity as low as 9×10^{-4} Ω.cm were deposited at a rate of 7.7 nm/min by changing D_{TS}.

The distance from target-to-substrate is one of the critical point to determine the mean free path of the sputtered species [100]. The increase of D_{TS} supported development of the mean free path of the sputtered species due to the collision decrease. According to Zhu and Wang [100], when the mean free path of the sputtered species is higher than the D_{TS}, the growth rate of thin films increases. Our observed data showed that below 45 mm deposition rate was high around 10 nm / min. At 45 mm the value reached minimum as 7.7 nm / min. This provided that both the D_{TS} and mean free path of the species were balanced. As D_{TS} increased above 45 mm, the deposition rate increased above their initial values due to the increase of sputtered collision. Moreover, unintentional heating of the substrate may influence the obtained results [41]. Although, substrate was not intentionally heated, sputter power may cause a heat up on the substrate which affects the surface mobility of adatoms.

4.1.2.2 Structural properties of ZnO thin films sputtered at different D_{TS}

Figure 4.12 shows typical XRD patterns of the ZnO thin films deposited at D_{TS} of 35 mm, 45 mm, 55 mm and 65 mm using the r.f. power at 165 W, without intentional heating. For all samples, the (002) peak is observed at a 2θ value of approximately 34.50°, which is very close to the standard ZnO crystal at 34.45° (JCPDS-ICSD Pdf no: 89-0510 space group no: 186).

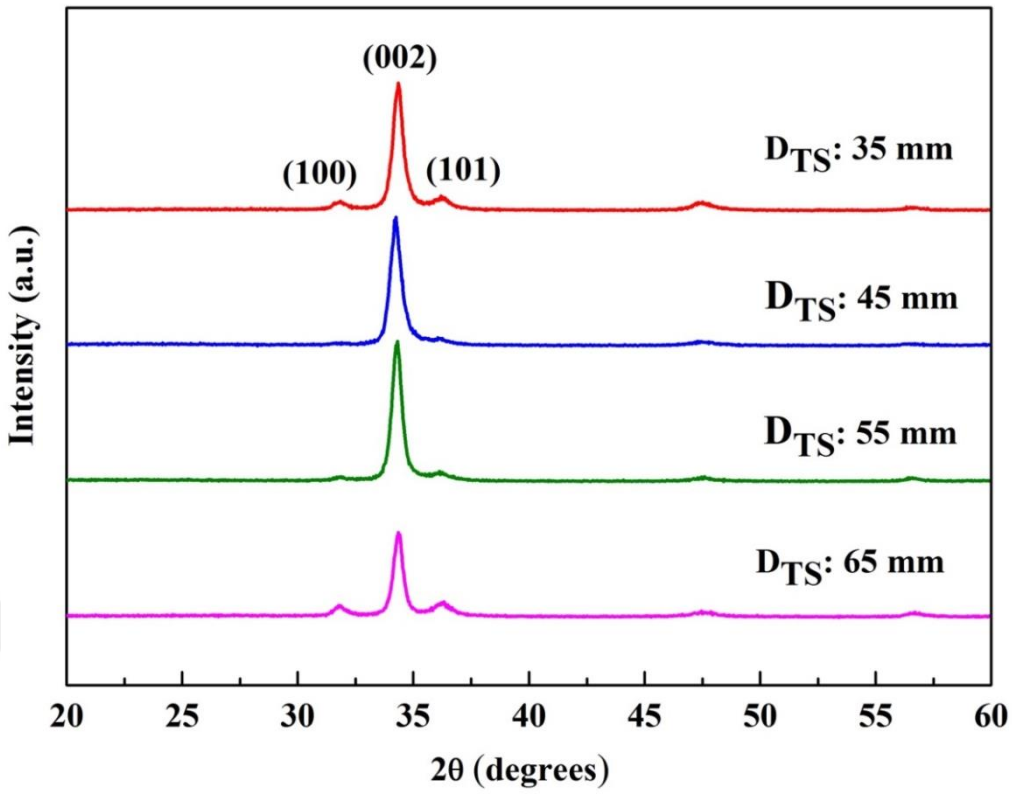

Figure 4.12 X-ray diffraction pattern of ZnO thin films deposited at different D_{TS}

This finding revealed that an oriented film growth was observed with the crystallographic c-(002) axis orientation perpendicular to the substrate surface. Since, the most preferred c-axis orientation was observed for a D_{TS} value of 45 mm; detailed examinations were further continued on that film. In Table 4.9 the position and the intensities of the peaks were given.

Table 4.9 The position and intensity of (002) peak, (002) peak intensity per unit thickness, position and relative intensity of (100) peak, position and relative intensity of (101) peak of ZnO thin films at different D_{TS}

D_{TS} (mm)	**Position of (002) (Degree)**	**Intensity (002) (a.u.)**	**(002) Peak intensity per unit thickness (cps/nm)**	**Position of (100) (Degree)**	**100 Rel. Int. (%)**	**Position of (101) (Degree)**	**101 Rel. Int. (%)**
35	34.38	1877.53	6.26	31.84	5.65	36.26	8.31
45	34.22	1915.63	19.16	31.78	0.69	36.16	4.32
55	34.35	2073.92	5.18	31.78	1.50	36.18	4.86
65	34.32	1244.44	3.00	31.78	11.04	36.23	14.22

According to the table, at low and high D_{TS} values, the appearance of the (101) and (100) peaks demonstrates a degradation of the preferred orientation. However, their intensities were lower.

Moreover, the Sherrer formula [38] was used to determine the variation of crystallite sizes with D_{TS}. The calculations are summarized in Table 4.10. Full-width at half-maximum (FWHM) values ranged from 0.5966° to 0.6967° with a minimum value of 0.5064° when D_{TS} was 45 mm, which correlated with a large crystallite size of 25.1 nm.

Table 4.10 Full width at half maximum and crystallite size variations at different D_{TS} of ZnO thin films

D_{TS} (mm)	**FWHM (degrees)**	**Crystallite Size (nm)**
35	0.5966	21.80
45	0.5064	25.10
55	0.5738	22.10
65	0.6967	18.00

It is worth to mention that the cross-sectional SEM images given in Figure 4.11 show random orientation of crystallites for lower and higher D_{TS} values instead of the columnar structure for a D_{TS} value of 45 mm. When D_{TS} was set at 45 mm, uniform layers with a regular columnar growth normal to the surface occurred.

4.1.2.3 Morphological properties of ZnO thin films sputtered at different D_{TS}

The surface morphology of the ZnO thin films was investigated using HRSEM and AFM, as shown in Figure 4.13 and Figure 4.14. The morphology and the roughness of the ZnO thin films changed with D_{TS}. The plan view SEM images in Figure 4.13 revealed that, for D_{TS} values of 35 mm and 55 mm, the morphology was more porous compared to films sputtered at other D_{TS} values. Films sputtered at 45 mm and 50 mm showed denser and more uniform structures. In addition, triangular grain structures appeared for films sputtered at D_{TS} values of 40 mm and 60 mm.

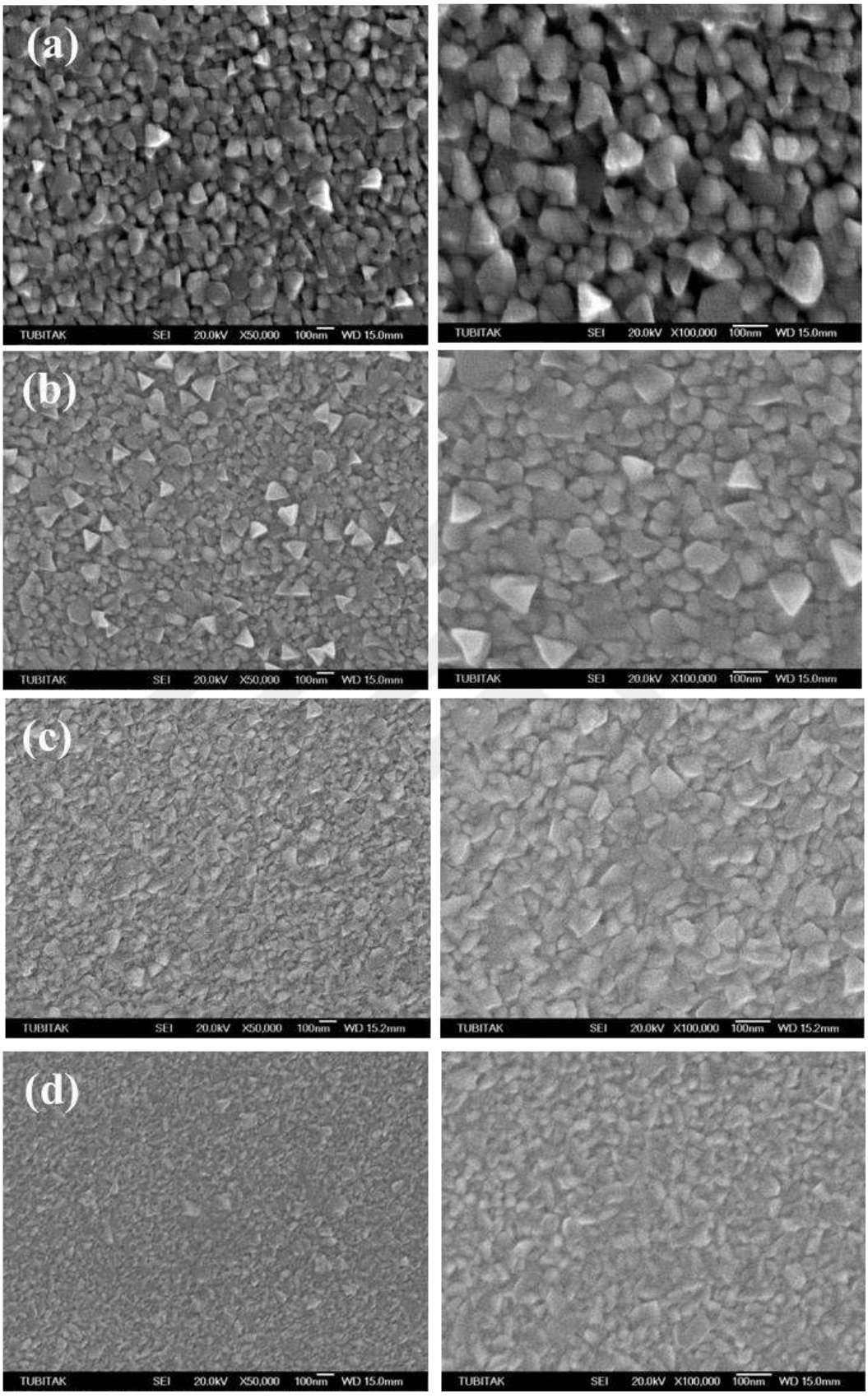

Figure 4.13 HRSEM surface morphology images of the ZnO thin films deposited at different DTS: (a) 35 mm, (b) 40 mm, (c) 45 mm and (d) 50 mm

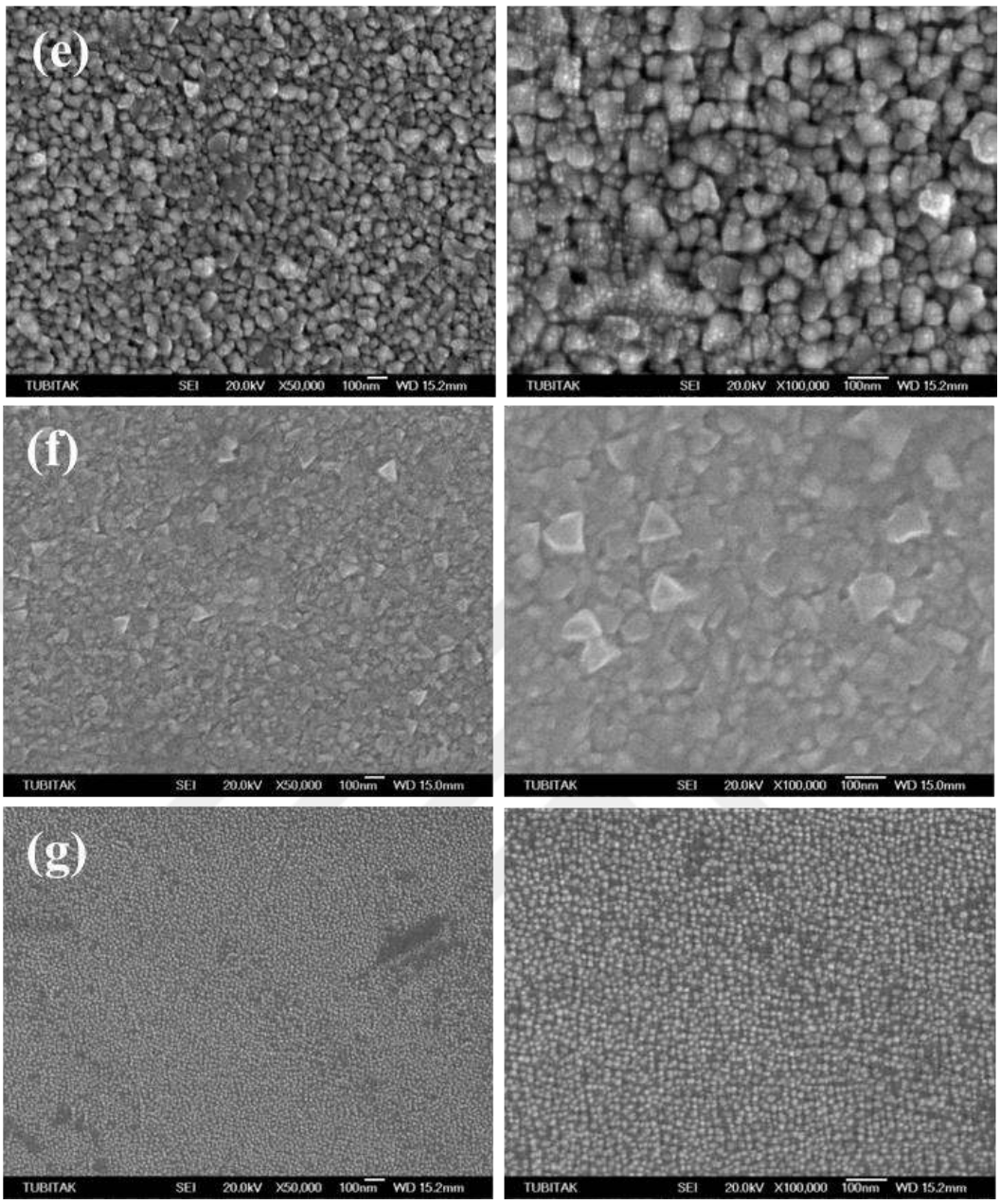

Figure 4.13 HRSEM surface morphology images of the ZnO thin films deposited at different D_{TS}: (e) 55 mm, (f) 60 mm, and (g) 65 mm

The AFM images shown in Figure 4.14 and the RMS values presented in Table 4.11 can be used to further understand the surface morphology of the films. The parameters obtained from the 5×5 μm^2 surface area showed that the root mean square (RMS) values vary in the range of 23 nm to 4.6 nm.

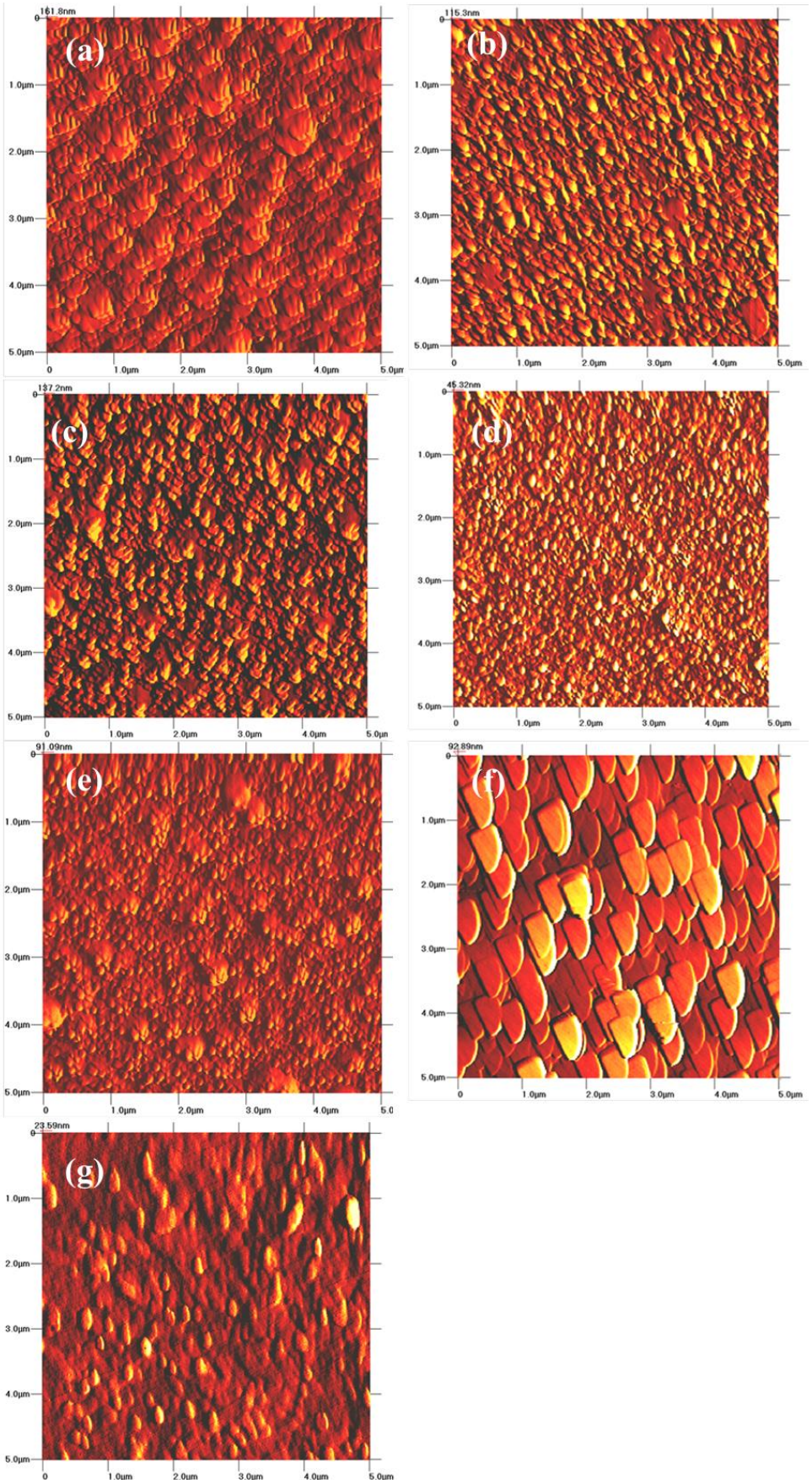

Figure 4.14 AFM images of ZnO thin films deposited at a D_{TS} of: (a) 35 mm, (b) 40 mm, (c) 45 mm, (d) 50 mm, (e) 55 mm, (f) 60 mm, and (g) 65 mm

The RMS and arithmetic mean roughness (Ra) of the films sputtered at D_{TS} of 45 mm and 50 mm were the lowest among all samples. Because the morphology of the film sputtered at D_{TS} of 45 mm exhibited a dense and compact film structure, it will be effective in light-trapping in thin film silicon solar cells [126].

Table 4.11 RMS, Ra, Rq and average height values of ZnO thin films at different D_{TS} values

D_{TS} (mm)	**RMS (nm)**	**Ra (nm)**	**Rq (nm)**	**Average Height (nm)**
35	22.77	18.40	22.80	64.81
40	13.08	10.1	12.60	37.40
45	5.91	4.29	5.44	15.89
50	4.56	3.18	4.16	11.57
55	10.83	7.89	10.50	29.44
60	15.19	12.20	14.90	36.30
65	2.02	1.59	2.05	4.93

Low deposition rates generally cause adatoms to transfer to grid sites and reduce the grain size. In the other case, adatoms accumulate without chemical bonding [6, 35, and 39].Because the deposition rate of the film sputtered at a D_{TS} of 45 mm was low, the size of the islands became smaller, resulting in smaller RMS and Ra values with a denser and flatter morphology.

4.1.2.4 Optical investigation of ZnO thin films sputtered at different D_{TS}

Figure 4.15 shows the total transmission properties of the ZnO thin films deposited at different D_{TS} values. The average transmittance of all samples varied from 68% to 89% in the wavelength region of 300 nm–800 nm. These values are similar to those of ZnO thin films deposited using other parameters [9].

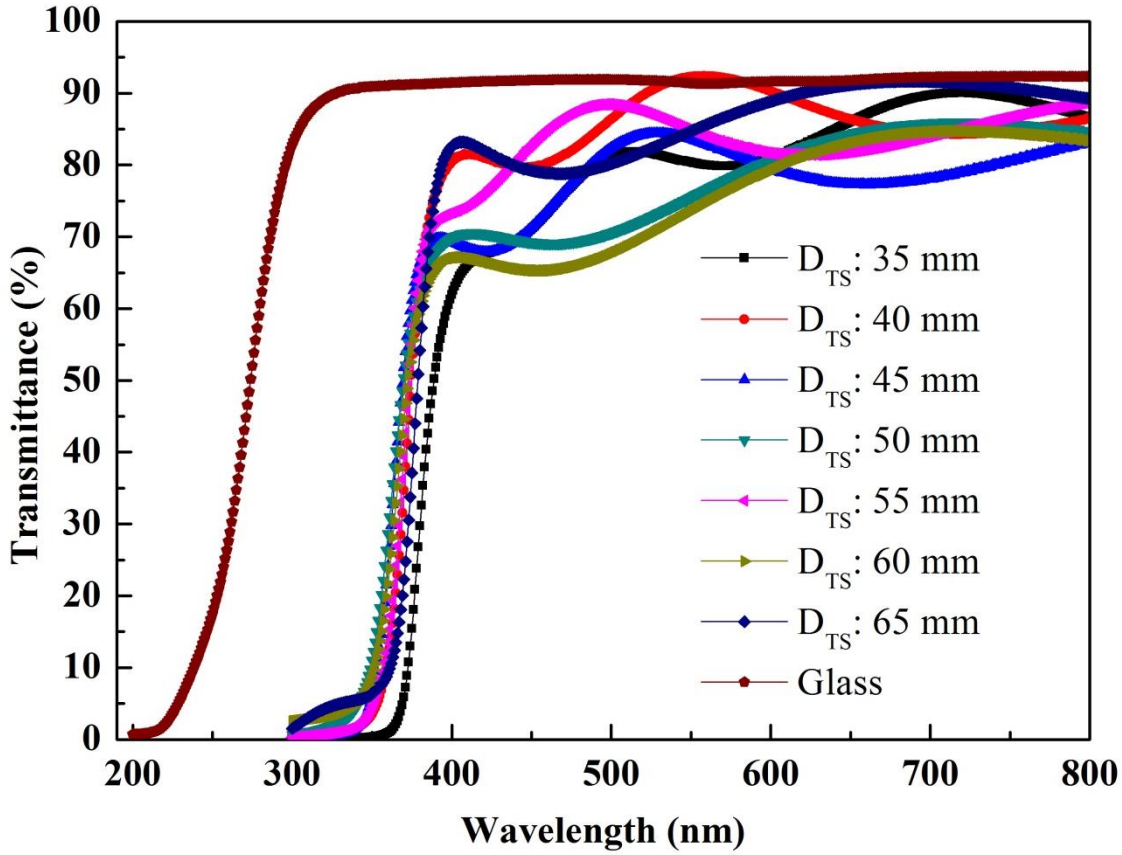

Figure 4.15 Total transmittance spectra of ZnO thin films prepared at different D_{TS} values

In addition, the band gap of the films was determined using the relation $\alpha h\nu = A (h\nu - E_g)^{1/2}$, where α is the optical absorption coefficient, hν is the photon energy, A is the edge width parameter and E_g is the optical band gap. E_g values were obtained by extrapolating the linear portion of the plots of $(\alpha h\nu)^2$ versus hν to α = 0 (Figure4.16 and Figure 4. 17).

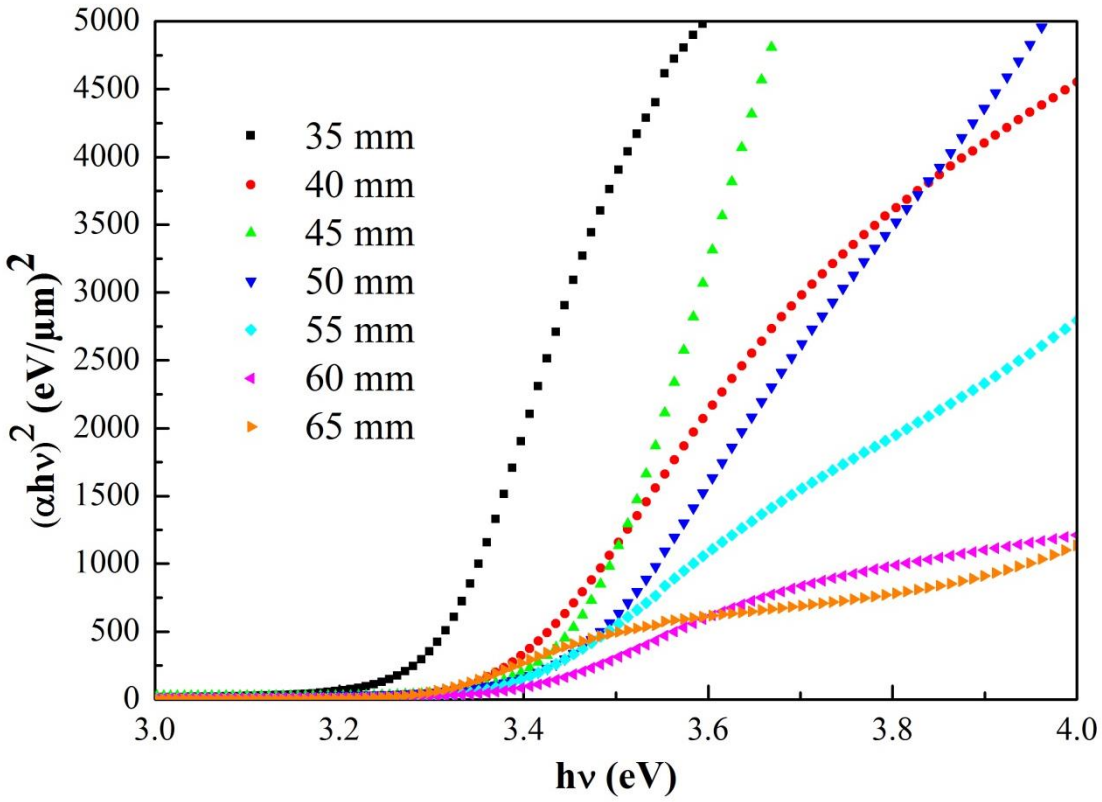

Figure 4.16 $(\alpha h\nu)^2$ versus $h\nu$ graph of ZnO thin films deposited at different D_{TS} values

According to the data, the band gap of the ZnO thin films was around 3.3 eV – 3.45 eV. Also, in Table 4.12 the average transmittance and energy band gap variations with D_{TS} is given in detail. The lowest value of 3.3 eV was observed from samples with low and high D_{TS} values. On the other hand, the highest band gap value was measured as 3.45 eV for the film sputtered at a D_{TS} of 45 mm [9].

Table 4.12 D_{TS}, average transmittance and energy band gap variations of ZnO thin films

D_{TS} (mm)	**Average Transmittance (%)**	**Egap (eυ)**
35	81.86	3.30
40	85.99	3.35
45	85.30	3.45
50	78.70	3.45
55	83.92	3.40
60	76.64	3.35
65	86.59	3.30

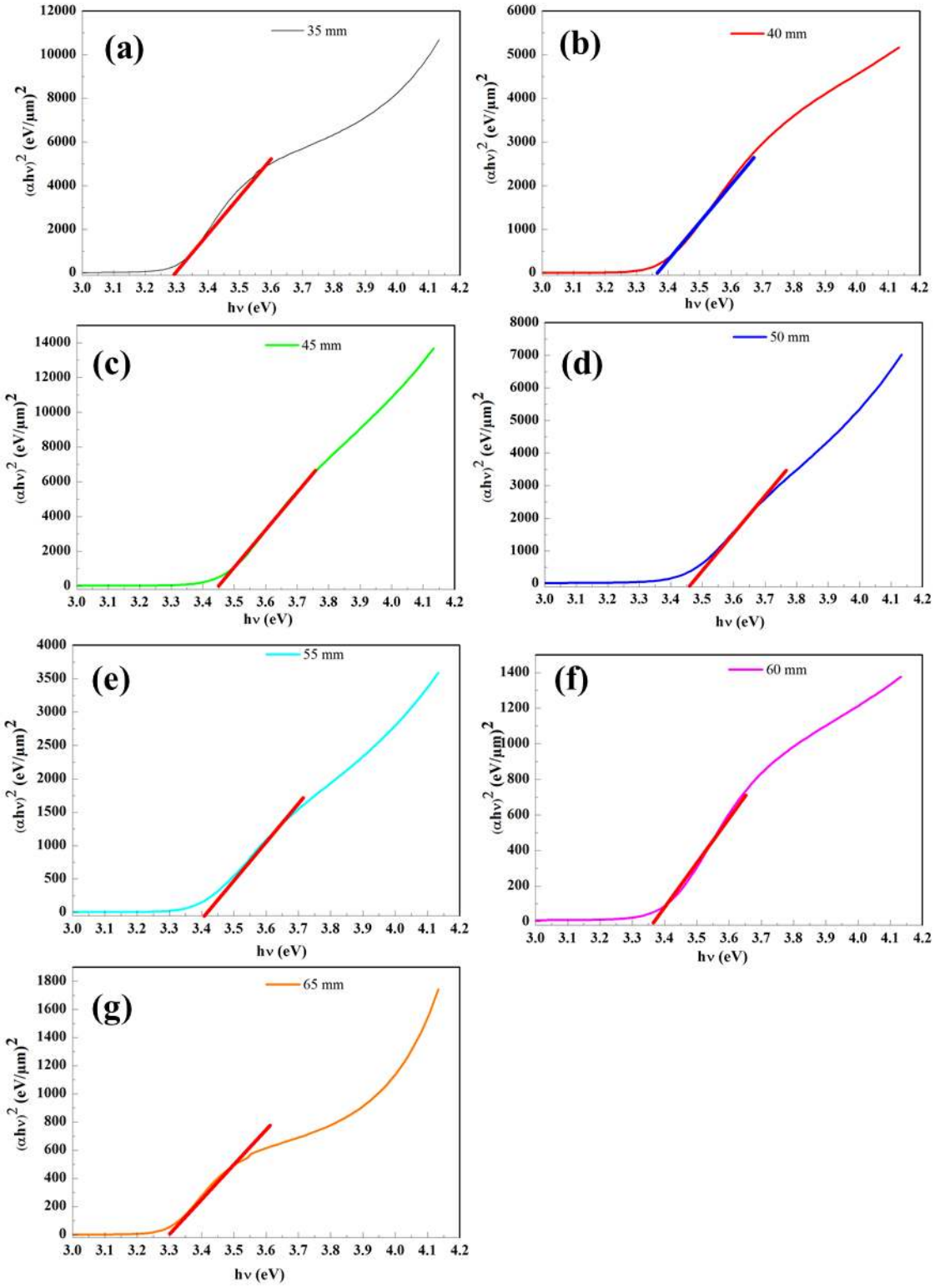

Figure 4.17 $(\alpha h\nu)^2$ versus hν of ZnO graphs thin films deposited at different D_{TS}: (a) 35 mm, (b) 40 mm, (c) 45 mm, (d) 50 mm, (d) 55 mm, (f) 60 mm, and (g) 65 mm

4.1.2.5 Summary of the D_{TS} variation influence on ZnO thin film properties

The present results indicate the important influence of D_{TS} on ZnO thin film deposition at a given sputtering pressure. In the deposition system, zinc oxide films with a resistivity as low as 9×10^{-4} Ω.cm, an optical transmission of 80 %, an RMS surface roughness of 4.9 nm and an optical band gap value of 3.45 eV were deposited with a growth rate of 7.7 nm/min at 165 W r.f. power and 45 mm D_{TS} sputter pressure. Under these deposition conditions, the deposition rate, film thickness, resistivity, crystallinity, roughness and optical parameters showed optimal values. The formation and growth of the ZnO films on glass surfaces depend on the surface mobility and diffusion of adatoms on the growing film surface, which is clearly at an optimum at 165 W and a D_{TS} of 45 mm. For lower and higher D_{TS} values, the variation of surface mobility and diffusion causes smaller crystallite sizes with random crystal growth and broken columns. HRTEM images of the film deposited at 165 W r.f. power and a D_{TS} of 45 mm clearly show a so-called transition zone of tightly packed local epitaxial growth on individual grains, and the film exhibits a relatively smooth surface [38, 39].

Moreover, FOM characteristics with D_{TS} variations were investigated. The Figure 4.18 was formed with the help of data present in Table 4.13. According to the results, both the average transmittance and the resistivity values were influenced from the D_{TS} variations. Therefore FOM values showed a decrees-increase-decrease trend. At 65 mm D_{TS} value, the FOM was measured as 103×10^4 $(\Omega.cm)^{-1}$, due to higher resistivity.

Table 4.13 D_{TS}, average transmittance and energy band gap variations of ZnO thin films

D_{TS} (mm)	**Average Transmittance (%)**	**Resistivity $\times10^{-3}$ (Ω.cm)**	**FOM $\times10^{4}$(Ω.cm)$^{-1}$**
35	90.95	3.67	24.7835
40	95.54	2.72	35.1266
45	94.77	0.91	103.923
50	87.44	1.81	48.3118
55	93.24	3.99	23.3695
60	85.15	4.46	19.0931
65	96.21	5.27	18.2563

The maximum FOM value was obtained at 45 mm D_{TS} value, with high transmitance and low resistivity values. Also both the structural and morphological properites achived at 45 showed better characteristics. consequently, 45 mm was selected as D_{TS} value for ZnO thin films.

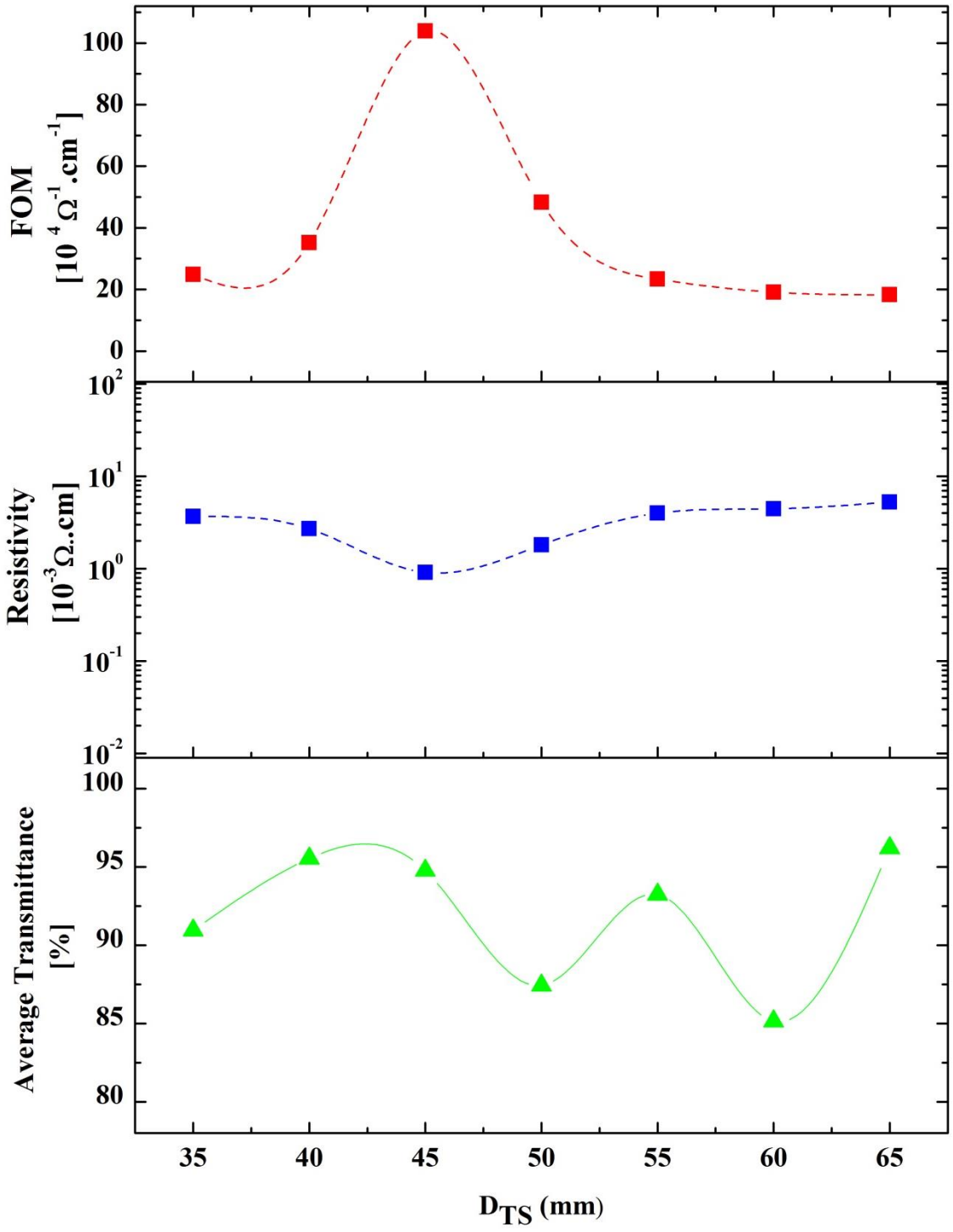

Figure 4.18 Effect of D_{TS} on average transmittance, resistivity and the figure of merit of ZnO thin films

4.1.3 Effect of argon gas pressure on ZnO thin films

In r.f. sputtering deposition technique, process gas pressure plays a very critical role to achieve a high quality thin film. In order to understand the influence in detail, the argon gas pressure was changed in small ranges. The variation was maintained from 0.15 Pa

to 0.60 Pa, in 0.05 - 0.1 Pa steps, while the r.f. power was 165 W and D_{TS} was 45 mm. The base pressure was around 10^{-5} Pa. The deposition was done for 30 minutes and before the deposition pre-sputtering was applied for 5 minutes. The working pressures obtained from gauge; variations with argon pressure and amount in sccm are present in Table 4.14.

Table 4.14 The working pressure variations with argon pressure and amount of ZnO thin films

Argon Pressure (Pa)	**Argon Amount (sccm)**	**Working Pressure (Pa)**
0.15	5	0.153
0.20	10	0.211
0.30	20	0.318
0.40	30	0.417
0.50	40	0.424
0.60	50	0.586

Electrical, structural, morphological and optical investigations were done to analyze the influence of Ar pressure on ZnO thin films. In the following sections these will be explained in detail.

4.1.3.1 Electrical properties of ZnO thin films sputtered at different Ar pressures

For the transparent conductive oxide thin films, the electrical value obtained by using any kind of measurement technique has great importance. Because it includes various information such as: structural formation and morphological properties of the films.

In this thesis, the electrical properties were determined by using thickness values of the ZnO thin films. The thickness values were obtained from the cross sectional view SEM images as present in Figure 4.19.

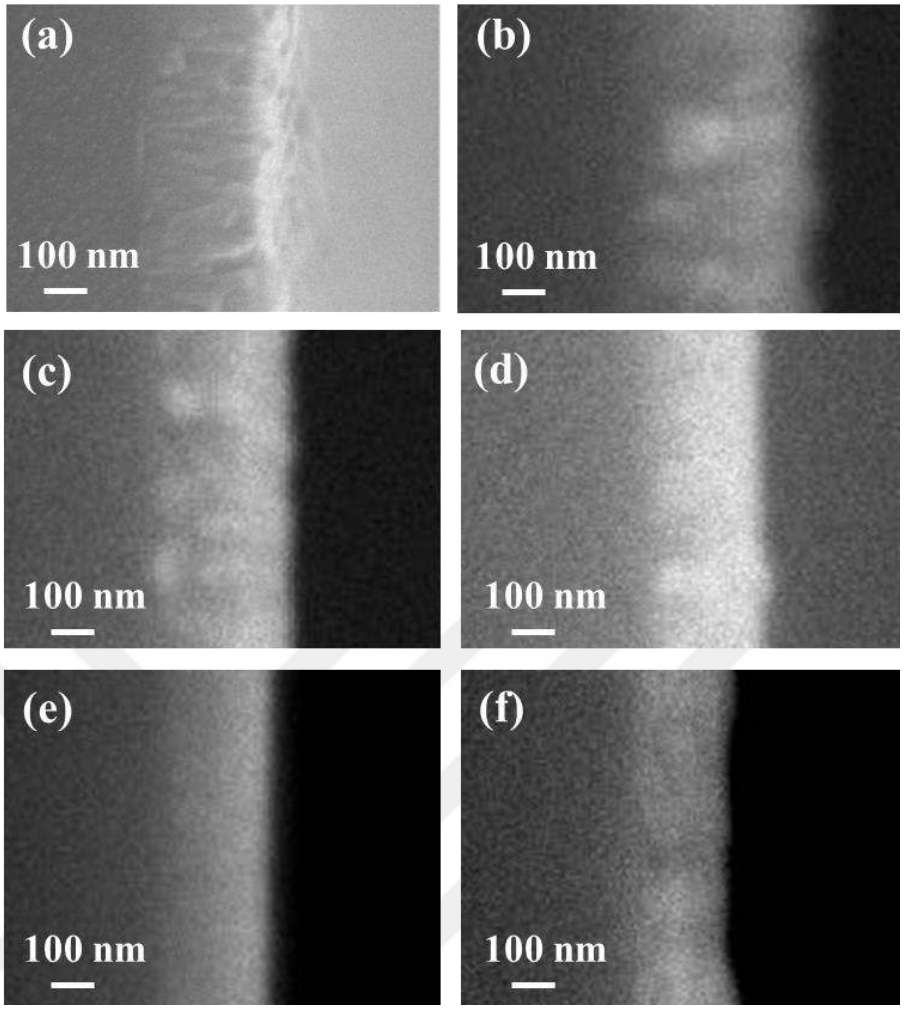

Figure 4.19 Cross sectional view SEM images of ZnO thin films deposited at various argon gas pressures: (a) 0.15 Pa, (b) 0.20 Pa, (c) 0.30 Pa, (d) 0.40 Pa, (e) 0.50 Pa and (f) 0.60 Pa

As a consequence of the thickness values, both the resistivity and the deposition rates of the ZnO thin films were determined. The results were shown in Table 4.15.

Table 4.15 Thickness, resistivity and deposition rate variations of ZnO thin films at different argon gas pressures

Argon Pressure (Pa)	**Thickness (nm)**	**Resistivity $\times 10^{-3}$ (Ω.cm)**	**Deposition rate (Å/min)**
0.15	400	3.08	133
0.20	350	3.01	116
0.30	300	1.16	100
0.40	230	2.15	76
0.50	220	2.89	73
0.60	210	4.04	70

According to Table 4.18, thickness values reduced with the increase of Ar pressure. However, the electrical resistivity values showed variations with gas pressure. They were obtained around 10^{-3} Ω.cm. In order to widen the influence of argon pressure on both resistivity and deposition rate, Figure 4.20 was formed.

In Figure 4.20 it is obvious that, although small argon gas pressure variations, the influence on both the resistivity and the deposition rate was high. The deposition rate decreased with the increase of argon pressure, while the resistivity values showed variations. Resistivity reduced until 0.3 Pa, than it increased with the increase of argon pressure.

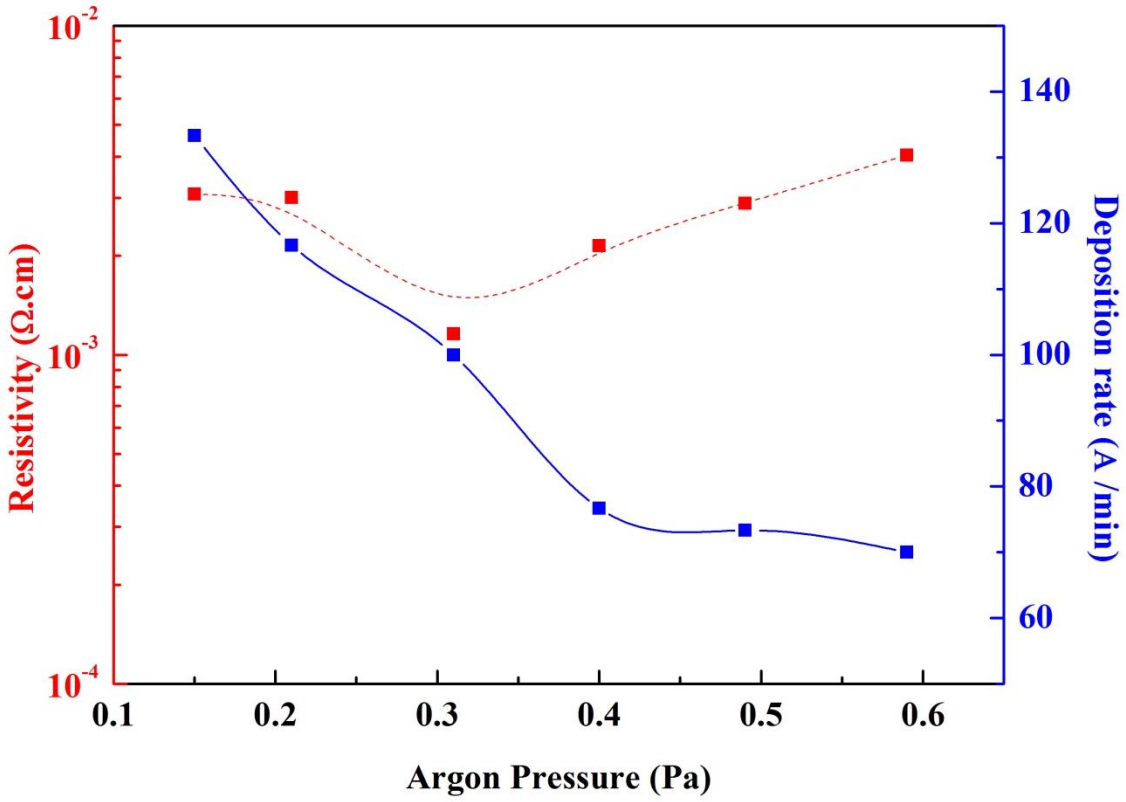

Figure 4.20 Resistivity and deposition rate variations at different argon gas pressures of ZnO thin films

4.1.3.2 Structural properties of ZnO thin films sputtered at different Ar pressures

In order to understand the structural formation differences of ZnO thin films at process gas pressure variations, structural investigations were done. In Figure 4.21 X-ray diffraction pattern of ZnO thin films deposited at different argon pressures is present. All the peak positions and intensities in this study were measured according to the ZnO x-ray card: Hexagonal system, P63mc (186) space group with JCPDS-International

Center for Diffraction Data 89-0510 pdf number. According to the card, 2 theta values of the (100), (002) and (101) peaks are obtained around 31.86°, 34.45° and 36.29° respectively.

According to Figure 4.3, (002) peak occurrence is dominant for all ZnO thin films. However, (100) and (101) peak occurrence was observed at various process gas pressures.

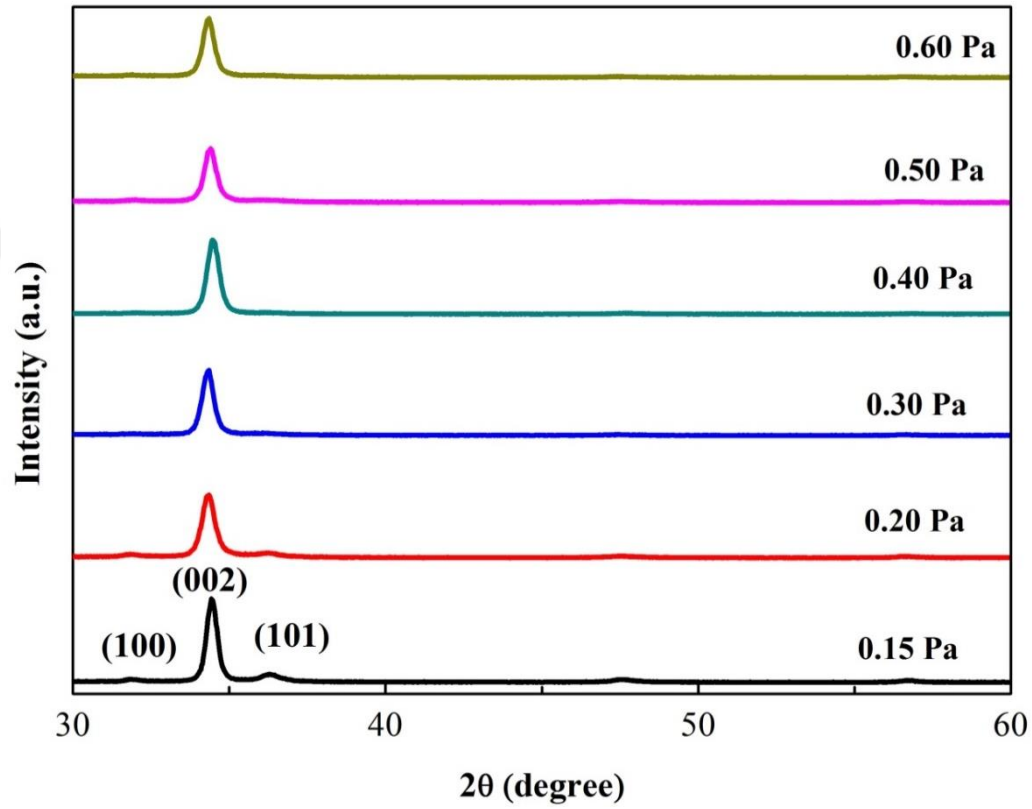

Figure 4.21 X-ray diffraction pattern of ZnO thin films deposited at different argon pressures

In Table 4.16, the values obtained from XRD measurements were given in detail. The (002) peak position was around 34.30°, while the intensities were on average around 5700 a.u. The lowest (002) intensity was obtained as 4557 a.u. at 0.5 Pa value. However, at 0.15 Pa the intensity of (002) peak was achieved as 7393 a.u. and the position was 34.42°. The position of (100) and (101) peaks were around 31.80° and 36.15°, respectively. The relative intensity values of these peaks were present in Table 6.3. Moreover, to clarify the relation between (002) peak and thickness of the film, (002) peak intensity values were divided to the thickness values. In Table 4.16, (002) peak intensity per unit thickness (cps/nm) variations for various gas pressures were also shown.

Table 4.16 The position and intensity of (002) peak, (002) peak intensity per unit thickness, position and relative intensity of (100) peak, position and relative intensity of (101) peak of ZnO thin films at different argon gas pressures

Ar pressure (Pa)	Position of (200) (Degree)	Intensity 002 (a.u.)	(002) Peak intensity per unit thickness (cps/nm)	Position of (100) (Degree)	100 Rel. Int. (%)	Position of (101) (Degree)	101 Rel. Int. (%)
0.15	34.42	7393.57	18.48	31.86	2.38	36.29	8.79
0.20	34.31	5543.91	15.84	31.82	3.31	36.15	4.94
0.30	34.29	5764.83	19.22	31.82	0.72	36.16	1.8
0.40	34.46	6564.02	28.54	31.96	0.51	36.19	1
0.50	34.31	4557.18	20.71	31.83	1.59	36.10	1.34
0.60	34.37	5296.26	25.22	31.94	1.84	36.17	2.2

The crystallite sizes of the ZnO thin films were determined by using Sherrer Formula (explained in Experimental Studies section) and the obtained results were present in Table 4.17. According to Table 4.17, the FWHM (full width at half maximum values) values showed similarities around 0.41°. The lowest FWHM value was obtained at 0.15 Pa as 0.36°, while at 0.20 Pa the highest value was measured as 0.45°. When the crystallite size variations were investigated, 23 nm at 0.15 Pa was achieved as the biggest size, when compared to the others [141,142].

Table 4.17 Full width at half maximum and crystallite size variations at different argon pressures of ZnO thin films

Ar pressure (Pa)	FWHM (Degree)	Crystallite Size (nm)
0.15	0.36	23.00
0.20	0.45	18.13
0.30	0.40	20.50
0.40	0.41	19.93
0.50	0.41	20.29
0.60	0.41	19.09

4.1.3.3 Morphological properties of ZnO thin films sputtered at different Ar pressures

The surface morphology with different argon gas pressures were investigated with the help of HRSEM and AFM. Plan view images of the ZnO thin films were present in Figure 4.22. According to Figure 4.22, the compactness of the films improved with the increase of argon pressure.

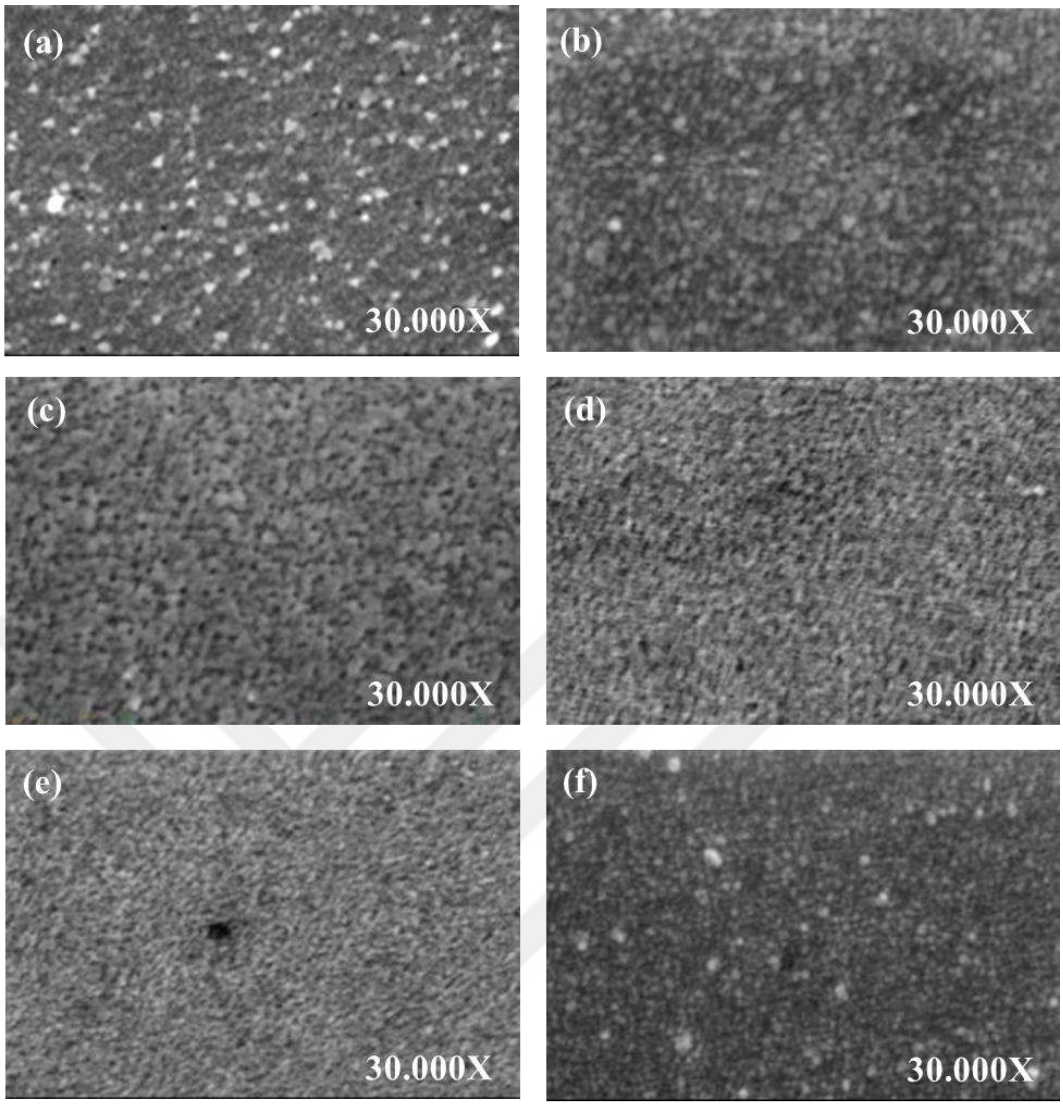

Figure 4.22 FESEM surface morphology images of the ZnO thin films deposited at different gas pressures (a) 0.15 Pa, (b) 0.20 Pa, (c) 0.30 Pa, (d) 0.40 Pa, (e) 0.50 Pa and (f) 0.60 Pa

Furthermore, AFM investigations from as small as 5 $\times$5 μm^2 regions were done to understand the gas pressure influence deeply. In Figure 4.23, AFM images and RMS values of ZnO thin films deposited at different argon gas pressures were shown.

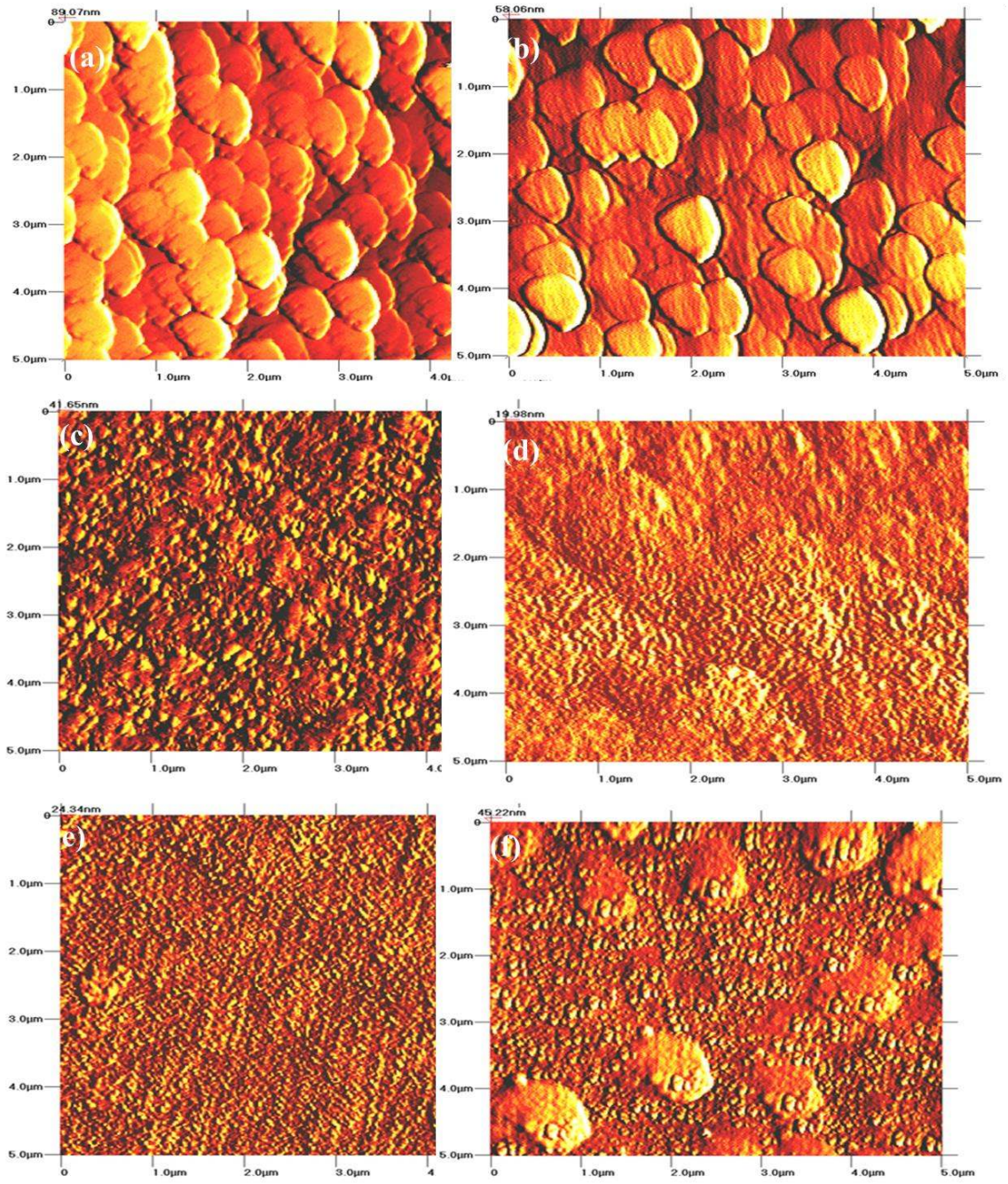

Figure 4.23 AFM images and RMS of ZnO thin films deposited at different gas pressures: (a) 0.15 Pa, (b) 0.20 Pa, (c) 0.30 Pa, (d) 0.40 Pa, (e) 0.50 Pa and (f) 0.60 Pa

As stated in Figure 4.5, the surface roughness values were high for small argon pressures as 11.22 nm and 9.55 nm at 0.15 Pa and 0.20 Pa, respectively. For the other gas pressures, the RMS variation showed increase-decrease-increase trend. At 0.40 Pa the RMS value reached the minimum as 2.12 nm (Table 4.18).

Table 4.18 Argon gas pressure and corresponding RMS, Ra, Rq and average height variations of ZnO thin films

Ar Pressure (Pa)	RMS (Sq) (nm)	Ra (nm)	Rq (nm)	Average Height (nm)
0.15	11.22	8.33	10.60	33.82
0.20	9.55	6.84	8.33	25.68
0.30	5.41	4.08	5.12	18.77
0.40	2.12	1.65	2.07	7.61
0.50	5.61	4.40	5.61	16.85
0.60	2.48	1.81	2.25	8.57

4.1.3.4 Optical investigation of ZnO thin films sputtered at different Ar pressures

The optical behavior of the ZnO thin films showed variations at different process gas pressure values. In Figure 4.24, total transmittance spectra of ZnO thin films were present. The average transmittance values were obtained above 80%. According to Table 4.19, the average transmittance was decreased with the increase of argon pressure. For 0.15 Pa, the transmittance value reached the maximum as 88.50%.

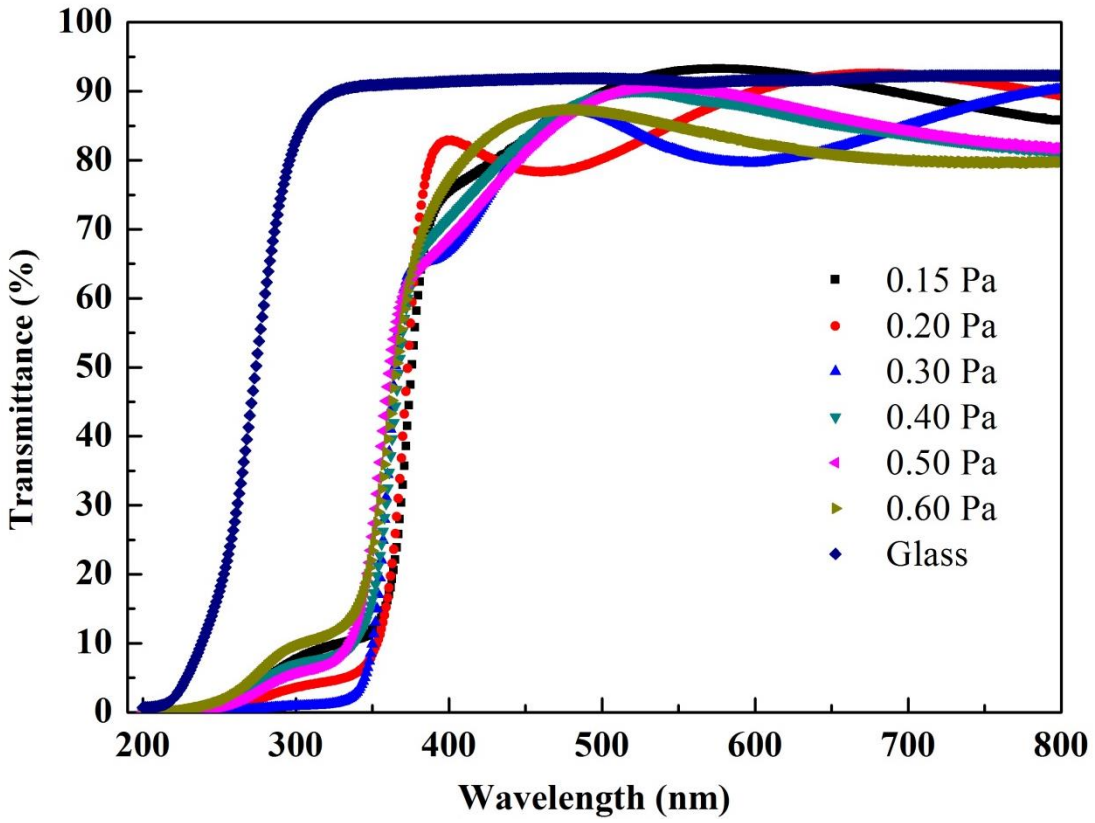

Figure 4.24 Total transmittance spectra of ZnO thin films prepared at different gas pressures

$(\alpha h\nu)^2$ versus $h\nu$ graphs of ZnO thin films deposited at different gas pressures were formed (Figure 4.25). When the electrical band gap of the ZnO thin films were

considered the effect of argon gas pressure is clearly seen in Figure 4.25. Moreover, $(\alpha h\nu)^2$ versus hν graphs of ZnO thin films were shown in Figure 4.26.

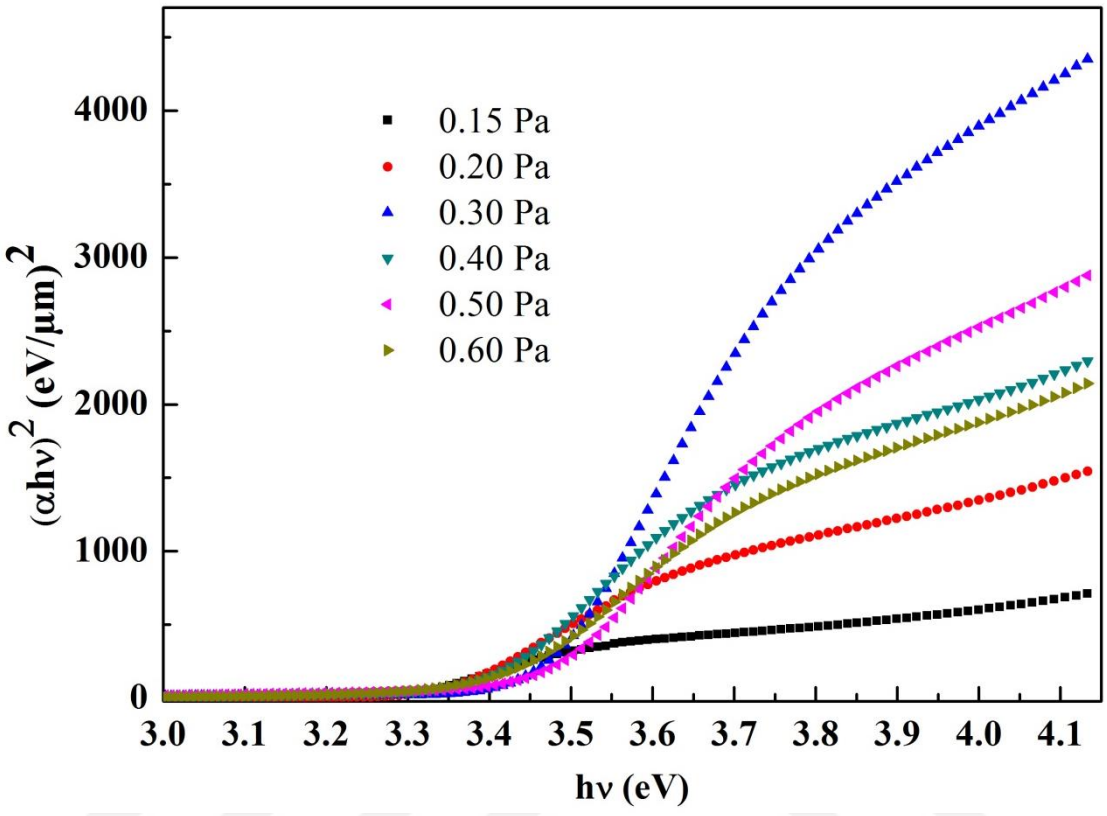

Figure 4.25 $(\alpha h\nu)^2$ versus hν of ZnO thin films deposited at different gas pressure

The energy band gap values measured from Figure 4.26 were also presented in Table 4.22. The obtained results revealed that, the energy band gap values influenced with argon gas pressure variations.

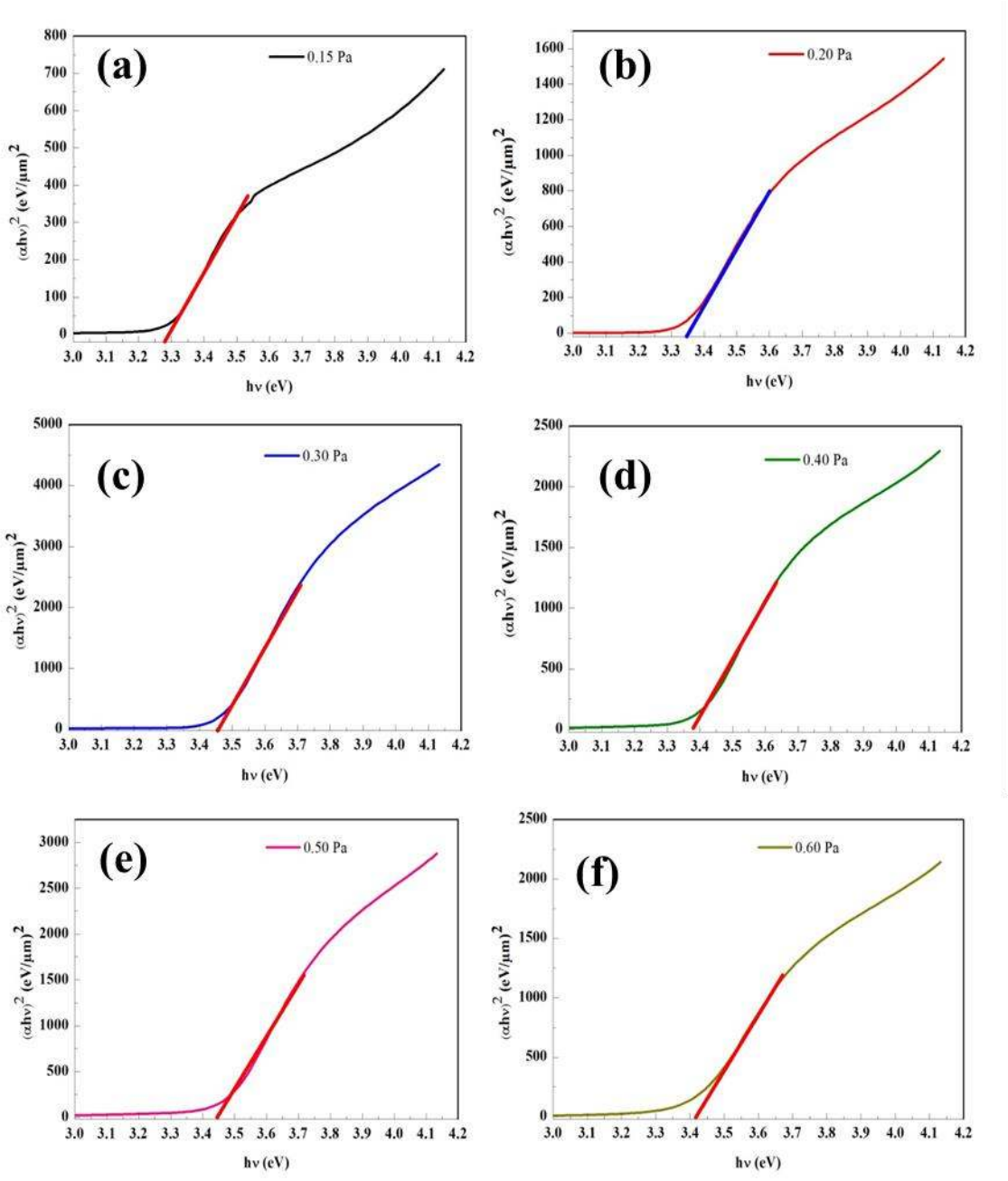

Figure 4.26 $(\alpha h\nu)^2$ versus hν graphs of ZnO thin films deposited at different gas pressures; (a) 0.15 Pa, (b) 0.20 Pa, (c) 0.30 Pa, (d) 0.40 Pa, (d) 0.50 Pa and (f) 0.60 Pa

The higher transmittance values were obtained at lower argon pressures. The band gap values were low as around 3.30 eV. This low Egap values might be achieved due to the higher surface roughness and thickness. The highest electrical band gap value was measured as 3.45 eV for 0.30 Pa.

Table 4.19 Argon gas pressure, average transmittance and energy band gap variations of ZnO thin films

Ar Pressure (Pa)	Average Transmittance (%)	Egap (eυ)
0.15	88.50	3.27
0.20	87.01	3.35
0.30	83.00	3.45
0.40	84.77	3.37
0.50	84.86	3.45
0.60	82.60	3.40

4.1.3.5 Summary of the Ar pressure variation influence on ZnO thin film properties

The effects of argon gas pressure variations on the properties ZnO thin films were examined. According to the achieved results, although the variations were small, the influence on the characteristics of the film was high. In order to make correlation between the properties, figure of merit (FOM) measurements (explained in Experimental Studies section) were done and the achieved results were shown in Figure 4.27.

Table 4.20 Resistivity, deposition rate, average transmittance and figure of merit values at argon pressure of ZnO thin films

Argon Pressure (Pa)	Average Transmittance (%)	Resistivity $\times 10^{-3}$ (Ω.cm)	FOM $\times 10^{4}(\Omega.cm)^{-1}$
0.15	98.33	3.08	31.9264
0.20	96.67	3.01	32.1188
0.30	92.22	1.16	79.5019
0.40	94.18	2.15	43.8087
0.50	94.28	2.89	32.6259
0.60	91.77	4.04	22.7172

The maximum FOM value was obtained as 795019 $(\Omega.cm)^{-1}$ for 0.30 Pa, while the others were measured around 204470 $(\Omega.cm^{)-1}$. Moreover, the obtained results were shown in Table 4.20.

These obtained results showed that; at 0.30 Pa can be selected as argon gas pressure value due to its higher FOM value with lower resistivity.

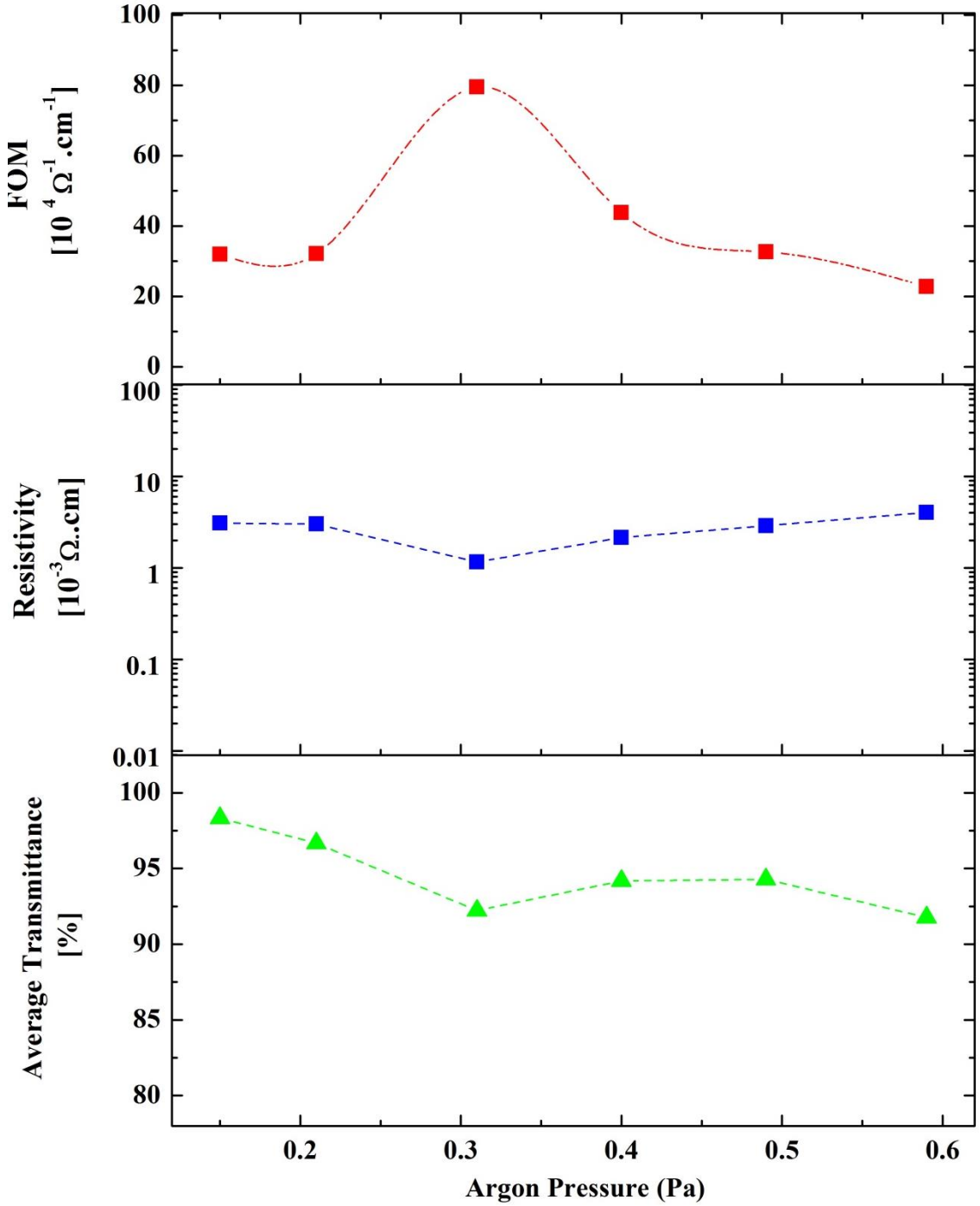

Figure 4.27 Effect of argon pressure on average transmittance, resistivity and the figure of merit of ZnO thin films

4.1.4 Effect of deposition time on ZnO thin films

After determination of the optimum deposition parameters, the influence of deposition time was investigated. The depositions were carried out at 0.30 Pa (20 sccm) argon gas pressure, 165 W r.f. power and 45 mm target-to-substrate distance. The deposition time was varied from 10 minutes to 30 minutes.

4.1.4.1 Electrical properties of ZnO thin films sputtered at different deposition times

Electrical behavior of ZnO thin films deposited at various deposition times were determined by using four point probe technique. The achieved results are present in Table 4.21.

Table 4.21 Resistivity, thickness and deposition rate variations at different deposition times of ZnO thin films

Deposition Time (min)	Thickness (nm)	Resistivity $\times 10^{-3}$ (Ω.cm)	Deposition Rate (Å/min)
30	300	1.16	100
20	160	2.99	80
15	70	1.34	46
10	100	3.3	10

Deposition rate of the ZnO thin films were measured by dividing the thickness values obtained from SEM (Figure 4.28). The thickness of the films decreased with the decrease of deposition time, as expected, while the resistivity values were obtained around 1×10^{-3} (Ω.cm).

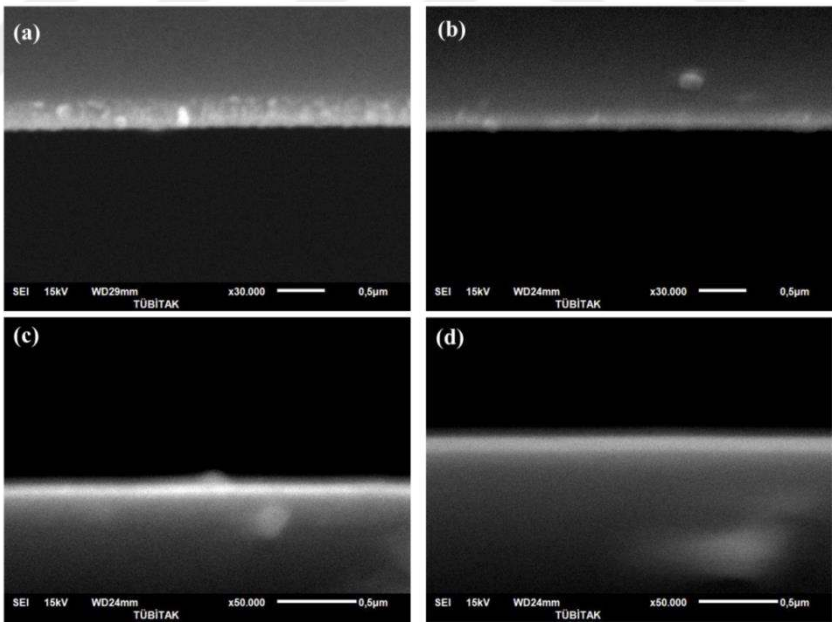

Figure 4.28 Cross sectional SEM image of the ZnO thin films deposited at different deposition time values: (a) 30 min, (b) 20 min, (c) 15 min and (d) 10 min

Also, the schematic view of resistivity and deposition rate with the variation of deposition time was shown in Figure 4.29. According to the achieved results, both the deposition rate and the time variations were linear. However, the resistivity values

showed increase-decrease-increase behavior. The smallest resistivity value was obtained for the ZnO thin film deposited for 30 minutes as 0.0016 Ω.cm

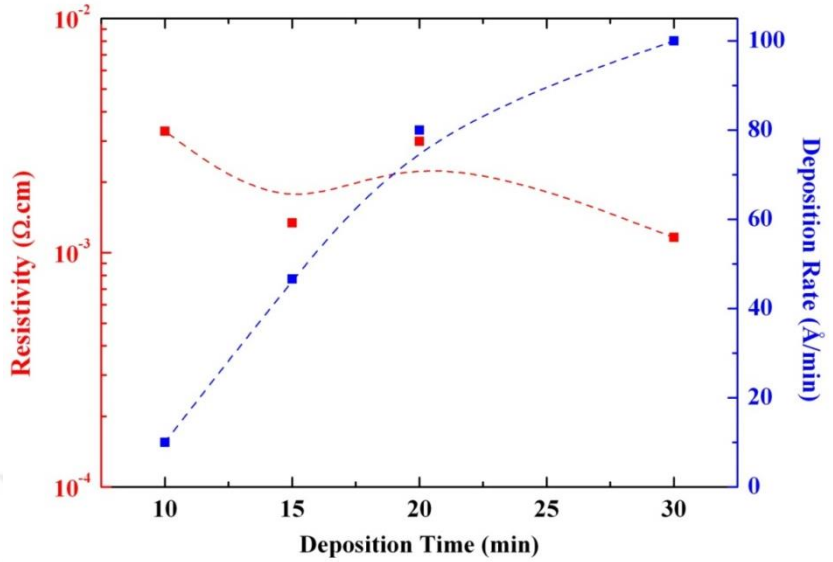

Figure 4.29 Resistivity and deposition rate variations at different deposition times of ZnO thin films

4.1.4.2 Morphological properties of ZnO thin films sputtered at different deposition times

The influence of deposition time on surface roughness variations were shown in Figure 4.30 and 4.31. According to Figure 4.30, morphology becomes smoother.

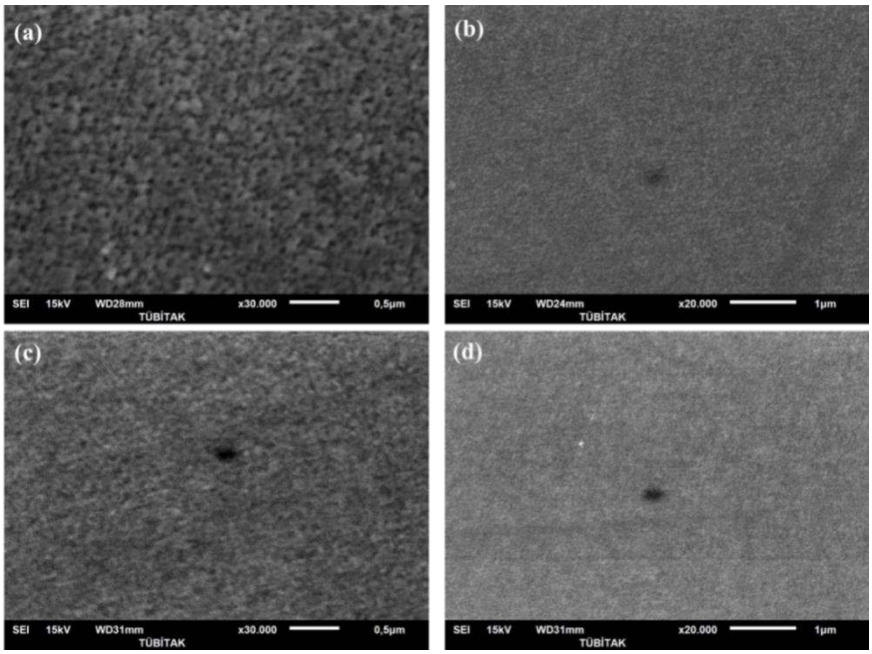

Figure 4.30 SEM surface morphology images of the ZnO thin films deposited at different deposition time values: (a) 30 min, (b) 20 min, (c) 15 min and (d) 10 min

The influence of deposition time variation plays a crucial role on ZnO thin films' surface characteristics. According to the achieved results, the highest RMS value was obtained as 8.09 nm for 10 min. deposited film. The ZnO crystallite may not find enough time to develop a smoother surface [140].

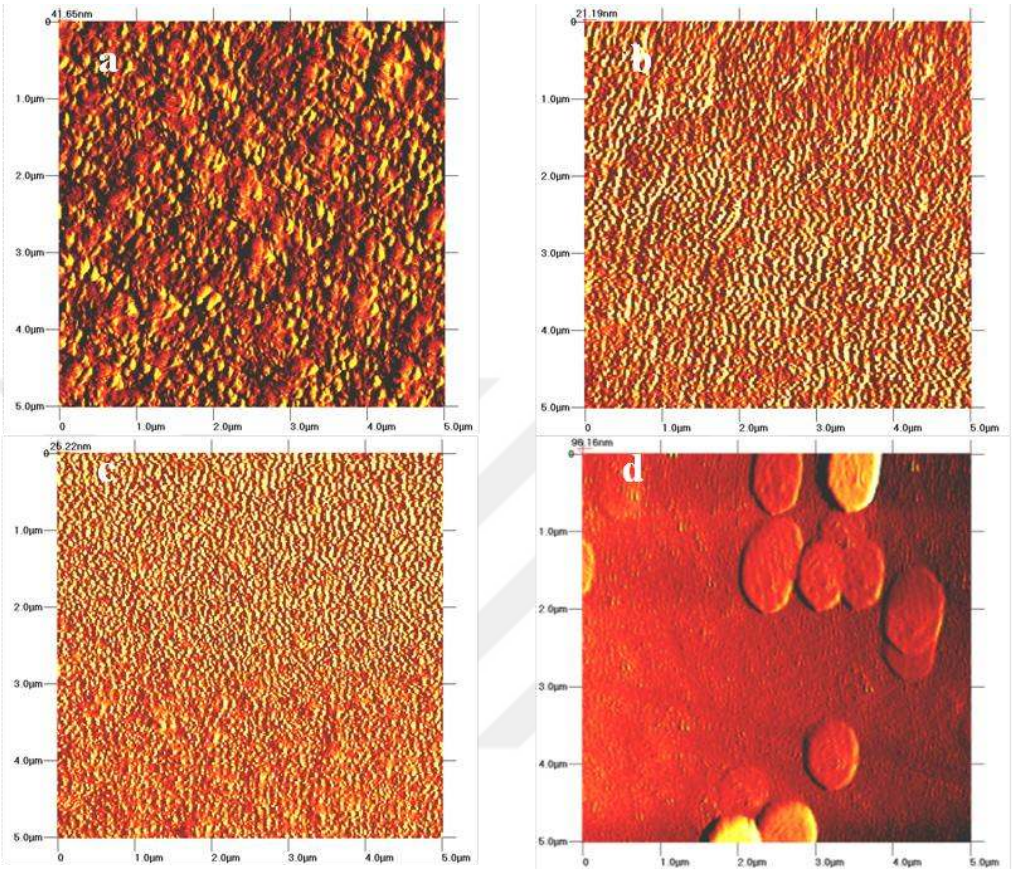

Figure 4.31 AFM analyses for deposition time variations for ZnO thin films: (a) 30 min, (b) 20 min (c) 15 min and (d) 10 min

The obtained RMS values were shown in Table 4.22. When the deposition time was small as 10 min, the RMS value increased. The reason of this could be explained as to achieve a smooth surface deposition time is not sufficient. At 20 min and 15 min values, more smooth surfaces were obtained compared to 30 min.

Table 4.22 Roughness variations for ZnO thin films at different deposition times

Deposition Time (min)	**RMS (Sq) (nm)**	**Ra (nm)**	**Rq (nm)**	**Average Height (nm)**
30	5.41	4.08	5.12	18.77
20	2.19	1.73	2.2	8.331
15	2.77	2.01	2.57	10.93
10	8.09	4.16	5.34	23.00

4.1.4.3 Optical investigation of ZnO thin films sputtered at different deposition times

The optical investigations of the ZnO thin films with deposition time variations were present in Figure 4.32 and in Table 4.23. According to the results, the optical properties were affected from deposition time. Jain and Kulshreshtha [109], reported that thicker coating supplied higher conductance and less transparency according to the relation of T = exp (-αt), where T is the optical transmittance, α is the optical absorption and t is the thickness of the film. However the results showed opposite to this observation. At low deposition times, thin films with lower optical transmittance were achieved.

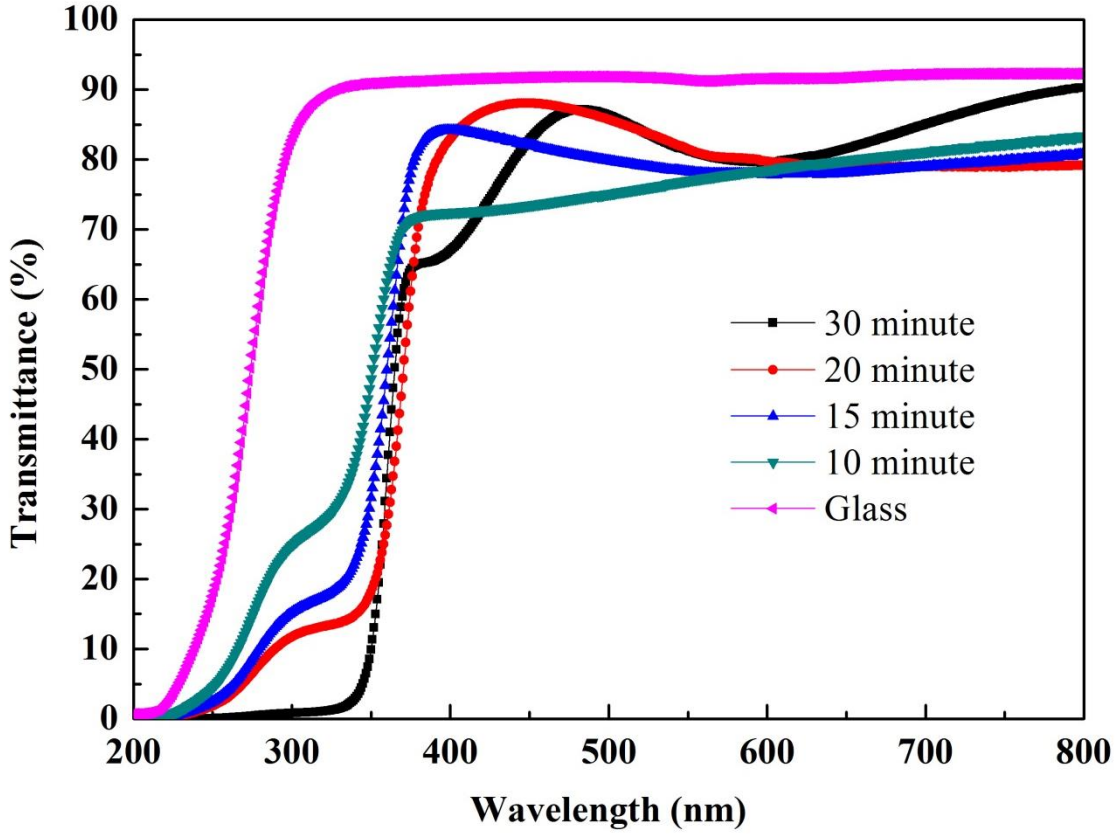

Figure 4.32 Total transmittance spectra of ZnO thin films prepared at different deposition time values

$(\alpha h\nu)^2$ versus $h\nu$ graphs of ZnO thin films deposited at different deposition times were formed in Figure 4.33 and 4.34.

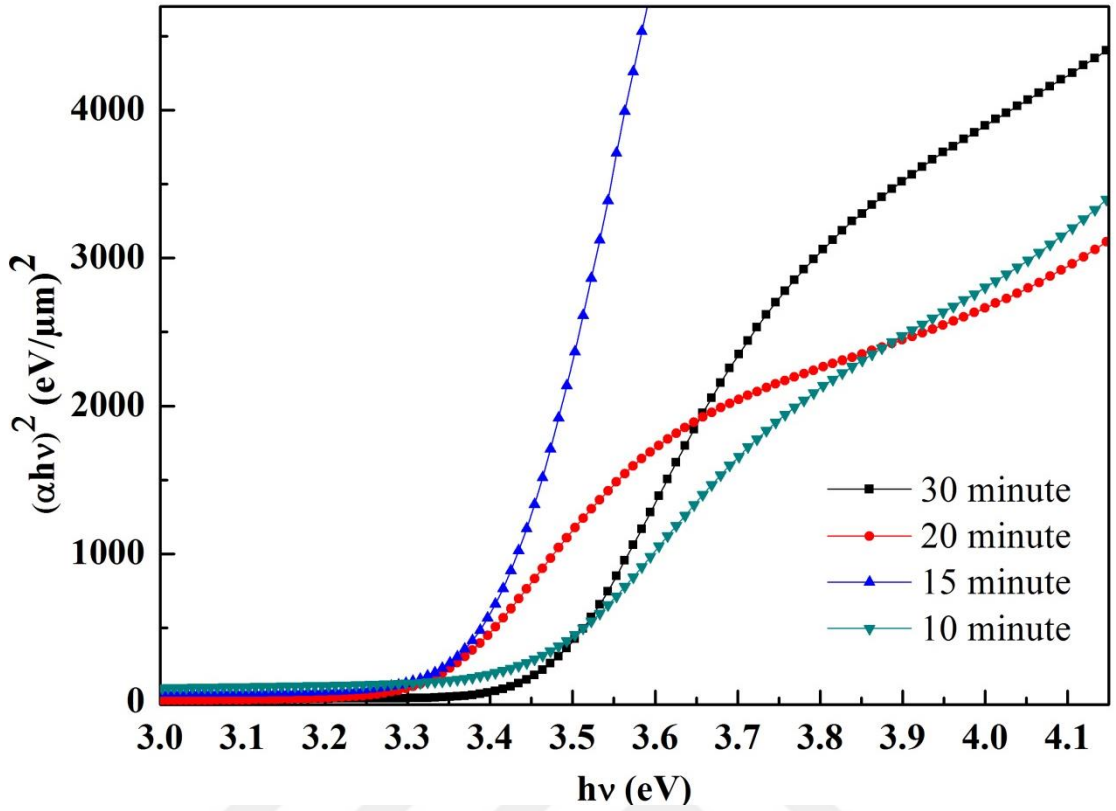

Figure 4.33 $(\alpha h\nu)^2$ versus hν graph of ZnO thin films deposited at different deposition time values

The energy band gap behavior of ZnO thin films were measured around 3.45 eV. At 20 min. deposition time, although the average transmittance value was high, Egap was calculated as 3.30 eV.

Table 4.23 Deposition time, average transmittance and energy band gap variations.

Deposition Time (min)	**Average Transmittance (%)**	**Egap (eυ)**
30	83.00	3.45
20	81.75	3.30
15	79.64	3.35
10	78.16	3.45

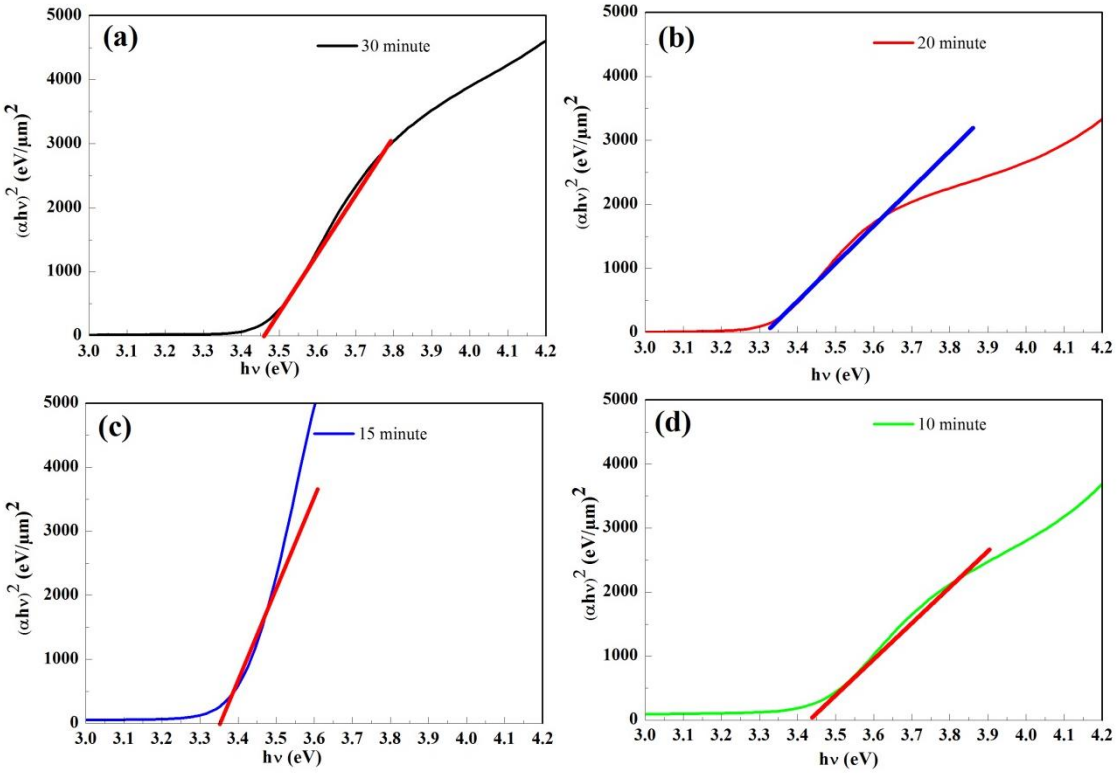

Figure 4.34 $(\alpha h\nu)^2$ versus hν of ZnO graphs thin films deposited at different deposition time values: (a) 30 min, (b) 20 min, (c) 15 min and (d) 10 min

4.1.4.4 Summary of the deposition time variation influence on ZnO thin film properties

The deposition time variation effect on ZnO thin films were observed from 10 min to 30 min. according to the obtained results, the deposition rate decreased with time reduction. However, both the thickness and resistivity values showed variations. Also, surface roughness was affected due to deposition time change. Therefore, FOM measurements were involved to determine the better deposition times. The results were shown in Figure 4.35 and Table 4.24.

Table 4.24 Resistivity, deposition rate, average transmittance and figure of merit values at different deposition times

Deposition Time (min)	Average Transmittance (%)	Resistivity $\times 10^{-3}$ (Ω.cm)	FOM $\times 10^{4}$(Ω.cm)$^{-1}$
30	92.22	1.16	79.5071
20	90.84	2.99	30.3826
15	88.49	1.34	66.0409
10	86.84	3.30	26.3172

According to FOM measurements the highest value was achieved for 30 min deposition time as 79.5071. In addition, for 15 min deposition time, the FOM value was obtained

as $66.0409\times10^{4}(\Omega.cm)^{-1}$. The achieved results revealed that for any kind of PV application high quality thin films can be obtained by chancing the deposition time. For instance, for solar cell applications 15 min can be selected as deposition time.

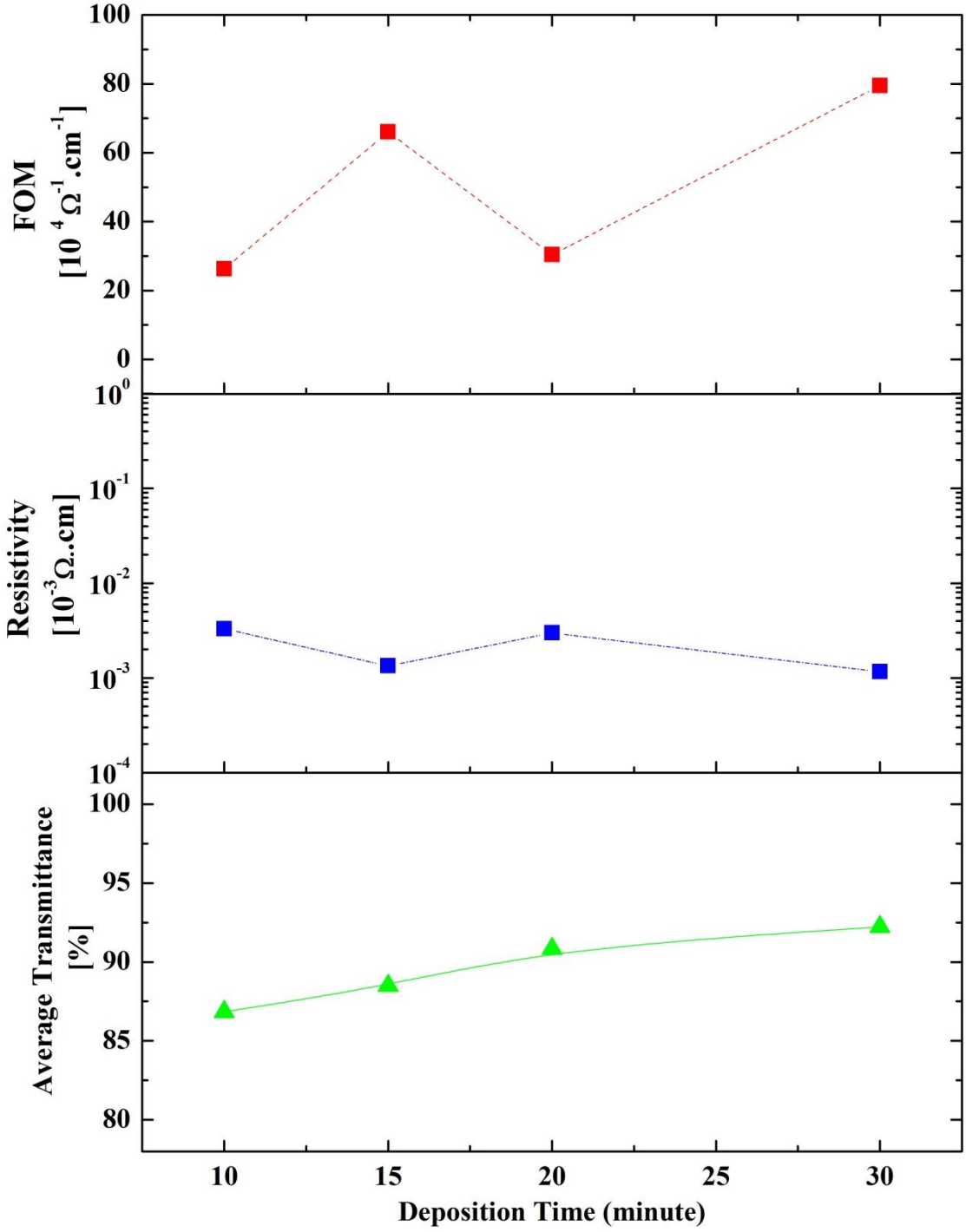

Figure 4.35 Effect of deposition time on average transmittance, resistivity and the figure of merit of ZnO thin films

4.1.5 TEM-HRTEM investigations of ZnO thin films

X-ray diffraction and SEM characterization techniques are not sufficient enough to analyze the grain growth mechanism of ZnO thin films deeply [40]. Consequently, both TEM and HRTEM characterizations were done. In Figure 4.36a-c low magnification TEM images of ZnO thin film at 165 W are shown. Epoxy, ZnO coating and substrate (glass) are shown respectively in Figure 4.36a. Other TEM pictures are at different magnifications.

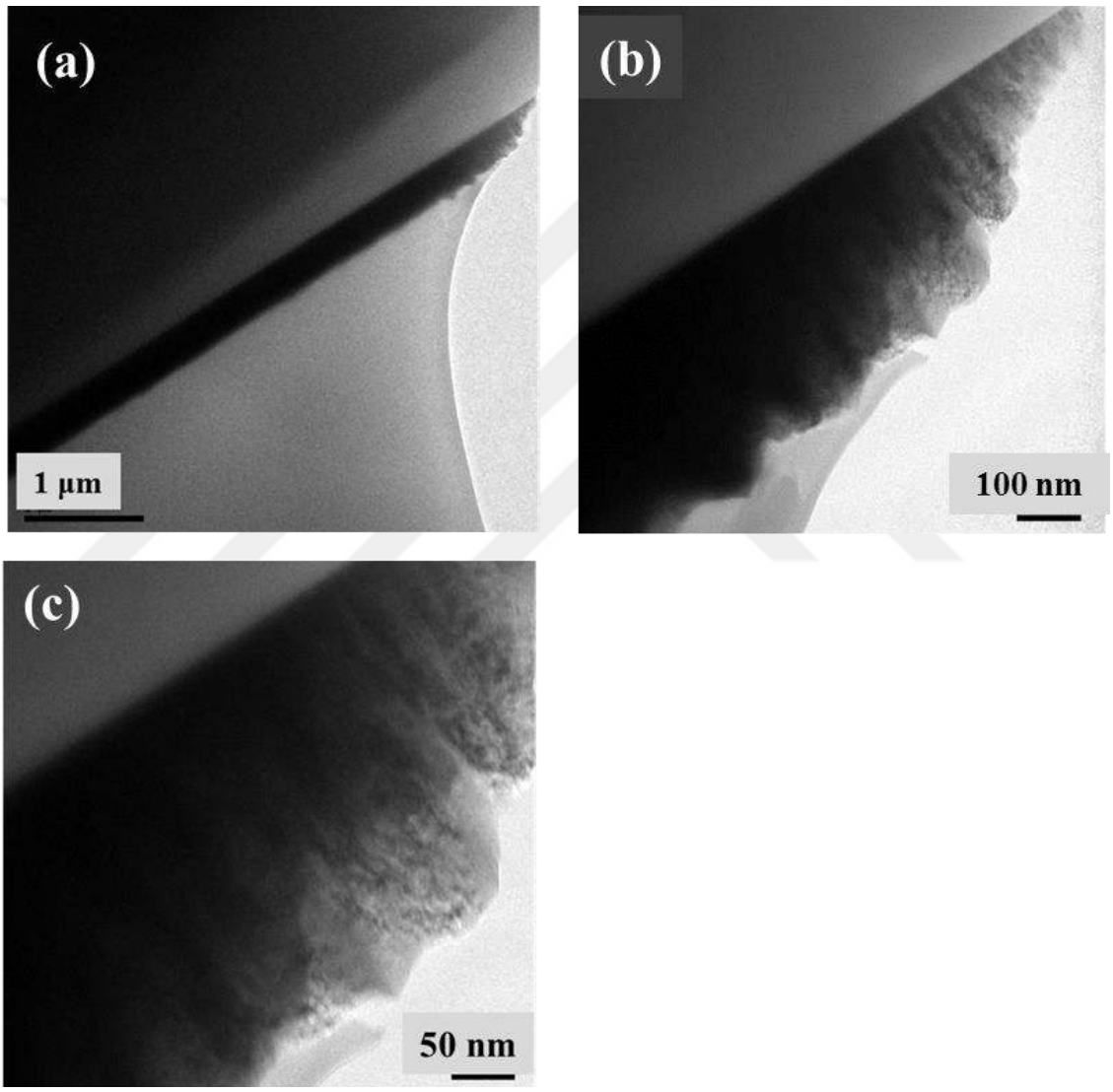

Figure 4.36 Low magnification TEM images of ZnO thin film deposited at 165 W

Although, investigation of atomic level research on crystal structure and atomic arrangement is difficult for the films deposited on glass substrates. HRTEM analyses were possible to perform. Figure 4.37 shows the cross-sectional bright field (BF) and dark field (DF) HRTEM images of the ZnO thin film sputtered at 45 mm D_{TS}.

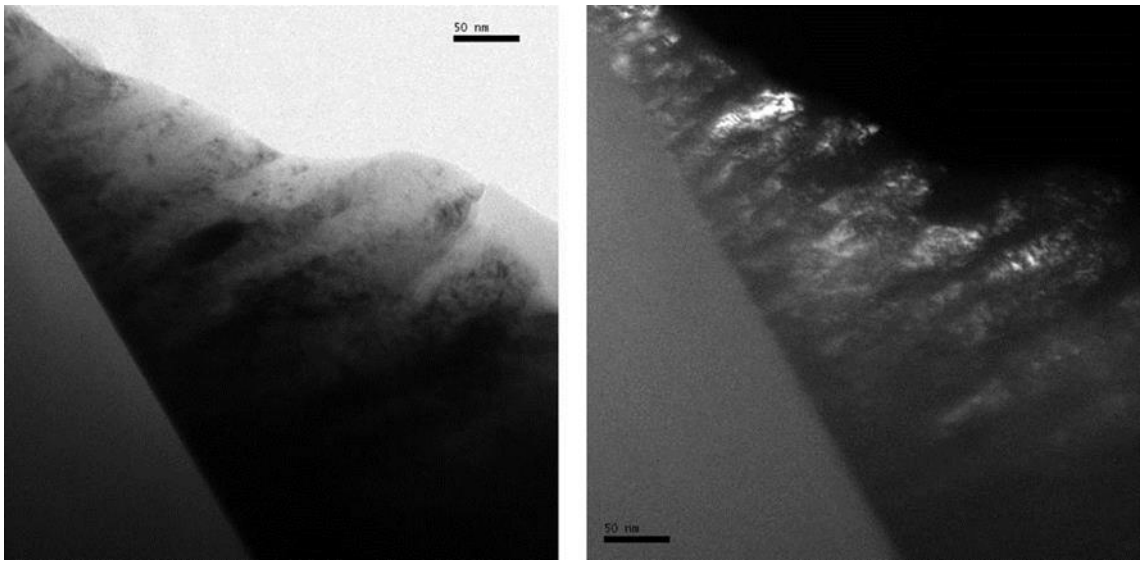

Figure 4.37 Cross-sectional bright field (BF) and dark field (DF) HRTEM images of ZnO thin film with a D_{TS} of 45 mm

The columnar grain structure was clearly visible in the images. The selected area electron diffraction (SAED) pattern of the ZnO thin film is presented in Figure 4.38. The SAED pattern of indicates the same film orientation ((002) c-axis) as that observed by XRD. Films were preferentially polycrystalline with the hexagonal structure, and they had a preferred orientation with the c-axis perpendicular to the substrate. However, there was a ±15 degree variation between the c-axis with the normal direction of the glass substrate.

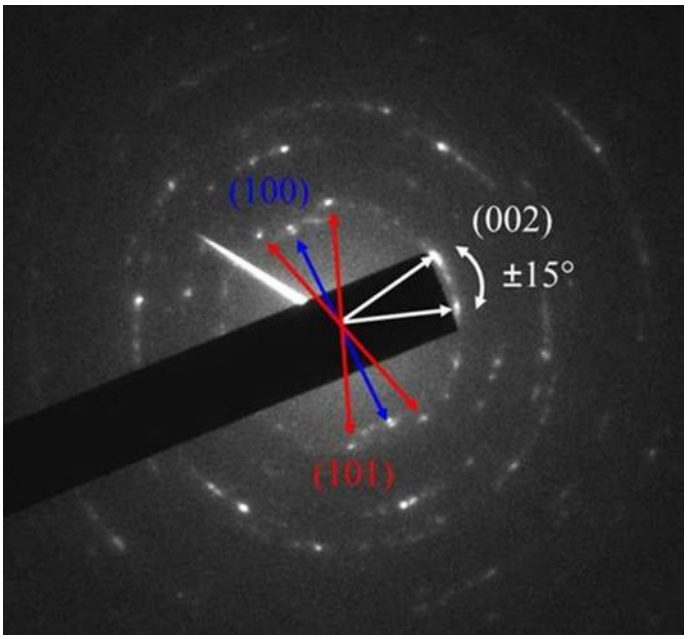

Figure 4.38 SAED of the ZnO thin film shown in Figure 4.37

The columnar growth as observed by SEM images was clearly seen by TEM pictures and it is stated that the ZnO thin film grows almost perpendicular to the substrate surface. Moreover, columnar grains were investigated by HRTEM techniques in detail. Representative HRTEM images were shown in Figure 4.39.

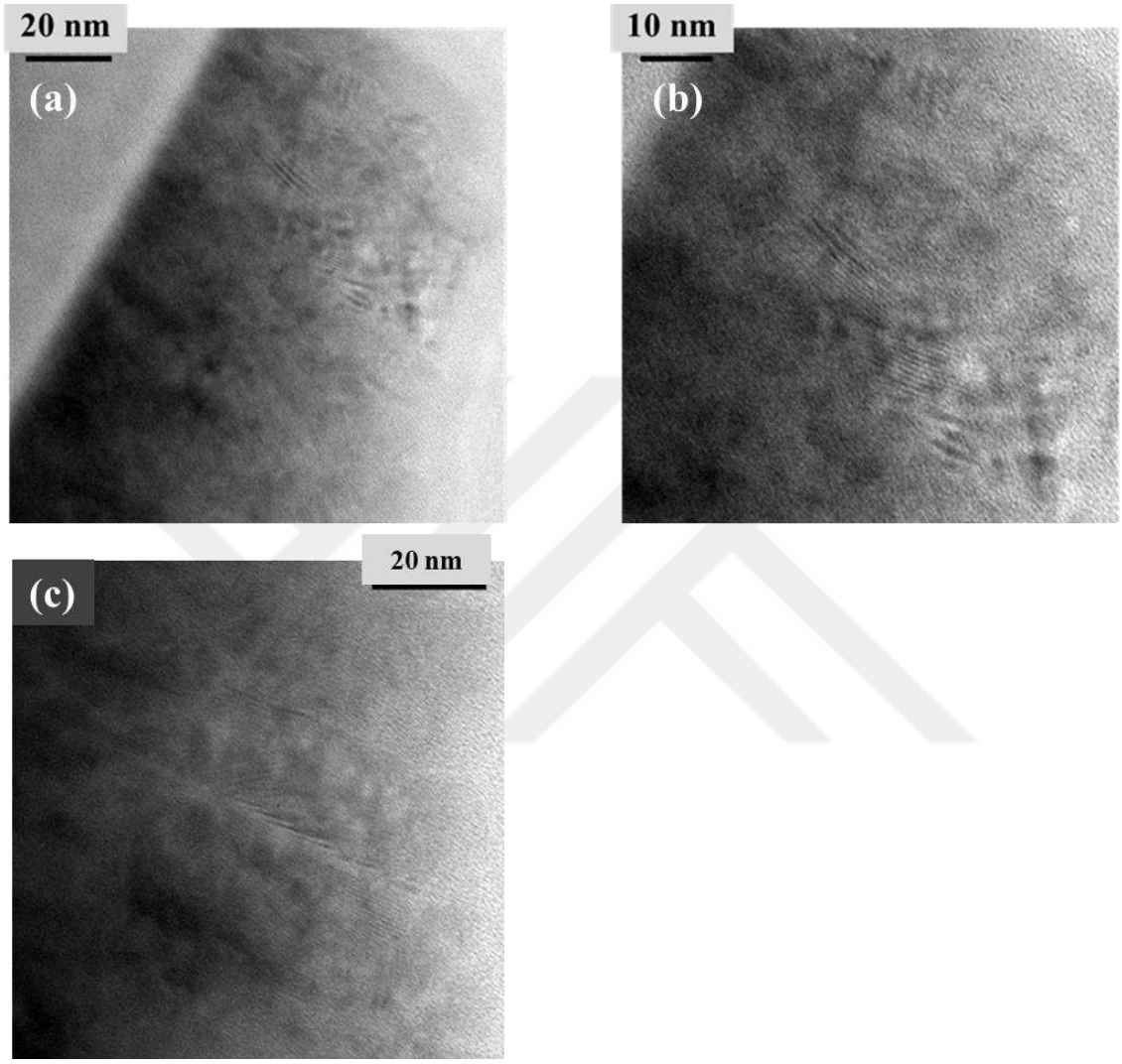

Figure 4.39 HRTEM images of ZnO thin film deposited at 165 W

HRTEM investigations also revealed nanostructures inside the columnar grains. Some nano-island structures were observed with different orientations (±15°). In Figure 4.40a HRTEM image of nano-island structure inside a columnar grain is seen. Figure 4.40b is enlarged and filtered view of the square in Figure 4.41a. The planar spaces were measured as 2.6 Å from higher magnifications and this was equal to the value of d-spacing of (002) plane of ZnO. Also, the orientation changes between the planes were calculated as ±15° with the help of FFT diffractogram shown in Figure 4.40(c).

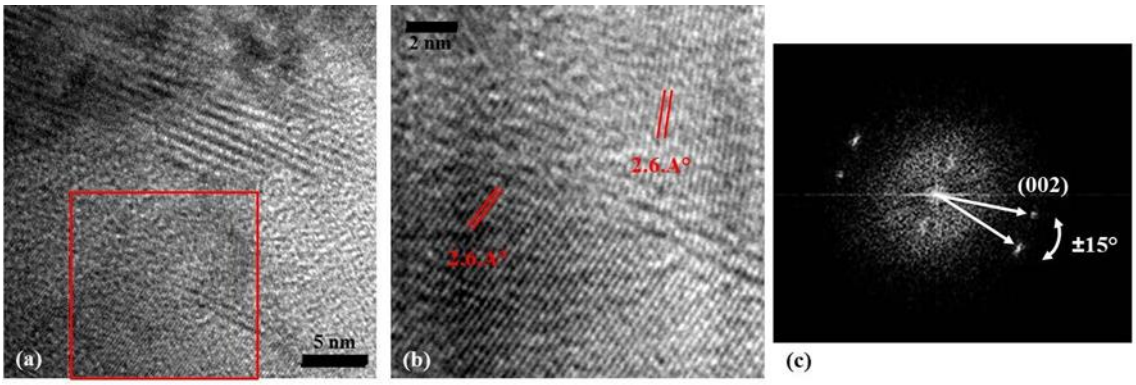

Figure 4.40 HRTEM images of nano-island structured grains. ((b) is enlarged and filtered view of the square in (a) showing d distances of 2.6 A (002)) and (c) FFT diffractogram of (b) which shows (002) spots with an angle variation of ±15°)

Plan view TEM and HRTEM investigations were also possible on small regions for the ZnO thin films sputtered on glass substrate. Figure 4.41 shows plan view TEM, HRTEM images and also corresponding diffraction pattern.

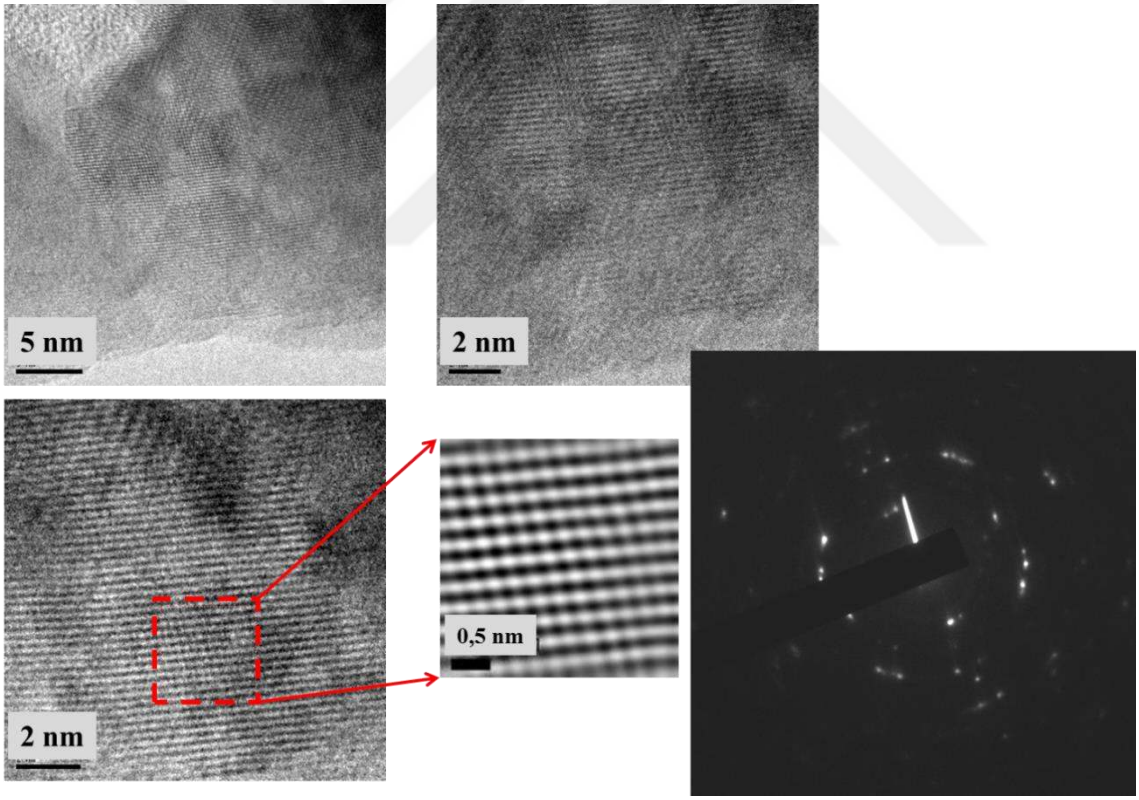

Figure 4.41 Plan view TEM, HRTEM images and also corresponding diffraction pattern for ZnO thin film sputtered on glass substrate at 165 W r.f. Power, 45 mm D_{TS}

Semi-quantitative elemental analysis was also performed by TEM-EDS. Both line analysis and elemental mapping was done which were given in Figure 4.42. As

observed from both line analysis and elemental mapping the elemental distribution is homogenous.

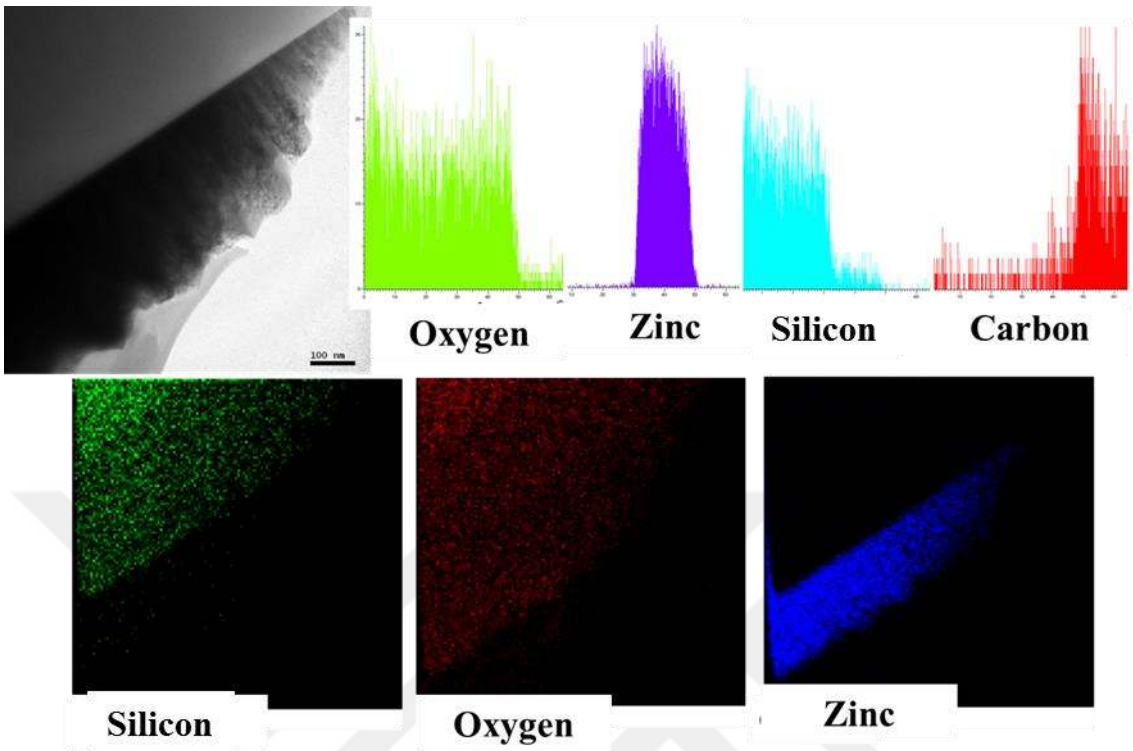

Figure 4.42 Plan view TEM, HRTEM images and also corresponding diffraction pattern for ZnO thin film sputtered on glass substrate

4.2 Investigation the Effect of Sputtering Parameters on Aluminum Doped Zinc Oxide ZnO:Al Thin Films

To understand the influence of sputtering parameters, ZnO:Al thin films were deposited on glass and silicon substrates by r.f. magnetron sputtering technique. All the investigations were done at room temperature conditions, without intentional heating. The effects of important deposition parameters such as argon gas pressure, r.f. power and target-to-substrate were investigated with small variations to understand the influence on electrical, optical and structural properties of the films.

4.2.1 Effect of r.f. power on ZnO:Al thin films

Sputtering power is one of the important parameter for ZnO:Al thin film deposition. Hence, to understand the influence detail, experimental investigations were done in small r.f. power variations. According to experimental procedure, argon was selected as a process gas and the target-to-substrate distance was placed as 45 mm. To eliminate the

substrate heating effect on thin film properties, all the process was carried at room temperature conditions. The base pressure was measured around 1×10^{-5} Pa with the help of diffusion pump. Before deposition, 5 minutes pre-sputtering was applied to remove any contaminants and sputtering was carried for 30 minutes. The r.f. power variation was examined from 100 W to 200 W, at 0.3 Pa argon gas pressure.

4.2.1.1 Electrical properties of ZnO:Al thin films sputtered at different r.f. powers

In order to understand the r.f. power variation on electrical properties of ZnO:Al thin films, resistivity values were measured with the help of four point probe technique. The achieved results were present in both Table 4.25 and Figure 4.43. The resistivity values were measured around $10^{-3}\Omega$.cm and increased with r.f. power.

Table 4.25 Thickness, resistivity and deposition rate variations at different r.f. powers

r.f. Power (W)	Thickness (nm)	Resistivity $\times 10^{-3}$ (Ω.cm)	Deposition rate (Å/min)
100	100	1.62	33
150	235	1.22	78
160	260	1.23	86
165	215	1.11	71
170	300	1.11	100
175	240	1.31	80
200	300	2.80	100

Also, the thickness values as seen in Table 4.27 were obtained from the cross sectional SEM images shown Figure 4.44. At 100 W r.f. power value, the thickness of the film was also low as 100 nm, while at 200 W it reached 300 nm.

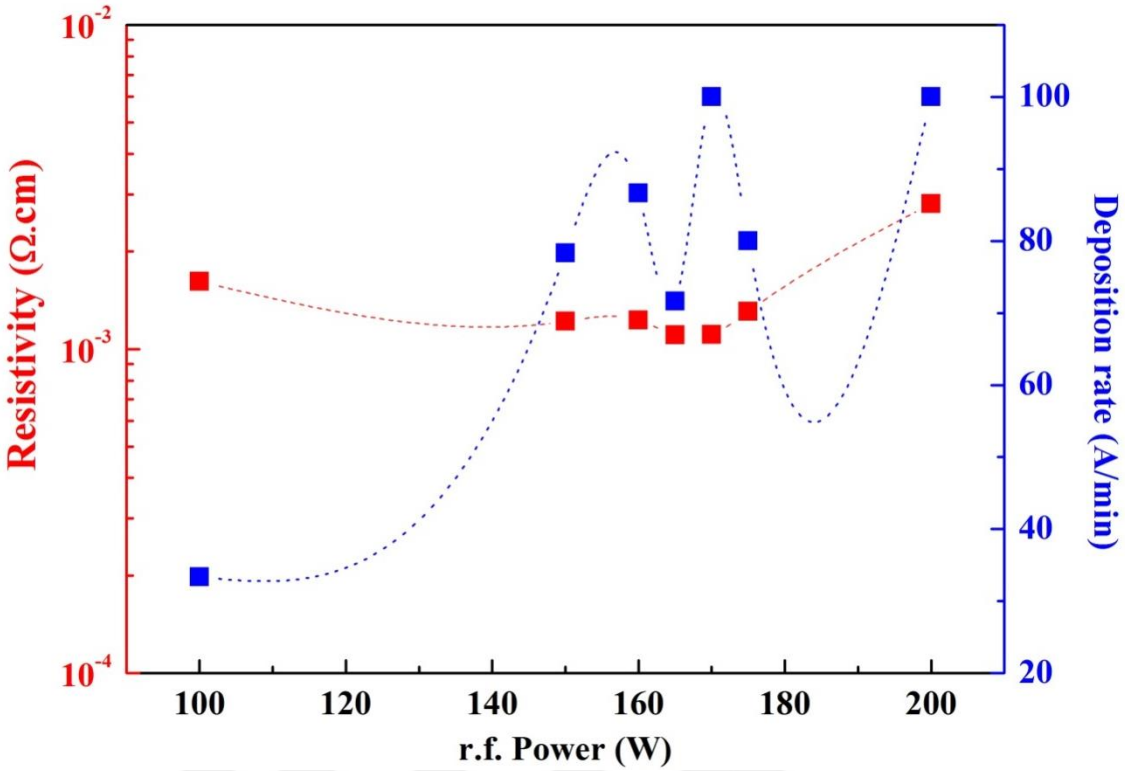

Figure 4.43 Resistivity and deposition rate variations at different r.f. power

The deposition rates of the films were calculated by dividing the thickness value to the deposition time, and achieved results were present in Table 4.27. Moreover, the deposition rate behavior of ZnO:Al thin films showed a wavy trend with r.f. power variation. Generally, it is known that the deposition rate of ZnO:Al thin films were improved with the increase of r.f. power, as observed in our study [131]. Therefore, at high r.f. power both argon ions in the plasma and the bombardment on the target increased [132].

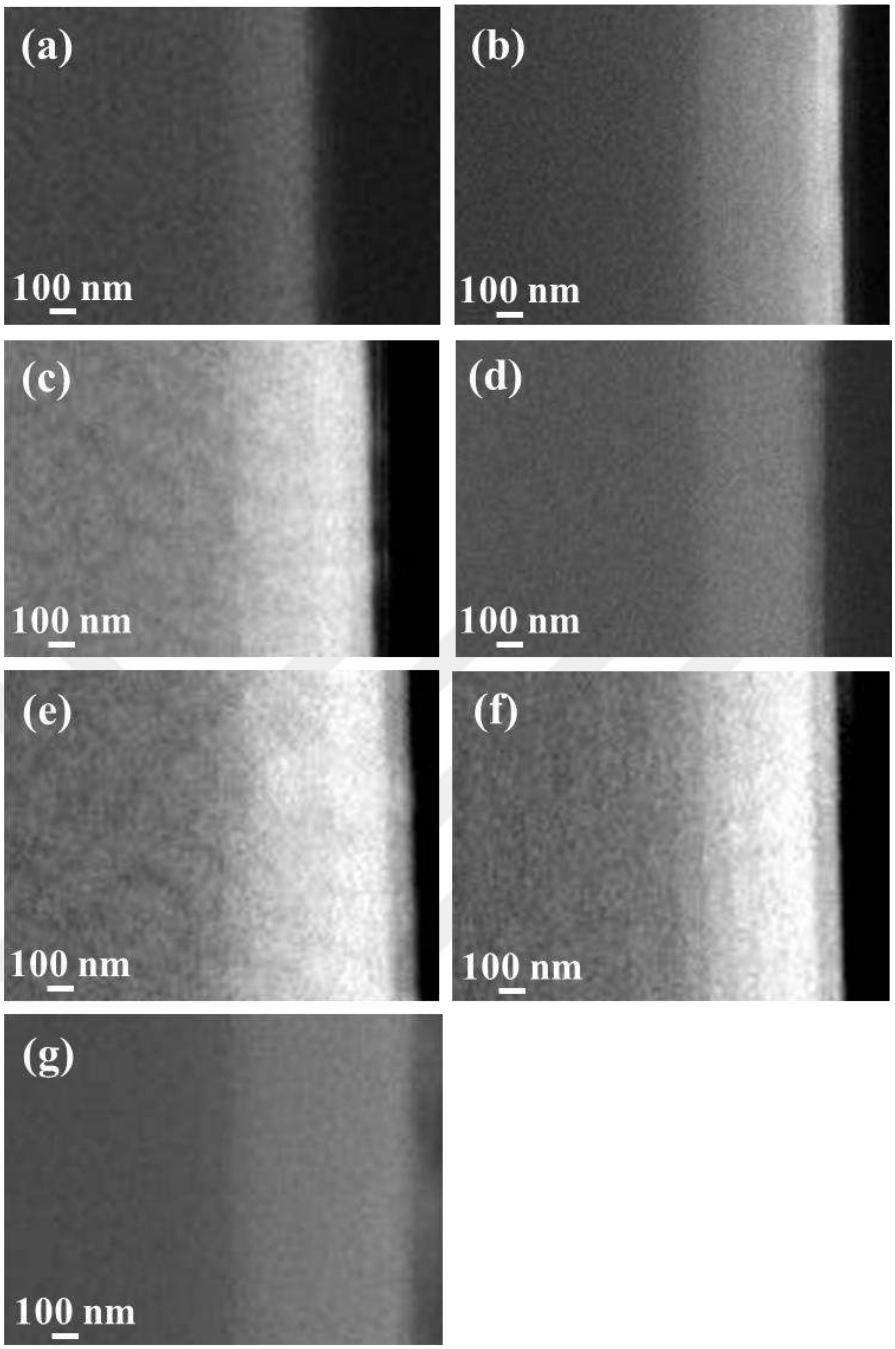

Figure 4.44 Cross sectional FESEM image of the ZnO:Al thin films deposited at different r.f. power values: (a)100 W, (b) 150 W (c) 160 W, (d) 165 W, (e) 170 W, (f) 175 W and (g) 200 W

4.2.1.2 Structural properties of ZnO:Al thin films sputtered at different r.f. powers

XRD investigations were done in the range of 100 W to 200 W, to understand the effect of r.f. power on structural properties. Figure 4.45 showed XRD spectrum of ZnO:Al thin films. The main peak was observed at around 34.20° ((002) peak) and this revealed

that the films were growth perpendicular to the substrate surface. However, the (101) and (100) peaks were also seen in Figure 4.45. With the help of XRD and cross sectional SEM results, thickness, position and intensity of (002), (002) peak intensity per unit thickness, the positions of (100) and (101), and their relative intensities, full with at half maximum and crystallite size values with the variation of r.f. power were observed and presented in Table 4.26.

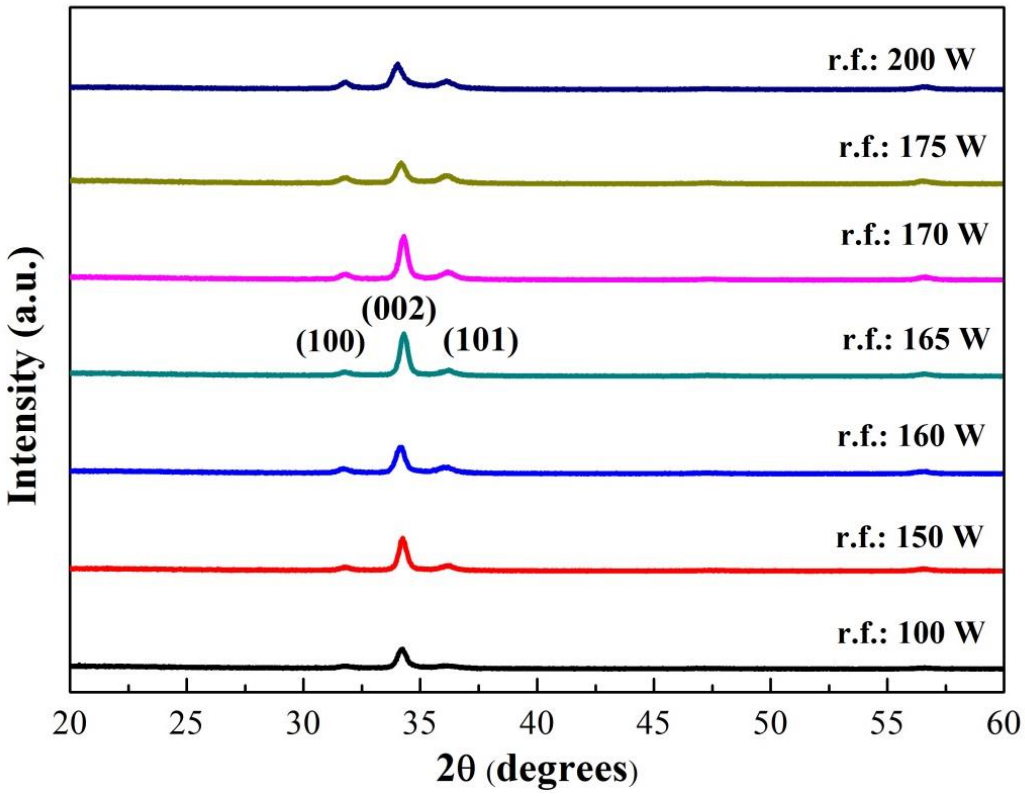

Figure 4.45 X-ray diffraction pattern of ZnO:Al thin films deposited at different r.f. powers

100 W and 200 W test conditions seem to be boundary since they showed much different and worse results than the rest. When 150 W-175 W range was studied in detail, some variation in results was obvious. A remarkable increase was observed for the (002) intensity values of small r.f. power variations. For instance, 34% increase was calculated between 160 W and 165 W (002) intensity. Similarly, in 165 W condition. (100) relative intensity was only 7.83% compared to 15.92% of 160 W. This double increase was also similar in (101) relative intensity values. This showed that only 5 W changes in the r.f. power may cause different properties of ZnO:Al thin films. FWHM or crystallite size results showed slight changes in the range of 150 to 175 W. For all, crystallite size was around 23 nm (4.33).

Table 4.26 Position of (200), intensity of (002), (002) peak intensity per unit thickness, position of (100), relative intensity of (100), position of (101), relative intensity of (101) peak for ZnO:Al thin films at different r.f. powers.

r.f. Power (W)	Position of (002) (Degree)	Intensity of (002) (a.u.)	(002) Peak intensity per unit thickness (cps/nm)	Position of (100) (Degree)	(100) Rel. Int. (%)	Position of (101) (Degree)	(101) Rel. Int. (%)
100	34.19	873.47	8.73	31.76	9.15	36.05	10.50
150	34.22	1361.65	5.79	31.75	9.52	36.15	14.42
160	34.11	1157.57	4.45	31.69	15.92	36.05	21.53
165	34.27	1750.08	8.13	31.75	7.83	36.16	11.72
170	34.26	1916.00	6.39	31.76	10.85	36.16	16.29
175	34.16	883.85	3.68	31.75	25.26	36.11	36.22
200	34.02	1096.71	3.66	31.76	24.97	36.03	27.21

Another interesting result was the thickness of the film being the same (300 nm) for 170 W and 200 W in despite of big change in crystallite size 22 nm compared to 15 nm (Table 4.27). The reason of this could be explained as the adatom mobility may limit the surface diffusion energy. Lee et al. [73] pointed out that higher r.f. power improves the reaction rate and this causes more damages on the surface and poor crystalline quality. Their study showed that the sputtering power must be proper to have an efficient nucleation and growth. Similarly, in our case 165 W condition was the best for nucleation and growth of ZnO:Al thin films.

Table 4.27 FWHM and crystalline sizes of ZnO:Al thin films at r.f. powers

r.f. Power (W)	FWHM (Degree)	Crystallite Size(nm)
100	0.42	19.39
150	0.36	22.64
160	0.39	21.27
165	0.36	23.03
170	0.37	22.40
175	0.44	18.52
200	0.55	14.95

In addition, at lower r.f. power value, although the growth rate was low, the grains formed in a smaller fashion. This is linked as, the energy of sputtered particles being not enough to maintain the necessary diffusivity to fill the energetically optimal places. This causes smaller crystallite size [89]. At 100 W, 19 nm was calculated as crystallite size which was smaller than the optimum r.f. power range. Oppositely, at high r.f. power due

to high sputtering rate, excess energy forms which causes degradation of growth of grains [89]. Again, small crystallite size is formed at high r.f. power values (200 W).

4.2.1.3 Morphological investigation of ZnO:Al thin films sputtered at different r.f. power

AFM investigation (Figure 4.46) was done for ZnO:Al films to figure out the dependence of surface morphology on r.f. power.

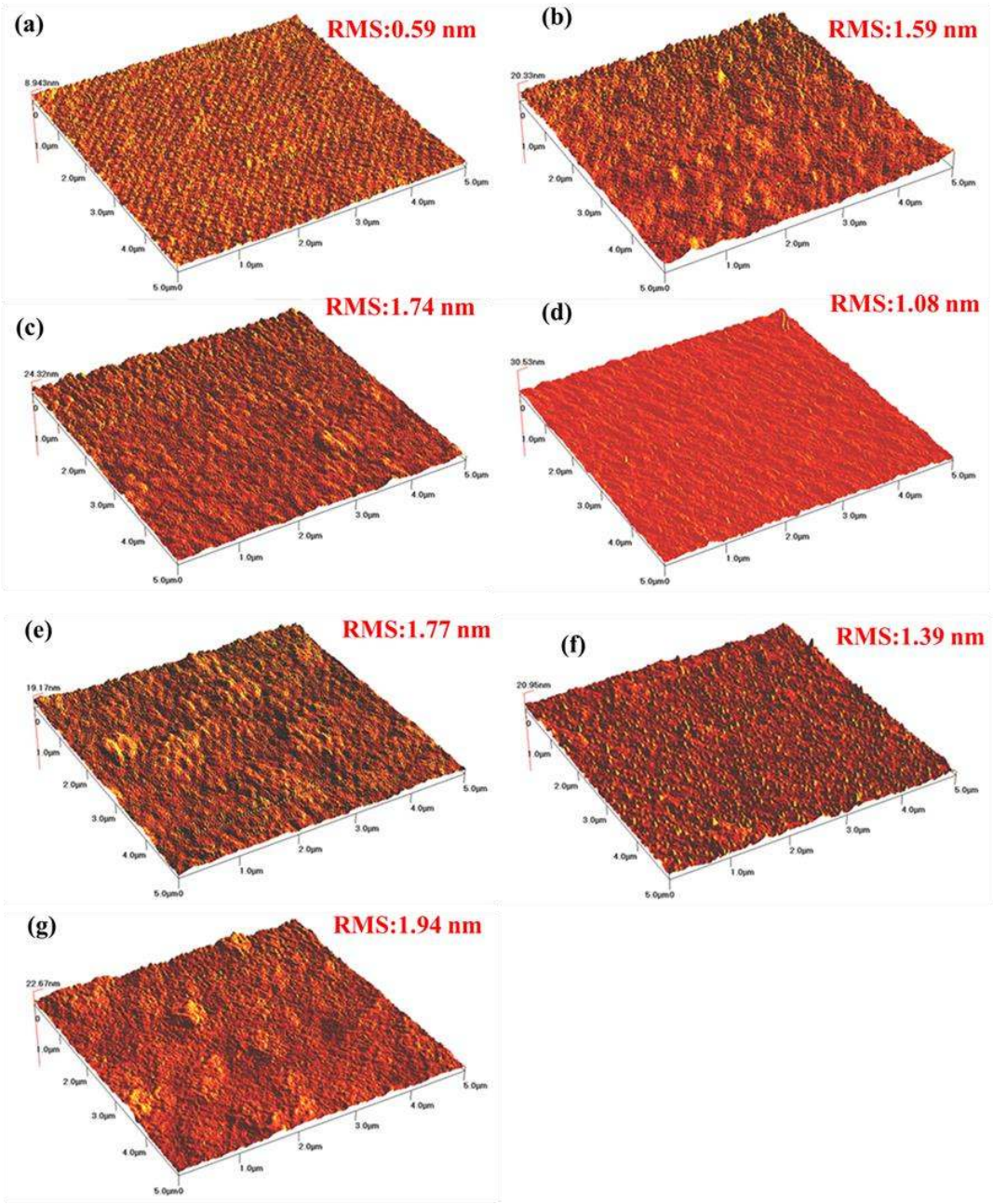

Figure 4.46 AFM images and RMS of ZnO:Al thin films deposited at different r.f. powers; (a) 100 W, (b) 150 W, (c) 160 W, (d) 165 W, (e) 170 W, (f) 175 W and (g) 200 W

The surface roughness was found to be 0.59 nm, 1.59 nm, 1.74 nm, 1.08 nm, 1.77 nm, 1.39 nm and 1.94 nm with r.f. power of 100 W, 150 W, 160 W, 165 W, 170 W, 175 W and 200 W, respectively. At low r.f. power values the RMS reached the minimum, while at high powers the value of RMS increased (Table 4.28). The reason of this might be due to the bombardment effect of the r.f. power [95]. Also, the RMS values of ZnO:Al thin films were lower than the ZnO thin films [109,138] , due to the doping effect of Al^{+3}.

Table 4.28 r.f. power and corresponding RMS, Ra, Rq and average height variations of ZnO:Al thin films

r.f. Power (W)	**RMS (Sq) (nm)**	**Ra (nm)**	**Rq (nm)**	**Average Height (nm)**
100	0.89	0.59	0.74	4.20
150	2.07	1.59	1.98	10.61
160	2.35	1.74	2.26	9.87
165	1.29	1.08	1.40	4.88
170	2.17	1.77	2.25	8.04
175	1.87	1.39	1.80	6.32
200	2.63	1.94	2.48	9.25

Furthermore, to examine the relation between crystallite sizes; obtained from XRD and the RMS values, with sputtering power variation Figure 4.47 was formed. According to Figure 4.47, at low and high r.f. power, the diversity between crystallite size and RMS value increased. At 100 W, with the help of lower deposition rate, the lowest RMS was obtained; however, this power was not sufficient to enhance the crystallite size. At 200 W while the grain size was the smallest, the RMS reached the maximum. This opposite behavior could be justified as; high energy of sputtered ion bombardments could be caused a surface damage [79]. For 150 W to 175 W variations, both the crystallite size and roughness values showed resemblance as; while one of them increases the other one decreases. At 165 W, largest crystallite was obtained with one of the smallest RMS (1.08 nm).

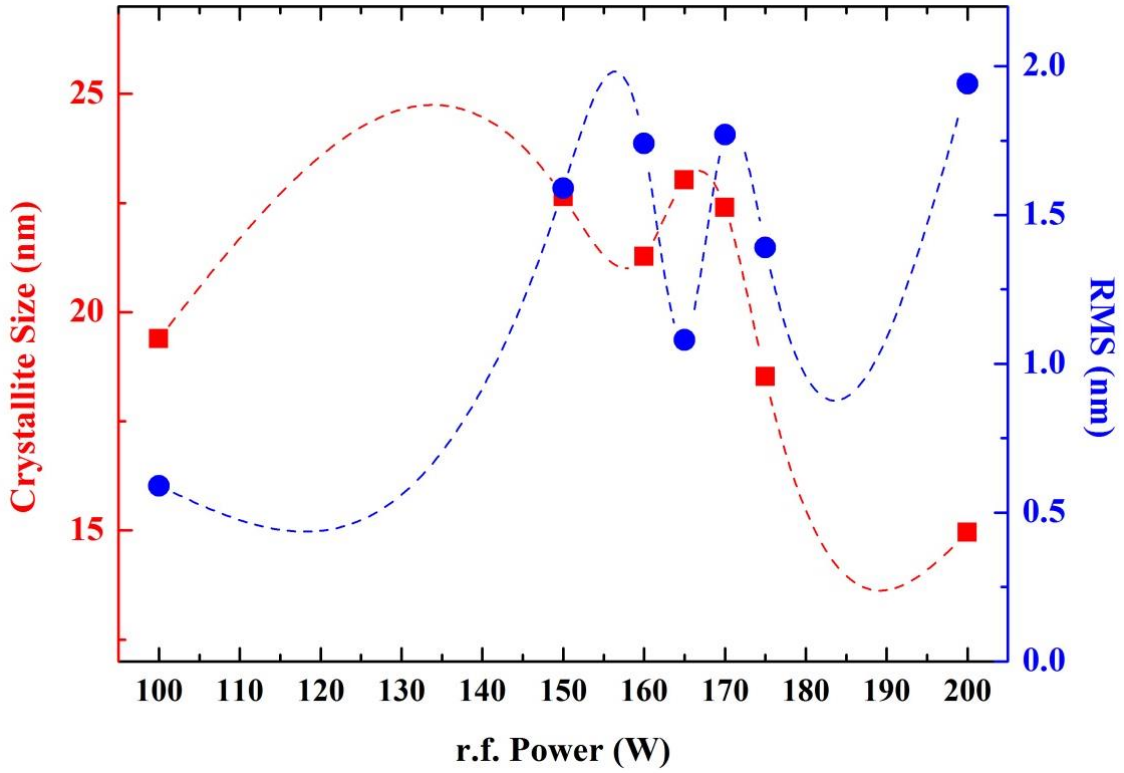

Figure 4.47 Crystallite size and RMS variations of ZnO:Al thin films at different r.f. powers

4.2.1.4 Optical investigation of ZnO:Al thin films sputtered at different r.f. power

Figure 4.48 represents the optical transmittance of ZnO:Al films deposited at various sputter power. It was seen that the average transmittance of the thin films in the visible range was greater than 85%. They were measured as; 82.95%, 85.01%, 86.36%, 86.34%, 84.75%, 86.48% and 86.92% from 100 W - 200 W range.

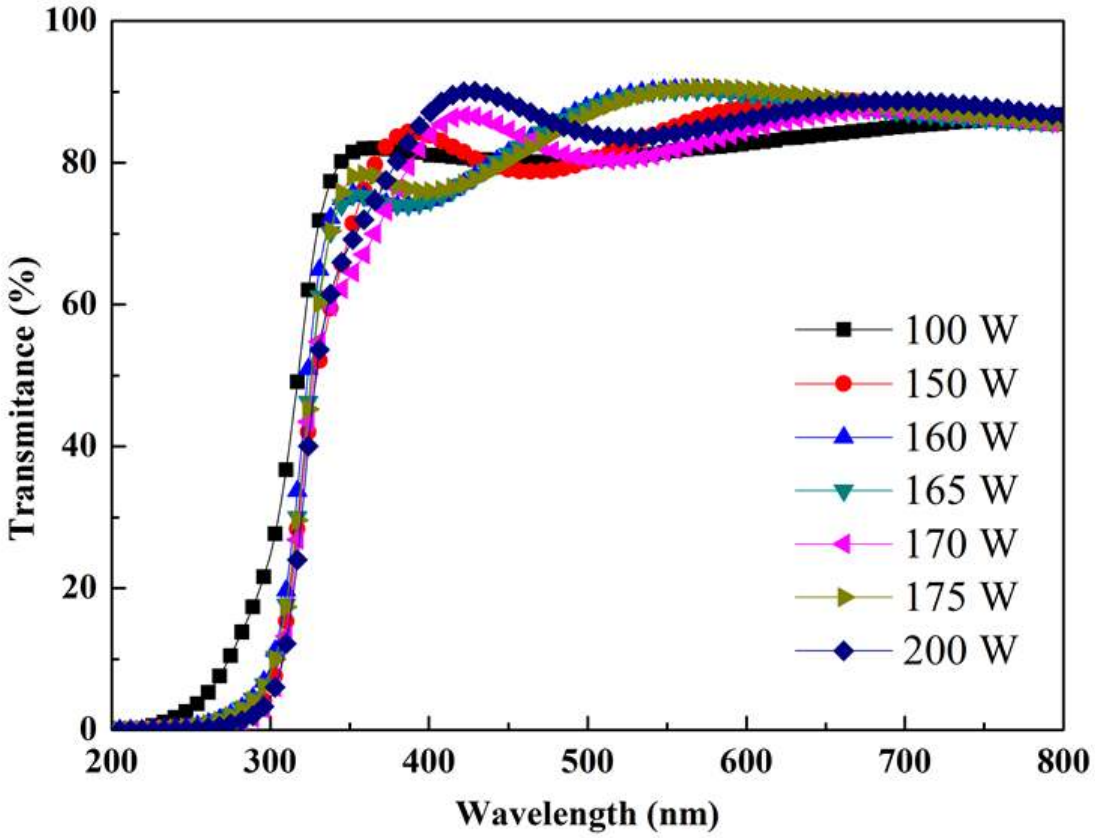

Figure 4.48 Total transmittance spectra of ZnO:Al thin films prepared at various r.f. power

The average transmittance of the films increased with the improvement of r.f. power from 100 W to 200 W. The optical transmittance supplied useful information about the optical band gap of the semiconductors [71]. Moreover, the optical band gaps of the ZnO:Al thin films were measured by extrapolating the linear portion the $(\alpha h\nu)^2$ versus $h\nu$ graph as shown Figure 4.49 and also in Figure 4.50.

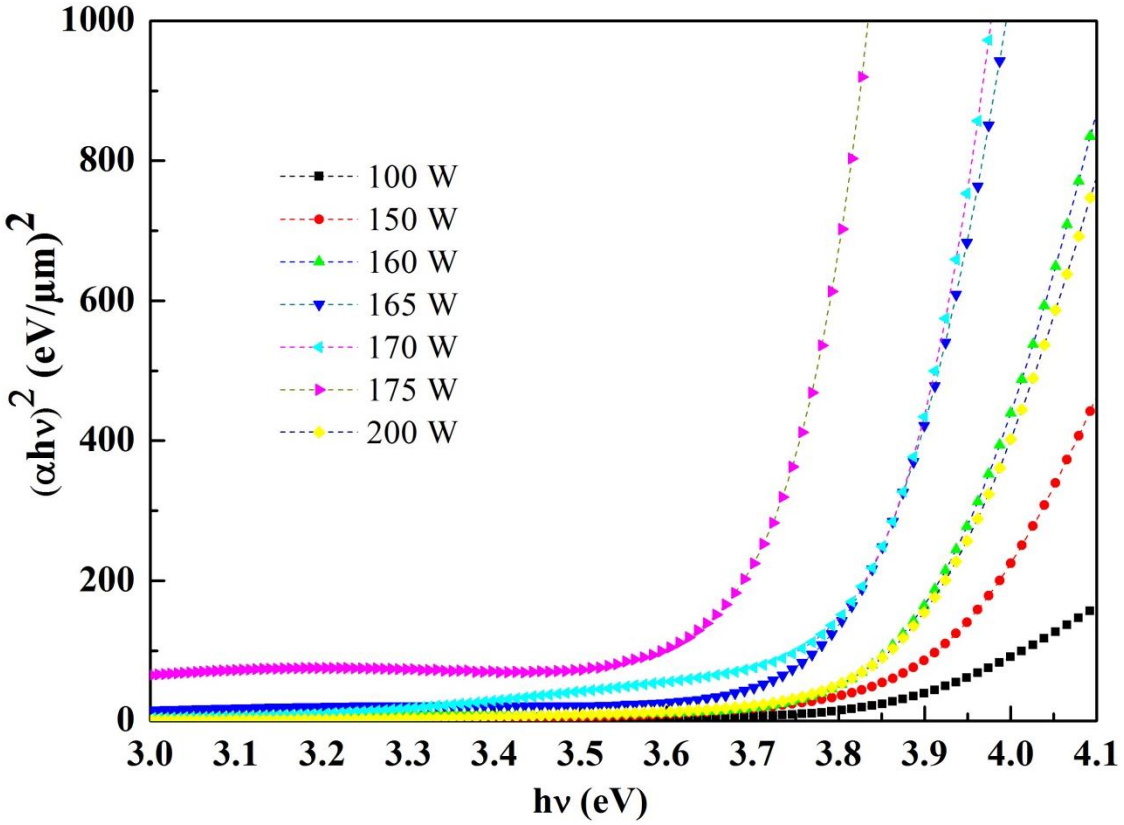

Figure 4.49 $(\alpha h\nu)^2$ versus hν graphs of ZnO:Al thin films prepared at various r.f power

Egap values of the ZnO: Al thin films were measured as 3.85 with the help of Figures 4.49 and 4.50. The achieved data examined that, the energy band gap of ZnO:Al thin films were not affected by r.f. power variation (Table 4.29).

Table 4.29 r.f power, average transmittance and energy band gap variations.

r.f. Power (W)	Average Transmittance (%)	Egap (eυ)
100	82.95	3.85
150	85.01	3.85
160	86.36	3.85
165	86.34	3.85
170	84.75	3.85
175	86.48	3.85
200	86.92	3.85

When the energy band gap behavior of ZnO:Al thin films were compared with ZnO thin films, the influence of r.f. power variation on ZnO thin films was more than ZnO:Al thin films. Also, the Egap value is improved with the help of Al.

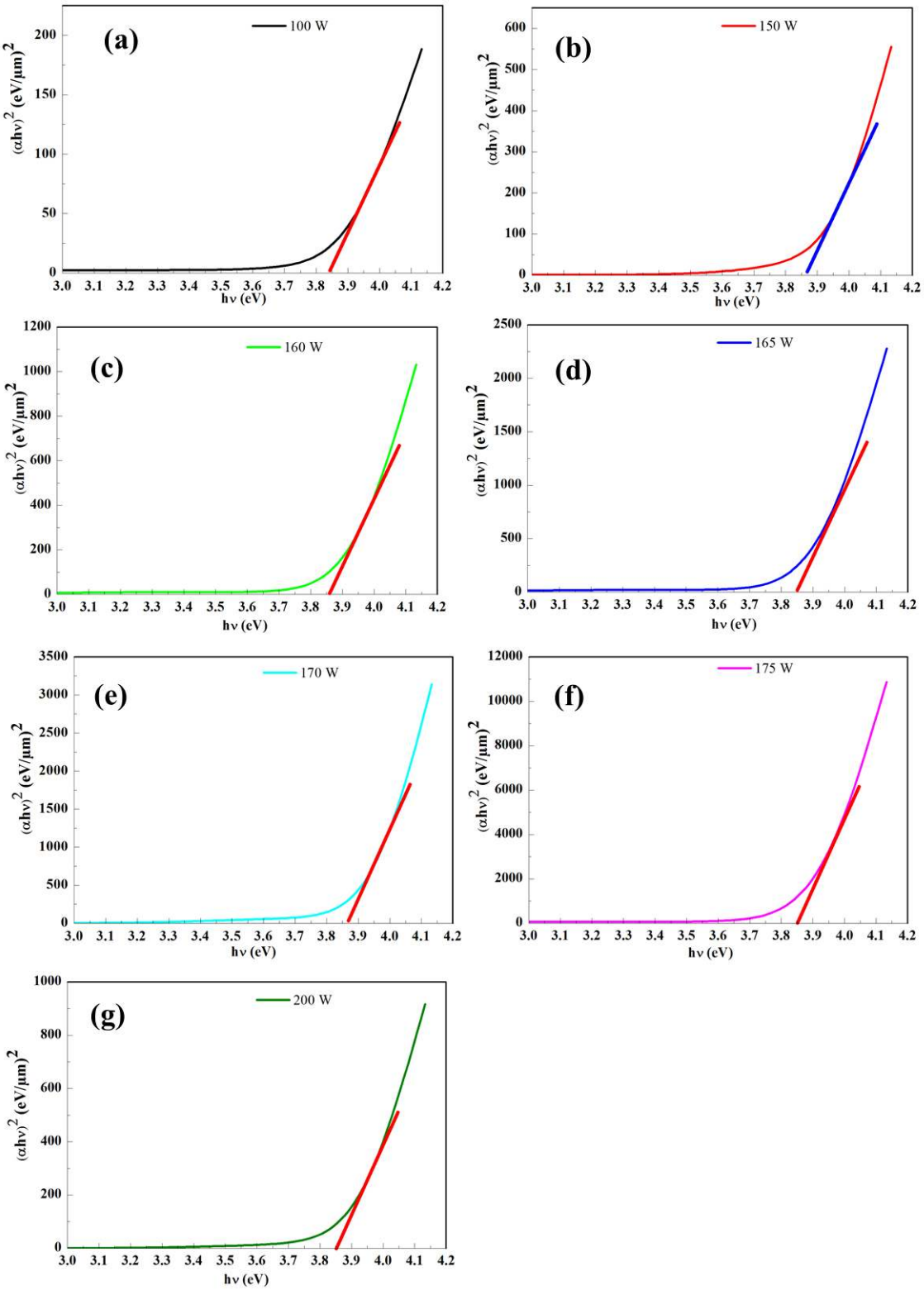

Figure 4.50 Extrapolated $(\alpha h\nu)^2$ versus hν graphs of ZnO:Al thin films prepared at various r.f. powers

4.2.1.5 Summary of the r.f. power variation influence on ZnO:Al thin film properties

The influence of r.f. power on deposition rate, resistivity and figure of merit values was investigated from 100 W to 200 W. The variations of the test results were seen in Figure 4.51. 100 W and 200 W were selected as lower and upper limits, due to the smaller FOM achieved at this r.f. power values.

Table 4.30 Resistivity, deposition rate, average transmittance and figure of merit values at r.f. power variations of ZnO:Al thin films

r.f. Power (W)	Average Transmittance (%)	Resistivity $\times 10^{-3}(\Omega.cm)$	FOM $\times 10^{4}(\Omega.cm)^{-1}$
100	92.16	1.62	57.01
150	94.46	1.22	77.63
160	95.95	1.23	78.03
165	95.93	1.11	86.67
170	94.16	1.11	84.91
175	96.08	1.31	73.56
200	96.57	2.8	34.44

In the study, the r.f. power was changed even with 5 W steps between ~150 W to 175 W. According to the results, this small variation was effective on both growth rate and FOM values. Especially, FOM values became high. The maximum FOM value (780030 $(\Omega.cm)^{-1}$) was achieved for 165 W r.f. value as placed in Table 4.30. These obtained results showed similarities with the literature. For instance, Kuo et al. [132] studied the influence of r.f. power on ZnO:Al thin films deposited at room temperature conditions and they obtained The experimental the resistivity value around $10^{-3}(\Omega.cm)$, while the maximum transmittance ~87%.

Moreover, in many research during the increase of r.f. power, there can be a temperature variation that affects the thin film properties. However, in the range of r.f. powers used in this work, no increase in the substrate temperature measured [133,137].Therefore, 165 W was selected as optimum r.f. power value for ZnO:Al thin film depositions.

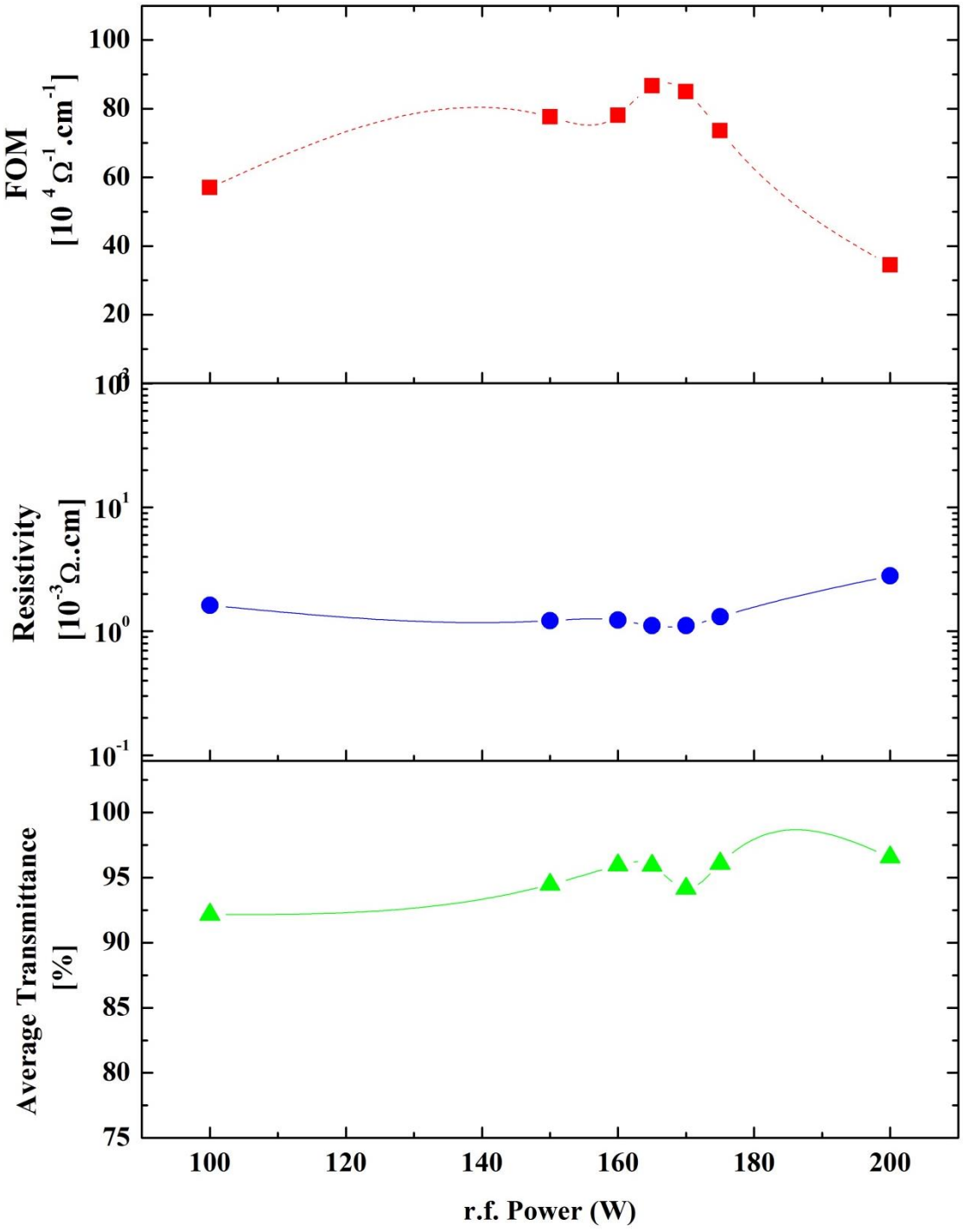

Figure 4.51 Effect of r.f. power on deposition rate, resistivity and the figure of merit of ZnO:Al thin films

4.2.2 Effect of target-to-substrate distance (D_{TS}) on ZnO:Al thin films

Target-to-substrate distance is another important parameter of sputtering for ZnO:Al thin films. The variation of D_{TS} influences not only the structural characteristics, but also morphological and electrical properties as well. In order to determine the optimum

deposition value for ZnO:Al thin films, D_{TS} was changed from 40 mm to 70 mm. the r.f. power was maintained as 165 W, while the working pressure, gas flow rate and deposition time were 0.3 Pa, 20 sccm and 30 minutes, respectively. Electrical, structural, morphological and optical properties were examined by using various characterization techniques.

4.2.2.1 Electrical properties of ZnO:Al thin films sputtered at different D_{TS}

The electrical properties of ZnO:Al thin films were determined by using both four point probe and the SEM techniques. The achieved results were shown in Table 4.31 and Figure 4.52.

Table 4.31 Thickness, resistivity and deposition rate variations of ZnO:Al thin films at different D_{TS}

D_{TS} (mm)	**Thickness (nm)**	**Resistivity $\times 10^{-3}$ (Ω.cm)**	**Deposition rate (Å/min)**
40	153	0.94	50
45	300	1.10	100
50	220	1.49	70
60	180	1.87	60
70	120	1.84	40

The resistivity values were around 10^{-3} Ω.cm, while thickness values of the film showed diversity. Also, Jeong and Lee [41] concentrated on the D_{TS} effect on ZnO:Al thin film deposition and found that increasing D_{TS} from 50 mm to 65 mm increased the resistivity rapidly. In their study, the lowest resistivity was 5×10^{-1} Ω.cm. obtained at 45 mm D_{TS}.

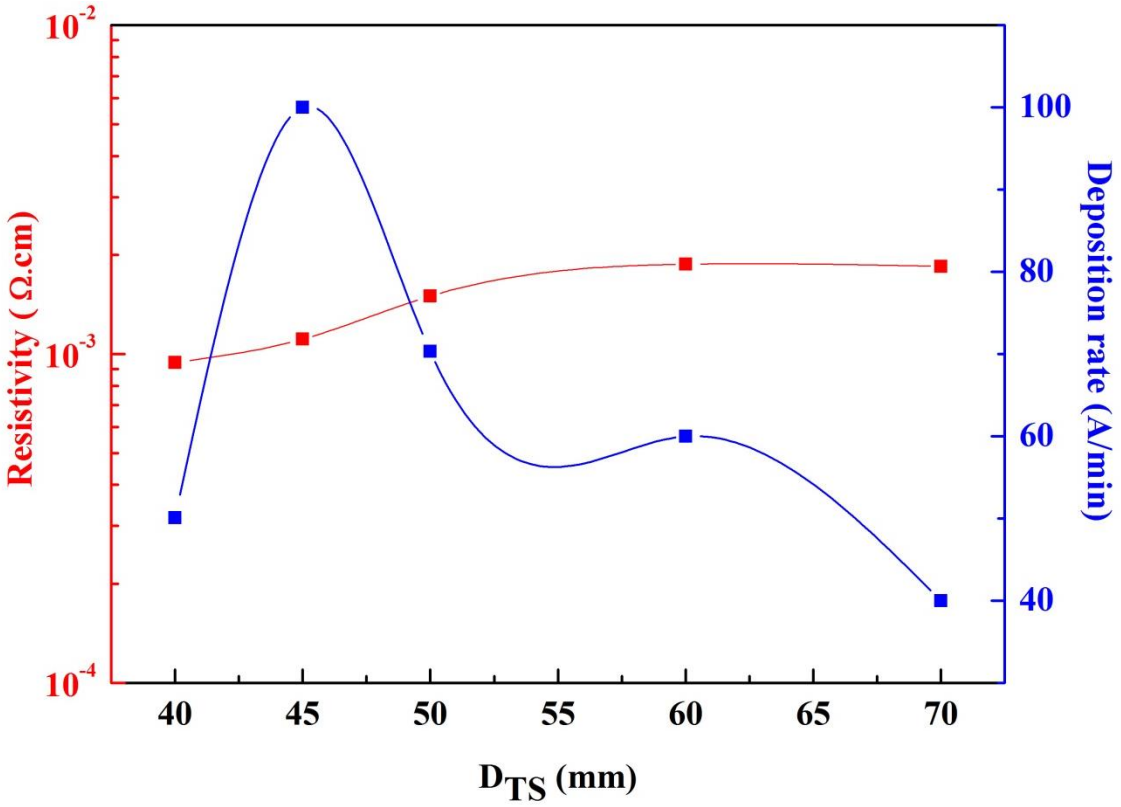

Figure 4.52 Resistivity and deposition rate of the ZnO:Al thin films as D_{TS} varied between 40 mm to 70 mm

The thickness values measured with the help of SEM (Figure 4.53) were low as 153 nm and 120 nm at 40 mm and 70 mm, respectively. However, at 45 mm and 50 mm both the thickness and deposition rate of the films increased. Generally, the growth rate of the film decreased with the increase of D_{TS} [41]. According to our results, the deposition rate decreased with D_{TS} increase from 45 mm to 50 mm.

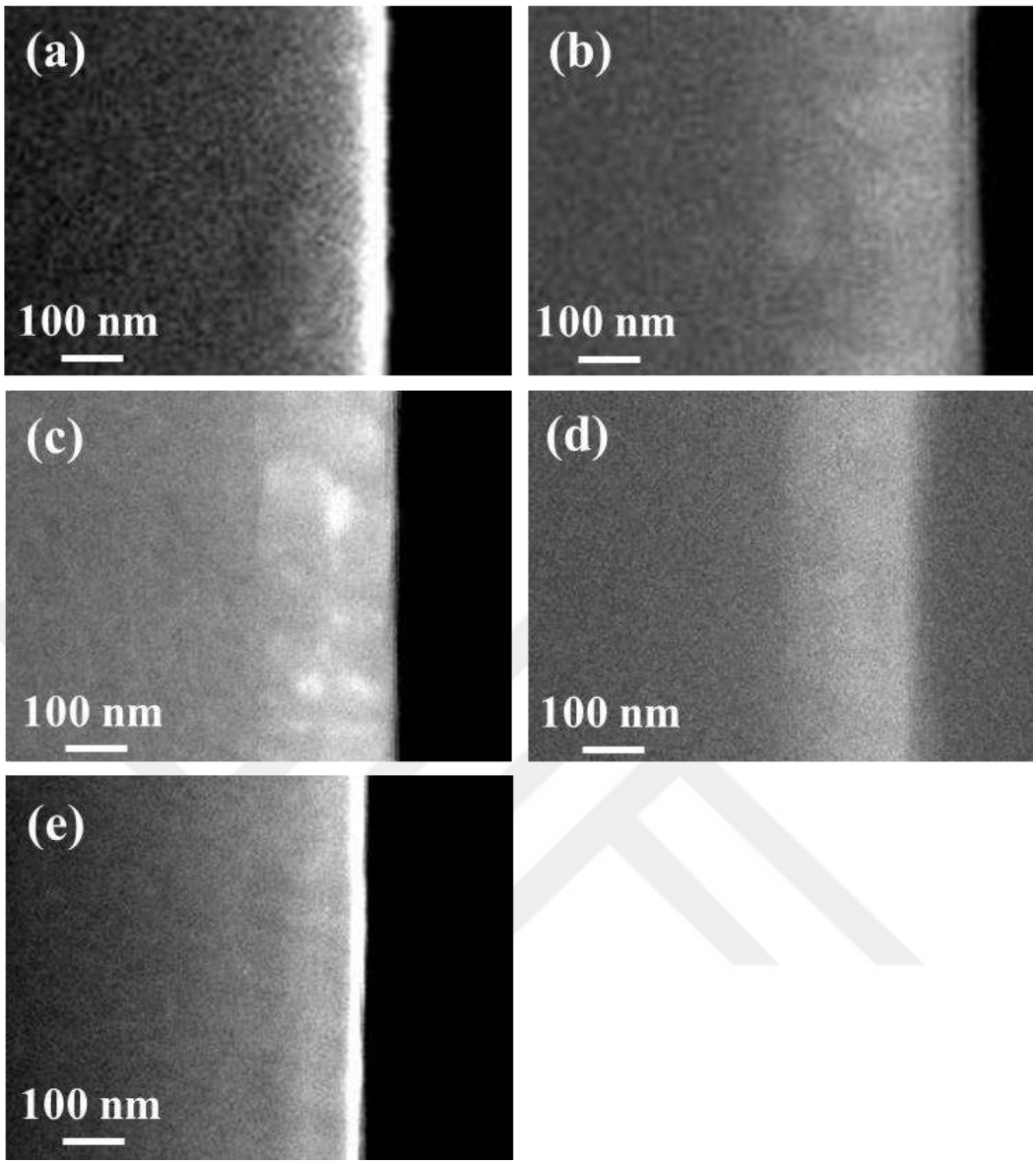

Figure 4.53 Cross-sectional HRSEM images of the ZnO:Al thin films deposited at different D_{TS}: (a) 40 mm, (b) 45 mm, (c) 50 mm, (d) 60 mm and (e) 70 mm

4.2.2.2 Structural properties of ZnO:Al thin films sputtered at different D_{TS}

The structural behavior of the ZnO:Al thin films deposited at different D_{TS} values were determined with the help of XRD system. In Figure 4.54, the XRD patterns of ZnO:Al deposited at D_{TS} of 40 mm, 45 mm, 50 mm, 60 mm and 70 mm is shown. The data, achieved from the figure is present in Table 4.38.

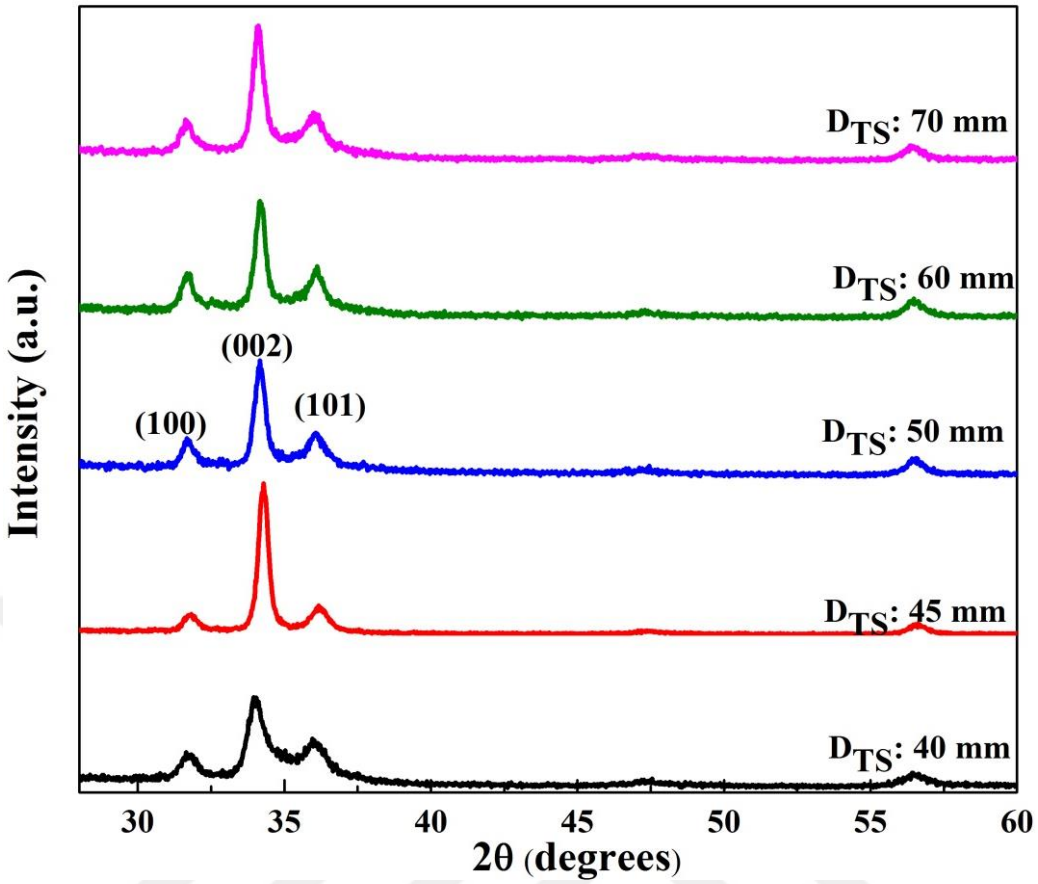

Figure 4.54 X-ray diffraction pattern of ZnO:Al thin films deposited at different D_{TS}

According to Figure 4.54, the growth of the films was c-(002) axis orientated that perpendicular to the substrate surface. Also, the occurrence of (100) and (101) peaks were clearly seen. Both the position and the relative intensity of these peaks were given in Table 4.32.

Table 4.32 The position and intensity of (002) peak, (002) peak intensity per unit thickness, position and relative intensity of (100) peak, position and relative intensity of (101) peak of ZnO:Al thin films at different D_{TS}

D_{TS} (mm)	**Position of (002) (Degree)**	**Intensity (002) (a.u.)**	**(002) Peak intensity per unit thickness (cps/nm)**	**Position of (100) (Degree)**	**100 Rel. Int. (%)**	**Position of (101) (Degree)**	**101 Rel. Int. (%)**
40	34.02	480.81	3.14	37.70	30.81	35.90	45.56
45	34.25	946.95	3.15	31.76	10.85	36.16	16.29
50	34.14	606.75	2.75	31.69	25.67	36.02	26.18
60	34.15	612.81	3.40	31.67	30.42	36.00	26.58
70	34.08	779.67	6.49	31.65	21.42	35.92	26.03

The position of (002) peaks were obtained nearly 34.10° while, the intensities showed variations with each other. At 45 mm D_{TS} value, the intensity of (002) peak reached maximum as 946.95 a.u and at 40 mm D_{TS}, it was measured minimum as 480.81 a.u. When (002) peak intensity per unit thickness values were compared, D_{TS} at 70 mm achieved the higher value as 6.49 cps/nm than D_{TS} at 45 mm, due to its low thickness. However, the relative intensities both (100) and (101) peaks for 70 mm D_{TS}, were higher than D_{TS} 45 mm.

Furthermore, the crystallite size variation of the ZnO:Al thin films at different D_{TS} values were measured with the help of Sherrer formula and the obtained results were shown in Table 4.33. When the target and the substrate was close as 40 mm and far as 70 mm the crystallite sizes, reached minimum values as 10.07 nm and 15.38 nm, respectively. However the crystallite size of the ZnO:Al thin films was calculated around 19 nm between 40 mm to 70 mm D_{TS} values. At 45 mm D_{TS}, the crystallite size value was measured as 19.60 nm with 0.41°full width at half maximum value.

Table 4.33 Full width at half maximum and crystallite size variations at different D_{TS}

D_{TS} (mm)	**FWHM (degrees)**	**Crystallite Size (nm)**
40	0.8154	10.07
45	0.4196	19.60
50	0.4499	18.27
60	0.4218	19.49
70	0.5342	15.38

4.2.2.3 Morphological properties of ZnO:Al thin films sputtered at different D_{TS}

The surface morphology of the ZnO:Al thin films was investigated using AFM (Figure 4.55). When the surface roughness of the ZnO:Al thin films compared with ZnO thin films, it is obvious that ZnO:Al thin films were more flat and the D_{TS} variation was not effected as much as ZnO thin films.

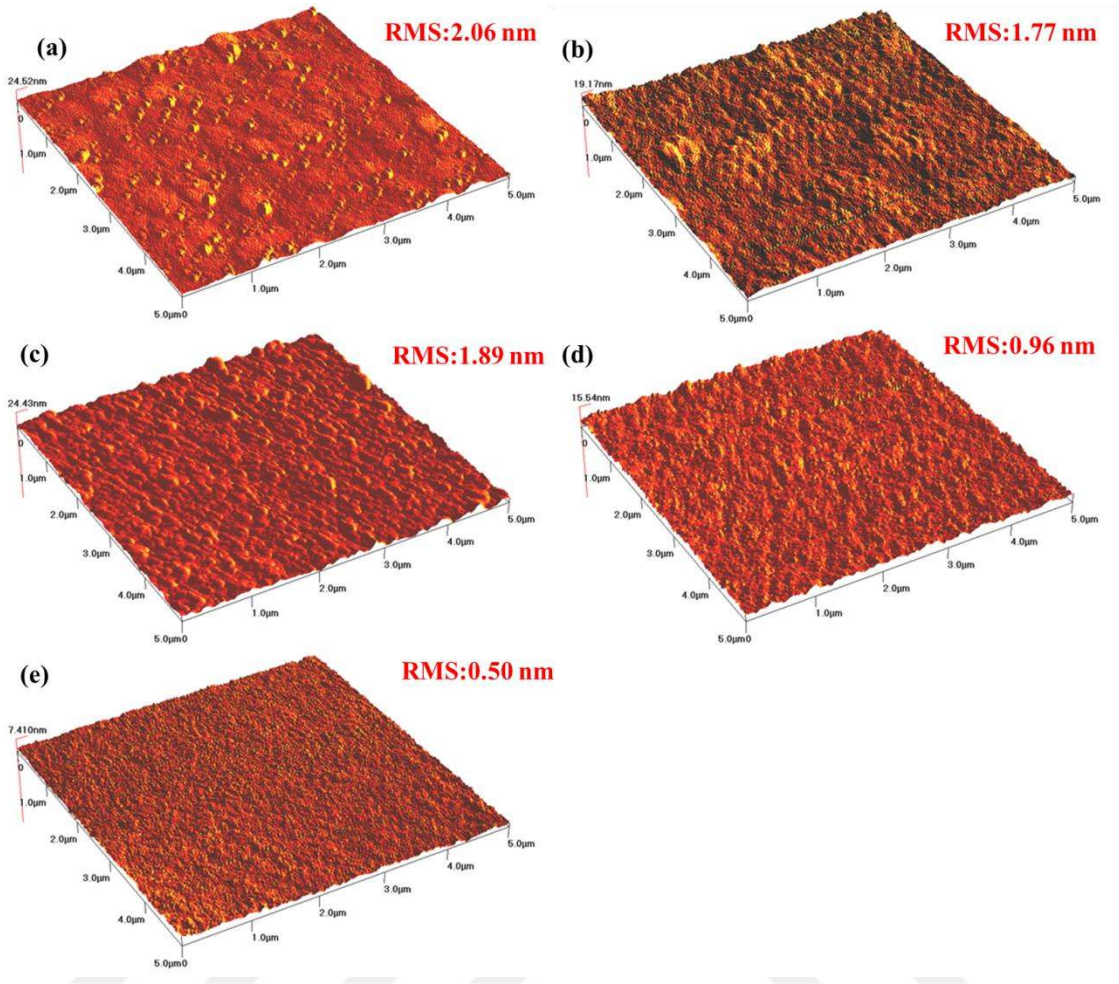

Figure 4.55 AFM images and RMS of ZnO:Al thin films deposited at different D_{TS}: (a) 40 mm, (b) 45 mm, (c) 50 mm, (d) 60 mm and (e) 70 mm

The D_{TS} values and corresponding RMS, Ra, Rq and average height variations were shown in Table 4.34. According to table, the RMS values were decreased with the increase of target-to-substrate distance. 0.50 nm was obtained as the lower roughness value at 70 mm D_{TS}, while at 40 mm D_{TS} it was 2.06 nm.

Table 4.34 D_{TS} values and corresponding RMS, Ra, Rq and average height variations

D_{TS} (mm)	**RMS (Sq) (nm)**	**Ra (nm)**	**Rq (nm)**	**Average Height (nm)**
40	2.78	2.06	2.62	7.76
45	2.17	1.77	2.25	8.94
50	2.60	1.89	2.40	6.94
60	1.36	0.96	1.21	6.33
70	0.68	0.50	0.62	3.13

4.2.2.4 Optical properties of ZnO:Al thin films sputtered at different D_{TS}

In Figure 4.56 the total transmission properties of the ZnO:Al thin films deposited at different D_{TS} values is shown. The average transmittance of all samples was obtained around 84 % in the wavelength region of 300 nm–800 nm. When the results compared with ZnO:Al thin films, the transmittance values were higher than ZnO thin films, due to the effect of Al^{+3}[136,148].

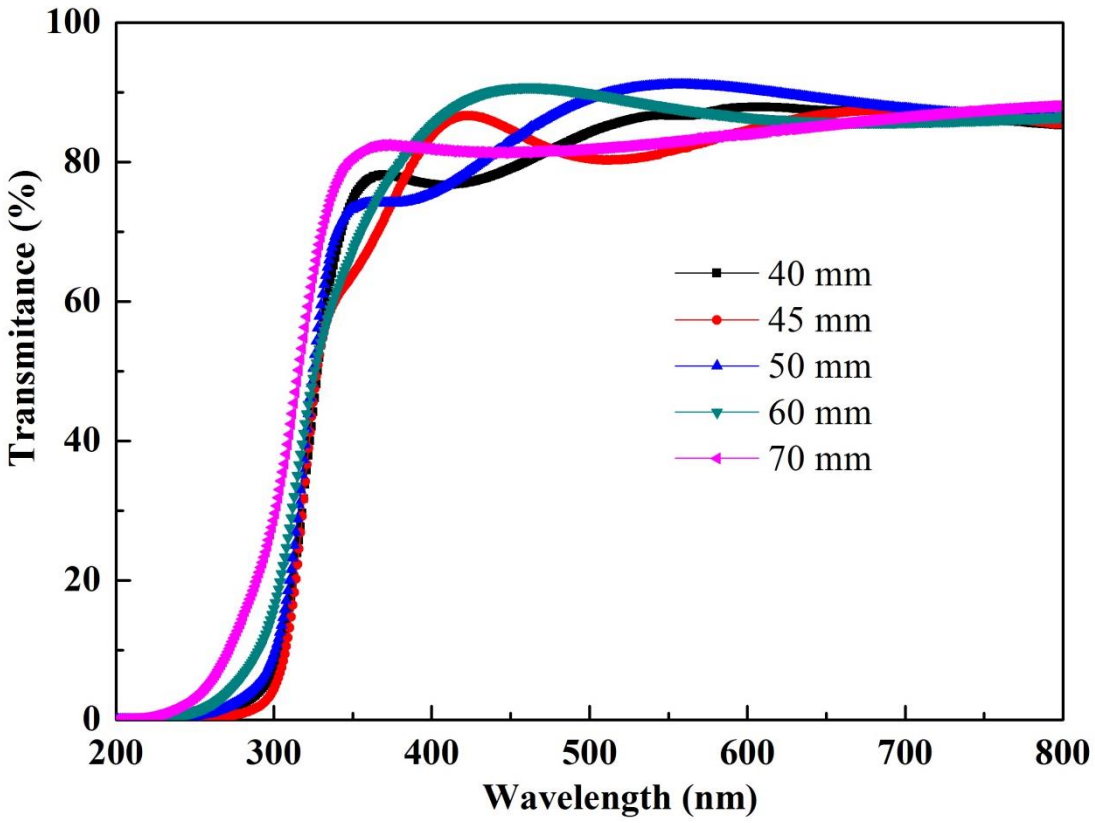

Figure 4.56 Total transmittance spectra of ZnO:Al thin films prepared at different D_{TS} values

In addition, the band gap of the films was determined using the relation $\alpha h\nu = A (h\nu - E_g)^{1/2}$, where α is the optical absorption coefficient, $h\nu$ is the photon energy, A is the edge width parameter and E_g is the optical band gap. E_g values were obtained by extrapolating the linear portion of the plots of $(\alpha h\nu)^2$ versus $h\nu$ to $\alpha = 0$ (Figure 4.57 and Figure 4. 58).

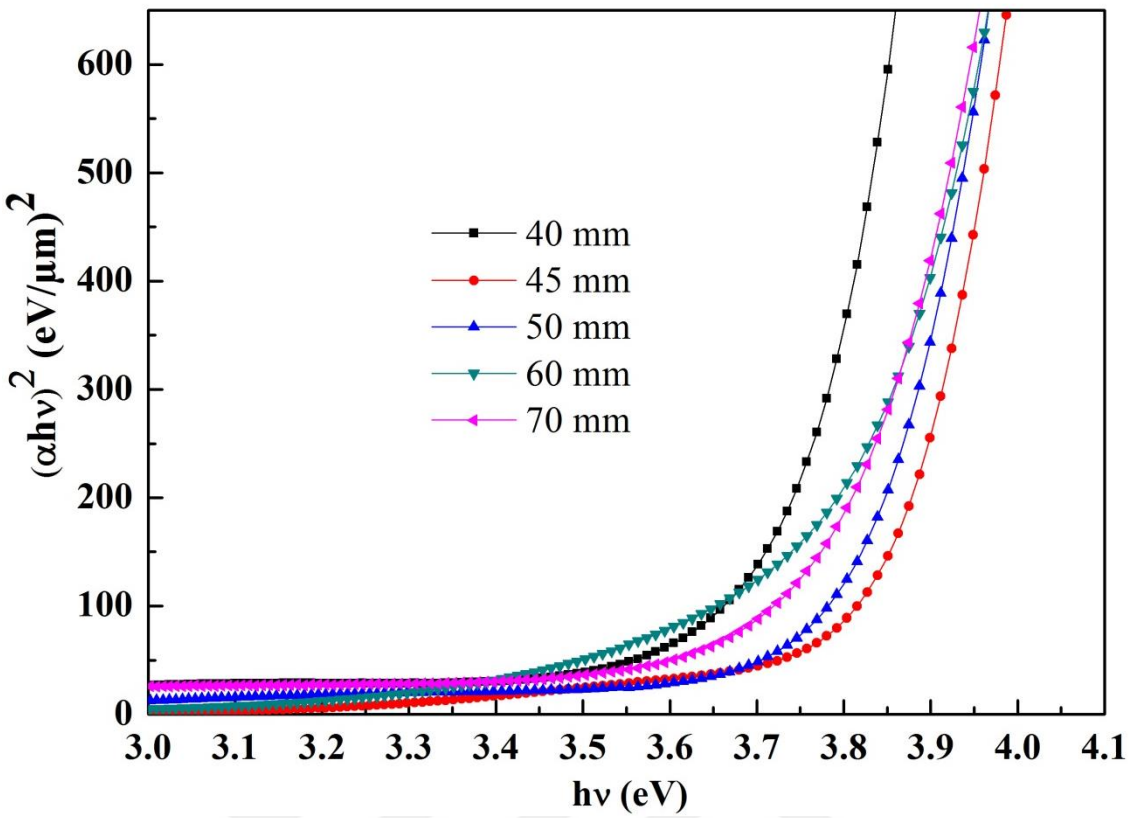

Figure 4.57 $(\alpha h\nu)^2$ versus hν graphs of ZnO:Al thin films prepared at various D_{TS} values

The energy band gap values of the ZnO:Al thin films deposited at different D_{TS} were obtained around 3.85 eV as shown in Table 4.35.

Table 4.35 D_{TS}, average transmittance and energy band gap variations

D_{TS} (mm)	**Average Transmittance (%)**	**Egap (eυ)**
40	84.93	3.85
45	84.74	3.90
50	87.23	3.85
60	87.39	3.85
70	84.28	3.85

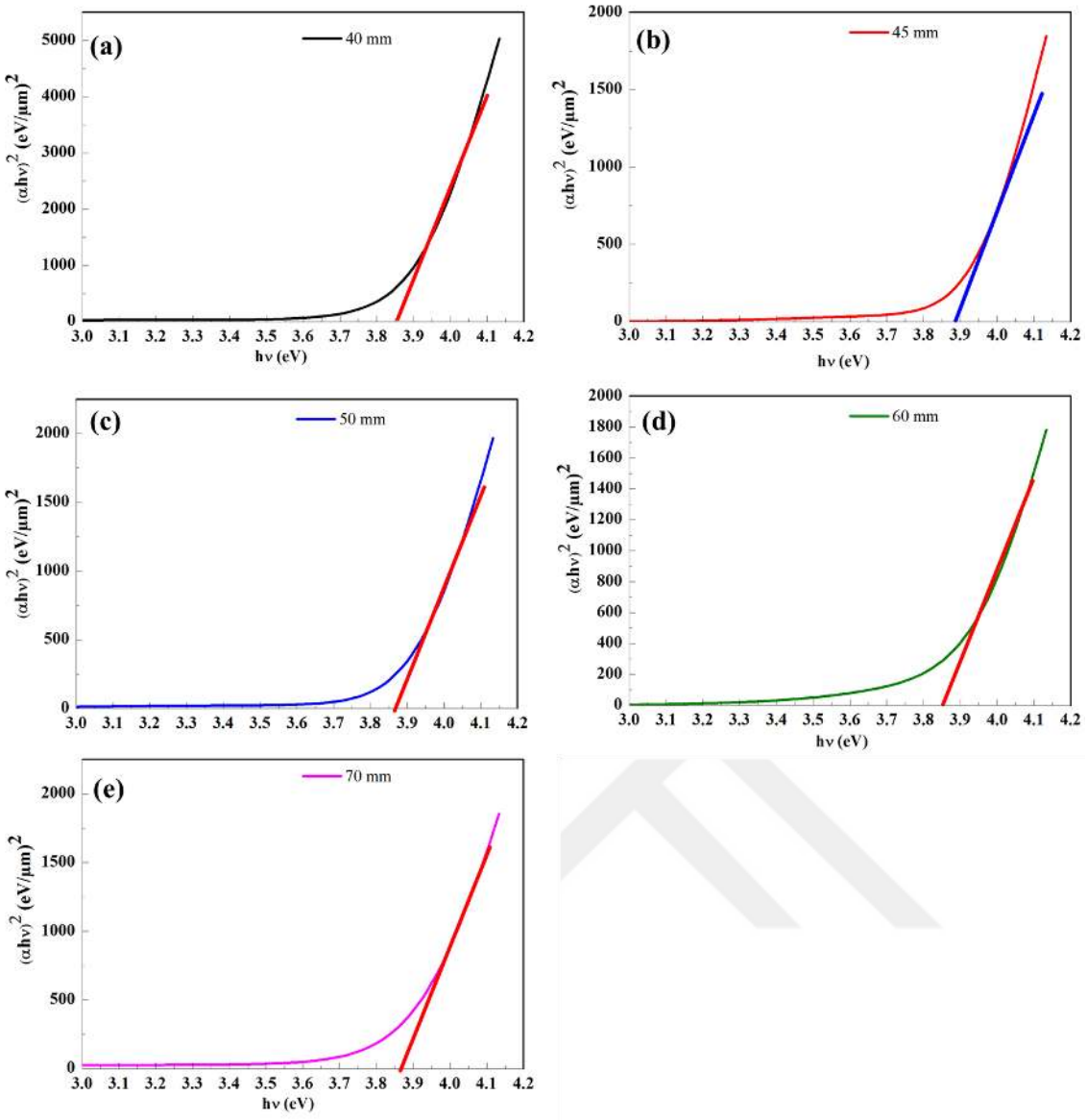

Figure 4.58 Extrapolated $(\alpha h\nu)^2$ versus $h\nu$ graphs of ZnO:Al thin films prepared at various D_{TS}

4.2.2.5 Summary of the ZnO:Al thin films sputtered at different D_{TS}

When the influnce of D_{TS} variation for ZnO:Al thin films were examined, it was obviously seen that resisitivity values were not effected as for ZnO thin films. They were obtained around 10^{-3} Ω.cm. However, the deposition rate behavior showed variations with D_{TS}. For both close and far target-to-substrate distances (40 mm and 70 mm), the thickness and the deposition rate values showed the minimum. Among these distance values, thickness of the ZnO:Al thin films increased. The reason of this variation could be explained as changes of the bombardment affect and mean path variation.

Moreover, when the influences on structural properties were compared, at all D_{TS} values (100), (002) and (101) peaks were all observed with different intensities. The highest (002) peak intensity per unit thickness value was achieved at 70 mm D_{TS} value as 6.49 cps/nm. However, the peak intensity of (002) reached the maximum at 45 mm. Also, at 45 mm D_{TS} value, the relative intensities of (100) and (101) reached the minimum. When crystallite sizes were compared at low and high distances they measured minimum as 10.07 nm and 15.38 nm, respectively. The larger crystallite was achieved at 45 mm D_{TS}.

According to roughness attitude due to D_{TS} variations,the RMS values decreased with increasing D_{TS}. At 70 mm the RMS value reached the minimum as 0.50 nm, while at 40 mm the RMS was obtained as 2.06 nm.

The optical charactesiscts of the ZnO:Al thin films did not showed big variations and they were obtained around 84%.

Furthermore, the FOM bahaviour of ZnO:Al thin films are shown in Figure 4.59 and Table 4.36. The achieved results, the FOM values decreased with icreasing the D_{TS}. At 40 mm D_{TS}, the FOM value reached the maximum as 100 $\times 10^{4}(\Omega.cm)^{-1}$ due to the higher average transmittance and lower resistivity. According to obtained results, 45 mm was selected as a D_{TS} parameter for ZnO:Al thin film deposition.

Table 4.36 D_{TS}, average transmittance and energy band gap variations of ZnO:Al thin films

D_{TS} (mm)	**Average Transmittance (%)**	**Resistivity $\times 10^{-3}$ (Ω.cm)**	**FOM $\times 10^{4}(\Omega.cm)^{-1}$**
40	94.36	0.94	100.0707
45	94.15	1.10	84.9013
50	96.92	1.49	64.6579
60	97.10	1.87	51.7590
70	93.64	1.84	50.6459

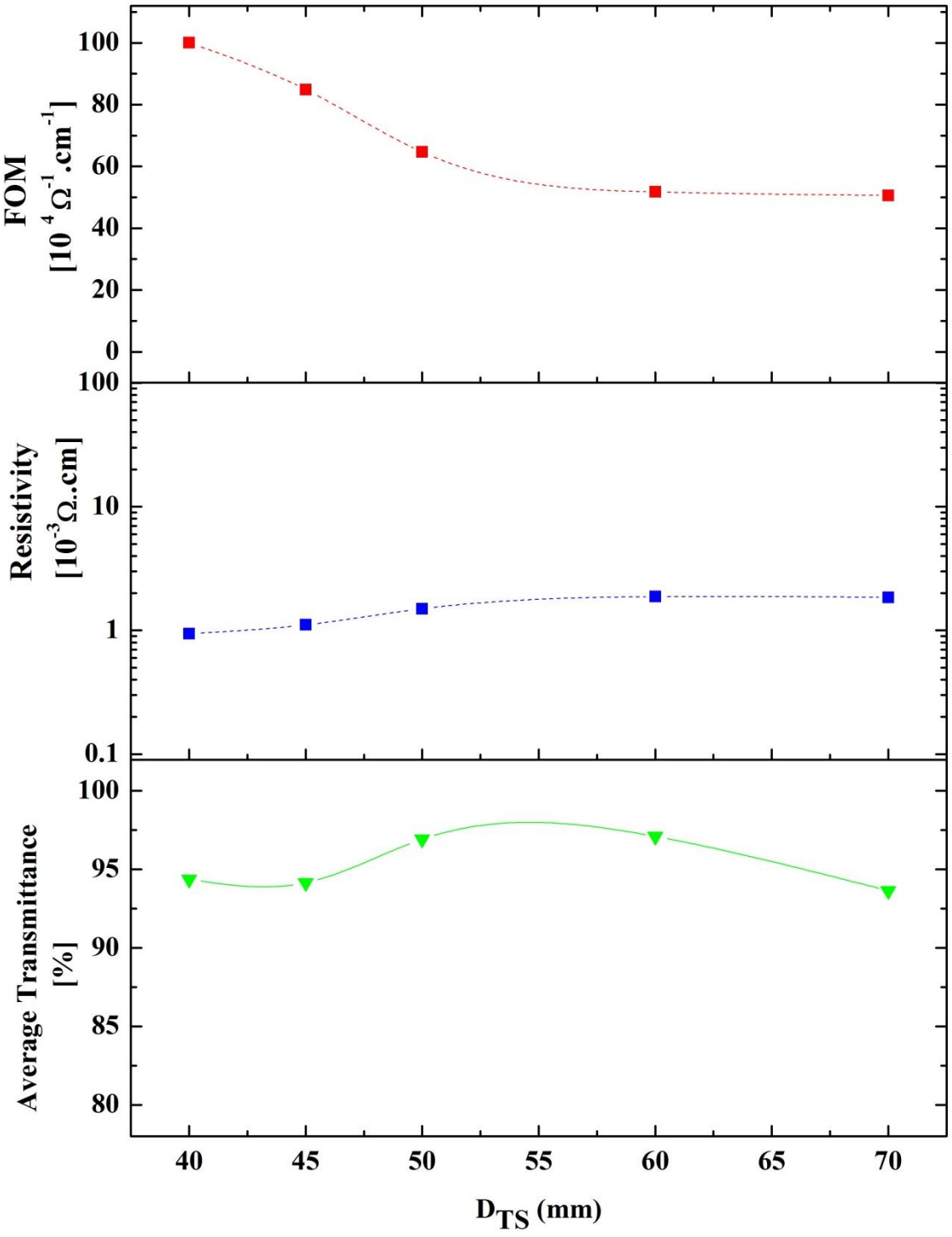

Figure 4.59 Effect of argon pressure on deposition rate, resistivity and the figure of merit of ZnO:Al thin films

4.2.3 Effect of argon gas pressure on ZnO:Al thin films

In order to understand the influence of process gas pressure variations on ZnO:Al thin film properties, the pressure was changed from 0.2 Pa to 0.60 Pa with 10 P steps. All the process was carried out non-reactively and without intentional heating. Argon was used as the process gas. The base pressure in the chamber was evacuated around 1×10^{-5} Pa using a diffusion pump. To remove any contaminants, pre-sputtering was applied for 5 minutes and deposition was carried for 30 minutes. The target-to-substrate distance was maintained as 45 mm and the r.f. power was maintained at 165 W.

4.2.3.1 Electrical properties of ZnO:Al thin films sputtered at different Ar pressures

The electrical characteristics of ZnO:Al thin films were tried to determine with the help of four point probe technique. The thickness variations were observed from the cross sectional SEM images as shown in Figure 4.60.

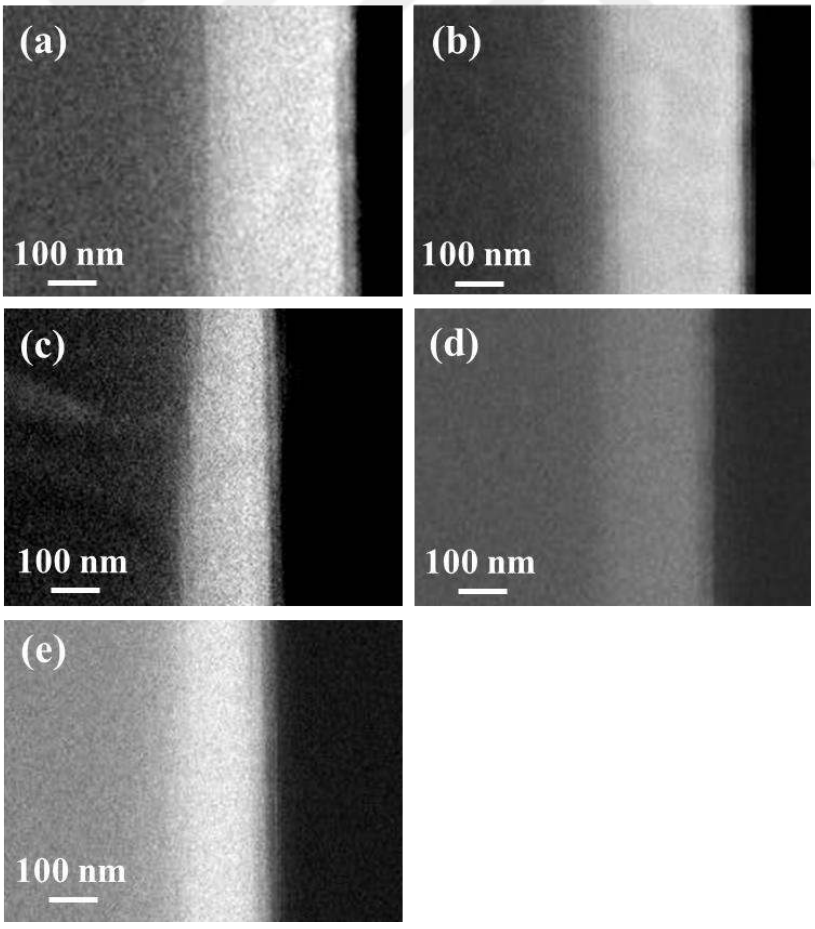

Figure 4.60 Cross sectional SEM image of the ZnO:Al thin films deposited at different process pressures: (a) 0.20 Pa, (b) 0.30 Pa, (c) 0.40 Pa, (d) 0.50 Pa and (e) 0.60 Pa

Also, in Table 4.37, both the resistivity and thickness variations with process pressure are present. According to Table 4.25, the resistivity values did not influence from the process pressure variation as much as thickness and deposition rate. All the resistivity values were obtained around 1.1 $\times 10^{-3}$ (Ω.cm). However, the deposition rate of ZnO:Al thin films showed a surging behavior. This is obviously seen in Figure 4.61.

Table 4.37 Thickness, resistivity and deposition rate variations at different argon gas pressures of ZnO:Al thin films

Ar pressure (Pa)	**Thickness (nm)**	**Resistivity $\times 10^{-3}$ (Ω.cm)**	**Deposition rate (Å/min)**
0.20	260	2.10	86
0.30	215	1.10	71
0.40	180	1.20	60
0.50	280	1.10	93
0.60	140	1.60	46

Resistivity and deposition rate variations at different argon gas pressures were given in Figure 4.60. Although the deposition rate appeared a high-low-high trend with small variations of process gas pressure, approximately it decreased with increasing the pressure.

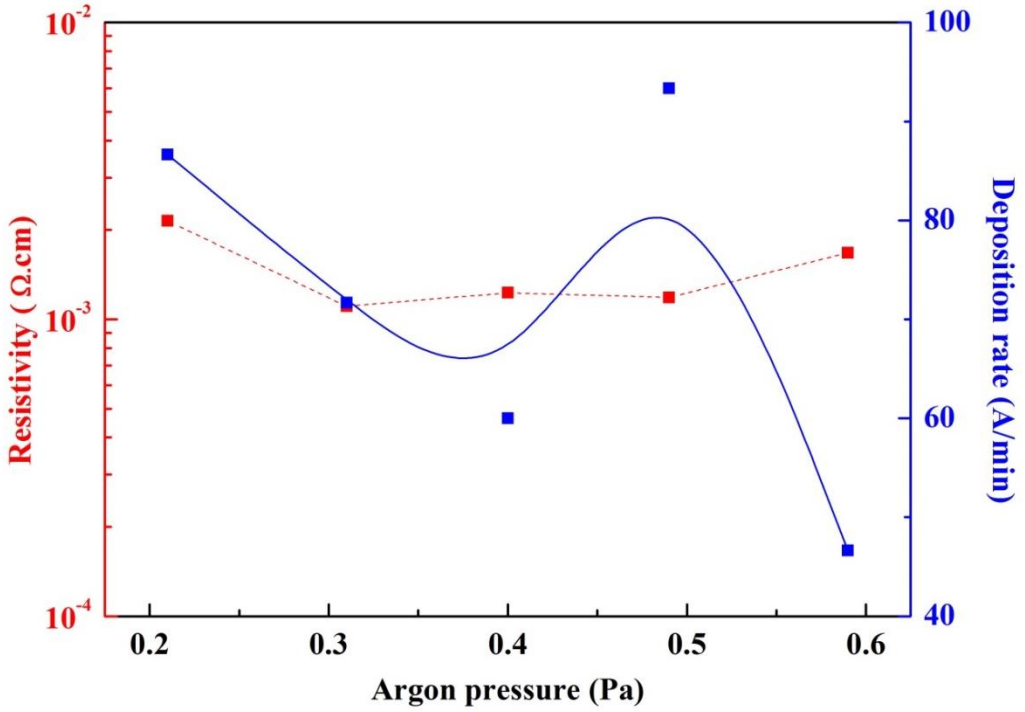

Figure 4.61 Resistivity and deposition rate variations at different argon gas pressures of ZnO:Al thin films

4.2.3.2 Structural properties of ZnO:Al thin films sputtered at different Ar pressures

In order to identify the effect of argon pressure on structural properties of ZnO:Al thin films, XRD investigations were done in the range of 0.2 Pa to 0.6 Pa. In Figure 4.62, 2θ and intensity variations of ZnO:Al thin films sputtered at different argon pressures were present.

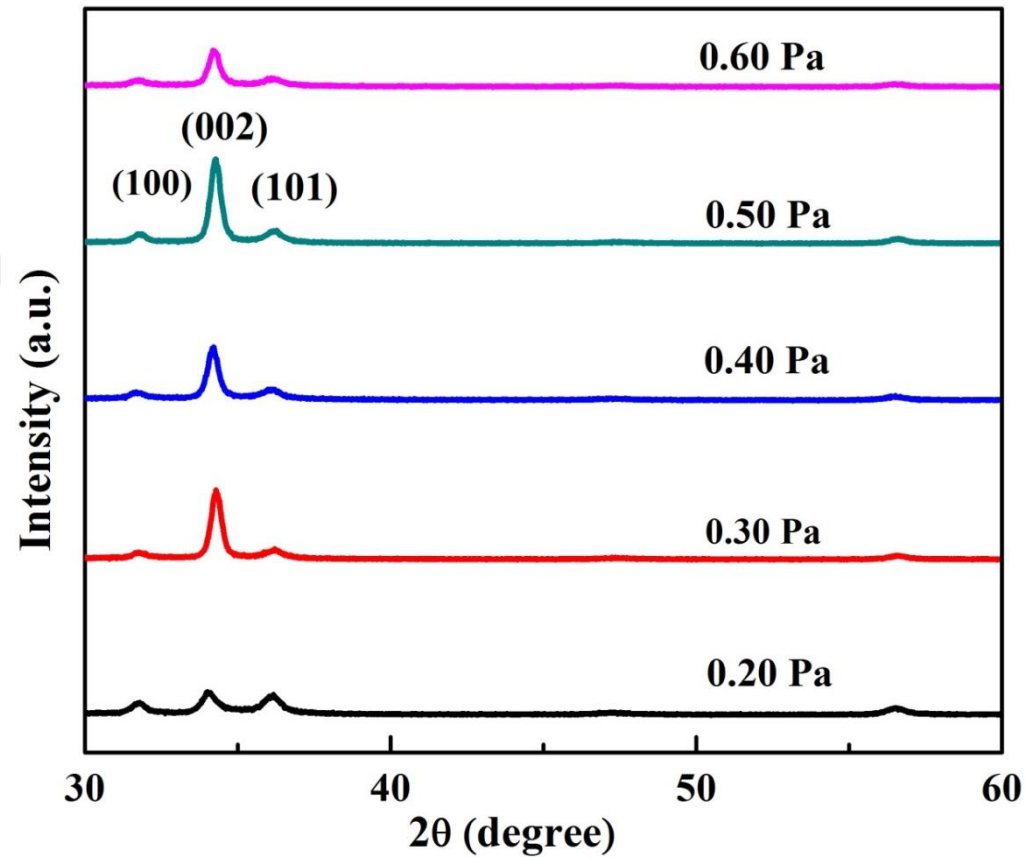

Figure 4.62 X-ray diffraction patterns of ZnO:Al thin films deposited at different argon gas pressures

According to Figure 4.61, the dominant (002) peak indicates that the films are oriented with their c-axis perpendicular to the substrate plane [104]. The position of (002) diffraction peak and intensity values present in Table 4.38 showed a decrease-increase-decrease trend. Mostly, (002) peaks were observed at around 34.20° and the highest (002) peak intensity was 2243.85 a.u. at 0.5 Pa argon gas pressure.

Moreover, in Figure 4.61 (101) and (100) peaks were observed and their positions and relative intensity values were shown in Table 4.38. The positions of (100) and (101) peaks were examined at around 31.70° and 36.16° respectively. The occurrence of these

peaks caused degradation of preferred orientation and their relative intensity values were maximum at 0.2 Pa and 0.6 Pa.

Park et al. [75] stated that the XRD peak intensity was affected from both the film thickness and spot size of X-ray. With respect to this idea, the intensity value of (002) peak was divided to the thickness and the results were presented in Table 4.38. The lowest (002) peak intensity per thickness ratio was measured at 0.2 Pa argon gas pressure as 2.27 cps/nm. However, at other gas pressures the ratios were changed between around 7 cps/nm to 8 cps/nm. At 0.3 Pa argon gas pressure the (002) peak intensity per thickness ratio reached a maximum as 8.13 cps/nm. Also, at 0.3 Pa the relative intensity values of (100) and (101) peaks ratio were lower than other gas pressures.

Table 4.38 The position and intensity of (002) peak, (002) peak intensity per unit thickness, position and relative intensity of (100) peak, position and relative intensity of (101) peak of ZnO:Al thin films at different argon pressures

Ar pressure (Pa)	**Position of (002) (Degree)**	**Intensity (002) (a.u.)**	**(002) Peak intensity per unit thickness (cps/nm)**	**Position of (100) (Degree)**	**(100) Rel. Int. (%)**	**Position of (101) (Degree)**	**(101) Rel. Int. (%)**
0.20	34.05	591.34	2.27	31.73	52.5	36.08	85.95
0.30	34.27	1750.08	8.13	31.75	7.83	36.16	11.72
0.40	34.16	1412.64	7.84	31.68	10.66	35.9	12.03
0.50	34.25	2243.85	8.01	31.76	9.64	36.16	13.29
0.60	34.20	985.39	7.03	31.71	13.36	36.12	17.97

The full width at half maximum (FWHM) values were investigated in detail (Table 4.39) and it was observed that the smallest value was obtained as 0.3571° for 0.3 Pa. Furthermore, the crystallite sizes of the ZnO:Al thin films were measured by using the Sherrer formula and they were calculated approximately 12 nm to 23 nm.

The increase in the intensity of the (002) peak and the peak narrowing; i.e. decrease in the full width at half maximum (FWHM), reveal the improvement in crystallinity of the thin films [31]. It is known that low growth rate, small crystallite size and poor crystallinity are outcomes of the high working pressure [99, 139]. At 0.2 Pa argon gas pressure, smallest crystallite size was obtained as 12 nm. On the contrary, high working pressure improves the sputtering rate, decreases the deposition energy, and small grains

were formed [99, 117]. Lower grain size was (20 nm) observed than the optimum pressure range as shown in Table 4.39.

It was proved that intensity of the (002) peaks, relative intensity values of the (100) and (101) peaks. FWHM values; therefore crystallite sizes showed distinct changes when the working pressure was varied. It is stated that, small changes of argon gas pressure was effective on structural characteristics of ZnO:Al thin films. Moreover, 0.3 Pa argon gas pressure was chosen as an optimum working pressure.

Table 4.39 FWHM and crystalline sizes of ZnO:Al thin films at different argon pressures

Ar pressure(Pa)	FWHM(Degree)	Crystallite Size(nm)
0.20	0.6733	12.20
0.30	0.3571	23.03
0.40	0.3877	21.20
0.50	0.3626	22.68
0.60	0.4148	19.82

4.2.3.3 Morphological investigation of ZnO:Al thin films sputtered at different Ar pressures

For morphological investigations, atomic force microscopy (AFM) images of ZnO:Al thin films obtained from the $5 \times 5\ \mu m^2$ surface area were shown in Figure 4.63. The root mean square (RMS) was observed as 4.96 nm, 1.08 nm, 0.99 nm, 2.69 nm and 2.43 nm from 0.2 Pa to 0.6 Pa argon gas pressures, respectively. It is clear that all of the surface roughness values are relatively low compared to the literature [27,103, 108 and 118].

The differences between the surface roughness values may seem low; however, it is worth to emphasize that when the gas pressure was increased only 0.1 Pa (from 0.4 to 0.5 Pa) the RMS increase was more than twice. According to the results, at lower gas pressures, the value of the RMS was high, while it decreased with increasing the pressure. In order to clarify the relation between the crystalline size (measured from XRD) and the RMS, Figure 4.64 and Table 4.40 were formed.

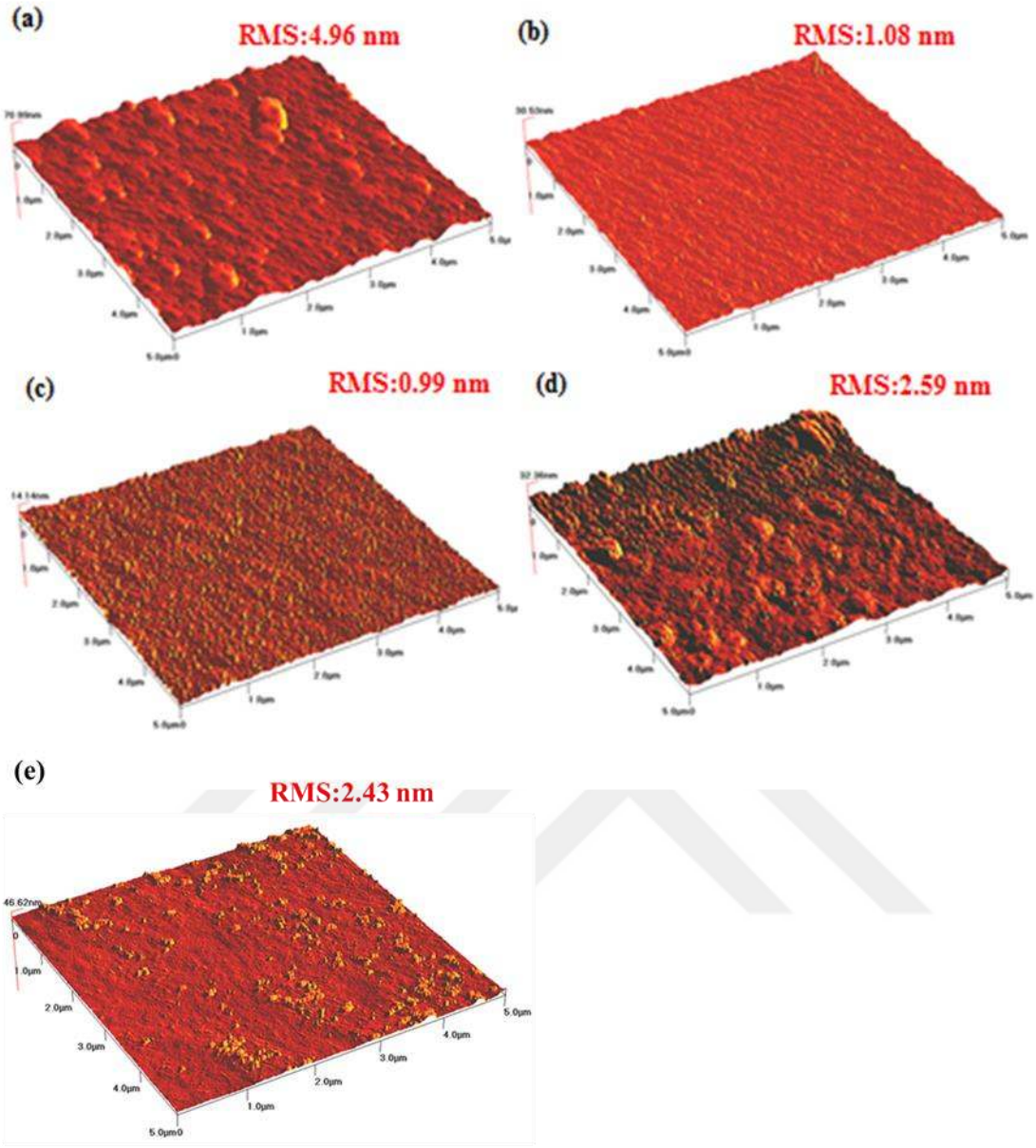

Figure 4.63 AFM images and RMS of ZnO:Al thin films deposited at different argon pressures: (a) 0.2 Pa, (b) 0.3 Pa, (c) 0.4 Pa, (d) 0.5 Pa, and (e) 0.6 Pa

According to Figure 4.63 and Table 4.41, the crystallite size values showed a decrease-increase-decrease trend, while, the RMS tendency was the opposite. At 0.2 Pa argon gas pressure, the crystallite size was minimum and the RMS value reached the maximum. However, at 0.3 Pa and 0.4 Pa the RMS values reached minimum with larger crystallite sizes.

Table 4.40 Argon gas pressure and corresponding RMS, Ra, Rq and average height variations of ZnO:Al thin films

Ar Pressure (Pa)	RMS (Sq) (nm)	Ra (nm)	Rq (nm)	Average Height (nm)
0.20	6.68	4.88	6.88	22.74
0.30	1.29	1.08	1.40	4.88
0.40	1.38	0.99	1.28	5.15
0.50	3.64	2.69	3.45	12.33
0.60	4.92	2.43	3.81	19.05

There is a direct relationship between the crystallite size and the surface roughness. Generally, as the crystallite size decreases the surface roughness increases. Therefore, surface area of the thin films increases. At the extreme test parameters (i.e. lowest and highest argon gas pressures) small crystallite size and high RMS were observed [26, 118]. At 0.2 Pa and 0.6 Pa. which were the lowest and the highest gas pressures for this study respectively, the low crystallite size and biggest surface roughness were seen due to the decrease in the carrier concentration and the mobility (Figure 4.64).

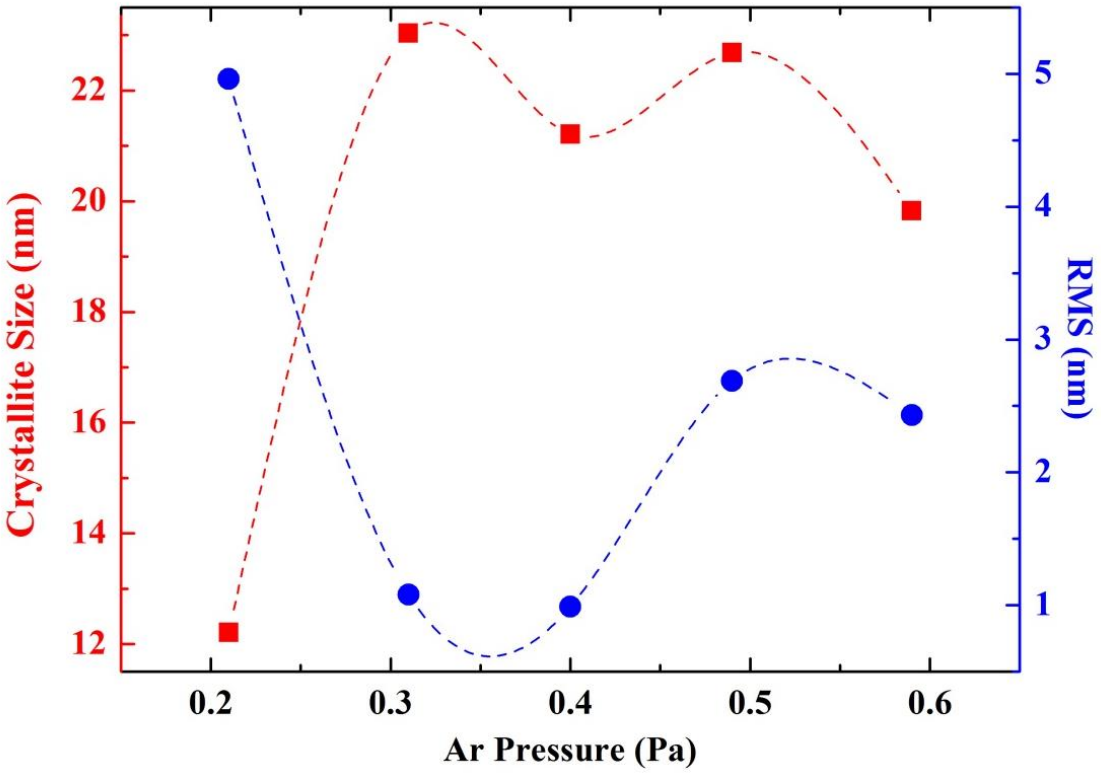

Figure 4.64 Crystallite size and RMS variations of ZnO:Al thin films at different argon pressures

4.2.3.4 Optical investigation of ZnO:Al thin films sputtered at different Ar pressures

Figure 4.65 shows the transmittance-wavelength range of 200 nm to 800 nm ZnO:Al thin films deposited at different argon gas pressures. The transmittance of all samples during the visible range was over 82%. The average transmittance of the ZnO:Al films were measured as; 84.70%, 86.34%, 86.93%, 83.82%, and 82.69% for the sputtered pressure from 0.2 to 0.6 Pa, respectively. As the deposition pressure increased, the average transmittance of the films reduced. Argon gas pressure, average transmittance and energy band gap variations were given in Table 4.29.

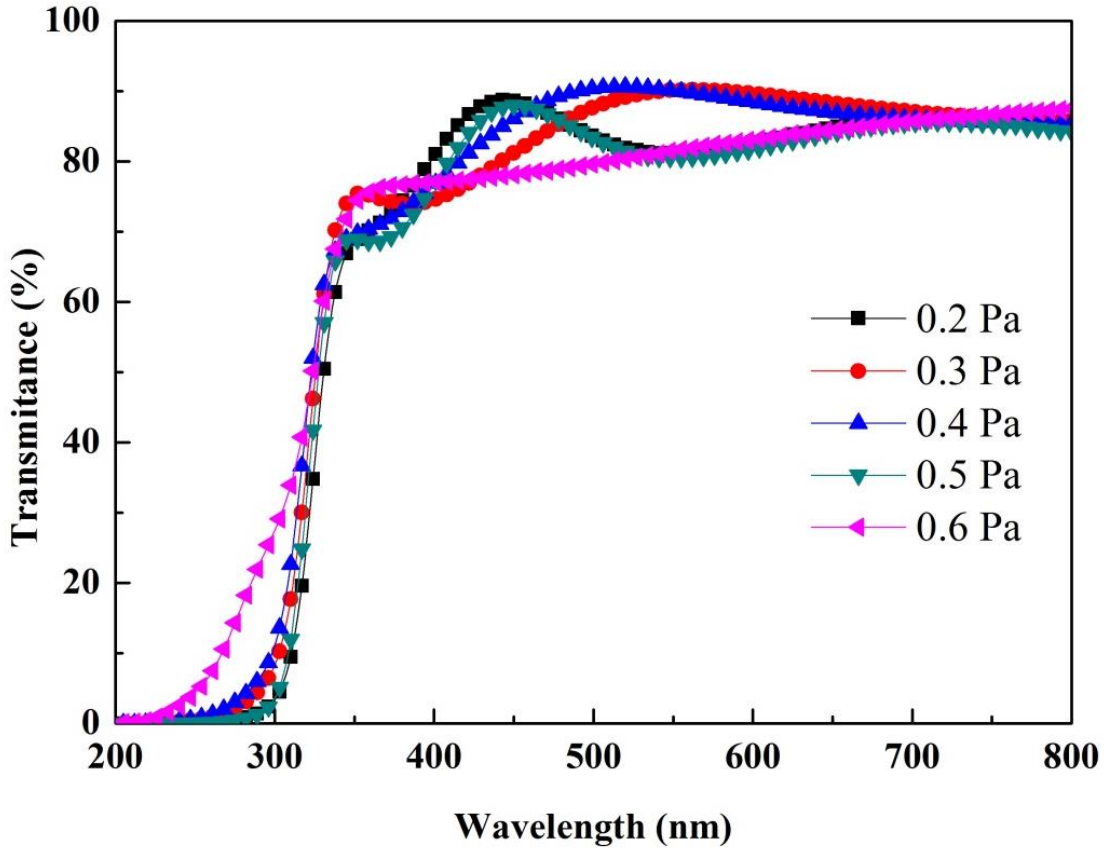

Figure 4.65 Total transmittance spectra of ZnO:Al thin films prepared at various argon pressures

The band gaps of the ZnO:Al thin films were determined with $(\alpha h\nu)^2$ versus hν graph (Figure 4.66) by extrapolating the linear portion the plots (Table 4.41 and Figure 4.67). According to the observed data, the band gap of the ZnO:Al thin films were around 3.8 eV.

Table 4.41 Argon gas pressure, average transmittance and energy band gap variations of ZnO:Al thin films

Ar Pressure (Pa)	Average Transmittance (%)	Egap (eυ)
0.20	84.70	3.85
0.30	86.34	3.85
0.40	86.93	3.85
0.50	83.82	3.87
0.60	82.69	3.75

Generally, the transmittances of the thin films were concerned with their crystallinity, stoichiometric ratio, surface roughness, and their defects [80,114]. According to Zhu et al. [60], a high crystallinity, low defect density, and low surface roughness should enhance the transmittance of the films. The observed results revealed that, when the argon gas pressure increased, the transmittance of the film decreased. The reason of this transmittance reduction could be explained as the decrease of crystallinity and increase of the surface roughness.

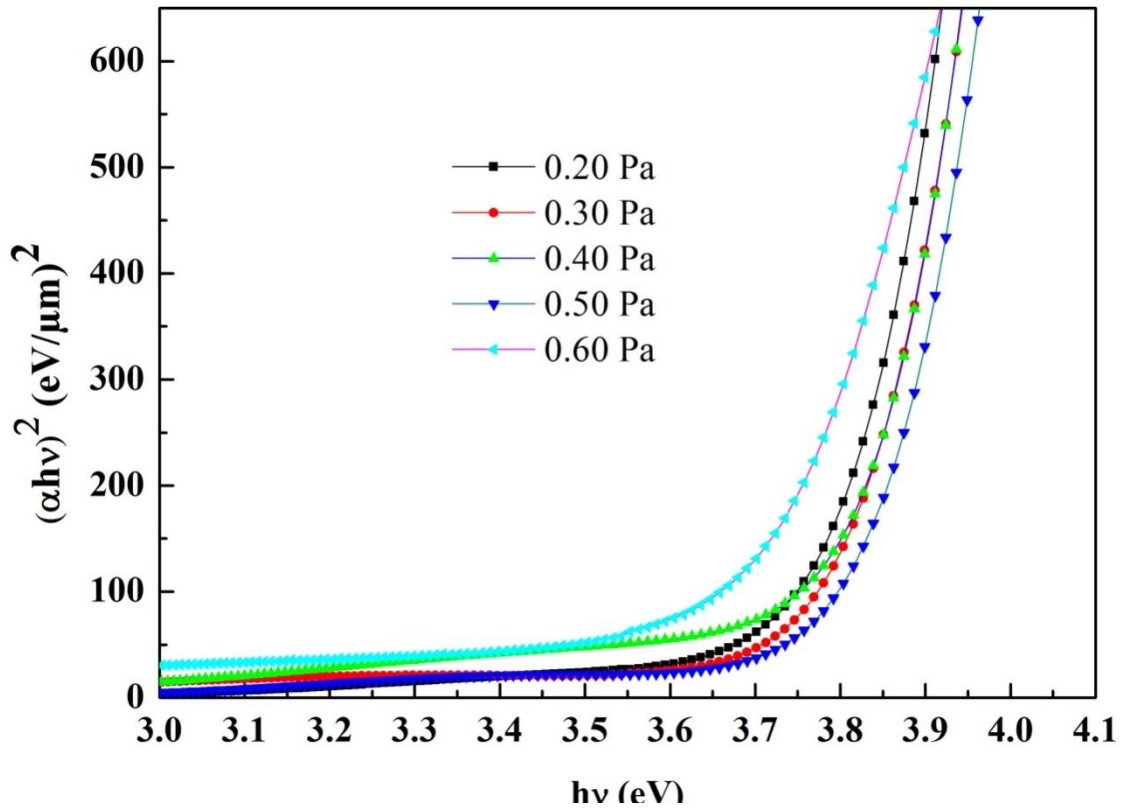

Figure 4.66 $(\alpha h\nu)^2$ versus hν graphs of ZnO:Al thin films prepared at various argon pressures

Furthermore, the optical band gaps (Eg) of the ZnO:Al thin films was estimated by extrapolating linear portions of $(\alpha h\nu)^2$ against photon energy (hν), for sputter gas

pressure variations. The obtained Eg values were around 3.65 eV and they were all larger than that of un-doped bulk ZnO (Eg ~3.3 eV) [79].

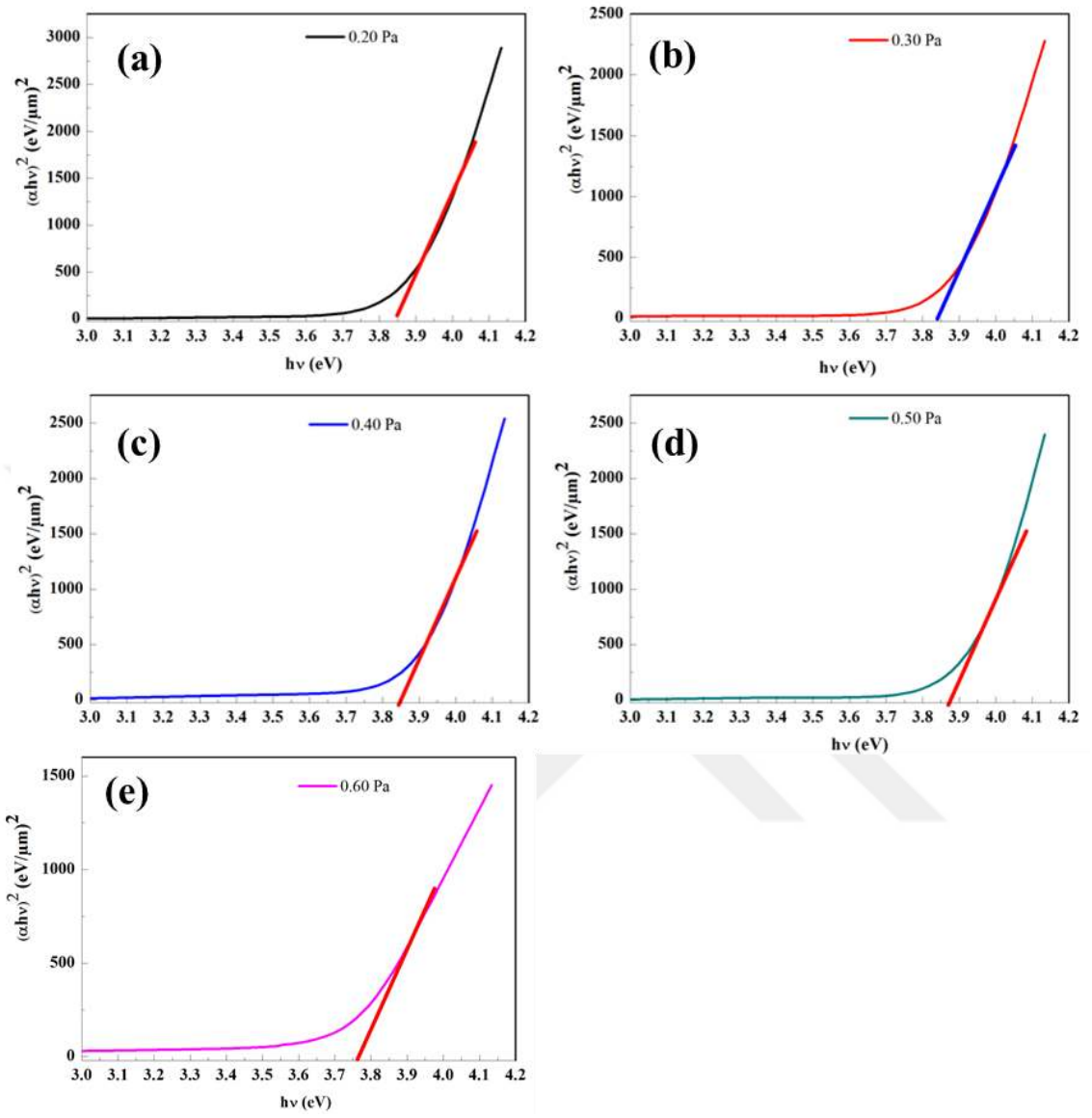

Figure 4.67 Extrapolated $(\alpha h\nu)^2$ versus hν graphs of ZnO:Al thin films prepared at various argon pressures

4.2.3.5 Summary of the Ar pressure variation influence on ZnO:Al thin film properties

According to Table 4.42 and Figure 4.68, all the ZnO:Al thin films deposited at room temperature have low resistivity values around 10^{-3} Ω.cm and high average transmittance above 80 %.

At 0.2 Pa argon pressure the deposition rate value was 86.6 Å/min and FOM value was lowest as 448148 $(\Omega.cm)^{-1}$(Figure 4.68). The reason of this decrease in FOM value

could be explained as, at minimum gas pressure, the amount of sputtered species declines due to fewer collisions between the gas and the sputtered species [60]. However, at 0.3 Pa argon pressure the FOM value reached a maximum as 872121 $(\Omega.cm)^{-1}$, while the deposition rate was 71.6 Å/min (Table 4.30). Although, the deposition rate values were different, the FOM values obtained at 0.4 and 0.5 Pa values were similar. When the argon gas pressure reached 0.6 Pa. both the FOM and the deposition rate values reached minimum. According to Bai et al. [99], at higher working gas pressures, the growth rate became lower due to the improvement of sputtering rate decreased the energy of sputtered particles. The achieved results shown in Figure 4.68 confirm that small variation of gas pressure affects both the resistivity and growth rate.

Table 4.42 Argon pressure, average transmittance and energy band gap variations of ZnO:Al thin films

Argon Pressure (Pa)	**Average Transmittance (%)**	**Resistivity $\times 10^{-3}$ (Ω.cm)**	**FOM $\times 10^{4}(\Omega.cm)^{-1}$**
0.20	94.11	2.10	44.8148
0.30	95.93	1.10	87.2121
0.40	96.58	1.20	80.4907
0.50	93.13	1.10	84.6666
0.60	91.87	1.60	57.4236

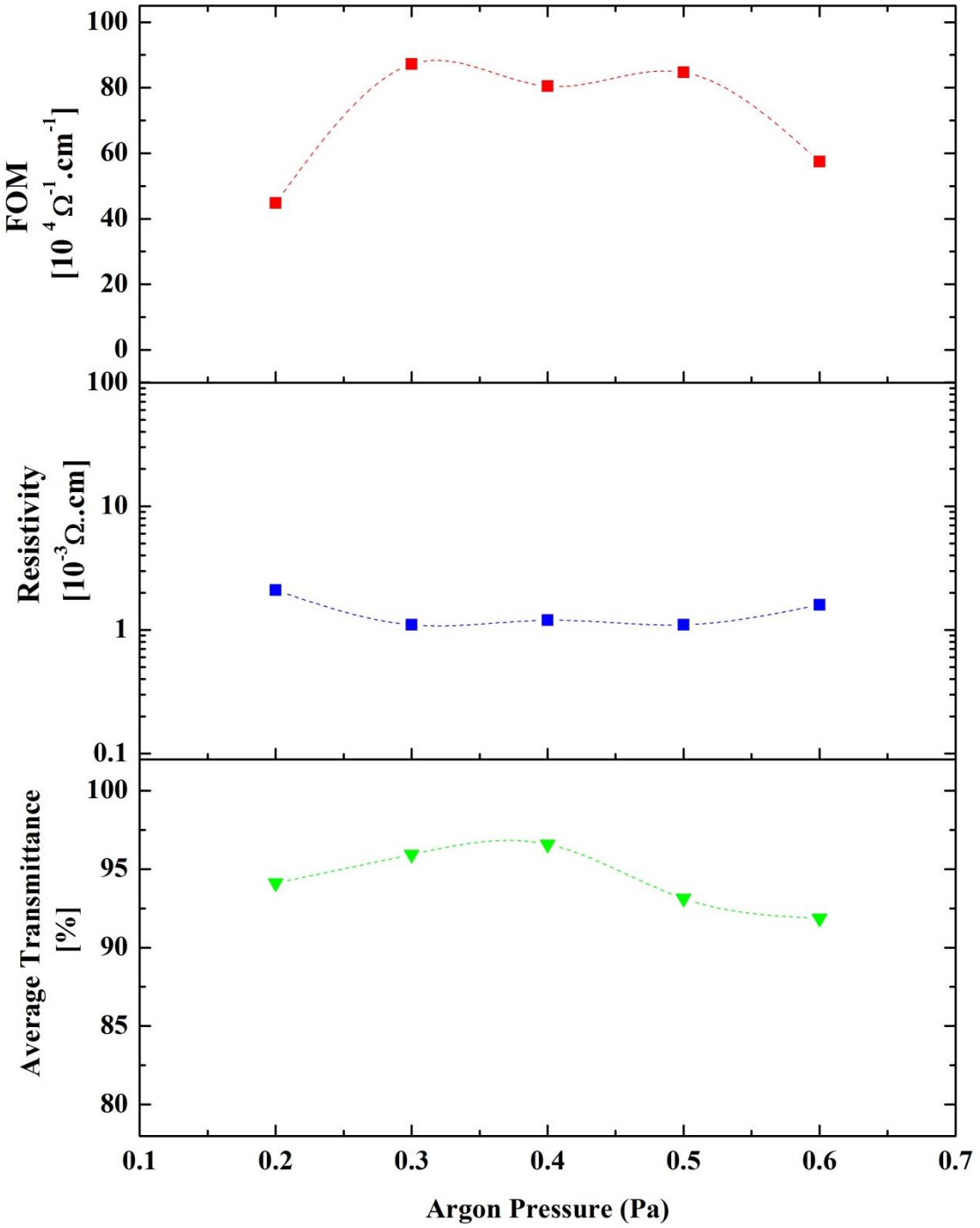

Figure 4.68 Effect of argon pressure on deposition rate, resistivity and the figure of merit of ZnO:Al thin films

4.2.4 TEM-HRTEM investigations of ZnO:Al thin films

In the view of this part of the study, we focused on understanding the grain growth mechanism of ZnO:Al thin films deeper with the help of TEM and HRTEM techniques. Plan view TEM and HRTEM investigations were done for the samples sputtered on (100) Si substrate for 165 W r.f. power and 0.3 Pa. In the Figure 4.69, bright field (BF)

and dark field (DF) TEM pictures and corresponding selected area electron diffraction (SAED) pattern were shown. Less than 100 nm sized grains were clearly observed. SAED pattern also revealed spotty rings which was a result of nano sized morphology. Plan view texture was also confirmed by SAED pattern.

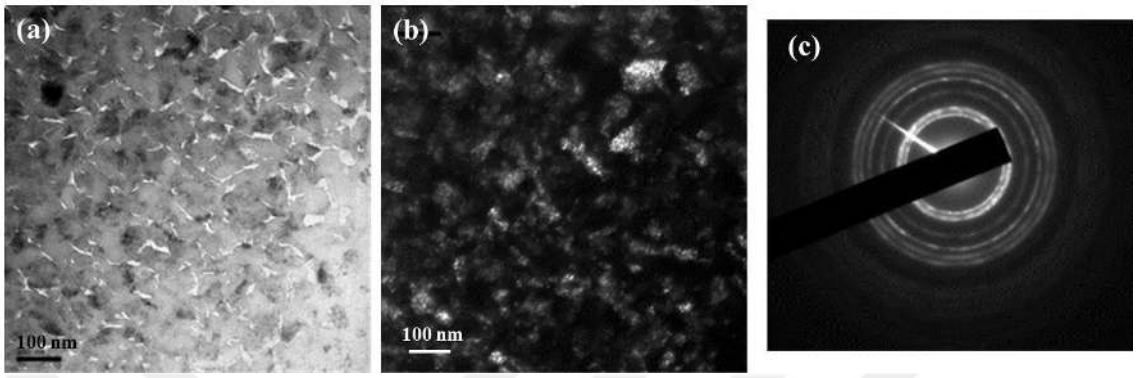

Figure 4.69 (a) Bright field (BF) (b) dark field (DF) TEM pictures and (c) selected area electron diffraction (SAED) pattern of ZnO:Al thin film sputtered on (100) Si substrate for 165 W r.f. power and 0.3 Pa

Semi-quantitative TEM-EDS analysis was also performed on plan view ZnO:Al TEM samples. In Figure 4.70, EDS result revealed close to ZnO 1:1 atomic ratio.

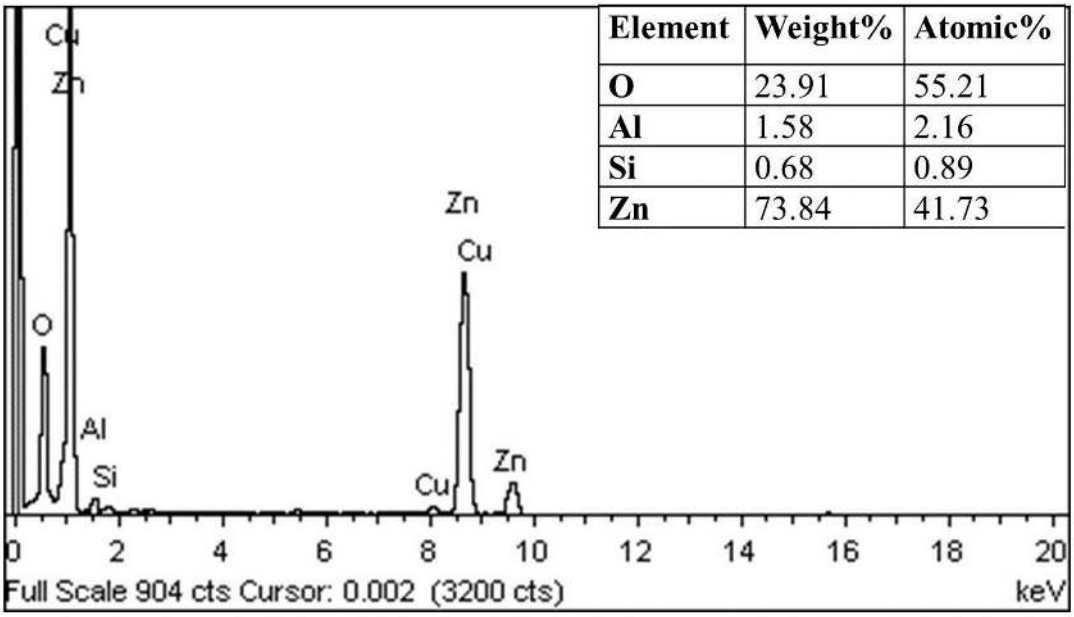

Element	Weight%	Atomic%
O	23.91	55.21
Al	1.58	2.16
Si	0.68	0.89
Zn	73.84	41.73

Figure 4.70 TEM-EDS spectrum and elemental composition of plan view ZnO:Al TEM sample (Si element is from the substrate and Cu element is from the TEM holder)

Moreover, Al content was measured close to 2 wt.%. From elemental mapping, homogenous distributions of aluminum, in addition to other elements (Zn. O) were observed (Figure 4.71).

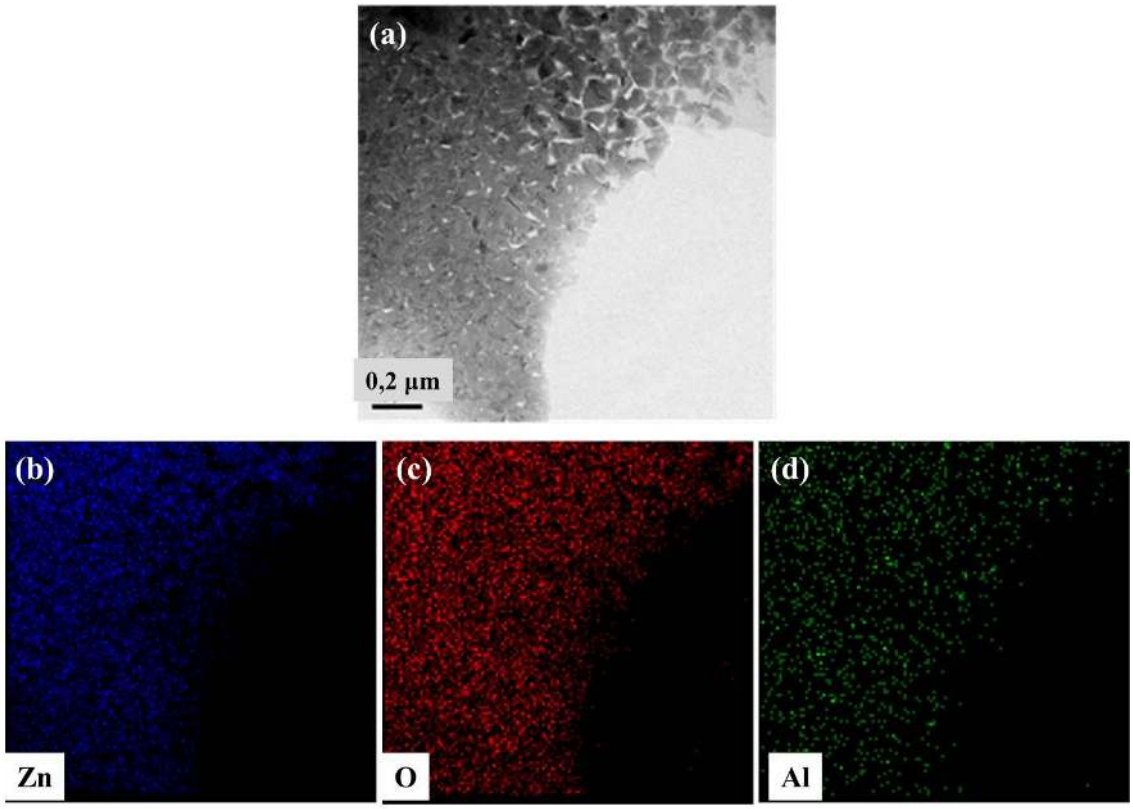

Figure 4.71 (a) Bright field TEM image and corresponding TEM-EDS map of: (b) O. (c) Zn and (d) Al elements for plan view ZnO:Al TEM sample

Achieving atomic lattice imaging was possible on some regions. An example HRTEM picture of plan view ZnO:Al TEM sample is shown in Figure 4.72. A d-spacing of 2.8 Å was measured which corresponds to (100) plane of ZnO. Since (100) plane is perpendicular to the (002) plane for ZnO, this plan view HRTEM image proves (002) texture.

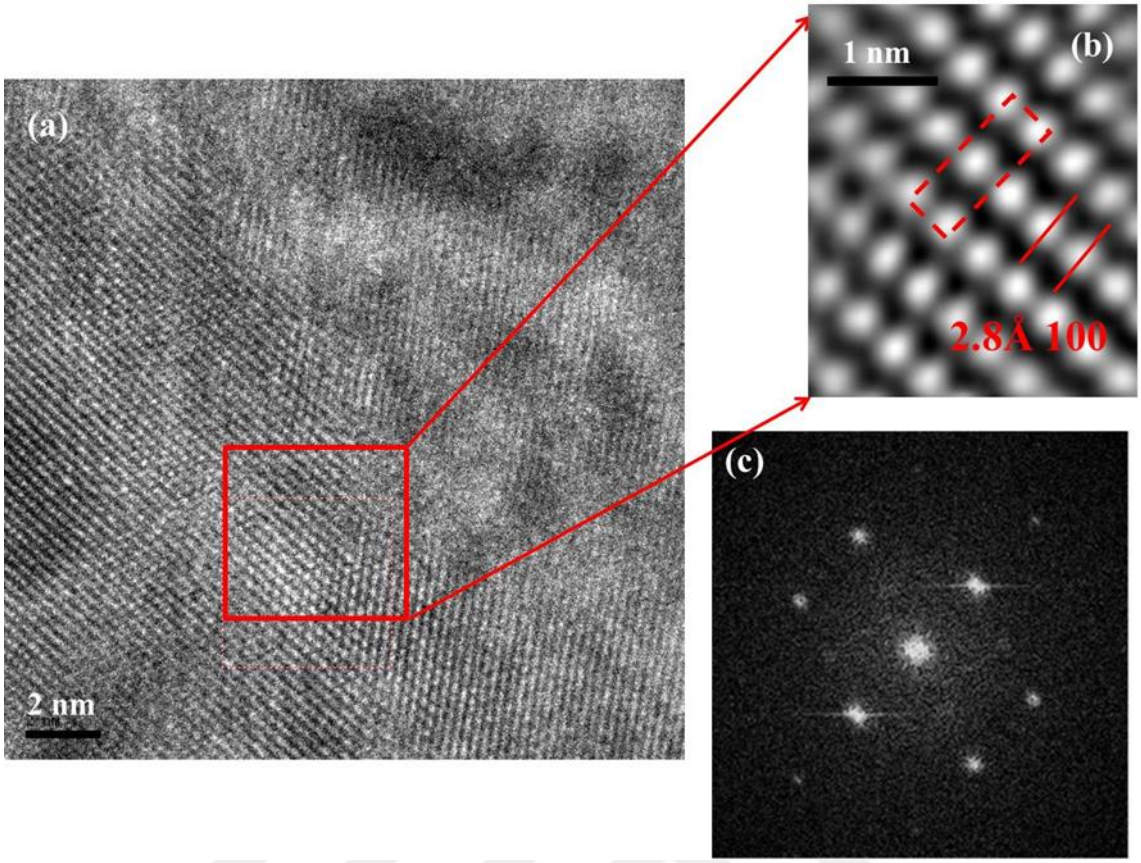

Figure 4.72 (a) Plan-view HRTEM picture, (b) enlarged and filtered view showing indexed atomic lattice and (c) Fast Fourier Transformation (FFT) diffractogram on [021] zone axis of ZnO

TEM technique was also used to investigate the cross sectional morphology and structures of ZnO:Al thin films deposited at 165 W r.f. power and 0.3 Pa on glass substrate.

In Figure 4.73, edge of a cross sectional TEM picture and HRTEM image were shown with the SAED pattern. HRTEM investigations revealed nanostructures inside the columnar grains. Grains were grown perpendicular to the glass substrate since mainly (002) orientation was observed. Some nano-island structures were seen with different orientations. In Figure 4.73 (b) HRTEM image of nano-island structure inside a columnar grain was shown. Also, the orientation changes between the planes were calculated as ±10° with the help of SAED pattern as in Figure 4.73 (c).

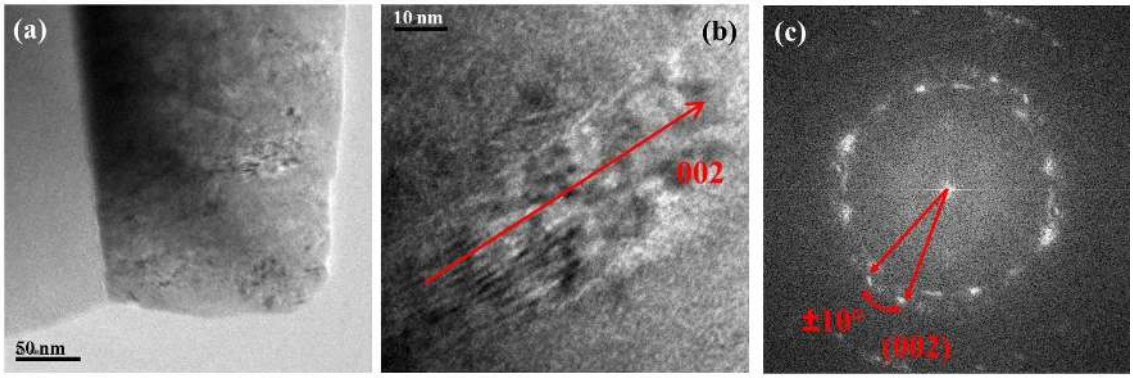

Figure 4.73 (a) Cross-sectional TEM and (b) HRTEM picture, and (c) SAED pattern of (a) for ZnO:Al thin films deposited at 165 W r.f. power and 0.3 Pa on glass substrate

4.3 Structural Zone Behavior of ZnO:Al Thin Films

The Thornton structure zone model was developed to understand the relation between the substrate temperature and the sputter pressure. According to the model, the ratio of substrate temperature T_S and melting temperature T_m and argon pressure are the critical parameters for metal sputtering. However, application of this model to TCO materials is not easy as metals especially for ZnO:Al thin films since the ratio of Ts/Tm becomes very small due to the high melting point value of ZnO (1975 °C). Therefore, Kluth et al. developed a new model named as modified Thornton. According to their model, the substrate temperature was taken into account instead of Ts/Tm ratio [39]. Also, their observations showed that the substrate temperature played a less important role than the sputter pressure for ZnO:Al thin films.

When the results of this thesis were tried to be analyzed in structure zone perspective, it was hard to apply to any of models straightforwardly. Firstly, the depositions were done without heating, and during sputtering, temperature variation was not accounted. Moreover, our observations revealed that other sputtering parameters such as sputtering power, target- substrate position have to be considered. Also, in most of the model, the variation ranges were high and our results proved that higher examination ranges were not sufficient.

Despite all of these differences, when Thornton model is modified to the observed results, Ts was selected as constant. The argon gas pressure variation revealed that with the increase of pressure, the morphological behavior was obtained as Zone T as shown in Figure 4.74. In this zone the structure is dense, the surface is smooth and grains are small and similar. Also, when the crystallite size variations of ZnO:Al thin films were

considered, in all deposition parameter variations, size showed a decrease-increase-decrease trend.

However, at 165 W r.f. power, 45 mm D_{TS} and 0.30 Pa the morphology behaved as Zone 2. In this zone, the crystal growth is controlled by surface diffusion. Also, denser layers with small columnar grains from top to bottom were observed.

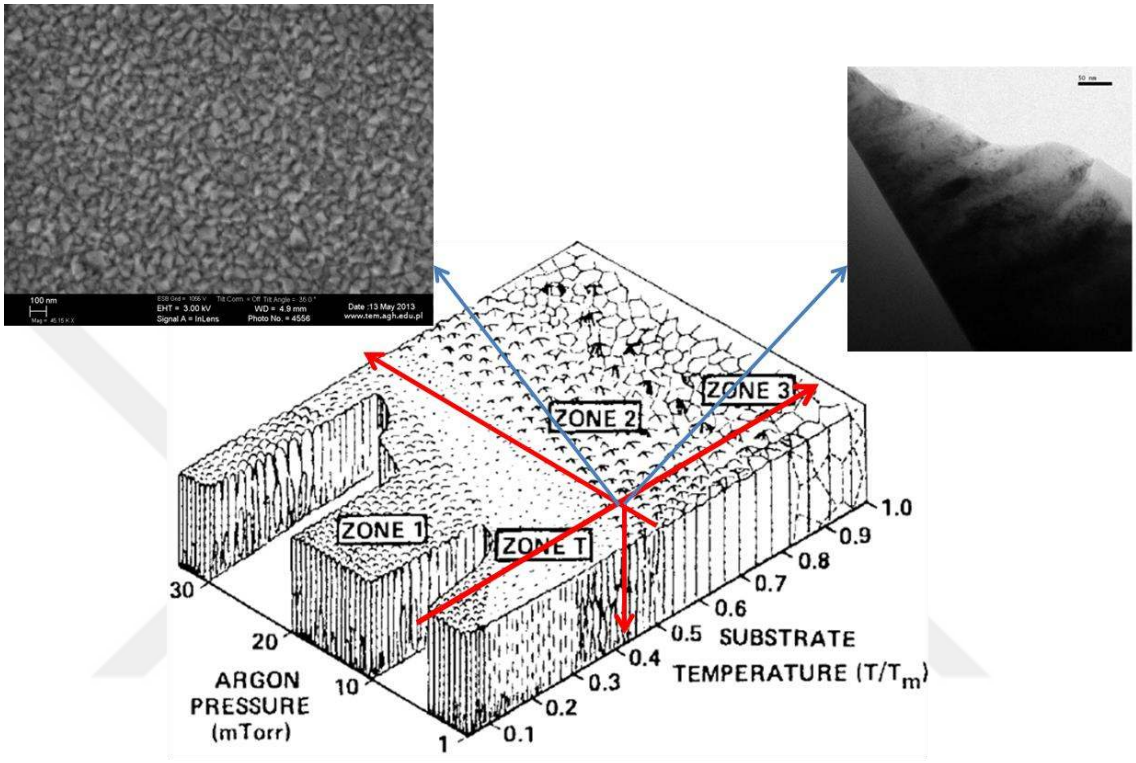

Figure 4.74 The modified Thornton model for ZnO:Al thin films

4.4 Application of ZnO:Al Thin Film to a-Si/c-Si:H Solar Cells

a-Si/c-Si:H solar cell was deposited on <100> oriented, p-type, 100mm diameter crystalline silicon wafer by using PECVD system. For intrinsic layer; RF power density; 12 mW/cm^2, temperature; 225 °C, pressure; 0.6 Torr and SiH_4 flow; 40 sccm were used as deposition parameters. n-doped layer was achieved by adding 20 sccm in the gas mixture.

ZnO:Al was used as a TCO material and deposited by r.f. sputtering system. The deposition conditions were; 165 W r.f. power, 0.30 Pa argon gas flow and 45 mm D_{TS}. The achieved structure is shown in Figure 4.75.

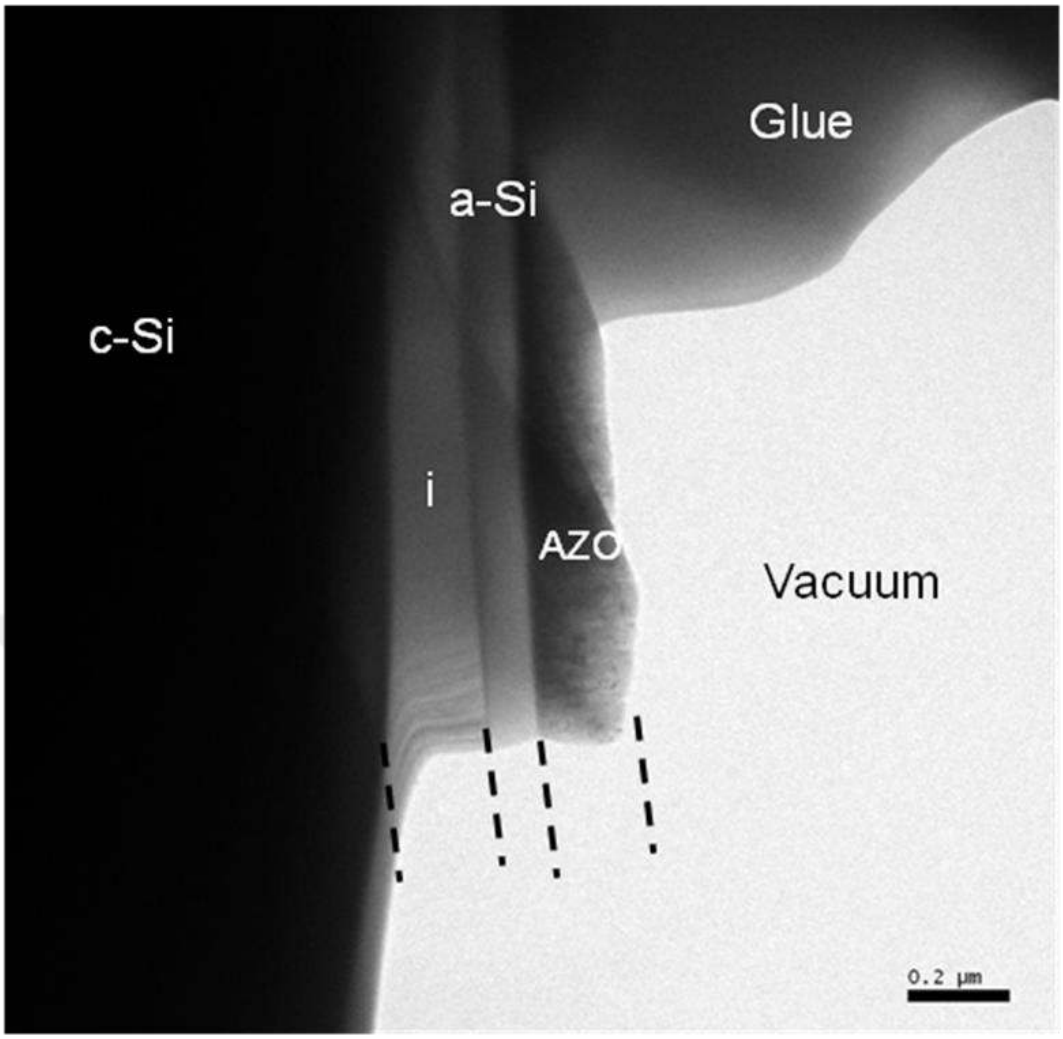

Figure 4.75 HRTEM picture of ZnO:Al, a-Si:H/c-Si structure.

According to the Figure 4.66, the thickness of (i) a-Si:H was measured around 192 nm, while the (n) a-Si was ~89 nm. Moreover, for ZnO:Al the thickness was 200 nm.

In order to identify the efficiency of the solar cell I-V measurements were applied and the achieved graph is represented in Figure 4.76.

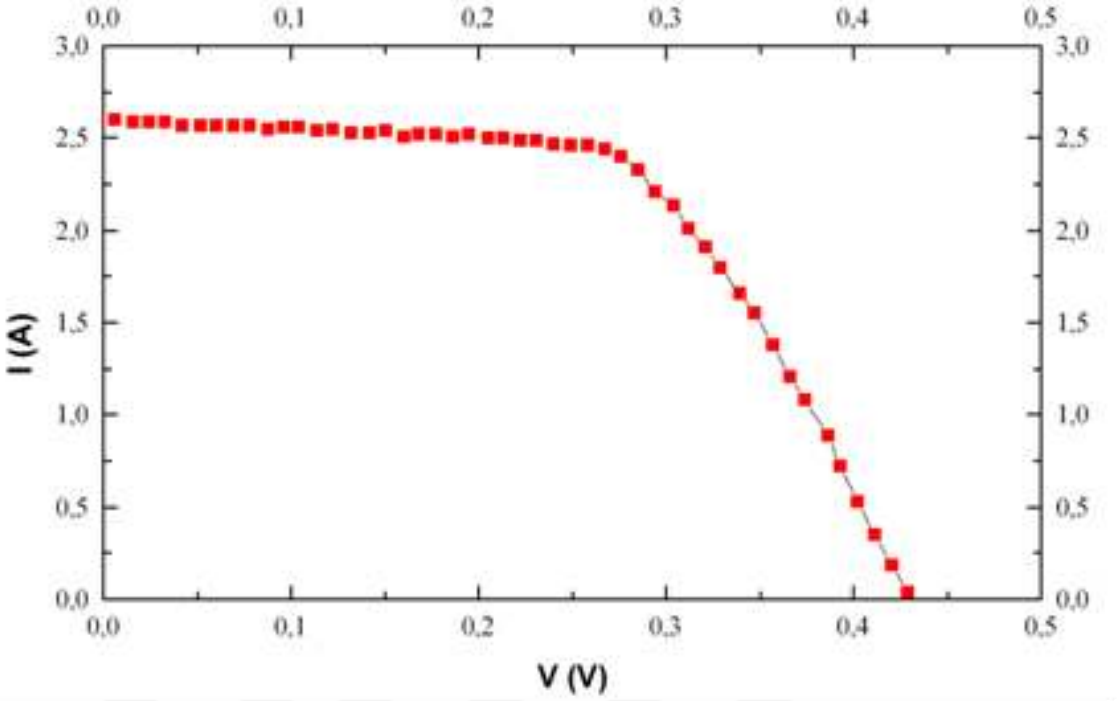

Figure 4.76 I-V curve of the solar cell after the optimization studies under AM 1.5G solar simulator light

After the calculation of the area under I/V curve, the solar cell efficiency was measured as 9.2% at the active area of 72 cm^2 under AM1.5G conditions.

CHAPTER 5

CONCLUSIONS and FUTURE STUDIES

The contribution of the thesis is to obtain new generation TCO materials as ZnO and ZnO:Al, for PV applications. In order to achieve this aim r.f. magnetron sputtering technique was used and the properties of thin films were analyzed in detail.

In sputtering, physical and morphological properties of the thin films are strongly correlated with parameters such as substrate temperature, process pressure, sputtering power and target-to-substrate distance. These parameters combine both the deposition rate and energy of sputtered particles, which control the stoichiometric composition, structural, electrical and optical properties of the film. To achieve a high quality thin film using sputtering technique, factors such the deposition rate, surface roughness, and crystallite size were carefully considered.

Therefore, in the present study, the effect of r.f. power target-to-substrate distance and argon gas pressure, on the deposition of both ZnO and ZnO:Al thin films were investigated. The range of applied parameters kept small. All the depositions were done at room temperature.

The summary of achieved results are divided into two sections for ZnO and ZnO:Al thin films.

The r.f. power was changed in the range of 145 W to 175 W with small variations with steps of 5 W for ZnO thin films and it was observed that:

- The minimum resistivity was measured as 0.9×10^{-4} Ω.cm at 165 W.
- The deposition rates were between 10 and 14.7 nm/min. The thickness values of the films were between around 300 nm to 400 nm.

- The XRD spectra showed (101) and (100) peaks, which cause degradation of preferred orientation for especially high r.f. powers. The crystallite sizes of the ZnO thin films were measured as 15-23 nm.
- The compactness of the grains improved with the increase of the r.f. power. Before the r.f. power reached a value of 160 W, the grains were circular in shape, and above that power, triangular grain structure occurrence happened.
- RMS values varied between 5.9 nm to 13.9 nm. The smallest RMS and largest grain size was achieved for 165 W r.f. power
- The optical transmittance was about 80 % for all r.f. power variations. The band gap of the ZnO thin films were around 3.40 eV. The value of 3.45 eV was measured only at 165 W r.f. power condition.
- FOM was the maximum as 971600 $(\Omega.cm)^{-1}$ for 165 W r.f. power.

The D_{TS} was varied from 35 mm to 65 mm in 5 mm steps at 165 W r.f. power and:

- As D_{TS} was increased towards 45 mm, the resistivity values of ZnO films decreased from 3×10^{-3} Ω.cm to 9×10^{-4} Ω.cm. ZnO thin films with a resistivity as low as 9×10^{-4} Ω.cm were deposited at a rate of 7.7 nm/min by changing D_{TS} .
- The most preferred c-axis orientation was observed for a D_{TS} value of 45 mm.
- It was observed that the films deposited at 45 mm and 50 mm showed denser and more uniform structures. The RMS changed 23 nm to as low as 4.6 nm.
- The average transmittance was 68-89%.The biggest band gap value was measured as 3.45 eV for the film sputtered at a D_{TS} of 45 mm. For 45 mm condition FOM was 103×10^{4} $(\Omega.cm)^{-1}$.

When the argon gas pressure was changed from 0.15 to 0.60 Pa, in 0.05-0.1 Pa steps, while the r.f. power was 165 W and D_{TS} was 45 mm for ZnO thin films,

- Thickness of the films changed from 210 nm up to 400 nm for a deposition rate of 7-13.3 nm/min. The deposition rate decreased with the increase of argon pressure.
- Crystallite sizes were measured with Scherrer method and, 23 nm at 0.15 Pa was achieved as the biggest size. The values changed in between 18.1 to 23 nm.

- The surface morphology with different argon gas pressures were investigated with the help of HRSEM and AFM. It was observed that, the compactness of the films improved with the increase of argon pressure. The surface roughness values were high for small argon pressures as 11.22 nm and 9.55 nm at 0.15 Pa and 0.20 Pa, respectively. At 0.40 Pa the RMS value reached the minimum as 2.12 nm.
- It was found that the average transmittance was decreased with the increase of argon pressure. For 0.15 Pa, the transmittance value reached the maximum as 88.50%. The biggest electrical band gap value was 3.45 eV which was for 0.30 Pa.
- The maximum FOM value was obtained as 795019 $(\Omega.cm)^{-1}$ for 0.30 Pa.

The effect of deposition time investigations was done for ZnO thin films in order to determine the optimum deposition time and enlarge the application area. Therefore deposition times were varied from 10 min to 30 min at 0.30 Pa process pressure, 45 mm D_{TS} and 165 W r.f. power value.

- The thickness of the ZnO thin films reduced from 300 nm to 70 nm, while the resistivity was measured around 10^{-3} (Ω.cm).
- The RMS values were obtained as about 4 nm for both 30 and 10 minutes. However, for 20 and 15 minutes, the RMS values were measured around 2 nm.
- The average transmittance variations support that the ZnO thin films were highly transparent around 80%.
- According to FOM results, at 30 min deposition time the high value was obtained as 795071$(\Omega.cm)^{-1}$. However at 15 min, the FOM value was obtained as 660409$(\Omega.cm)^{-1}$.

As a summary for ZnO thin film investigations:

➢ The deposition rate, film thickness, resistivity, crystallinity, roughness and optical parameters of the film deposited at 165 W r.f. power, a D_{TS} of 45 mm and 0.30 Pa sputter pressure showed optimal values. With these parameters, the ZnO films were deposited with a growth rate of 7.7 nm/min and had a resistivity as low as 9×10^{-4} Ω.cm, an optical transmission of 80 %, an RMS surface roughness of 4.9 nm and an optical band gap value of 3.45 eV.

- According to XRD, HRSEM and HRTEM characterizations the thin films were polycrystalline with a hexagonal structure and a preferred (002) orientation with the c-axis perpendicular to the substrate.
- It was found that even the r.f. power variation range was small as 150 W to 175 W, the influence on the characteristics of the ZnO film was high.
- The columnar structure occurrence of the ZnO thin film was observed with TEM at lower magnifications and also with HRSEM. Moreover, the planar spacing was measured as 2.6 A° which is a d-spacing of (002) ZnO. The angles between the planes were calculated as ±15° with the help of FFT diffractogram. Similarly, the orientation differences of the nano-islands were in that range.
- The RMS behavior from AFM, showed an interesting trend that can be helpful in thin film PV applications.
- The optical investigations exhibited that the films had higher transparencies above 80 % with the band gap of 3.40 eV in visible range.
- The resistivities were achieved as around 10^{-3} Ω.cm. The highest FOM value was measured at 165 W as 97.16 $\times 10^{4}$ $(\Omega.cm)^{-1}$ and provided that under this deposition conditions the ZnO thin films could be used as a TCO material.

Moreover, the influence of argon gas pressure and r.f. power on the structural, electrical and optical properties of ZnO:Al thin films deposited on glass and silicon substrates at room temperature were also studied.

Both argon gas pressure and r.f. power effects were examined in small variation steps ranged from 0.2 Pa to 0.6 Pa and 100 W to 200 W, respectively. The conclusions of the ZnO:Al investigations are:

- The achieved results showed that the influences of small variation on the characteristics of the ZnO:Al thin films were high. The resistivity values were around 10^{-3} Ω.cm for all the ZnO:Al thin films.
- According to the XRD analyses results, the film structures were c-axis oriented. The crystallite sizes were varied from 14 nm to 23 nm from Scherrer method.
- The RMS, from AFM, changed from 4.96 nm to 0.59 nm.

- The optical investigations exhibited that the films had higher transparencies above 85 % with the band gap of 3.70 eV in visible range.
- At optimum deposition parameters: 0.3 Pa argon gas pressure and 165 W r.f. power; the figure of merit value was measured as 780300$(\Omega.cm)^{-1}$, deposition rate was 71.6 (Å/min) and the average transmittance reached 86.34%.
- In addition, with TEM and HRTEM examinations, it was seen that the grains were grown perpendicular to the substrate and (002) orientation was observed. Also, nano-island structures were seen with slightly different orientations. The angle changes between the (002) planes were calculated as ±10° with the help of SAED pattern. Additionally, semi-quantitative TEM-EDS analysis was performed on plan view ZnO:Al TEM samples, and homogenous distribution of elements was observed.

When the obtained results transferred to Thornton model, the argon pressure influence on structural behavior was better understood (by selecting the Ts/Tm variation constant). Therefore, the argon pressure variation of ZnO:Al thin films revealed that the thin films were placed in Zone T structure in which dense and smooth surfaces were observed. Also, in this zone, the grains are small as it was examined in the deposited ZnO:Al thin films. Moreover, the films deposited at 165 W r.f. power, 45 mm D_{TS} and 0.30 Pa showed Zone 2 behavior, due to its columnar grain growth from top to bottom.

According to the achieved results, the reason of the variations on electrical, structural, optical and the morphological properties of both the ZnO and the ZnO:Al thin films with sputter parameter variations could be summarized as;

- When the r.f power is increased, the amount and mean free path of the amount of sputtered species were developed and the collisions decreased. The reaction rate increased by causing various surface damages with poor crystalline quality. Therefore, the sputtering power must be sufficiently low to have an efficient nucleation and growth.
- When target-to-substrate distance is increased, the mean free path of the sputtered species increased, too. The deposition rate of thin films increased, while the collision decreased.
- The mobility of the atoms adsorbed at the surface is affected by temperature variations. The sputter power may have caused a heat up on the substrate which affects the surface mobility of adatoms. Also, a cool surface reduces the adatom

mobility and tends to result in the formation of crystallites with porous and rough surfaces. However, high substrate temperature may cause re-evaporation and decreases the deposition rate of the film, which increases the quality of the films.

- The lower working pressure conditions may have increased both the r.f. power and D_{TS} effects.
- At room temperature conditions, the ions sputtered from the target can not achieve an optimum bonding between substrate atoms and film atoms due to the inadequate heating energy. Also, the difficulties of forming and growing of sputtered ion nucleation may occur. Furthermore, the bad adherence to the substrate causes high resistivity due to a strong contribution of the grain boundaries in charge scattering.
- High energy sputtered ion bombardments could cause a surface damage.
- The reason of small crystallite size could be explained as the surface diffusion energy may be limited by the adatom mobility.
- The rough and poor crystalline film occurrence might be due to the rate of surface damage being larger than the rate of repair.
- The sputtering species play a critical role to determine the adatom mobility for crystallite growth. When the r.f. power increases, both the species energy and the mobility increase. This improvement of adatom mobility for crystallite growth exhibits the behavior of the crystallinity.

In addition to the coating studies, ZnO:Al was applied as TCO layer in a-Si: H/c-Si heterojunction solar cells. The solar cell devices were tested with the current-voltage measurements and the electroluminescense measurements.

The small variations of deposition parameters showed that ZnO:Al thin films application cannot be limited only a-Si/c-Si:H solar cell. They can be transferred into various PV applications such as amorphous/micromorphous silicon, CdTe, CIGS and also plastic electronics such as organic lighting, organic photovoltaics etc.

As a future study, other doping agents such as Mg or In can be tried for r.f. magnetron sputtering. Moreover, layer-by-layer coating or hybrid coating can be tried. Nanoparticle, nanorod or nanoparticle addition to the coating may be another alternative to improve the physical, electrical and optical properties of the TCO materials.

These coating structures can be applied as a solar cell and detailed test can be performed on those cells.

REFERENCES

[1] Jäger-Waldau, A., (2013). PV Status Report 2012, Publications Office of the European Union, Luxembourg.

[2] Nam, E., Kang, Y.H., Jung, D. and Kim, Y. S., (2010). "Anode Material Properties of Ga-Doped ZnO Thin Films By Pulsed DC Magnetron Sputtering Method For Organic Light Emitting Diodes", Thin Solid Films, 518: 6245-6248.

[3] Paine, D. C., Yaglioglu, B., Beiley, Z. and Lee, S., (2008). "Amorphous IZO-Based Transparent Thin Film Transistors", Thin Solid Films, 516: 5894-5898.

[4] Ebisawa, J. and Ando, E., (1998). "Solar Control Coating on Glass", Current Opinion in Solid State & Materials Science, 3: 386-390.

[5] Calestani, D., Zha, M., Mosca, R., Zappettini, A., Carotta, M.C., Natale, V. D. and Zanotti, L., (2010). "Growth of ZnO Tetrapods for Nanostructure-Based Gas Sensors", Sensors and Actuators B, 144: 472-478.

[6] Müller, J., Rech, B., Springer J. and Vanecek M., (2004). "TCO and Light Trapping In Silicon Thin Film Solar Cells", Solar Energy, 77: 917- 930.

[7] Selvan, J. A. A., Delahoy, A. E., Guo, S. and Li, Y. M., (2006). "A New Light Trapping TCO For nc-Si:H Solar Cells", Solar Energy Materials & Solar Cells, 90: 3371-3376.

[8] Zhu, S., Su, C.H., Lehoczky, S. L., Peters, P. and George, M.A., (2000). "Pressure Effects in ZnO Films Using Off-Axis Sputtering Deposition", Journal of Crystal Growth, 211: 106-110.

[9] Chaabouni, F., Abaab, M. and Rezig, B., (2004). "Effect of The Substrate Temperature On The Properties of ZnO Films Grown By RF Magnetron Sputtering", Materials Science and Engineering B, 109: 236-240.

[10] Gong, L. Lu, J. and Ye, Z., (2010). "Transparent and conductive Ga-doped ZnO films grown by RF magnetron sputtering on polycarbonate substrates", Solar Energy Materials & Solar Cells, 94:937–941.

[11] Joshi, R.N., Singh, V.P., and Clure, J.C.M., (1995). "Characteristics of Indium Tin Oxide Films Deposited By R.F. Magnetron Sputtering", Thin Solid Films, 257:32–35.

[12] Lien, S. Y., (2010). "Characterization and optimization of ITO thin films for application in heterojunction silicon solar cells", Thin Solid Films, 518:10–13.

[13] Yue, H., Wu A., Feng, Y., Zhang, X., and Li T., (2011). "Structures and properties of the Al-doped ZnO thin films prepared by radio frequency magnetron sputtering", Thin Solid Films, 519:5577–5581.

[14] Marotti, R. E., Giorgi, P., Machado, G. and Dalchiele, E.A., (2006). "Crystallite Size Dependence of Band Gap Energy For Electrodeposited ZnO Grown At Different Temperatures", Solar Energy Materials & Solar Cells, 90: 2356-2361.

[15] Ding, J., Chen, H., Zhao, X. and Ma, S., (2010). "Effect of Substrate And Annealing On The Structural And Optical Properties of ZnO:Al Films", Journal of Physics and Chemistry of Solids, 71: 346-350.

[16] Inamdar, D. Agashe, C. Kadam, P. and Mahamuni, S., (2012). "Doping optimization and surface modification of aluminum doped zinc oxide films as transparent conductive coating", Thin Solid Films, 520:3871–3877.

[17] Jin, B.J., Im, S. and Lee, S.Y., (2000). "Violet and UV Luminescence Emitted From ZnO Thin Films Grown On Sapphire By Pulsed Laser Deposition", Thin Solid Films, 366:107-110.

[18] Periasamy, C., Prakash, R. and Chakrabarti, P., (2010). "Effect of Post Annealing On Structural And Optical Properties of ZnO Thin Films Deposited By Vacuum Coating Technique", J Mater Sci: Mater Electron, 21: 309-315.

[19] Lee, Y. H., Song, M. H., Ju, B. K., Shin, D. K. and Oh, M. H., (1997). "Thin Film Phosphor Prepared by Physical Vapor Deposition for Field Emission Display Application", J. Vac. Sci. Technol. B, 15: 512-515.

[20] Nunes, P., Fortunato, E. and Martins, R., (2001). "Thin Film Phosphor Prepared By Physical Vapor Deposition for Field Emission Display Application" Thin Solid Films, 383: 277-280.

[21] Li, J., Huang, J. H., Zhang, Y. L., Yang, Y., Song, W. J. and Li, X.M.,(2011). "Effects of Rapid Thermal Annealing In Different Ambients On Structural, Electrical, And Optical Properties of ZnO Thin Films By Sol-Gel Method", J Electroceram, 26: 84-89.

[22] Natsume, Y. and Sakata, U., (2000). "Zinc Oxide Films Prepared By Sol-Gel Spin-Coating", Thin Solid Films, 372: 30-36.

[23] Sundaram, K.B. and Khan, A., (1997). "Characterization and Optimization of Zinc Oxide Films By r.f. Magnetron Sputtering", Thin Solid Films, 295: 87-91.

[24] Dumont, E., Dugnoille, B. and Bienfait, S., (1999). "Simultaneous Determination of The Optical Properties and of the Structure of R.F.-Sputtered ZnO Thin Films", Thin Solid Films, 353:93-99.

[25] Minami, T., Yamamoto, T. and Miyata, T., (2000). "Highly Transparent and Conductive Rare Earth-Doped ZnO Thin Films Prepared By Magnetron Sputtering", Thin Solid Films, 366: 63-68.

[26] Igasaki, Y. and Kanma, H., (2001). "Argon Gas Pressure Dependence of The Properties Of Transparent Conducting ZnO:Al Films Deposited On Glass Substrates", Applied Surface Science, 169: 508-511.

[27] Yoo, J., Lee, J., Kim, S., Yoon, K., Park, I.J., Dhungel, S.K., Karunagaran, B., Mangalaraj, D. and Yi, J., (2005). "High Transmittance and Low Resistive ZnO:Al Films for Thin Film Solar Cells", Thin Solid Films, 480: 213-217.

[28] Cho, J.S., Kim, Y.J., Lee, J.C., Park, S.H. and Yoon, K.H., (2011). "Structural and Optical Properties of Textured ZnO:Al Films On Glass Substrates Prepared By In-Line RF Magnetron Sputtering" Solar Energy Materials & Solar Cells, 95:190-194.

[29] Lu, Y.M., Hwang, W.S., Liu, W.Y. and Yang, J.S., (2001).Effect of RF Power on Optical and Electrical Properties of ZnO Thin Film by Magnetron Sputtering", Materials Chemistry and Physics, 72: 269-272.

[30] Chopra, K. L., Major, S. and Pandya, D. K., (1983). "Transparent Conductors--A Status Review", Thin Solid Films, 102: 1-46.

[31] Henseler, M.J.H., Lee, W.C.T., Miller, P., Durbin, S.M. and Reeves, R.J., (2006). "Optical and Photoelectrical Properties of ZnO Thin Films and the Effects of Annealing", Journal of Crystal Growth, 287: 48-53.

[32] Minami, T., Nanto, H. and Takata, S., (1983). "UV Emission from Sputtered Zinc Oxide Thin Films", Thin Solid Film, 109: 379-384.

[33] Hlaing, W.M., McCluskey, O., M.D., Huso, J. and Bergman, L., (2007). "Infrared and Raman Spectroscopy of ZnO Nanoparticles Annealed in Hydrogen", J. Appl. Phys., 102: 043529-043529-5.

[34] Sittinger, V., Ruske, F., Werner, W., Szyszka, B., Rech, B., Hüpkes, J., Schoöpe, G. and Stiebig, H., (2006). "ZnO:Al films Deposited by in-line Reactive AC Magnetron Sputtering for a-Si:H Thin Film Solar Cells", Thin Solid Films, 496:16- 25.

[35] Lee, W., Shin, S., Jung, D.R., Kim, J., Nahm, C., Moon, T. and Park, B., (2012). "Investigation of Electronic and Optical Properties in AlGaCodoped ZnO Thin Films", Current Applied Physics, 12: 628-631.

[36] Bouderbala, M., Hamzaoui, S., Amrani, B., Reshak, A. H., Adnane, M., Sahraoui, T. and Zerdali, M., (2008). "Annealing Effect on Properties of Transparent and Conducting ZnO Thin Films", Physica B, 403: 3326– 3330.

[37] Mattox, D.M., (1998).Handbook of Physical Vapor Deposition (PVD) Processing: Film Formation, Adhesion, Surface Preparation and Contamination Control, Noyes Publications, Westwood, New Jersey.

[38] Thornton, J.A., Influence of Apparatus Geometry and Deposition Conditions on the Structure and Topography of Thick Sputtered Coatings, J. Vacuum Science Technology 11 (1974) 666-670.

[39] Kluth, O., Schöpe, G., Hüpkes, J., Agashe, C., Müller, J. and Rech, B., (2003). "Modified Thornton Model for Magnetron Sputtered Zinc Oxide: Film Structure and Etching Behaviour", Thin Solid Films, 442: 80-85.

[40] Gao, W. and Li, Z., (2004). "ZnO Thin Films Produced by Magnetron Sputtering", Ceramics International, 30:1155-1159.

[41] Jeong, S.H., Lee, J.W., Lee, S.B. and Boo, J.H., (2003). "Deposition of Aluminum-Doped Zinc Oxide Films by RF Magnetron Sputtering and Study of Their Structural, Electrical and Optical Properties", Thin Solid Films, 435:78-82.

[42] Gordon, R.G., (2000). "Criteria for Choosing Transparent Conductors",MRS Bulletin, 52-57.

[43] Calnan, S. and Tiwari, A.N., (2010). "High Mobility Transparent Conducting Oxides For Thin Film Solar Cells",Thin Solid Films, 518: 1839–1849.

[44] Sovernigo, E., (2006). Deposition, Characterization and Optimization of The I-ZnO/ZAO Layer System For New High Efficiency Cu(In,Ga)Se_2 Solar Cells, Master Degree Thesis,Università Degli Studi Di Padova, Italia.

[45] Ginley, D. S., (2010). Handbook of Transparent Conductors, Springer New York Heidelberg Dordrecht, London.

[46] Zhang, Z., Bao, C., Yao, W., Ma, S., Zhang, L. and Hou, S., (2011). "Influence of Deposition Temperature On The Crystallinity of Al-doped ZnO Thin Films at Glass Substrates Prepared by RF Magnetron Sputtering method", Superlattices and Microstructures, 49: 644-653.

[47] Fortunato, E., Ginley, D., Hosono, H. and Paine, D. C., (2007). "Transparent Conductive Oxides for Photovoltaics", MRS Bulletin, 32: 242-247.

[48] Ozgür, U., Alivov, Y.I., Liu, C., Teke, A., Reshchikov, M.A., Dogan, S., Avrutin, V., Cho, S.J. and Morkoç, H., (2005). "A Comprehensive Review of ZnO Materials and Devices", Journal of Applied Physics, 98:1–103.

[49] Hu, J.-H. and Gordon, R.G., (1992). "Textured Aluminum-Doped Zinc Oxide Thin Films From Atmospheric Pressure Chemical-Vapor Deposition", J. Appl. Phys., 71: 880–890.

[50] Minami, T., (2005). "Transparent Conducting Oxide Semiconductors for Transparent Electrodes", Semicond. Sci. Technol. 20: 35–44.

[51] Beyer, W., Hüpkes J. and Stiebig H., (2007). "Transparent Conducting Oxide Films For Thin Film Silicon Photovoltaics", Thin Solid Films, 516: 147–154.

[52] Jagadish, C., (2006). Basic Propertiesand Applications of ZnO, Australian National University, Canberra, ACT 0200, Australia.

[53] Ellmer, K., Klein A. and Rech B.,(2008).Transparent Conductive Zinc Oxide Basics and Applications in Thin Film Solar Cells, Springer, Berlin Heidelberg, New York.

[54] Wagner, M. R., (2005). Optical Spectroscopy of Defects and Impurities in ZnO, Diploma Thesis, Technical University Berlin Faculty II: Mathematics and Science Institute of Solid State Physics, Germany.

[55] Kim, J.H., Ahn, B.D., Kim, C.H., Jeon, K.A., Kang, H.S. and Lee, S.Y., (2008). "Heat Generation Properties of Ga Doped ZnO Thin Films Prepared by RF-Magnetron Sputtering for Transparent Heaters", Thin Solid Films, 516:1330-1333.

[56] Bose, S., Ray, S. and Barua, A. K., (1996). "Textured Aluminum-Doped ZnO Thin Films Prepared By Magnetron Sputtering", J. Phys. D: Appl. Phys., 29: 1873–1877.

[57] Park, K. C., Young D., Kun, M. and Kim, H., (1997). "The Physical Properties Of Al-Doped Zinc Oxide Films Prepared By RF Magnetron Sputtering", Thin Solid Films, 305: 201-209.

[58] Ellmer, K., Kudella, F., Mientus, R., Schieck, R. and Fiechter, S., (1994). "Influence Of Discharge Parameters On The Layer Properties Of Reactive Magnetron Sputtered ZnO:Al Films", Thin Solid Films, 247:15-23 15.

[59] Wang, H., Xu, J., Ren, M. and Yang, L., (2008). "Room Temperature Deposition And Properties Of ZnO:Al Thin Films By Nonreactive DC Magnetron Sputtering", J Mater Sci: Mater Electron, 19:1135–1139.

[60] Park, S.M., Gu, G.H. and Park, C.G., (2011). "Effects of Mg Doping to Optimize the Properties of ZnO:Al for Transparent Conductive Oxide (TCO) Films", Phys. Status Solidi A, 208:2688-2691.

[61] Choi, B.G., Kim, I.H., Kim, D.H, Lee, K.S., Lee, T.S., Cheong, B., Baik, Y.-J. and Kim, W.M., (2005). "Electrical, Optical and Structural Properties of Transparent and Conducting ZnO Thin Films Doped With Al and F by RF Magnetron Sputter", Journal of the European Ceramic Society, 25: 2161–2165.

[62] Houng, B. and Chen, H. B., (2012). "Investigation of AlF3 Doped ZnO Thin Films Prepared By RF Magnetron Sputtering", Ceramics International, 38: 801–809.

[63] Assuncao, V., Fortunato, E., Marquesa, A., A guasa, H., Ferreiraa, I., Costab, M.E.V. and Martinsa, R., (2003). "Influence of the Deposition Pressure On The Properties Of Transparent And Conductive ZnO:Ga Thin-Film Produced By R.F. Sputtering At Room Temperature", Thin Solid Films, 427: 401–405.

[64] Lai, K.-C., Liu, C.-C., Lu, C.-h., Yeh, C.-H. and Houng, M.-P., (2010). "Characterization of ZnO:Ga Transparent Contact Electrodes For Micro Crystalline Silicon Thin Film Solar Cells", Solar Energy Materials & Solar Cells, 94:397–401.

[65] Wu, F., Fang, L., Zhou, K., Pan, Y.J., Peng, L.P., Huang, Q.L., Yang, X.F. and Kong, C.Y., (2010)."Effect of Thickness on the Properties of Ga-doped Nano-ZnO Thin Films Prepared by RF Magnetron Sputtering", J Supercond. Nov. Magn., 23: 905–908.

[66] Chu, S.-Y., Water, W. and Liaw, J.-T., (2003). "Influence of Post Deposition Annealing On The Properties Of ZnO Films Prepared By RF Magnetron Sputtering", Journal of the European Ceramic Society, 23: 1593–1598.

[67] Chang, S.-C. and Shiao, M.-H., (2007). "Smooth Indium Zinc Oxide Film Prepared by Sputtering a In2O3: ZnO 95:5 Target", Microelectronics Journal, 38: 1202–1206.

[68] Kim, D.-G., Lee, S., Kim, D.-H., Lee, G.-H.and Isshiki, M., (2008). "Temperature Dependence of the Microstructure and Resistivity of Indium Zinc Oxide Films Deposited By Direct Current Magnetron Reactive Sputtering", Thin Solid Films, 516: 2045–2049.

[69] Aw, K.C., Tsakadze, Z., Lohani, A. and Mhaisalkar, S., (2009). "Influence of Radio Frequency Sputtering Power towards the Properties of Indium Zinc Oxide Semiconducting Films", ScriptaMaterialia, 60: 48–51.

[70] Cao, H.T., Pei, Z.L., Gonga, J., Suna, C., Huang, R.F. and Wen, L.S., (2004). "Transparent Conductive Al and Mn Doped ZnO Thin Films Prepared By DC Reactive Magnetron Sputtering", Surface and Coatings Technology, 184: 84–92.

[71] Zhu, B. L., Zhao, X. Z., Su, F. H., Li, G. H., Wu, X. G., Wu, J. and Wu, R., (2010). "Low Temperature Annealing Effects on the Structure and Optical Properties of ZnO Films Grown by Pulsed Laser Deposition" Vacuum, 84: 1280-1284.

[72] Kim, D., Yun, I. and Kim, H., (2010). "Fabrication of Rough Al Doped ZnO Films Deposited By Low Pressure Chemical Vapor Deposition For High Efficiency Thin Film Solar Cells", Current Applied Physics, 10: 459- 462.

[73] Choi, Y. J., Gong, S. C., Johnson, D. C., Golledge, S., Yeom, G. Y. and Park, H. -H., (2013). "Characteristics Of The Electromagnetic Interference Shielding Effectiveness Of Al-Doped ZnO Thin Films Deposited By Atomic Layer Deposition", Applied Surface Science, 269: 92-97.

[74] Kim, Y. S. and Tai, W. P., (2007). "Electrical and Optical Properties of Al-Doped ZnO Thin Films By Sol–Gel Process", Applied Surface Science, 253:4911-4916.

[75] Hoon, J. W., Chann, K. Y. and Tou, T. Y., (2013). "Zinc Oxide Films Deposited By Radio Frequency Plasma Magnetron Sputtering Technique" Ceramics International, 39: 269-273.

[76] Swann, S., (1988). Magnetron Sputtering, Physics in Techno1ogy, 19: 67-75.

[77] Wasa, K. and Hayakawa S., (1992). Handbook of Sputter Deposition Technology Principles, Technology and Applications, Noyes Publications, Fairview Avenue, Westwood, New Jersey.

[78] Jackson, K. A., (2004). Kinetic Processes Crystal Growth, Diffusion, and Phase Transitions in Materials, Wiley-VCH Verlag, Weinheim.

[79] Bunshah, R. F., (1994). Handbook of Deposition Technologies for Films and Coatings Science, Technology and Applications, Noyes Publications, Mill Road, Park Ridge, New Jersey.

[80] Martin, P.M., (2009). Handbook of Deposition Technologies for Thin Films and Coatings, Elsevier, United States.

[81] Grundman, M., (2010). The Physics of Semiconductor", Springer-Verlag, Berlin Heidelberg.

[82] McGuire, G. E., (1988). Semiconductor Materials and Process Technology Handbook, Noyes Publications, United States.

[83] Lieberman, M. A., Lichtenberg A. J.,(2005). Principles of Plasma Discharges and Materials Processing, John Wiley & Sons, Inc., Hoboken, New Jersey.

[84] Markvart, T. and Castafier L., (2005). Practical Handbook of Photovoltaics: Fundamentals and Applications, Elsevier, United States

[85] Wasa, K., Kitabatake, M. and Adachi, H., (2004). Thin Film Materials Technology, Sputtering of Compound Materials, William Andrew Publishing, Springer-Verlag.

[86] Piascik, J. R.,(2007). Evaluation of Structure and Material Properties of RF Magnetron Sputter-Deposited Yttria-Stabilized Zirconia Thin Films, Doctor of Philosophy, University of North Carolina, Chapel Hill.

[87] Seshan, K., (2002). Handbook of Thin-Film Deposition Processes and Techniques, Noyes Publications, United States of America.

[88] Nunes, P., Costa, D., Fortunato, E. and Martins, R., (2002). "Performances Presented By Zinc Oxide Thin Films Deposited By R.F. Magnetron Sputtering Vacuum", 64: 293-297.

[89] Saad, M. and Kassis, A., (2012). "Effect of Rf Power On The Properties of Rf Magnetron Sputtered ZnO:Al Thin Films" Materials Chemistry and Physics, 136: 205-209.

[90] Song, D., Widenborg, P., Chin, W. and Aberle, A.G., (2002). "Investigation of Lateral Parameter Variations of Al-Doped Zinc Oxide Films Prepared On Glass Substrates By Rf Magnetron Sputtering", Solar Energy Materials & Solar Cells, 73: 1-20.

[91] Zhang, Y., Du, G., Liu, D., Wang, X., Ma, Y., Wang, J., Yin, J., Yang, X., Hou, X. and Yang, S., (2002). "Performances Presented By Zinc Oxide Thin Films Deposited By R.F. Magnetron Sputtering", Journal of Crystal Growth, 243: 439 - 443.

[92] Youssef, S., Combette, P., Podlecki, J., Asmar, R. A. and Foucaran, A., (2009). "Structural and Optical Characterization of ZnO Thin Films Deposited By Reactive RF Magnetron Sputtering", Crystal Growth & Design, 9:1088 - 1094.

[93] Kim, K.K., Song, J.H., Jung, H.J., Choi, W.K., Park, S.J. and Song, J.H., (2000). "The Grain Size Effects On The Photoluminescence Of ZnO α-Al2O3 Grown By Radio-Frequency Magnetron Sputtering", Journal of Applied Physics, 87: 3573 - 3575.

[94] Kim, K.K., Song, J.H., Jung, H.J., Choi, W.K., Park, S.J., Song, J.H. and Lee, J.Y., (2000). "Photoluminescence and Heteroepitaxy of ZnO on Sapphire Substrate 0001 Grown By RF Magnetron Sputtering", J. Vac. Sci. Technol. A, 18:2864 - 2868.

[95] Kim, H. W. and Kim, N. H., (2003). "Structural Studies of Room-Temperature RF Magnetron Sputtered ZnO Films under Different RF Powered Conditions", Materials Science and Engineering B, 103: 297 - 302.

[96] Zhao, Y.J., Jiang, D.Y., Zhao, M., Deng, R., Qin, J.M., Gao, S., Liang, Q.C. and Zhao, J.X., (2013). "Effects of Power On Properties of ZnO Thin Films Grown By Radio Frequency Magnetron Sputtering", Applied Surface Science, 266: 440 - 444.

[97] Jeong, W.J., Kim, S.K. and Park, G.C., (2006). "Preparation and Characteristic of ZnO Thin Film With High and Low Resistivity For an Application of Solar Cell", Thin Solid Films 506– 507: 180-183.

[98] Yang, W., Liu, Z., Peng, D.-L., Zhang, F., Huang, H., Xie, Y. and Wua, Z., (2009). "Room-Temperature Deposition Of Transparent Conducting Al-Doped ZnO Films By RF Magnetron Sputtering Method", Applied Surface Science, 255: 5669–5673.

[99] Duygulu, N.E. Kodolbas, A.O. and Ekerim, A., (2013). "Influence of R.F Power on Structural Properties of ZnO Thin Films", Journal of Crystal Growth, 381:51–56.

[100] Zhu, B.L., Wang, J., Zhu, S.J., Wu, J., Zeng, D.W. and Xie, C.S., (2012). "Optimization of Sputtering Parameters for Deposition of Al-Doped ZnO Films by RF Magnetron Sputtering In Ar+H_2 Ambient At Room Temperature", Thin Solid Films, 520: 6963 -6969.

[101] Kim, D. K. and Kim, H. B., (2012). "Dependence of the Properties of Sputter Deposited Al-Doped ZnO Thin Films on Base Pressure", Journal of Alloys and Compounds, 522: 69-73.

[102] Bai, S.-N. and Tseng, T.-Y., (2009). "Electrical and Optical Properties of ZnO:Al Thin Films Grown by Magnetron Sputtering", J. Mater. Sci: Mater Electron, 20:253–256.

[103] Liao, Y.-P., Zhang, J.-H., Li, S.-X., Guo, Z.-S., Cao, J., Zhu, W.-Q., and Li, X., (2010). "Structural Evolution of ZnO Films Deposited By R.F. Magnetron Sputtering On Glass Substrate", Phys. Status Solidi A, 207: 1850–1853.

[104] Van De Pol, F. C. M., Blom, F. R. and Popma, Th J. A., (1991). "R.F. Planar Magnetron Sputtered Zno Films I: Structural Properties", Thin Solid Films, 204: 349 – 364.

[105] Bishop, C.A., (2007) Vacuum Deposition onto Webs, Films, and Foils, William Andrew Publishing, 13 Eaton Avenue, Norwich, United States of America.

[106] Messier, R., Giri, A. P., R. and Roy, A., (1984). "Revised Structure Zone Model For Thin Film Physical Structure", Journal of Vacuum Science & Technology A, 2: 500-503.

[107] Adamik, M., Barna, P.B. and Tomov, I., (1998). "Columnar Structures in Polycrystalline Thin Films Developed by Competitive Growth", Thin Solid Films, 317: 64–68.

[108] Cras, J.J., Rowe-Taitt, C.A., Nivens, D.A. and Ligler, F.S., (1999). "Comparison of chemical cleaning methods of glass in preparation for silanization" Biosensors & Bioelectronics, 14: 683–688.

[109] Jain, V.K. and Kulshreshth, A. P., (1981). "Indium-Tin-Oxide Transparent Conducting Coatings on Silicon Solar Cells and Their "Figure of Merit"", Solar Energy Materials, 4:151–158.

[110] Beneking, C., Rech, B., Wieder, S., Kluth, O., Wagner, H., Frammelsberger, W., Geyer, R., Lechner, P., Rübel, H. and Schade, H., (1999). "Recent Developments Of Silicon Thin Film Solar Cells On Glass Substrates", Thin Solid Films, 351: 241–246.

[111] Granqvist, C.G., (2007). "Transparent Conductors as Solar Energy Materials: A Panoramic Review", Solar Energy Materials & Solar Cells, 91: 1529–1598.

[112] Letcher, T., (2008). Future Energy: Improved, Sustainable and Clean Options for our Planet, Elsevier, Amsterdam, the Netherlands.

[113] Mishima, T., Taguchi, M., Sakata, H. and Maruyama, E., (2011). "Development Status of High-Efficiency HIT Solar Cells", Solar Energy Materials & Solar Cells, 95: 18–21.

[114] Tsunomura, Y., Yoshimine, Y., Taguchi, M., Baba, T. Kinoshita, T., Kanno, H., Sakata, H., Maruyama, E. and Tanaka, M., (2009). "Twenty-two Percent Efficiency HIT Solar Cell", Solar Energy Materials & Solar Cells, 93: 670–673.

[115] Goetzberger, A., Hebling, C. and Schock, H.-W., (2003). "Photovoltaic Materials, History, Status and Outlook", Materials Science and Engineering R, 40: 1–46.

[116] Pehlivan, O., (2013). Growth and Morphological Characterization of Intrinsic Hydrogenated Amorphous Silicon Thin Film For a-Si:H/c-Si Heterojunction Solar Cells, Doctor of Philosophy in Physics Department, Middle East Technical University, Ankara.

[117] Lee, J.C., Kang, K.H., Kim, S.K., Yoon, K.H., Park, I.J. and Song, J., (2000). "RF Sputter Deposition of the High-Quality Intrinsic and n-Type ZnO Window Layers For Cu(In, Ga)Se_2- Based Solar Cell Applications", Solar Energy Materials and Solar Cells, 64: 185–195.

[118] Klug, H.P. and Alexander L.E., (1974). X-ray Diffraction Procedures, John Wiley and Sons, New York.

[119] Lu, M., (2008). Silicon Heterojunction Solar Cell and Crystallization of Amorphous Silicon, Doctor of Philosophy in Physics Department, University of Delaware, United States.

[120] Luque, A. and Hegedus S., (2011). Handbook of Photovoltaic Science and Engineering, John Wiley and Sons, United Kingdom.

[121] Dimova-Malinovska, D., Tzenov, N., Tzolov, M. and Vassilev, L., (1998). "Optical and Electrical Properties of R.F. Magnetron Sputtered ZnO:Al Thin Films", Materials Science and Engineering B, 52: 59- 62.

[122] Lee, J., Lee, D., Lim, D. and Yang, K., (2007). "Structural, Electrical And Optical Properties of ZnO:Al Films Deposited On Flexible Organic Substrates For Solar Cell Applications", Thin Solid Films, 515: 6094 – 6098

[123] Kim, H., W., and Kim, N. H., (2003). "Structural Studies of Room-Temperature RF Magnetron Sputtered ZnO Films under Different RF Powered Conditions", Materials Science and Engineering B, 103:297-302.

[124] Lin, S. S. and Huang, J. L., (2004). "Effect of Thickness on the Structural and Optical Properties of ZnO Films by R.F. Magnetron Sputtering Surface & Coatings Technology", 185: 222-227.

[125] Park, Y. J., Kim, H. N. and Shin, H. H., (2009). "Effects of Deposition Temperature On The Crystallinity of Ga-Doped ZnO Thin Films On Glass Substrates Prepared By Sputtering Method", Applied Surface Science, 255: 7532-7536.

[126] Yoo, J., Lee, J., Kim, S., Yoon, K., Park, I. J., Dhungel, S. K., Karunagaran, B., Mangalaraj, D. and Yi J., (2005). "High Transmittance and Low Resistive ZnO:Al Films For Thin Film Solar Cells", Thin Solid Films, 480:213-217.

[127] Tari, O., Aronne, A., Addonizio, M. L., Daliento, S., Fanelli, E. and Pernice, P., (2012). "Sol–Gel Synthesis of ZnO Transparent and Conductive Films: A Critical Approach", Solar Energy Materials & Solar Cells, 105: 179-186.

[128] Ndong, R. O., Ferblantier, G., Kalfioui, M. A., Boyer, A. and Foucaran, A., (2003). "Properties of RF Magnetron Sputtered Zinc Oxide Thin Films", Journal of Crystal Growth, 255: 130-135.

[129] Sim, K. U., S. Shin, W., Moholkar, A.V., Yun, J. H., Moon, J. H. and Kim, J. H., (2010). "Effects of Dopant (Al, Ga, and In) on the Characteristics of ZnO Thin Films Prepared By RF Magnetron Sputtering System", Current Applied Physics, 10: 463-467.

[130] Bouderbala, M.,Hamzaoui, S., Stambouli, A.B. and Bouziane, H., (1999). "Effects of the Position Substrate Upon the Structural Behaviour, Electrical and Optical Properties of Zinc-Oxide Films Used in Solar Cells", Applied Energy, 64: 89-96.

[131] Rahmane, S., Djouadi, M.A., Aida, M.S., Barreau, N., Abdallah, B. and Zoubir, N. H., (2010). "Power and Pressure Effects Up on Magnetron Sputtered Aluminum Doped ZnO Films Properties", Thin Solid Films, 519: 5- 10.

[132] Kuo, S.-Y. Liu, K.-C. Lai, F.-I. Yang, J.-F. Chen, W.-C. Hsieh, M.-Y. Lin, H.-I., and Lin, W.-T., (2010). "Effects of RF Power on the Structural Optical and Electrical Properties of Al-Doped Zinc Oxide Films", Microelectronics Reliability 50:730–733.

[133] Fernandez, S. Martinez-Steele, A. Gardai, J.J. and Naranjo, F.B., (2009). "Radio Frequency Sputter Deposition Of High-Quality Conductive And Transparent ZnO:Al Films On Polymer Substrates For Thin Film Solar Cells Applications", Thin Solid Films, 517:3152–3156.

[134] Grovenor, C. R. M., Hentzells, H. T. G. and Smith, D. A., (1984). "The Development of Grain Structure during Growth of Metallic Films", Acta metal., 32: 773-781.

[135] Barna, P.B. and Adamik, M., (1998). "Fundamental Structure Forming Phenomena of Polycrystalline Films and the Structure Zone Models", Thin Solid Films, 317: 27–33.

[136] Ri, K.H. Wang, Y. Zhou, W.L. Gao, J.X. Wang, X.J. and Yu, J., (2011). "The Structural Properties Of Al Doped ZnO Films Depending On The Thickness And Their Effect On The Electrical Properties", Applied Surface Science, 258:1283–1289.

[137] Wang, Z.A. Chu, J.B. Zhu, H.B. Sun, Z. Chen, Y.W. and Huang, S.M., (2009). "Growth of ZnO:Al Films By RF Sputtering At Room Temperature For Solar Cell Applications", Solid-State Electronics, 53:1149–1153.

[138] Song, D., (2008). "Effects of r.f Power on Surface-Morphological Structural And Electrical Properties Of Aluminum-Doped Zinc Oxide Films By Magnetron Sputtering", Applied Surface Science, 254:4171–4178.

[139] Kar, J.P. Kim, S. Shin, B. Park, K.I. Ahn, K.J. Lee, W. Cho, J.H. and Myoung, J.M., (2010). "Influence of Sputtering Pressure On Morphological. Mechanical and Electrical Properties of Al-Doped ZnO Films", Solid-State Electronics, 54:1447–1450.

[140] Zhu, B.L. Zhu, S.J. Wang, J. Wu, J. Zeng, D.W. and Xie, C.S., (2011). "Thickness Effect On Structure And Properties Of ZAO Thin Films By RF

Magnetron Sputtering At Different Substrate Temperatures", Physica E, 43:1738–1745.

[141] Zhu, H. Hüpkes, J. Bunte, E. Gerber, A. and Huang, S.M., (2010). "Influence Of Working Pressure On ZnO:Al Films From Tube Targets For Silicon Thin Film Solar Cells", Thin Solid Films, 518:4997–5002

[142] Fu, E.G, Zhuang, D.M., Zhang, G., Ming, Z., Yang, W.F. and Liu, J.J., (2004). "Properties Of Transparent Conductive ZnO:Al Thin Films Prepared By Magnetron Sputtering", Microelectronics Journal, 35: 383–387.

[143] Hong, R.J. Jiang, X. Szyszka, B. Sittinger, V. Xu, S.H. Werner, W.W. and Heide, G., (2003). "Comparison of the ZnO:Al films deposited in static and dynamic modes by reactive mid-frequency magnetron sputtering", Journal of Crystal Growth, 253:117–128.

[144] Kluth, O. Schöpea, G. Rech, B. Menner, R. Oertel, M. Orgassa, K. and Schock, H.W., (2006). "Comparative Material Study On RF And DC Magnetron Sputtered ZnO:Al films", Thin Solid Films, 502:311–316.

[145] Wang, F., Wu, M.Z, Wang, Y.Y., Yu, Y.M., Wu, X.M and Zhuge, L.J., (2013). "Influence Of Thickness And Annealing Temperature On The Electrical Optical And Structural Properties of AZO Thin films", Vacuum, 89: 127–131

[146] Chang, J.F. Wang, H.L. and Hon, M.H., (2000). "Studying of transparent conductive ZnO: Al thin films by RF reactive magnetron sputtering", Journal of Crystal Growth, 211:93–97.

[147] Choi, B.G. Kim, I.H. Kim, D.H. Lee, K.S. Lee, T.S. Cheong, B. Baik, Y.-J. and Kim, W.M., (2005). "Electrical Optical and Structural Properties of Transparent and Conducting ZnO Thin Films Doped with Al and F by R.F Magnetron sputter", Journal of the European Ceramic Society, 25:2161–2165.

[148] Malinovska, D.D. Tzenov, N. Tzolov, M. and Vassilev, L., (1998). "Optical And Electrical Properties Of R.F. Magnetron Sputtered ZnO:Al Thin Films", Materials Science and Engineering B, 52:59–62.

CURRICULUM VITAE

PERSONAL INFORMATION

Name Surname :Nilüfer DUYGULU

Date of birth and place :16.08.1981-Eskişehir

Foreign Languages :İngilizce

E-mail :niluferduygulu@gmail.com

EDUCATION

Degree	Department	University	Date of Graduation
Master	Metalurji ve Malzeme Müh.	Yıldız Teknik Üni	2007
Master	Seramik, Cam ve Yapı Malzemeleri Enstitüsü	T.U.Bergakademie Freiberg	2006-2007
Undergraduate	MalzemeBilimiveMühendisliği	AnadoluÜniversitesi	2005
High School		Eskişehir Anadolu Lisesi	2000

WORK EXPERIENCE

Year	Corporation/Institute	Enrollment
2007 -	Yıldız Teknik Üniversitesi	Araştırma Görevlisi

PUBLISHMENTS

Papers

1. **N. Evcimen Duygulu**, , A.O. Kodolbas, A. Ekerim, Influence of r.f Power on Structural Properties of ZnO Thin Films, Journal of Crystal Growth, 381, 51–56, (2013).

2. **N. Evcimen Duygulu**, Aylin Bekem, Isıl İşlemin Emaye Özellikleri Üzerine Etkisinin İncelenmesi, Türkiye Seramik Federasyonu Dergisi, Sektör: 43, sf.140-149Temmuz-Ekim (2013)

Conference Papers

1. **Duygulu Evcimen N**, Yılmaz O., Pehlivan O., Kodolbaş A. O., Ekerim A., Influence of Deposition Parameters on ZnO and ZnO:Al Thin Films, E-MRS 2013 Fall Meeting, Sempozyum K, 16-20 Ekim, Polonya (2013)

2. **Duygulu Evcimen N,** Kodolbaş A. O., Duygulu Ö., Ekerim A., Structural, Optical and Electrical Properties of Zinc Oxide and Aluminum Doped Zinc Oxide for Photovoltaic Applications, Solar TR2 2012, Antalya, Türkiye (2012).

3. **Evcimen N,** Ekerim A.,Investigation of 5 mol% YSZ Electrolyte for SOFC, TMS (The Minerals, Metals & Materials Society),3 Şubat 2011, San Diego, C.A, Proceeding CD-room pp.457-464 (2011)

4. **Ekerim A.,** Evcimen N, Sezer R., ToplamVerimli Bakımın Ekonomik Analizi, 15.Uluslararası Metalurji ve Malzeme Kongresi, 11-13 Kasım 2010, İstanbul, Türkiye , (Davetli konuşmacı).(2010)

5. **Evcimen N.,** Sezer R., Ekerim A.,Characteristic Investigation of YSZ Electrolyte for SOFC, ICHP2 -2010 (International Conference on Hydrogen Production-2010), 16-18 Haziran, İstanbul, Türkiye, AN-61 (Oral Presentation).(2010)

6 Evcimen N., Bayrak Y., Ekerim A., Application of ECAP on Commercial Purity Aluminum, TMS (The Minerals, Metals & Materials Society),14-19 Mart 2010, Seattle, W.A. (Oral Presentation).(2010)

7. Ekerim A., Altınbay A., **Evcimen N.,** Effect of Composition and Heat Treatment to Mechanical Properties on Cast Steels, 14.Uluslararası Metalurji ve Malzeme Kongresi, 16-18 Ekim 2008, (Oral Presentation), İstanbul, Türkiye (2008)

8. Önemli U., **Evcimen N.,** Ekerim A., Elektro Cüruf Ergitme Prosesi ve Prosesin Modellenmesi, IMSP 2008, 12 th International Materials Symposium, 15- 17 Ekim, 2008, Denizli, Türkiye.(Poster Presentation) (2008)

9. Özer G., Evcimen N., Ekerim A., High Purity Pig Iron Production by Using Steel Scrap and Comparison with Sorelmatel, 5. Uluslararası İleri Teknolojiler Sempozyumu (IATS'09), 13-15 Mayıs 2009, Karabük, Türkiye.(Oral Presentation)(2009)

Projects

1. a-Si:H/c-Si HeteroeklemGüneşPillerininFabrikasyonuveArayüzeyKusurlarınınİncelenmesi,TÜBİTAK, Proje No:108T016, Proje Koordinatörü: Doç. Dr. Alp Osman KODOLBAŞ (2008-2012).

2. a-Si:H/c-Si HeteroeklemGünesPilleriİçinSaydamİletkenOksitTabakalarınınBüyütülmesiveTermodinamikAnaliziProje No: 2012-07-02-DOP03-YTÜ BAPK DOP Projesi Araştırmacı (01/06/2012-01/10/2014)

3. KompozitPeletlerdenDemirTanesiÜretimindeRedükleyiciOlarakPlastikAtıkKullanımınınAraştırılması", KAP, Proje No: 2011-07-02-KAP02, YTÜ BAPK KAP Projesi – Araştırmacı (01/011/2011-01/10/2013)